UC Berkeley
UC Berkeley Electronic Theses and Dissertations

Title
DEVELOPMENT AND APPLICATION OF NOVEL DIAGNOSTICS TO PROBE DYNAMICALLY COMPRESSED MATERIALS

Permalink
https://escholarship.org/uc/item/92t6g0mh

Author
Ali, Suzanne

Publication Date
2015

Peer reviewed|Thesis/dissertation

eScholarship.org Powered by the California Digital Library
University of California

Development and Application of Novel Diagnostics to Probe Dynamically Compressed Materials

By

Suzanne Jihad Muhammad Ali

A dissertation submitted in partial satisfaction of the

requirements for the degree of

Doctor of Philosophy

in

Chemistry

in the

Graduate Division

of the

University of California, Berkeley

Committee in charge:

Professor Raymond Jeanloz, Co-Chair

Professor Richard Saykally, Co-Chair

Professor Tanya Cuk

Professor Geoff Marcy

Fall 2015

Development and Application of Novel Diagnostics to Probe Dynamically Compressed Materials

Copyright 2015

By

Suzanne Jihad Muhammad Ali

Abstract

Development and Application of Novel Diagnostics to Probe Dynamically Compressed Materials

By

Suzanne Jihad Muhammad Ali

Doctor of Philosophy in Chemistry

University of California, Berkeley

Professor Raymond Jeanloz, Co-Chair

Professor Richard Saykally, Co-Chair

Two particular experimental approaches have been experiencing increased interest, that of dynamic spectroscopy and that of 2D measurements. The first allows us to obtain a better understanding of the electronic and chemical processes taking place under shock loading while the second provides a detailed view into the microscopic and macroscopic heterogeneities which directly influence material behavior and have been difficult to identify in the bulk material. In order to better understand these behaviors and their origins, two approaches have been utilized. A novel dynamic broadband optical reflectivity diagnostic was developed to probe changes in material properties on the scale of electronic structure and an existing, but only recently developed high resolution velocimetry system was used to observe the aforementioned changes on larger, microstructural scales.

In order to expand understanding of the chemical and mechanical responses of condensed matter to dynamic shock compression two projects were undertaken. The first was the development of a broadband optical reflectivity diagnostic with both time and wavelength resolution. The Shock Wave Optical Reflectivity Diagnostic (SWORD) has enabled us to study the dynamic optical reflectivity in shocked samples over the visible and near-infrared, across a time span of nanoseconds and with a resolution of 0.5 ns and 10 nm. Laser velocimetry was used in tandem with the SWORD to determine kinematic properties of the shocked samples, such as pressure and density. This novel diagnostic has been applied to the semiconductor-to-metal transition in single-crystal germanium and used to observe both a general reflectivity increase on metallization and a wavelength dependent response as a function of pressure.

The second project involved the application of the recently developed two dimensional Velocity Interferometry System for Any Reflector (2D VISAR,

alternatively Janus High Resolution Velocimeter, JHRV) to study anisotropic shock wave propagation and dynamic heterogeneous deformation and fracture in diamond. In combination with the aforementioned laser velocimetry (also VISAR), we have obtained velocity histories and two-dimensional velocity maps and images of the shocked target at various time points after breakout. Significant anisotropy in both the elastic and inelastic waves was observed in single-crystal diamond samples. Characteristic length scales for the fracture of polycrystalline diamond samples of varying grain size were also determined.

Table of Contents

ABSTRACT *1*

ACKNOWLEDGEMENTS ..... *III*

SECTION I – DEVELOPMENT AND TESTING OF THE SHOCK WAVE OPTICAL REFLECTIVITY DIAGNOSTIC *1*

CHAPTER 1: INTRODUCTION 1

CHAPTER 2: GENERATING AND CHARACTERIZING HIGH PRESSURE STATES USING LASER-DRIVEN DYNAMIC COMPRESSION 3

Experimental Techniques and Target Design *3*

Characterizing the Shocked State: Rankine-Hugoniot Relations *4*

Existing Diagnostics *7*

CHAPTER 3: CONSTRUCTION AND CALIBRATION OF A BROADBAND OPTICAL REFLECTIVITY DIAGNOSTIC 8

Abstract *8*

Part I: Design and Construction *8*

Part II: Analysis *16*

Part III: Calibration *20*

Part IV: Future Improvements *21*

CHAPTER 4: OPTICAL PROPERTIES OF SHOCK COMPRESSED GERMANIUM 22

Abstract *22*

Introduction *23*

Methods *24*

Results *25*

Discussion and Conclusions *32*

SECTION II – ANISOTROPIC DEFORMATION AND FRACTURE 39

ABSTRACT 40

INTRODUCTION 41

CHAPTER 1: EXPERIMENTAL DETAILS 44

Target Design *44*

Planar Shock Targets *45*

Spherical Shock Targets *46*

Raw Data *46*

CHAPTER 2: ANISOTROPIC WAVE PROPAGATION IN DIAMOND 51

Abstract *51*

Introduction *51*
Methods *54*
Results *55*
Discussion *71*
Conclusions *72*
Future Work *72*
CHAPTER 3: HETEROGENEOUS DEFORMATION AND FRACTURE IN POLYCRYSTALLINE DIAMOND 73
Abstract *73*
Introduction *73*
Methods *75*
Results *76*
Discussion *108*
Conclusions *117*
Future Work *117*
REFERENCES ***120***

Acknowledgements

I'd like to thank my advisers, Raymond Jeanloz at UC Berkeley and Rip Collins at LLNL. As an adviser, Raymond gave me the freedom to study what interested me and was always ready to provide advice and resources (and patience with my tendency to obsess over the experiments themselves and forget about the science…). Rip provided support for most of the experiments detailed in this dissertation as well as guidance and advice.

I'd also like to thank the other Jeanloz group members, Arianna Gleason, Dylan Spaulding, and Zach Geballe for providing both office entertainment and excellent advice. Dylan in particular paved the way for much of my optical reflectivity research at LLNL. Cindy Bolme was an excellent teacher, I'm fairly certain I wouldn't be nearly as competent in lab without her patient tutelage. (I also wouldn't be as obsessive about proper washer use and nylon-tipped thumbscrews...) Ray Smith was also incredibly helpful in lab, particularly for the 2D VISAR experiments. Peter Celliers was an invaluable resource for both experimental optics questions as well as data analysis. He developed the analysis code I used for the JHRV data and helped me learn how to use it and disentangle some of the more troublesome shots. Jon Eggert provided the initial motivation for some of the JHRV data and was an invaluable source of information regarding solid state physics. Dave Erskine was always ready to help with data analysis questions. (And both could be relied upon to get as excited about science as everyone should be). Damian Swift provided assistance with HYADES and general entertainment. Amy Lazicki and Malcolm McMahon's group at Edinburgh gave me the chance to test my reflectivity diagnostic on new materials. I'd also like to thank the rest of the Shock Physics Group at Lawrence Livermore National Lab. Tim, Stephanie, Walt, Antonio, and Carol provided both help with target fabrication and advice about target design. At the Jupiter Laser Facility I'd like to thank all three Jims, Carl, Rob, Gary, Dave, Scott, Chuck, Steven, John, and Ed for invaluable technical assistance and patience with my frequent (and occasionally ridiculous) requests. I'd also like to thank the facility head, Bob Cauble, for advice and constant reminders that I need to write up.

Other collaborators I am indebted to are Andrew Ng, Ying Tsui and Zhijiang Chen who were all involved in the ESSI experiment, Stephine Brygoo who worked on some of the 2D VISAR experiments and Marius Millot for some early experiments which helped me get my bearings in Target Area 1.

Finally, I'd like to thank my parents for a bunch of things, (including paying for college and generally being awesome). And thanks Jongjin. Thanks Meatball.

Section I – Development and Testing of the Shock Wave Optical Reflectivity Diagnostic

Chapter 1: Introduction

Materials undergoing dynamic compression, whether with shock, multi-shock or ramp loading, can exhibit dramatic changes in physical and chemical properties that are evident in the optical properties of the sample. Measurement of sample reflectivity is vital for characterizing changes in chemical bonding, and the associated electronic structure, of materials [1-7]. Although current diagnostics are sufficient for many Hugoniot measurements [8, 9], documenting time- and wavelength-dependent optical properties remains a challenge. Velocimetry does provide kinematic information, but requires significant volume changes in order to indicate phase changes or chemical reactions, and is often incapable of distinguishing important changes in the electronic structure of the sample. Single channel pyrometry across the visible wavelengths is also frequently used to estimate the temperature of shocked materials and in tandem with velocimetry can provide more detailed information about the material's path through pressure-temperature space, but the single-channel nature of the diagnostic and frequent blackbody (or nearly blackbody) assumption of the material's emissivity often results in large potential errors due to uncertain wavelength-dependent emissivity [10, 11]. While an acceptable assumption for many experiments, if the shocked material undergoes any changes in optical properties or if the emissivity of the material is considerably different from a blackbody value, measurement of thermal emission by single-channel pyrometry does not accurately represent temperature of the sample. Recent publications highlight the need for broadband reflectivity measurements as a means of determining the wavelength-dependent emissivity of shock-compressed metals and, in part, dielectrics [10, 11].

X-ray diffraction of shock compressed materials can provide an unequivocal identification of phase transitions, as it probes the local material order; however, it is rarely able to provide information on chemistry and can be difficult to use on amorphous or liquid materials, due to the limited range of reciprocal space that can normally by documented in dynamic-compression experiments. Spectroscopy provides much of our atomic-scale understanding of chemical and physical properties at ambient conditions, yet it has – until recently – proven too challenging for use with laser-induced compression. This lack of diagnostic capability is predominately a result of the inherent difficulty in attempting to observe optical changes in materials under conditions of extreme pressure, a difficulty

primarily related to the nanosecond temporal scales and micron-to-millimeter sample sizes of interest. A nanosecond pulse duration laser drive propagates a shock wave through a target material over the course of nanoseconds, excluding the use of many common spectrophotometric techniques, as these techniques utilize low intensity light sources and may scan through the desired wavelengths [12]. In order to address the temporal and spatial constraints mentioned above, researchers have tended toward two approaches. Interesting work has been done developing broadband optical spectroscopy diagnostics for use on gas gun and explosively driven experiments, which utilize millimeter-to-centimeter sample sizes and time scales on the order of microseconds [13-18]. While these experiments provide a great deal of information on material properties under compression, the large sample sizes and lower temporal resolution can limit the visibility of faster property changes, such as chemical reactions; also, the pressure range is limited compared to that of laser-driven shocks. The high photon intensities and broad spectral range required for data collection over short time-scales can be obtained using broadening of an ultra-fast laser in a dielectric medium, a method developed over the past forty years [19-21]. Using this broadening technique, a considerable amount of work has been done in the last decade developing transient absorption spectroscopy of laser driven shock compressed samples [22-27]. This has provided a great deal of insight into the chemical changes accompanying compression; however the measurements are limited to a single time point per shot and therefore do not probe time-dependent spectral changes.

Building on the aforementioned work, we have developed a diagnostic system that allows us to measure the optical properties of laser-compressed materials over nanosecond time scales at visible and near-infrared wavelengths. The requisite high-intensity white light was produced via supercontinuum generation in a non-linear optical medium and sub-nanosecond time resolution was achieved using an optical pulse stacker. Using this diagnostic, we documented a two-fold increase in reflectivity for shock-compressed germanium as it transformed from the ambient diamond structure to a more metallic structure, most likely the β-Sn structure that has been observed in static diamond-anvil cell experiments [3, 28]. Chapter 2 will discuss the experimental techniques used to reach high pressures and temperatures and Chapter 3 will discuss the development of the SWORD in detail. In Chapter 4, the first use of the SWORD to study phase transitions is presented.

Chapter 2: Generating and Characterizing High Pressure States Using Laser-Driven Dynamic Compression

Experimental Techniques and Target Design

When a high intensity laser pulse impinges upon the surface of an absorbing material, the material ablates, resulting in expanding plasma. Conservation of momentum dictates that the expansion of this plasma results in the creation of a compression wave which propagates through the material, in a direction opposite that of the plasma expansion. This pressure wave can then steepen into a shock front, driving the sample material to a high-pressure, high-temperature state. A typical target design for a laser driven shock compression experiment is shown in Figure 1. A 10-20 micron layer of plastic, usually Kapton or n-parylene, is used as the laser absorber, as it is an effective ablator and therefore works well to couple the laser energy into a compression wave.

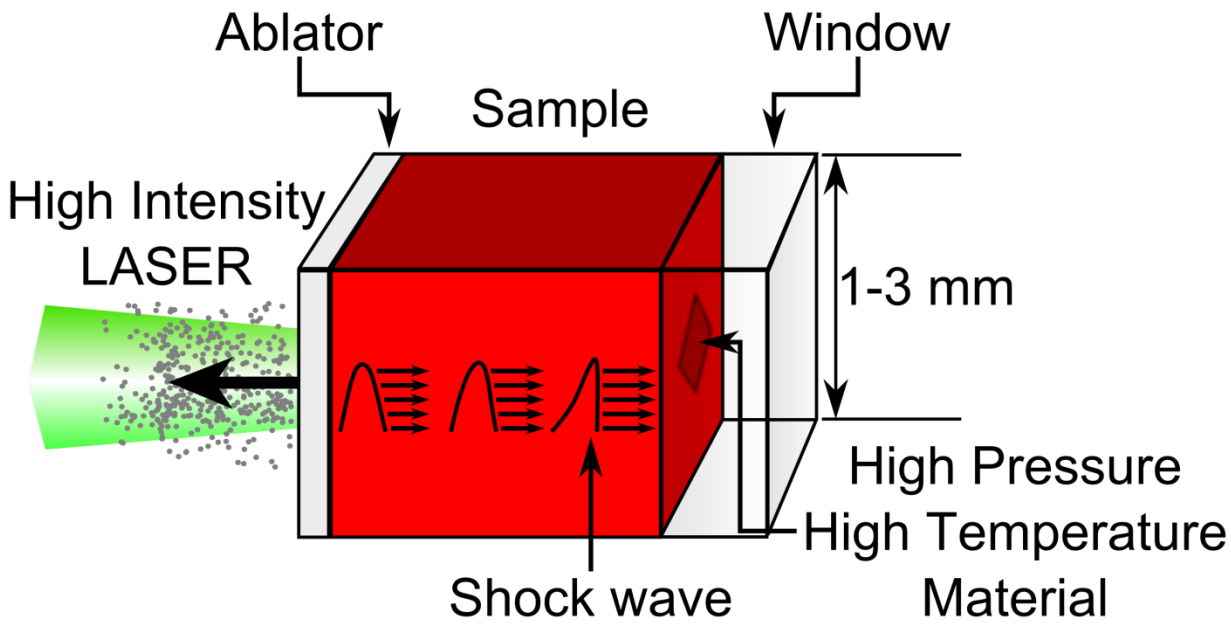

Figure 1 Representative schematic of a target for use in laser drive shock compression experiments. The laser drive is incident on the left side ablator, while diagnostics probe the high pressure, high temperature material on the right side.

For the optically opaque samples which constitute the majority of the materials discussed in this dissertation, the compressed material is observed as the shock wave exits

the surface opposite the ablator. This surface is tamped with an optically transparent window, as shown on the right side of Figure 1, in order to confine the material, as opposed to allowing it to release into vacuum.

The experiments presented in this dissertation were all conducted at the Janus target area in the Jupiter Laser Facility at Lawrence Livermore National Laboratory. The Janus facility consists of two Nd:glass lasers, each capable of delivering ~300 J at the frequency-doubled 527 nm with a 4 to 6 ns square pulse.

Characterizing the Shocked State: Rankine-Hugoniot Relations

An interior schematic of a shocked sample is shown in Figure 2. As the shock front moves through the material, a particle wave is generated. In optically opaque samples, it is this particle wave speed which is observed as the shock wave exits the opaque material. Conservation of mass, momentum, and energy at the shock front provide equations which can be used to relate physical quantities on either side.

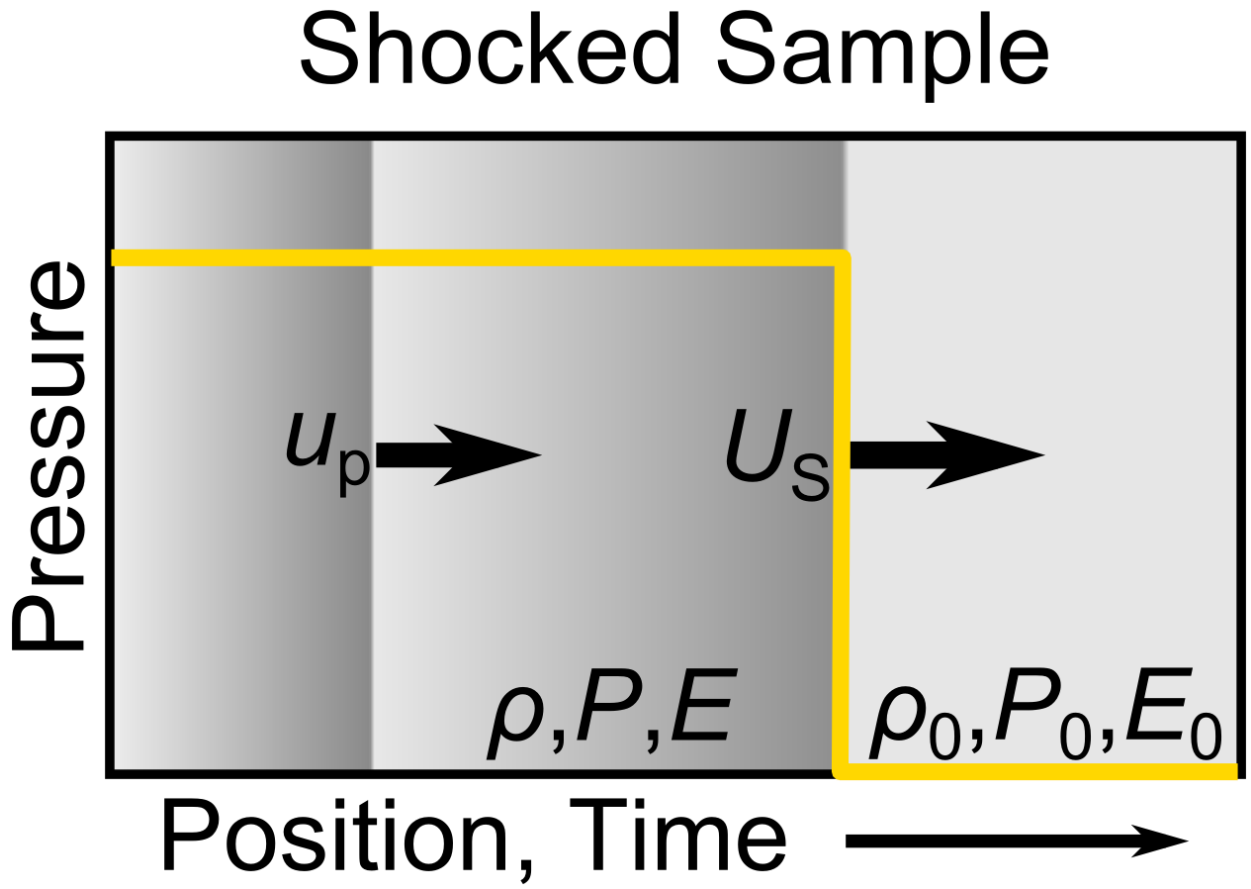

Figure 2 Cartoon schematic of a shock wave transiting a material. Material on the right side is still under ambient conditions and the shock wave is moving from left to right.

Assuming a steady, plane, one-dimensional shock wave with no heat flow or external energy sources and unit cross-sectional area, equations relating conditions on either side of the shock front can be readily derived from the three conservation equations.

Conservation of Mass	$\rho_0 U_s = \rho(U_s - u_p)$	**1.1**
Conservation of Momentum	$P - P_0 = \rho_0 U_s u_p$	**1.2**
Conservation of Energy	$E - E_0 = \frac{1}{2}(P_0 + P)(V - V_0)$	**1.3**

As a set, these three equations contain five variables, meaning that determination of any two is sufficient to define the Hugoniot equation of state for a given material. Experimental constrains typically allow for the observation of shock and particle velocities and it is typically from those two variables pressure, density, and internal energy are determined.

Conservation of Mass

Conversation of mass across the shock front dictates that the mass on the left side of the shock front, must be equal to the mass on the right side of the shock front, resulting in equation 1.1. For a unit area, the mass of the material which is overtaken by the shock wave in time δt, $\dot{m}$ is equivalent to the initial density, ρ_0, multiplied by the velocity of the shock front, U_S. As matter cannot be created or destroyed, $\dot{m}$ must also be equivalent to the final density, ρ, multiplied by the velocity on the other side of the shock front, $U_S - u_p$, leading to equation 1.1. A common analogy presented to aid in understanding of this principle is that of an observer positioned stationary, atop the shock wave, watching the material pass. As an amount of material passes through, it is compressed, so the density increases, but it is also moving at a lower velocity, so the overall mass stays the same.

Conservation of Momentum

As a result of conservation of momentum, the force acting on one side of the shock front must be equal to the force on the other side. The dynamic force in front of the shock front is equal to the initial pressure, and expressing the force on an object as the time derivative of the momentum, we obtain

$$P - P_0 = \dot{p} = \frac{\delta(mv)}{\delta t} \qquad \textbf{1.4}$$

We know the time derivative of the mass to be equal to the initial density, ρ_0, multiplied by the velocity of the shock front, U_S, and we can restate equation 1.4 as equation 1.5, which readily simplifies to equation 1.2 above.

$$P - P_0 = \frac{\boldsymbol{\delta(\rho_0 U_s \delta t\, u_p)}}{\boldsymbol{\delta t}} \qquad \textbf{1.5}$$

Conservation of Energy

Finally, the work done on the material must be equal to the change in total energy, in this case the sum of the kinetic and internal energy. The work done on the system can be expressed as force, which is just the pressure change for a unit area, multiplied by the distance, which is velocity multiplied by time or $u_p\,\delta t$. This is expressed in equation 1.6.

$$(P - P_0)u_p\delta t = \Delta E_{internal} + \Delta E_k \qquad \mathbf{1.6}$$

The kinetic and internal energies can be expressed in terms of the variables of interest, as in equation 1.7.

$$\Delta E_{internal} + \Delta E_k = \Delta E_{internal}\rho_0 U_s\delta t + \frac{1}{2}{u_p}^2\rho_0 U_s\delta t \qquad \mathbf{1.7}$$

In order to obtain equation 1.3, equation 1.2 must be substituted into equation 1.7.

$$(E - E_0) = \frac{P(P-P_0)-\frac{1}{2}(P-P_0)^2}{(\rho_0 U_s)^2} \qquad \mathbf{1.8}$$

Substituting equation 1.2 into 1.1 provides equation 1.9, which when substituted into equation 1.8 results in the form of the conversation-of-energy equation in equation 1.3.

$$(\rho_0 U_S)^2 = \frac{(P-P_0)}{(V_0-V)} \qquad \mathbf{1.9}$$

Existing Diagnostics

Velocity Interferometry System for Any Reflector (VISAR)

The VISAR diagnostic, initially described by Barker and Hollenbach in 1972 and later by Celliers et al., in 2004, is used to determine shock or particle velocities in a target [8, 29]. A 532 nm seeded Nd:YAG probe laser with a pulse duration on the order of 50 ns is reflected from the surface of the target and sent through a Mach-Zehnder interferometer with a delay element in one leg. The resulting interference pattern is then observed by imaging it onto a streak camera, recording the phase as a function of time, ϕ(t). Movement of the sample as a result of the compression wave results in a Doppler shift in the reflected probe laser and eventually a phase-shift in the interference fringes produced by the interferometer. The optical thickness aforementioned delay element sets the sensitivity of the VISAR. Velocity can be obtained from the measured phase change using equation 1.10.

$$u(t-\frac{1}{2}\tau) = (\phi(t)+b)\frac{\lambda}{2\tau n_0(1+\delta)} \qquad \textbf{1.10}$$

u is the velocity at time t minus one half τ, which is the time delay introduced by the etalon. As stated above, ϕ(t) is the phase as a function of time and b is a number of integral fringe shifts. λ is the probe beam wavelength. The final two terms are optical corrections; n_0 is the index of refraction of the window material and (1+δ) corrects for optical dispersion through the etalon material. It should be noted that b is unknown and in order to determine the absolute velocity two VISAR diagnostics with different delay element thicknesses must be used. Errors in the velocity determined using this technique are typically on the order of 5%.

Unless otherwise noted, the VISAR imaging system utilized a 1 mm diameter field-of-view on the target surface, as described by Celliers et al [29].

Streaked Optical Pyrometer

Relatively few of the experiments described here utilized the SOP, primarily due to the fact that the lower limit on temperatures measured using this diagnostic is approximately 2,500 K, well above predicted temperatures for the experiments discussed later. The SOP is, however, used frequently and a brief discussion of the technique and limitations is relevant to future applications of the broadband reflectivity diagnostic discussed in detail in the next chapter. A detailed description of this diagnostic can be found in the dissertation of Dylan Spaulding, as well as in Reference [10].

The SOP system collects the thermal emission in the visible from the sample, streaked in time on a streak camera. The intensity of this emission can be related to the temperature of the sample through careful calibration with a material with a known temperature-pressure relationship.

Single Wavelength Optical Reflectivity

The reflected intensity of the VISAR probe can be used to obtain optical reflectivity measurements at a single wavelength. A small fraction of the probe light is split off prior to any interaction with the target and directed through an optical fiber to the same streak camera used to record the VISAR fringes. Reference images taken prior to the shot provide a relationship between this intensity fiducial and the ambient target reflectivity, R_0. On the actual shot, the intensity fiducial provides a reference for the pulse shape and intensity in time and allows for the comparison of the reflectivity of the sample pre- and post- shock using the following equation:

$$R(t) = R_0 \frac{I_{reflected}(t)}{I_{reference}(t)}$$

As this measurement is taken over a narrow wavelength, limited information as to the changing optical properties of the material can be ascertained.

Chapter 3: Construction and Calibration of a Broadband Optical Reflectivity Diagnostic

Abstract

A normal-incidence visible and near-infrared Shock Wave Optical Reflectivity Diagnostic (SWORD) was constructed to investigate changes in the optical properties of materials under dynamic laser compression. Documenting wavelength- and time-dependent changes in the optical properties of laser-shock compressed samples has been historically difficult, primarily due to the small sample sizes and short time scales involved, but we succeeded in doing so by broadening a series of time delayed 800-nm pulses from an ultrafast Ti:sapphire laser to generate high-intensity broadband light at nanosecond time scales. This diagnostic was demonstrated over the wavelength range 450 to 1150 nm with up to 16 time-displaced spectra during a single shock experiment. Simultaneous off-normal incidence velocity interferometry (VISAR) characterized the sample under laser-compression, and also provided an independent reflectivity measurement at 532 nm. The shock-driven semiconductor-to-metallic transition in germanium was documented by way of reflectivity measurements with 0.5 ns time resolution and a wavelength resolution of 10 nm.

Part I: Design and Construction

Overview

Despite prevalent use in studies of materials under ambient conditions and static pressure, wavelength dependent reflectivity has not been extensively studied under

dynamic compression. This is primarily due to the difficulty inherent in generating broadband light of sufficient intensity to allow for the observation of time dependent changes in reflectivity over a period of nanoseconds. Traditional methods for generating light with a broad wavelength range are unable to produce the high intensities required for observation of reflectivity changes over a period of nanoseconds. It is only recently, with the increasing prevalence and accessibility of ultrafast lasers that it has become possible to generate broadband light with both sufficient intensity and consistency to allow for its use as an illumination source in reflectivity experiments.

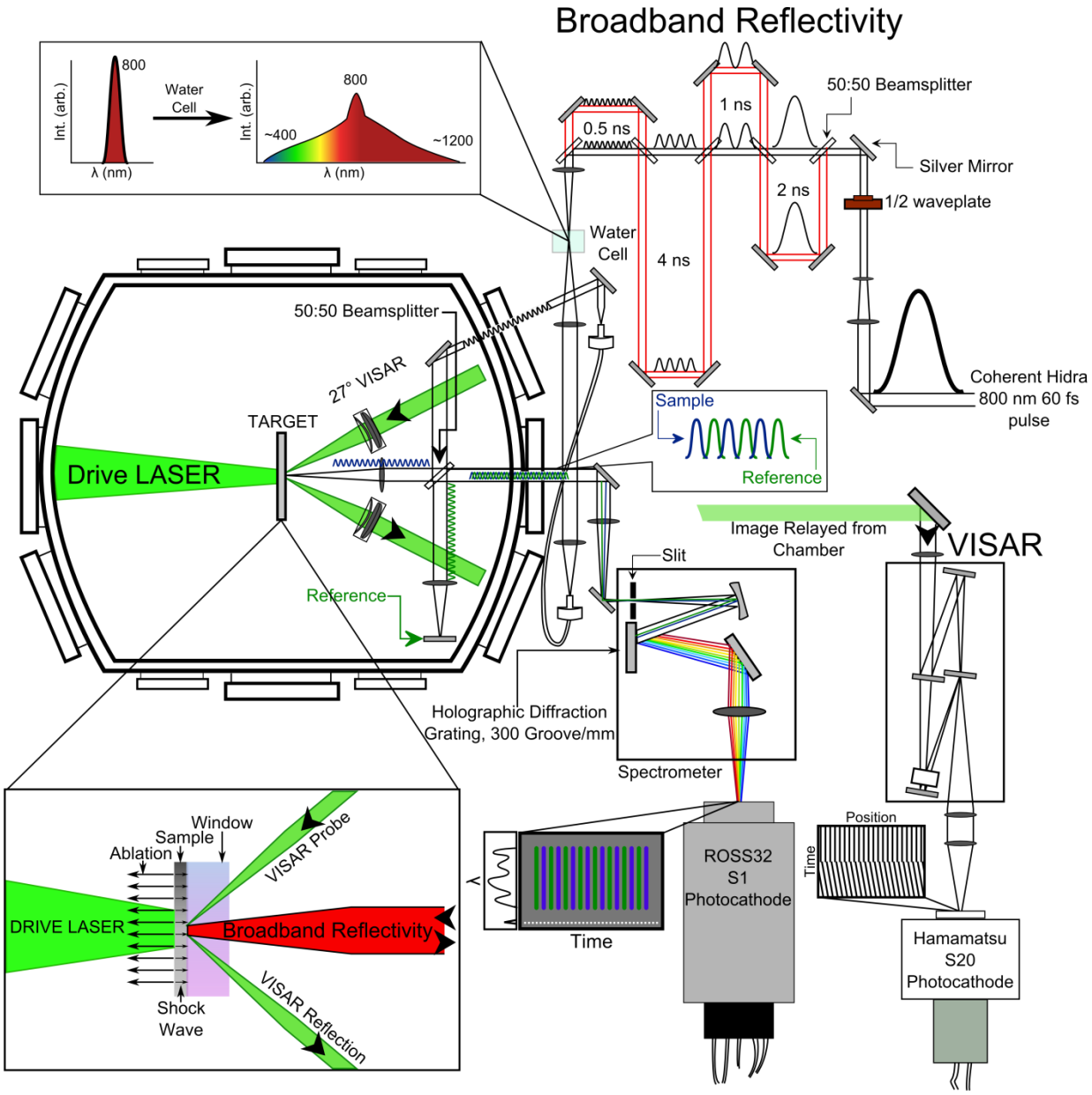

Figure 3 Optical schematic of the broadband reflectivity system with target inset in bottom left. The ultrafast pulse entered the pulse stacking system outlined in the upper right corner. The stacked pulses were focused into the water cell which generated wavelength broadened

light as shown in the upper left corner. The sample and reference pulses from the target chamber were collected in a spectrometer and swept in time on the ROSS streak camera. The VISAR 532 nm probe beam entered the chamber and was directed to the target at a 27 degree angle and collected at -27 degrees by an identical set of imaging optics. The optical path from the chamber to the VISAR interferometer was not shown due to space constraints. A full schematic of the VISAR optical setup can be found in reference [29].

A Coherent HIDRA pumped by a Continuum PowerLite 8000 was used as the ultrafast laser source for the broadband reflectivity diagnostic, providing 20-25 mJ of energy at 800 nm with variable pulse duration between 50 fs and 100 fs. As shown in the upper right side of Figure 3, the collimated ultrafast pulse was stacked in time using a series of adjustable time delay paths. The temporal delay provided by the differing path lengths allowed for a degree of time resolution, as well as the ability to collect multiple spectra over the course of a single shock compression experiment. The ultrafast pulse was directed through a series of 50:50 beamsplitters, each of which directed approximately half of the beam intensity into an air delay path of known length. Each subsequent beamsplitter also served to recombine the delayed pulse such that it was collinear with the zero delay beam path. Four beamsplitters and four delay paths were used to generate sixteen pulses. A pulse-to-pulse time interval of 0.5 ns was used for the experiment, with delay path lengths set to 15 cm, 30 cm, 60 cm, and 120 cm (0.5 ns, 1 ns, 2 ns, and 4 ns). As the reflection/transmission ratio of the beamsplitters was dependent on beam polarization, half-waveplates were installed in two of the delay paths, as well as immediately prior to the pulse stacker. In order to obtain equal intensities for all sixteen pulses, it was necessary to iteratively adjust the rotation of the three half-waveplates while observing the pulse intensities on a streak camera. The spectral broadening process discussed below was highly nonlinear; relatively small differences in the pulse intensities across the sixteen pulses would be amplified, often resulting in a loss of intensity at wavelengths further from the fundamental [19]. Although it would have precluded the complicated referencing procedure discussed below, due to the difficulty in obtaining 50:50 beamsplitters and half-waveplates with a working range that encompassed the entire wavelength range produced in the broadened beam, it was determined that the pulse stacking must occur before the ultrafast pulse was broadened. This location for the pulse stacking also had the added benefit of lowering the beam power that was focused into the optically nonlinear medium for broadening, reducing the likelihood of damaging the material or any optics handling the reduced beam diameter.

The stacked collimated pulses were focused using a 500-mm achromat into a 1-cm-long water cell, wherein a set of nonlinear optical processes, most importantly self-focusing and self-phase modulation, result in a broadened spectrum of approximately 400 to 1200 nm, as shown in Figure 3 [21, 30-33]. As mentioned above, the spectral broadening in the dielectric material is highly nonlinear in its dependence on the laser intensity [21, 31, 33, 34], requiring the generation of independent spectral references for each of the time delayed pulses, as will be discussed in more detail below.

The white light was collimated using a 500-mm achromat and, after passing through a notch filter to remove the excess fundamental laser light at 800 nm, injected into a 1-m-

long 200-micron-diameter core high-damage threshold fiber using a 40x microscope objective. Injection into a fiber served two important purposes; the first was to spatially homogenize the broadened light and the second was to effectively decouple the sensitive alignment of the pulse stacker from the alignment to the target and the detector. The illumination from the fiber was collected immediately outside the vacuum chamber, collimated to a 3.8-cm-diameter, and directed through a broadband antireflection-coated chamber window. Within the chamber the broadened light was passed through a 45-degree beamsplitter with 50±5% transmission in the wavelength range of interest (Edmund Optics 45-854 in the visible, 45-855 in the near-infrared). At the beamsplitter the reflected light was directed toward the target and the transmitted light was directed toward a static reference. Both beams were independently focused onto their respective surfaces using matching f/4.5 imaging systems with a focal length of 15 cm. The reflected light was recombined at the original beamsplitter with a 0.25-ns delay between each sample and reference pulse arising from the 7.5-cm path-length difference between the two beam paths. The light from the sample and reference was focused using a 50-mm focal length achromat into a home built spectrometer with a low wavelength dispersion that enabled the detector to capture either the full visible range or the near infrared from 800-1200 nm. The spectrometer output was imaged on a Rochester Optical Streak System (ROSS) camera with a sweep window of 16 ns. The ROSS camera used an S1 photocathode with efficiency between 20% and 85% in the wavelength range 400-1600 nm, allowing reflectivity measurements across the visible and near-infrared [35-37].

Alignment of the VISAR probe, reflectivity probe, and drive laser was accomplished employing a target consisting of a 250-micron transparent square of quartz with a ~200 nm coating of aluminum into which a cross had been etched. The three beam paths were co-aligned to this etched cross, ensuring that the diagnostics were observing the center of the laser shocked region.

The raw data consist of an interleaved set of 16 sample pulses and 16 reference pulses. A characteristic set of raw data can be seen in Figure 4A, with false color emphasizing the difference between the sample and reference pulses. A series of 10-20 images were taken prior to the shock compression to obtain the scaling factor accounting for the difference between the reference and sample optical paths.

Pulse Stacking

The pulse stacking system is shown in detail in Figure 4. A total of five waveplates are used along the optical path in order to obtain uniform intensity distribution across all sixteen pulses. At the final beamsplitter, half of the light is directed towards the white light generation system and half of the light is directed down an alignment path to a Watec 902b CCD camera. Initially, intensity distribution across the pulses is non-uniform, primarily due to the 10-20% difference in reflected intensity between the s and p polarizations. This intensity distribution is corrected through the alignment of the five waveplates at the positions indicated in the diagram. Following waveplate alignment, the camera is also used as one of the two planes necessary used to overlap the pulses, with the other plane being a card in the upstream beam path.

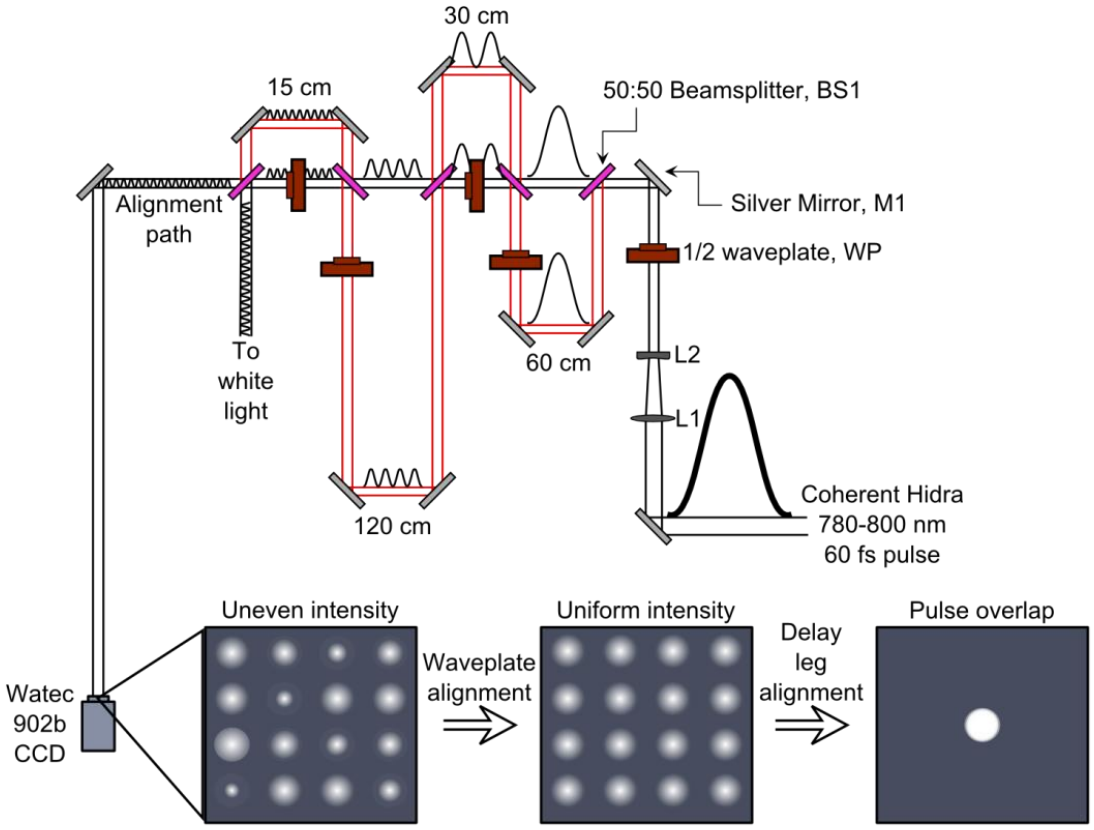

Figure 4 Detailed diagram of the pulse stacking system for the SWORD. The four delay legs are marked with the total distance added along each path.

Optic	Description/Part Number
L1	500 mm focal length achromat/Thorlabs AC508-500-B
L2	-200 mm focal length achromat/Thorlabs ACN254-200-B
WP	waveplate/CVI QWPO-800-10-2
M1	2” silver mirror/Thorlabs PF20-03-P01
BS1	50% NIR beamsplitter/CVI BTF-NIR-50-SQW-5001M-C

Supercontinuum Generation and Fiber Alignment

Figure 5 consists of a more detailed schematic of the white light generation portion of the SWORD described above. Typical spectra produced using this white light generation system are shown in Figure 6.

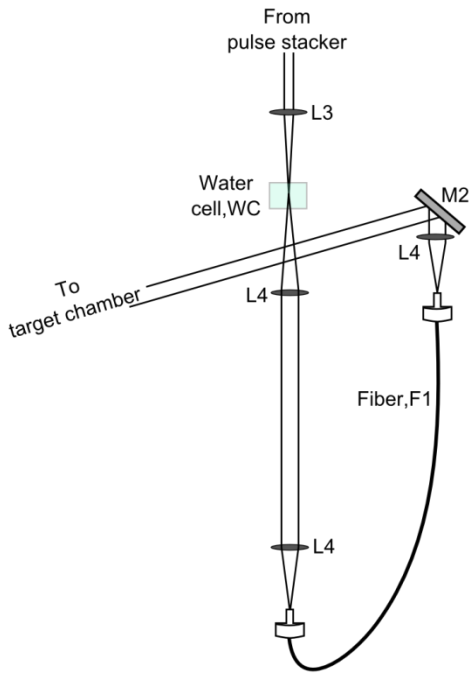

Figure 5 Detailed diagram of the supercontinuum generation system in the SWORD. The pulses from the pulses stacker enter the system from the top, are focused into a water cell and then collimated and injected into a fiber. The output from the fiber is collimated and directed toward the target chamber.

Optic	Description/Part Number
L3	500 mm focal length achromat/Thorlabs AC508-500-B
L4	500 mm focal length achromat, uncoated/ CVI AAP-500-50.8
WC	2 cm length quartz cell/Custom design
F1	1 mm core glass fiber/Thorlabs FT1000UMT
M2	3” silver mirror/Thorlabs PF30-03-P01

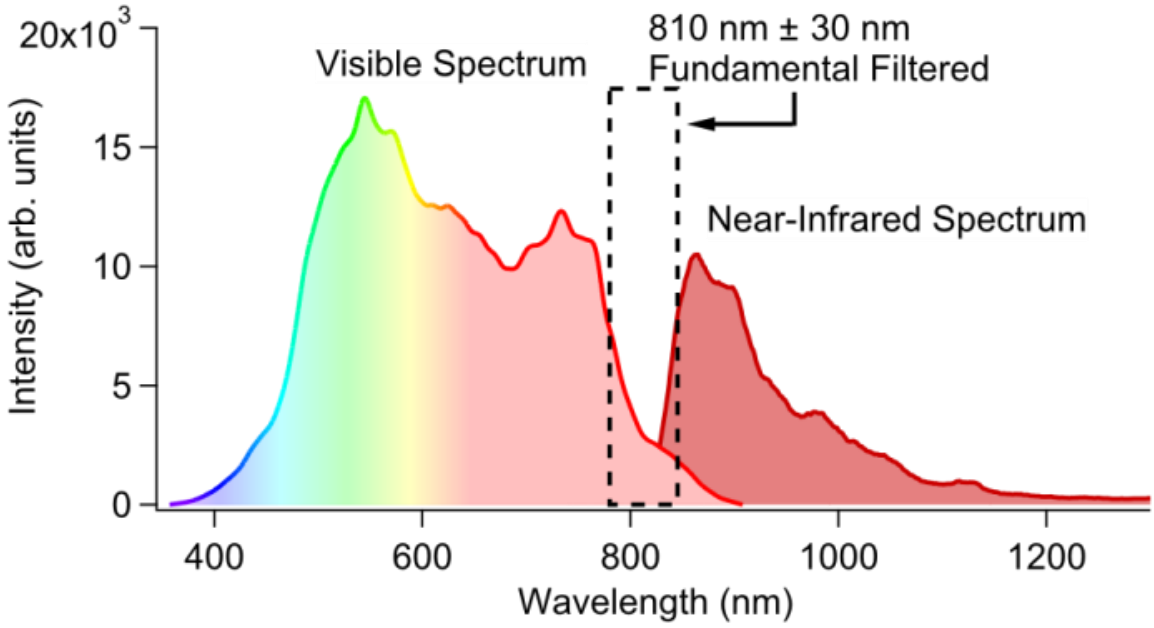

Figure 6 Representative spectra generated using the white light supercontinuum generation in a 1 cm water cell. A filter was used to attenuate the remaining fundamental light centered at 810 nm.

Target Alignment and VISAR

Figure 7 contains a detailed diagram of the target chamber arrangement. An alignment procedure was developed in order to ensure that the SWORD, the VISAR, and the drive laser were all aligned to the same point on the target. An alignment camera with a long-working-distance objective was placed on the drive side of the target and used to view the drive side surface of the target. An alignment target was made by taking a 250 micron thick α-quartz with a 200 nm thick aluminum coating and manually etching a cross in the aluminum. When placed in the target holder, the cross can be viewed from both the laser drive side using the aforementioned alignment camera and the diagnostic side, using the VISAR imaging system described previously [29]. Once the target was in a position such that the cross shape was centered on the VISAR imaging system, a video monitor with a flat surface was marked with the position of the cross on the drive side alignment camera. The SWORD illumination was aligned to the center of the marked position, ensuring that the VISAR and SWORD diagnostics observed the same location on the target. With a target in place, an alignment diode collinear with the drive laser was aligned to the center of the

cross marked on the video monitor, ensuring that the drive beam was aligned to the same location as the diagnostics.

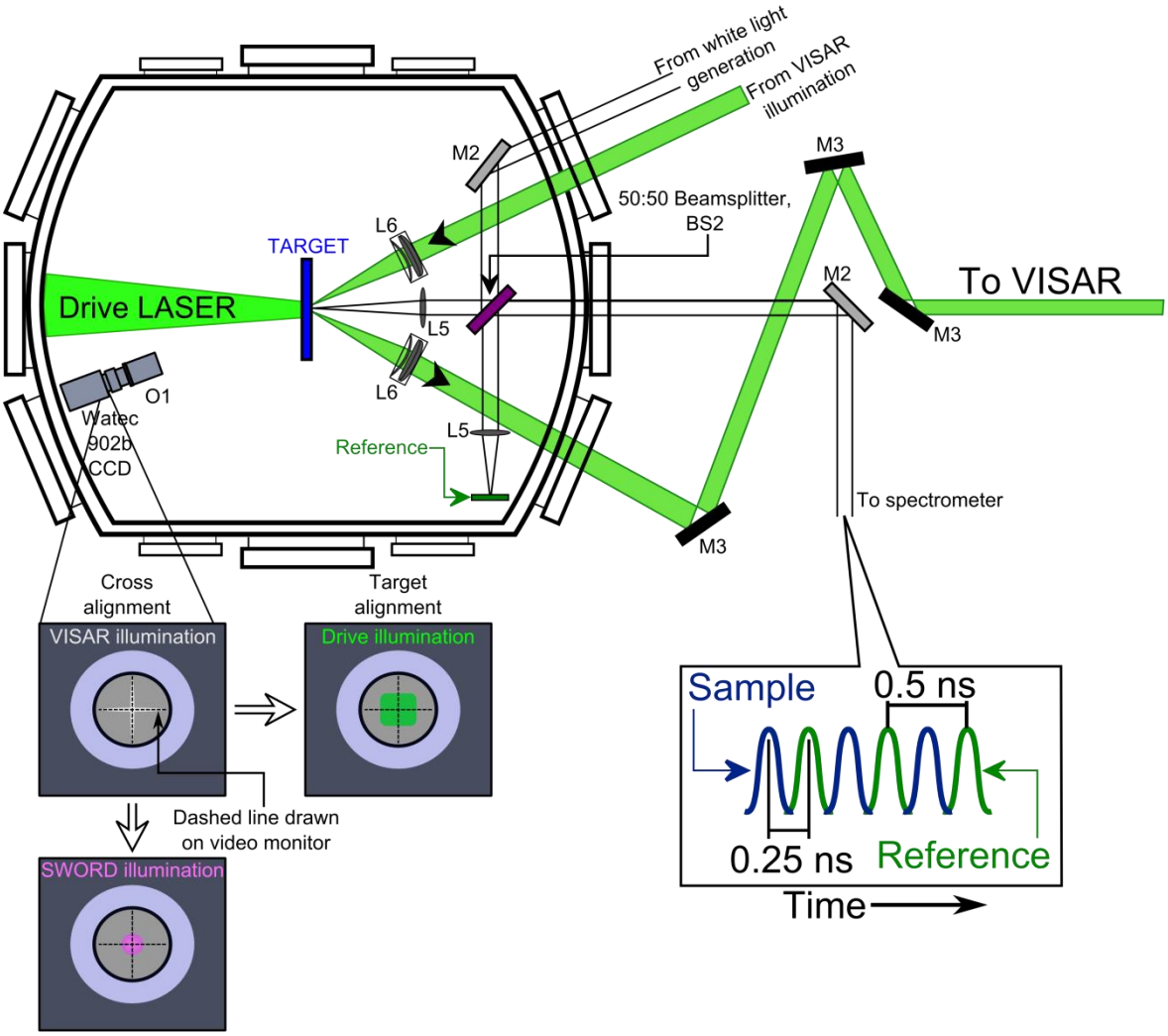

Figure 7 Detailed diagram of the target chamber and alignment diagnostics.

Optic	Description/Part Number
M2	3” silver mirror/Thorlabs PF30-03-P01
M3	3” aluminum mirror/Thorlabs PF30-03-P01
BS2-VIS	50 mm x 75 mm visible 50% beamsplitter/Edmund Optics 45-854
BS2-NIR	50 mm x 75 mm NIR 50% beamsplitter/Edmund Optics 45-855
L5	F/3 uncoated focusing lens/CVI AAP-150-50.8
L6	meniscus and achromat, F/3/CVI MENP-50.0-4.5-350.0-C-532 and AAP-250.0-50.8-425-675
O1	Variable magnification focusing objective/Source unknown

Spectrometer and Streak Camera

The final stretch of the SWORD is shown in Figure 8. The pulses reflected from the target and reference enter a home built spectrometer designed with a low dispersion in order to maximize the observable wavelength range.

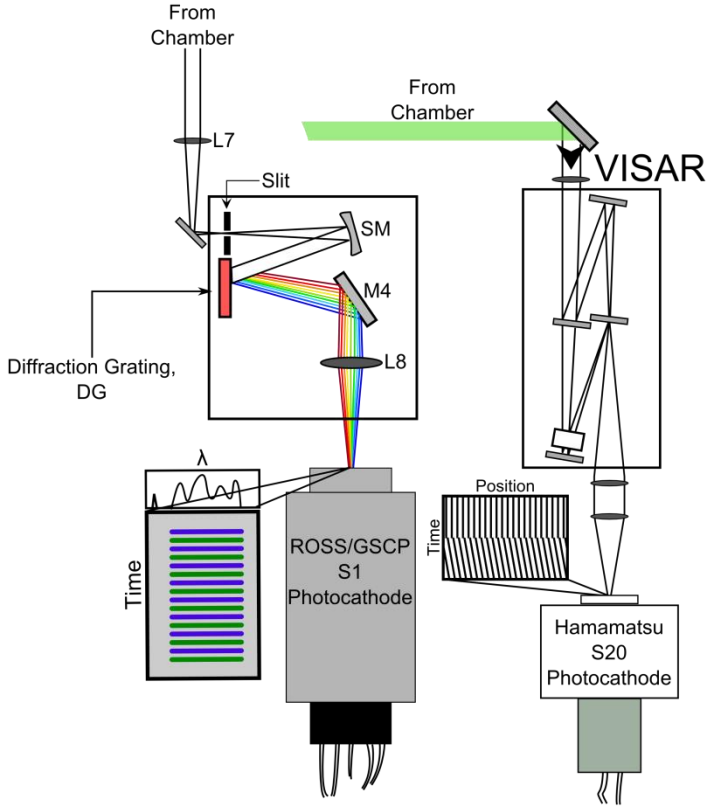

Figure 8 SWORD spectrometer and streak camera setup and VISAR optical setup.

Optic	Description/Part Number
L7	uncoated focusing lens/CVI AAP-50-50.8
L8	uncoated focusing lens/CVI AAP-200-50.8
SM	silver spherical mirror/Thorlabs CM750-200-P01
DG	holographic diffraction grating, 300 rulings per millimeter/Source unknown
M4	2” silver mirror/Thorlabs PF20-03-P01

Part II: Analysis

The analysis consists of two parts; the first is the extraction of the spectra from the streak camera records and the second is the scaling and normalization of those spectra relative to a standard. For the purposes of detailing the analysis process as clearly as possible, the data shown in this section is from a stationary target, in other words, one in which no reflectivity change as a function of time is expected. As can be seen in Figure 11, due to a combination of factors including spectral chirp and a degree of nonlinearity in the streak tube, the spectra are neither parallel nor of equal width across the image. A small

amount of jitter in the timing system, on the order of 0.1-0.3 ns, also serves to complicate the data extraction procedure.

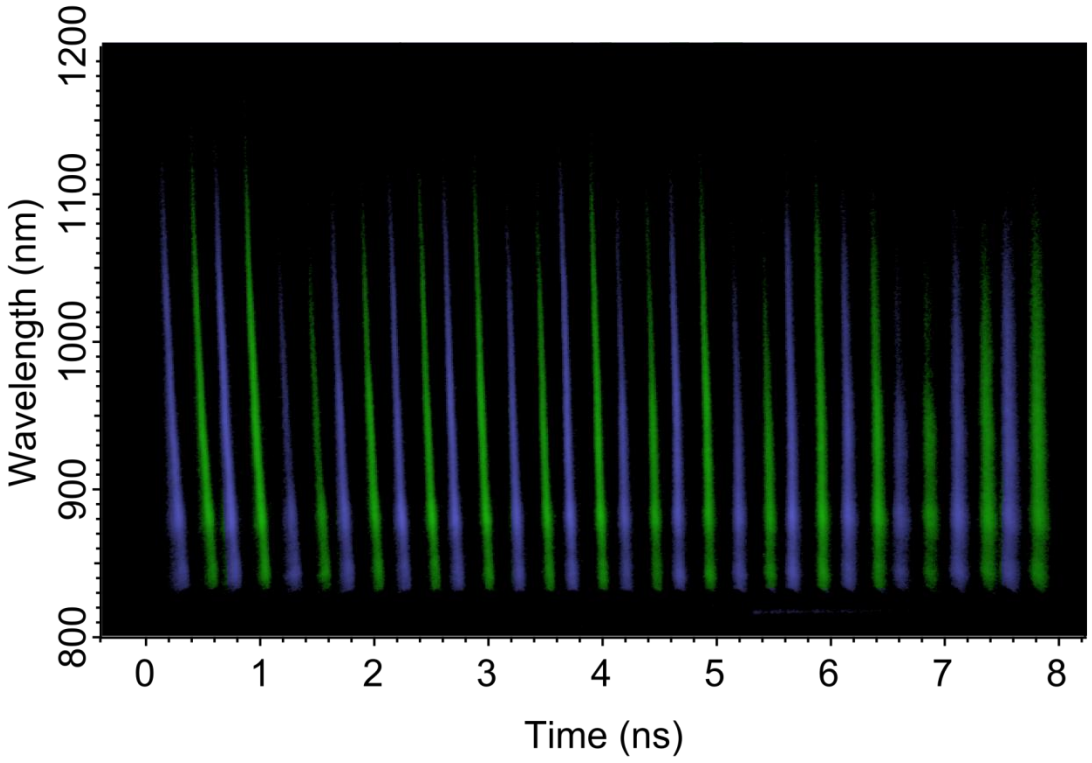

Figure 9 Raw data from the broadband reflectivity diagnostic. False color has been used for clarity; the 16 blue pulses are sample pulses and the 16 green pulses are reference pulses, following the schematic in Figure 3. The time scale shown is relative to the arrival of the first SWORD pulse.

Data Extraction

The data extraction technique can be separated into two parts; the first part is the determination of the location of each spectrum and the second is the extraction of each spectrum from the image. To determine the location of each reflected pulse on the image, a series of equally spaced line outs at constant wavelength were taken and the minima were located; each local minimum indicated the termination of one pulse and the beginning of the next. Due to the difficulty in developing a peak-finding algorithm capable of determining the minimum position prior to the earliest pulse, the first pulse maximum was located and the position of the minimum was set to a number of pixels earlier (generally the width of the pulse and an additional five pixels to ensure that no light was missed). For the majority of that data presented in this dissertation, the line outs were taken every 10 pixels from the beginning of the wavelength range (~780-850 nm) to the point at which the intensity of the pulse was too low to allow for effective peak location. A second order polynomial is then fit to each set of points and used to define the border between each spectrum. An example of this can be seen in FG.

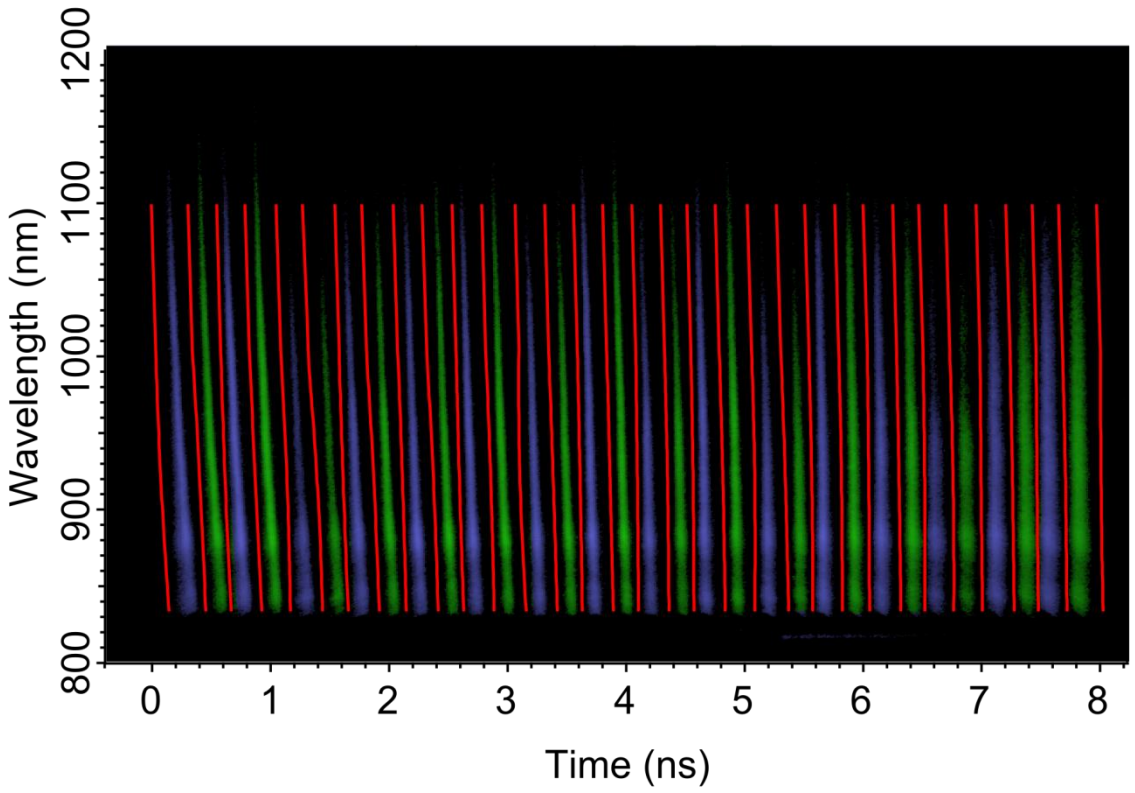

Figure 10 The raw spectra from Figure 9 are shown with the lines determining the minima in red.

The final step in the data extraction process is the integration of each column of pixels in the temporal dimension between the minima locations defined earlier. The results of such integration can be seen in Figure 11.

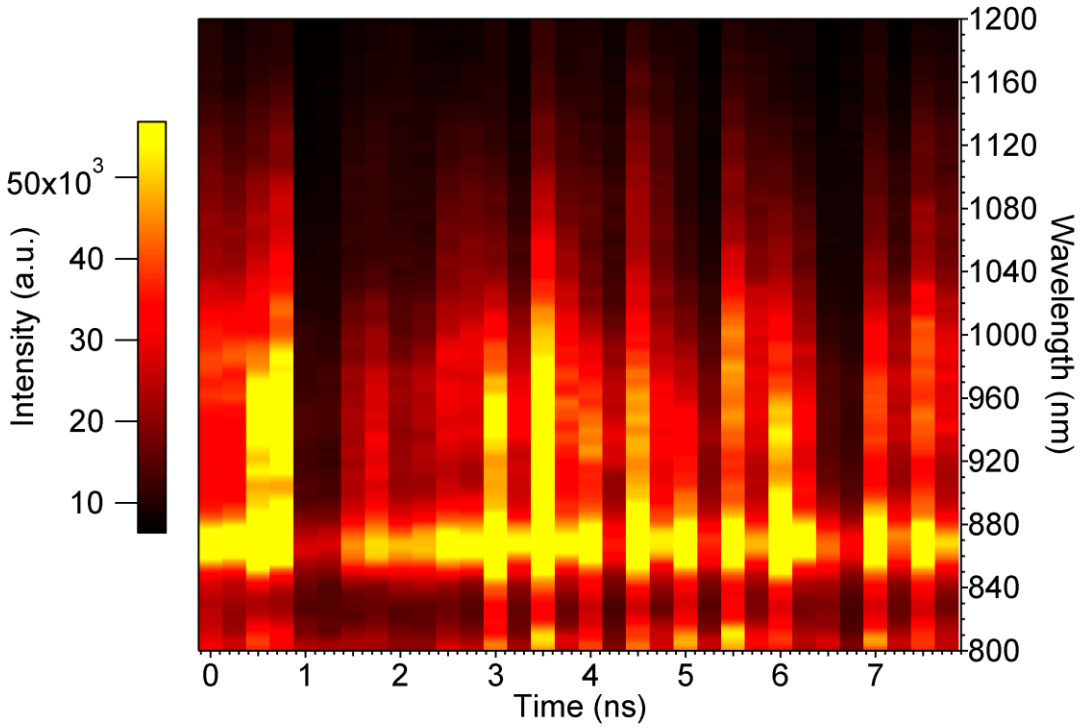

Figure 11 Integrated intensities extracted from the raw data in Figure 9.

Scaling and Normalization

The extraction process is applied to the static reference images in order to obtain a scaling factor accounting for the slight optical path difference between the pulses reflecting from the sample surface and those reflecting from the reference surface. This scaling factor is determined for each target and the resolution limit of the diagnostic is determined by applying this scaling factor to a series of unshocked images and observing the deviation from an ideal value of one. For a series of images taken using an unshocked target, any series of scaling factors obtained using one image should be identical to those obtained using another image of the same target and any deviation from unity was indicative of systematic errors in the instrumentation.

The final spectra were obtained by extraction from the image and then scaling to account for optical path differences between the sample and reference. An example of a static (pre-shock) sample is shown in Figure 12 and Figure 13.

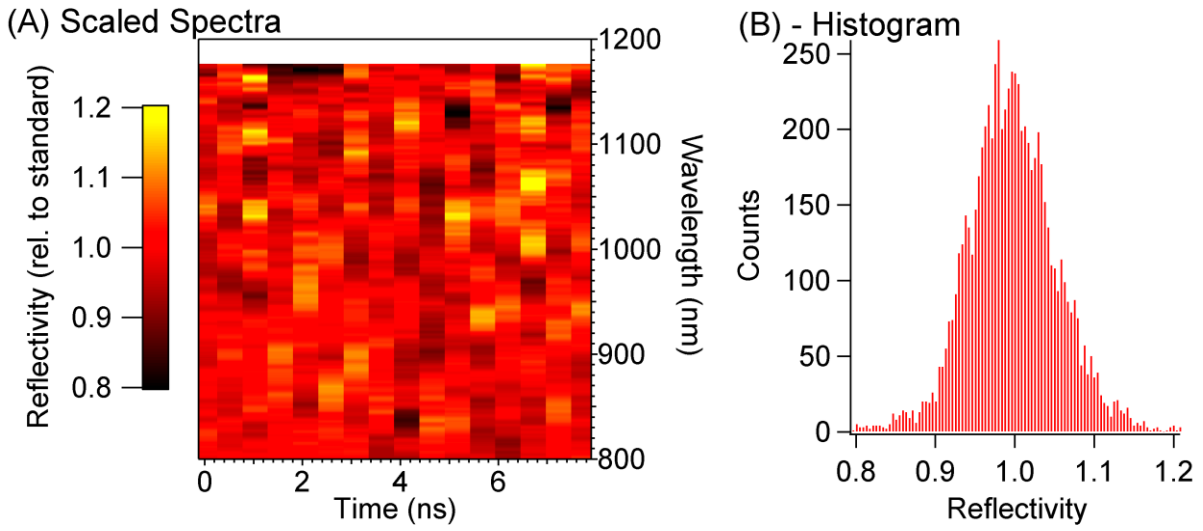

Figure 12 (A) Reflectivity spectra obtained by scaling the sample intensities to the static reference intensities in Figure 11. (B) Histogram of reflectivity values in A.

As the noise in the data produced by this diagnostic is predominately driven by photon statistics, signal-to-noise in the final spectra can be improved by averaging four to eight reference spectra in order to obtain the scaling factor required to compare the reference spectra to the sample spectra. In the histogram in part B of Figure 12, the spread in the reflectivity value with respect to an ideal value of one is shown to be approximately ±10%. Averaging four static datasets, as shown in Figure 13, reduces this spread by half, as would be expected if the scatter is due to photon statistics.

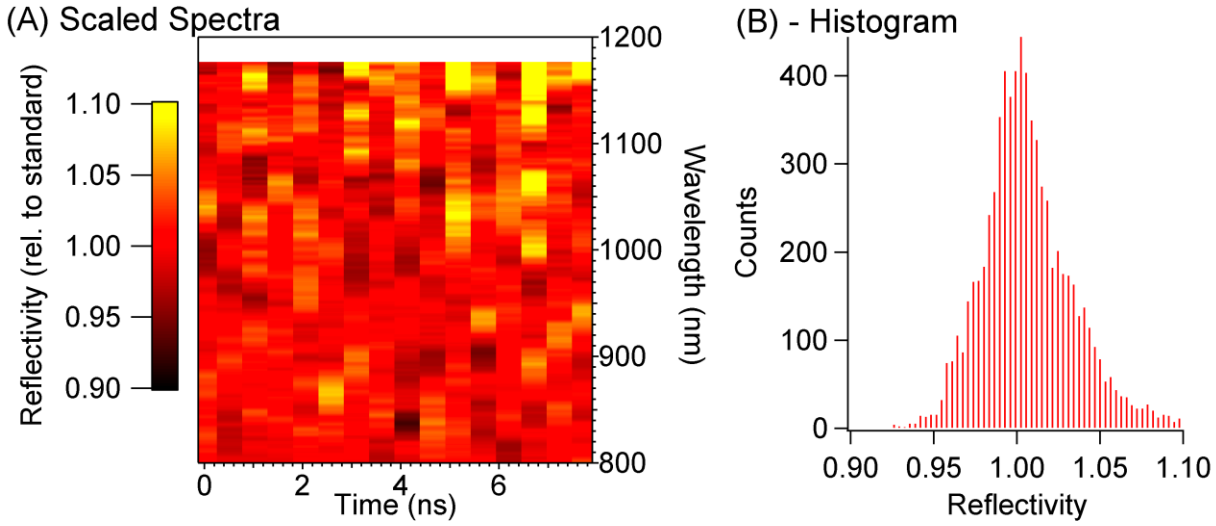

Figure 13 (A) Reflectivity spectra obtained by averaging four static datasets. (B) Histogram of reflectivity values in A.

Part III: Calibration

In order to test this new broadband reflectivity diagnostic, a series of laser-shock experiments were conducted on single crystal germanium. Germanium has previously been

shown to go through a phase transition at ~10 GPa under static compression, from a diamond-like semiconductor to a β-Sn semi-metal [2, 38-41]. A significant increase in electrical conductivity, and therefore reflectivity, is expected at this transition in Ge, from a structure with a more covalent to a more metallic bonding character [42, 43]. The most significant change in the reflectivity of germanium under pressure, as observed by Hanfland *et al*., occurs in the NIR, with the increase ranging from 130% to 200% between 800 and 1200 nm for compression to 13.6-GPa and 140% to 200% for compression to 34.4-GPa. Changes in the visible reflectivity were also observed; however, the magnitude of the reflectivity increase is less significant and peaks at 156% at 425 nm. Initial experiments were designed to test the feasibility of the SWORD and, as such, reflectivity spectra were taken primarily in the NIR. Following the success of these early experiments, later experiments obtained data spanning wavelength ranges from the visible to the NIR. These initial and follow-up experiments are discussed in the next chapter.

Part IV: Future Improvements

There are two key areas where improvements to the SWORD can be readily made. The signal-to-noise in the diagnostic suffers from low photon counts due to the limited dynamic range of the ROSS camera. The ultrafast laser pulses, which are on the order of 100-200 fs in duration, tend to saturate the camera at relatively low energy, resulting in pinching and distortion of the spectra. Using fiber-induced chirp to spread the pulse out in time prior to both interaction with the target (which will reduce damage to the sample surface due to high pulse intensity) and collection in the streak camera will resolve this problem. The second improvement involves further tweaking of the spectrometer to lower dispersion and improve wavelength range, allowing the collection of spectra over a broader wavelength range (800 nm instead of 400 nm).

Chapter 4: Optical Properties of Shock Compressed Germanium

Abstract

The shock-driven semiconductor-to-metallic transition in germanium was studied using the novel Shock Wave Optical Reflectivity Diagnostic (SWORD) to obtain reflectivity measurements across the visible and near-infrared with 0.5 ns time resolution and a wavelength resolution of 10 nm. Significant changes in the reflectivity are observed at the phase transition and as a function of pressure in the metallic germanium. A Drude-Lorentz fit to the spectra suggests the presence of a strong absorption peak which shifts from 1.5 eV (830 nm, 12000 cm^{-1}) at 18 GPa to 1.7 eV (720 nm, 14000 cm^{-1}) at 29 GPa.

Introduction

Accurate calculation of the band structure of semiconductors via readily available techniques such as density functional theory (DFT) has been shown to be difficult, with errors in the calculated band gap of approximately 50% [44, 45]. Viable methods for improving the accuracy tend to be computationally expensive; they involve the calculation of a more complete approximation for the exchange-correlation function, as is the case for the GW approximation [46-48]. Specialized pseudopotentials can be used to improve the accuracy of calculations, but they can only be validated over relatively small ranges of conditions and are therefore of limited use for high pressure experiments, particularly dynamic high pressure experiments where spectroscopic techniques for determining the electronic structure are not well developed [49]. In order to expand the range over which calculations can be validated (and therefore improve the accuracy of calculations), and better understand the effect of pressure on the electronic structure of semiconductors, the newly developed Shock Wave Optical Reflectivity Diagnostic (SWORD) was used to study the visible and near-infrared reflectivity of shock compressed germanium across the semiconductor-to-metal transition [50].

The earliest study of germanium under compression was conducted by Bridgman in 1951, followed by Minomura and Drickamer in 1962 [2]. There have been a limited number of previous shock-wave studies of germanium, with earliest being that of Graham et al. in 1965 and 1966 [8, 39] and Pavlovskii in 1967 [51]. These authors studies were interested in observing the semiconductor-to-metal phase transition that accompanies the phase transition at ~10 GPa under static compression, from a diamond-like semiconductor to a β-Sn semi-metal, as shown in Figure 14 [2, 38-41]. A significant increase in electrical conductivity, and therefore reflectivity, is expected at this transition in Ge, from a structure with a more covalent to a more metallic bonding character [42, 43]. Previous static experiments also indicate a degree of wavelength dependence in this reflectivity increase, which might potentially be observed using the broadband reflectivity diagnostic [52]. The most significant change in the reflectivity of germanium under pressure, as observed by Hanfland *et al*., occurs in the NIR, with the increase ranging from 130% to 200% between 800 and 1200 nm for the 13.6-GPa compression and 140% to 200% for the 34.4-GPa compression. Changes in the visible reflectivity were also observed; however, the magnitude of the reflectivity increase is less significant and peaks at 156% at 425 nm.

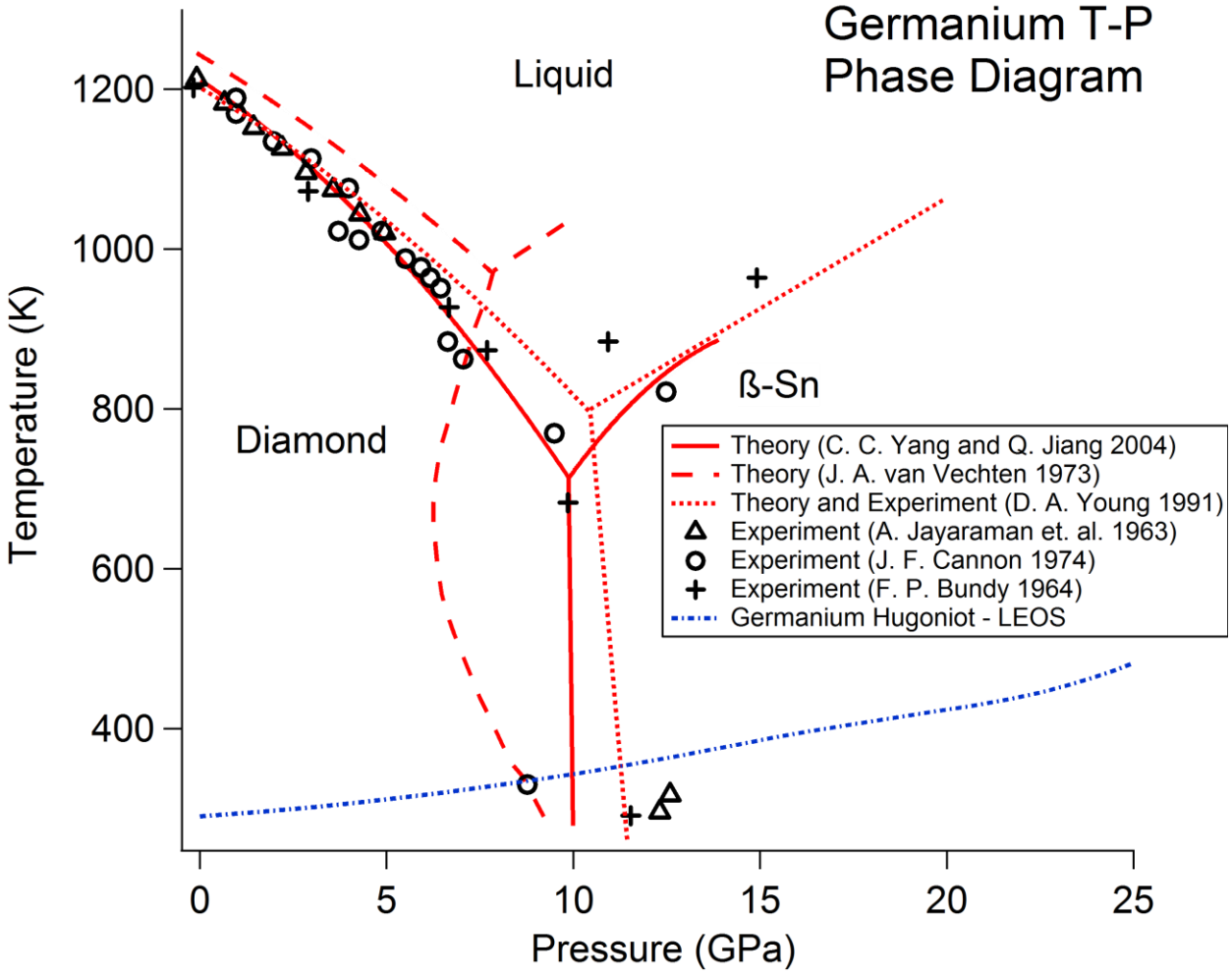

Figure 14 Germanium phase diagram with calculated Hugoniot in blue.

Methods

Sample Preparation

Samples were prepared as layered stacks, as shown in Figure 15. The plastic ablator, parylene, was deposited onto the aluminum, which was diamond turned on both surfaces. The germanium sample was pressed between the window and the aluminum pusher using a four-point fixture which could be mounted on the target holder. This was done to avoid the presence of any glue layers, particularly between the LiF window and the germanium sample.

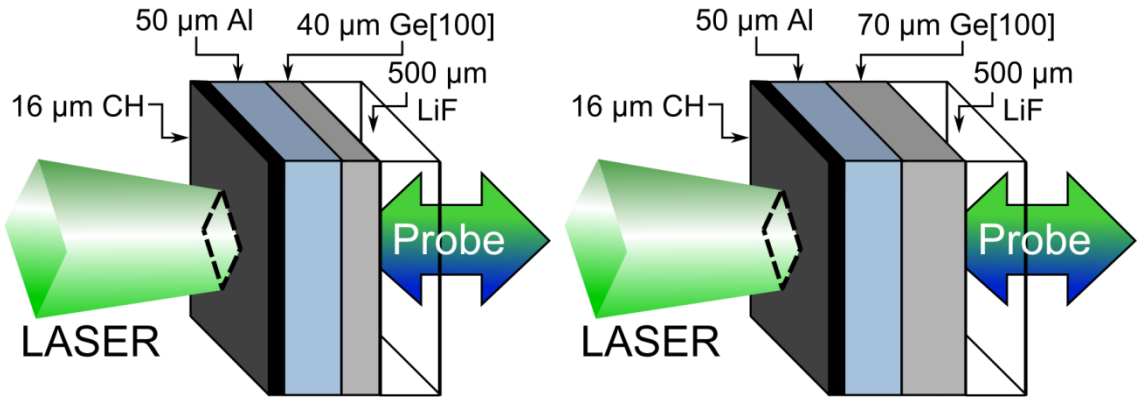

Figure 15 Target design for the experiments presented. The material of interest, in this case germanium, was placed between a lithium fluoride window to prevent spall and an aluminum pusher with an ablative plastic layer on the drive side. Two thicknesses of germanium sample were used.

Experimental Details

The experiments presented were conducted at the Janus target area at the Jupiter Laser Facility. A single drive laser beam was used for the experiments, as energies exceeding ~250 J were not required and a 4 ns square pulse was used unless otherwise noted. To ensure drive planarity and uniform energy deposition across the target, a phase plate was used in the drive laser beam, producing a 1 mm^2 square focal spot on the target. Of the diagnostics discussed in Chapter 2, only VISAR and single-wavelength reflectivity were used, in combination with the SWORD. Temperatures in the germanium samples were not expected to exceed 1000 K, well under the minimum detectable temperature for the SOP. In the experiments presented below, u_p was the variable measured with the highest precision. As the samples were thin, transit times were also obtained, however, the precision with which those values can be used is limited due to the fact that the shock waves were not supported throughout the transit time. The shock waves are most likely decaying as they propagate through the sample.

Results

Velocimetry

In order to collect reflectivity normal to the target surface, VISAR was collected at 27 degrees from normal and the resulting data were corrected for both the presence of LiF windows and the angle deviation from normal. Three laser energy regimes were used to study the response of germanium to shock compression: a low energy regime where the three-wave structure of the elastic, plastic, and phase transition waves could be readily observed; a medium energy regime where the initial elastic wave was highly overdriven, but the three waves were still separated in time within our resolution; and finally a high energy regime wherein the target was shocked directly into the phase transition. Results from all three energy levels are shown below.

Three Wave Structure

The three wave structure previously observed by Graham et al. and later by Gust and Royce was also observed in this experiment and found to be in good agreement with those previous results [39-41]. Based on conclusions from both previous experiments, the three wave structure observed in this experiment can be assigned as shown in Figure 16**Error! Reference source not found.**, with the initial wave being the elastic precursor, followed by two inelastic waves, the first of which is a plastic wave and the second a phase transition wave. An initial inelastic wave essentially separates into two waves; the first inelastic wave brings the material up to the state at which the phase transition begins and the second brings the material to the final pressure state once the phase transition is complete.

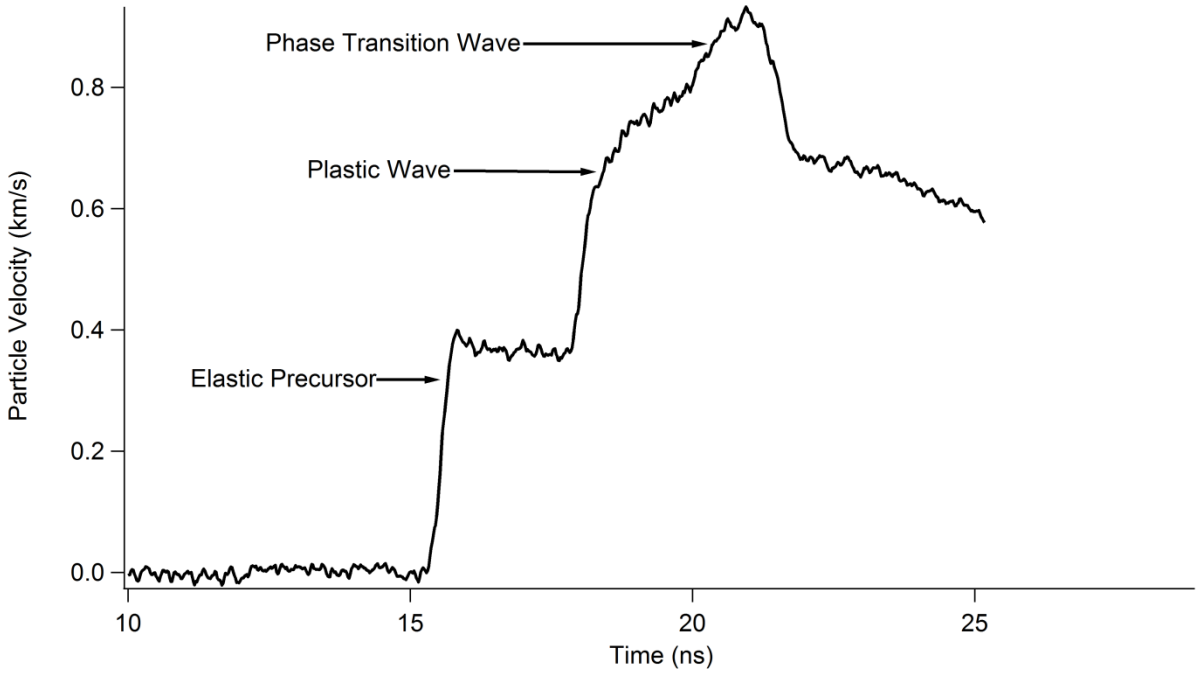

Figure 16 Three wave structure from the VISAR.

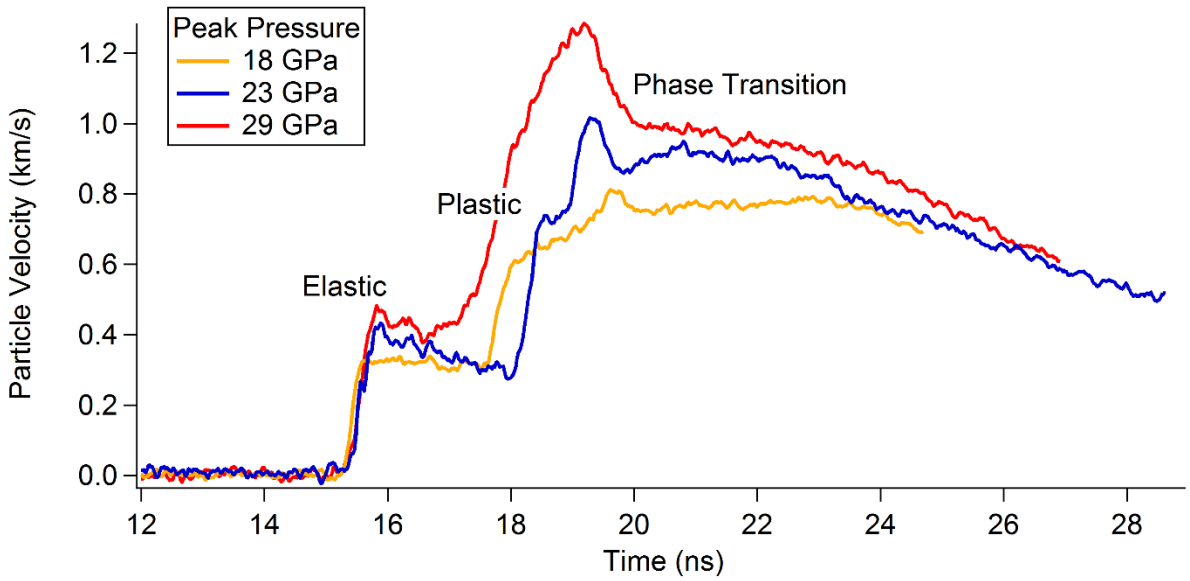

Figure 17 Particle velocity traces for three different shot energies. The plastic and phase transition waves increase with greater energy input. The unexpected delay between the elastic and plastic waves for the 23 GPa trace is most likely due to the interaction between the reflected elastic wave and the plastic wave.

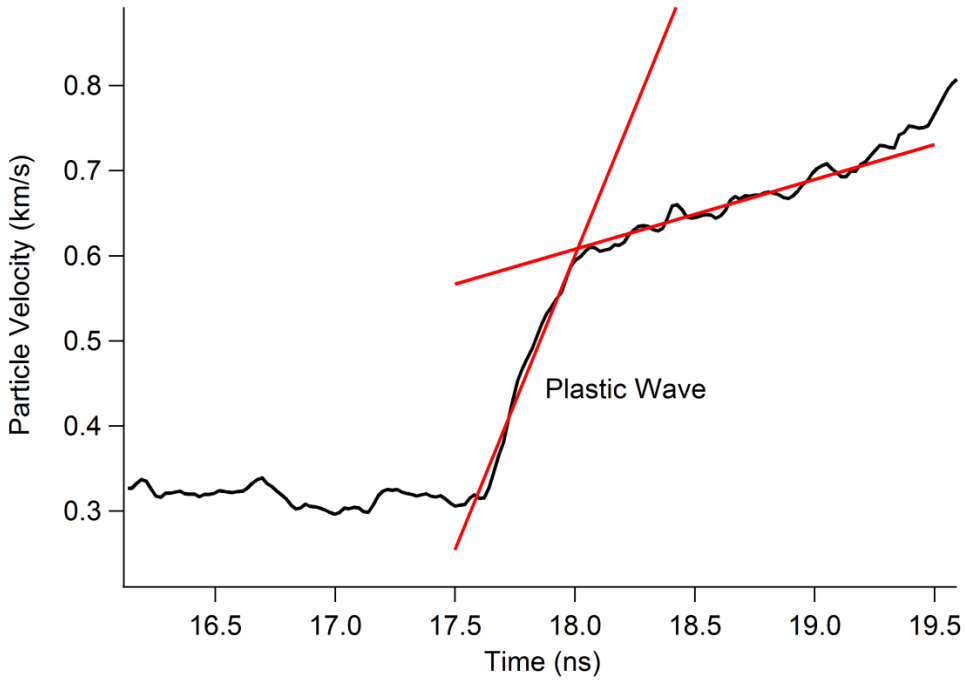

Figure 18 Method used for determining the plastic wave velocity. Intersection of the two fit lines was used to determine velocity for plastic waves with indistinct plateaues.

In the case of a target with a window of lower shock impedance than the sample, as is described here with a germanium sample and LiF window, the elastic precursor and first plastic waves can reflect from the sample-window interface and propagate back through the germanium. This complicates the analysis as the reduction in stress in the first or second plastic waves due to this wave interaction can prevent the material from reaching the phase transition state at the interface. This problem is avoided in shots with higher peak pressure where the material is directly driven into the metallic state.

Reflectivity

In order to test this new broadband reflectivity diagnostic, a series of laser-shock experiments were conducted on single crystal germanium in the target configuration shown in Figure 15. Initial experiments were designed to test the feasibility of the SWORD and, as such, reflectivity spectra were taken primarily in the NIR. Following the success of these early experiments, later experiments obtained data spanning wavelength ranges from the visible to the NIR. An example set of SWORD spectra from the initial NIR experiments in shown in Figure 19, with traces from the spectra and VISAR combined in Figure 20.

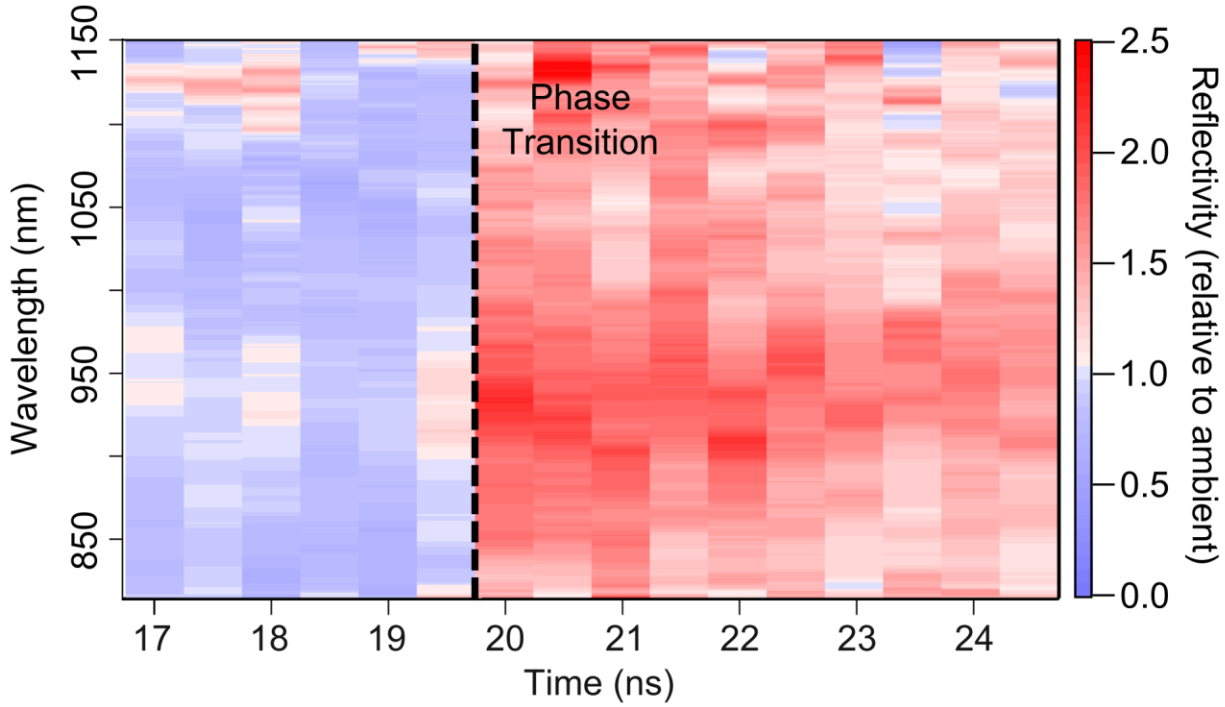

Figure 19 Reflectivity spectra obtained by comparing the sample intensities to the static reference intensities. Following elastic wave arrival at 15 ns and inelastic wave arrival at 17.5 ns, there was small decrease (5-10%) in the intensity of the reflected sample pulses, most likely due to a slight roughening of the target surface. An 80-90% increase in the reflectivity of the germanium sample was observed at 19.5 ns, which indicates the germanium phase transition accompanied by closure of the band gap.

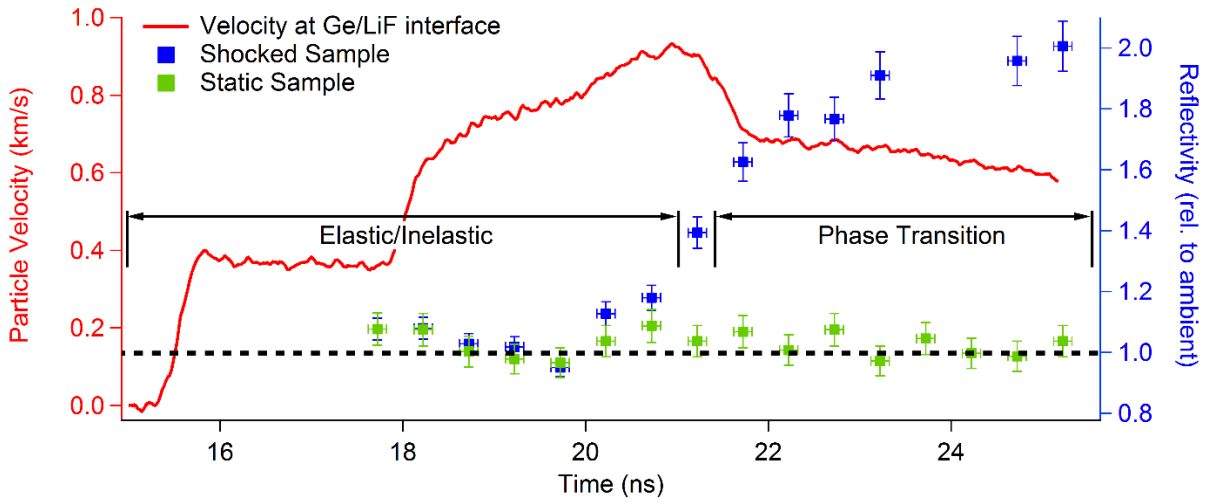

Figure 20 Reflectivity between 900 and 950 nm extracted from Figure 19. The small decrease in reflectivity that accompanied the elastic and inelastic precursors can be observed between 17 and 19 ns, with the significant increase that accompanied the phase transition beginning at 19.5 ns. The dashed black line at a reflectivity of one is a guide for the eye. The red line is particle velocity at the germanium-LiF interface obtained from the VISAR. The elastic wave begins prior to the SWORD time window, but rise of the inelastic wave can be seen at 17.5 ns and the arrival of a phase transition wave can be observed at 19.5 ns.

Phase Transition from VISAR and SWORD

Combined VISAR velocity profiles and SWORD reflectivity spectra are shown in Figure 21 through Figure 24. Figure 21 and Figure 22 contain data from the lowest energy shots, where the three-wave structure was clearly visible. In both shots the phase transitions are accompanied by a significant (at least two-fold) increase in reflectivity in the NIR, while the previous two waves do not appear to have a significant effect on the NIR reflectivity. On some shots a greater inconsistency was observed on arrival of the first inelastic wave, suggesting that there is a small degree of surface roughening taking place at the germanium-LiF interface. The utility of the SWORD in disambiguating waves is clear from Figure 23, which still has the three wave structure, but without the clear steps of the previous two figures. From the absence of any reflectivity change on arrival of the first wave, we can identify it as an overdriven elastic wave. The second wave results in a reflectivity decrease, suggesting that it is the first inelastic wave, and then the third wave begins to increase the reflectivity again, particularly in the NIR, identifying it as a phase transition wave. Figure 24 contains data from a high-energy shot where the germanium was shocked directly into the phase transition. No three wave structure is observed, and importantly, the wavelength dependence of the reflectivity across the spectral range has changed from the ambient, with a loss of reflectivity in the visible.

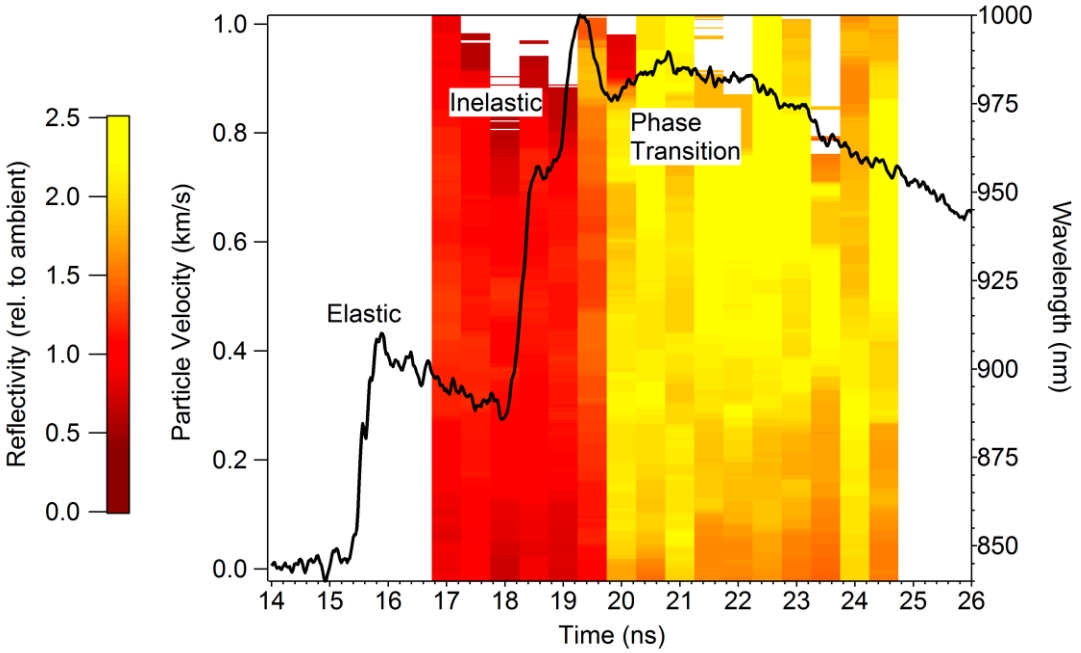

Figure 21 Velocity lineout from the VISAR is in black, overlaid on reflectivity data from the SWORD.

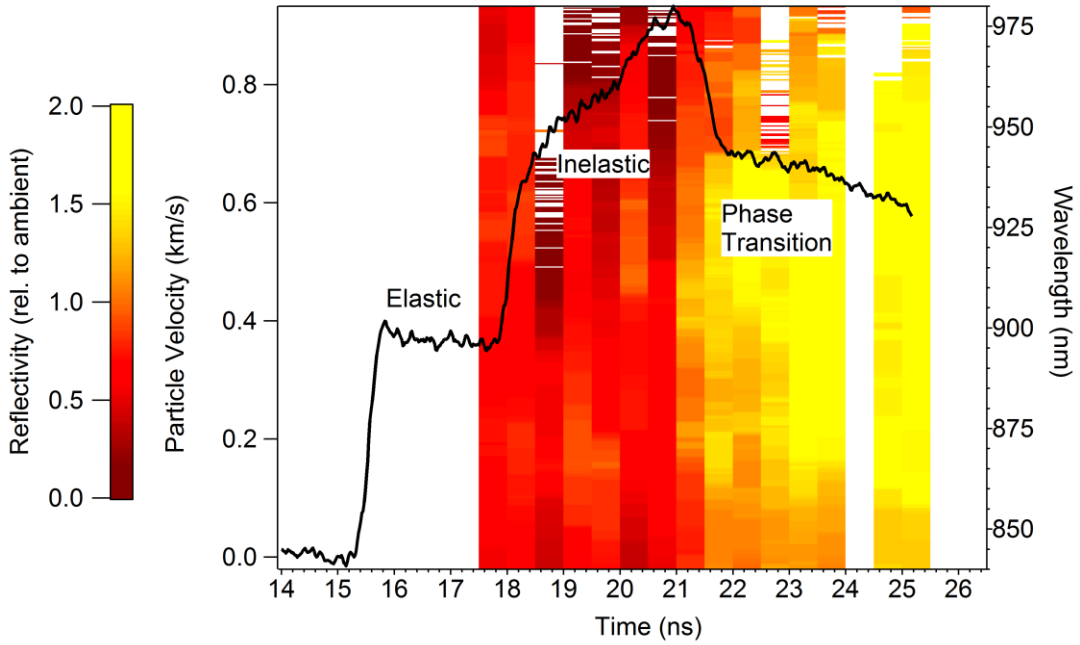

Figure 22 Velocity lineout from the VISAR is in black, overlaid on reflectivity data from the SWORD. The gap around 20 ns is a result of unacceptably low signal for that particular pair of spectra.

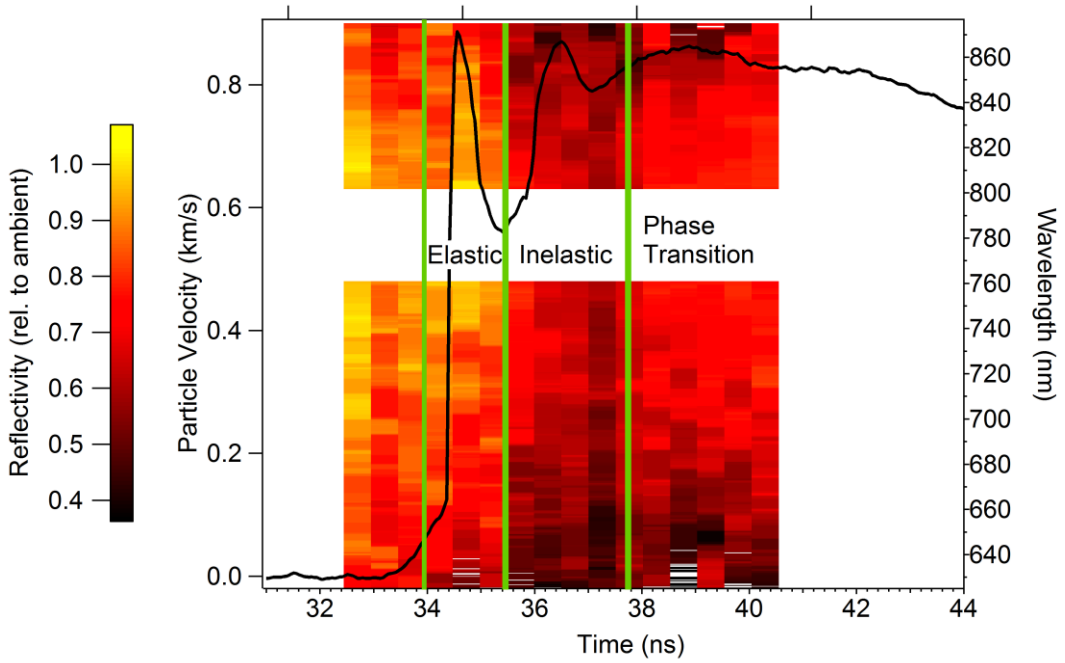

Figure 23 Velocity lineout from the VISAR is in black, overlaid on reflectivity data from the SWORD. The gap between 750 nm and 790 nm is a result of filtering to remove a 780 nm fundamental peak.

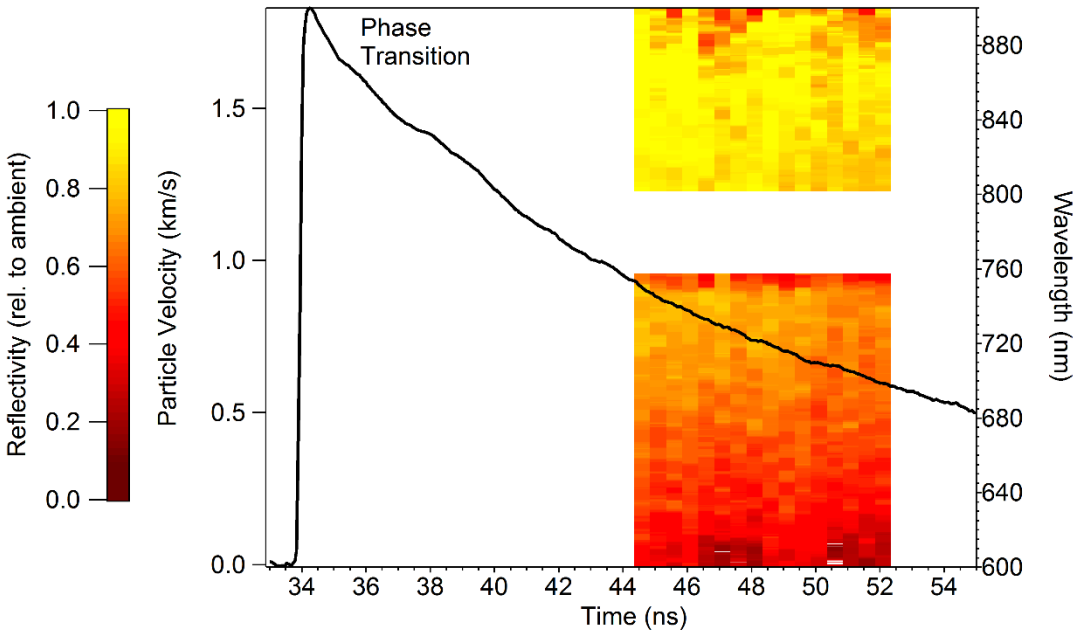

Figure 24 Velocity lineout from the VISAR is in black, overlaid on reflectivity data from the SWORD. The gap between 750 nm and 800 nm on the SWORD data is a result of filtering to remove a 780 nm fundamental peak.

Discussion and Conclusions

Figure 25 and Figure 26 present velocity and pressure data from this experiment in the context of previous data. Our data agree with that of Gust and Royce, as well as that of Marsh. The elastic-wave data in Figure 25 which is offset from that of Gust and Royce is the result of overdriving without shocking directly into the phase transition. Both figures confirm that the third wave we observe is well within the range over which the phase transition has previously been observed.

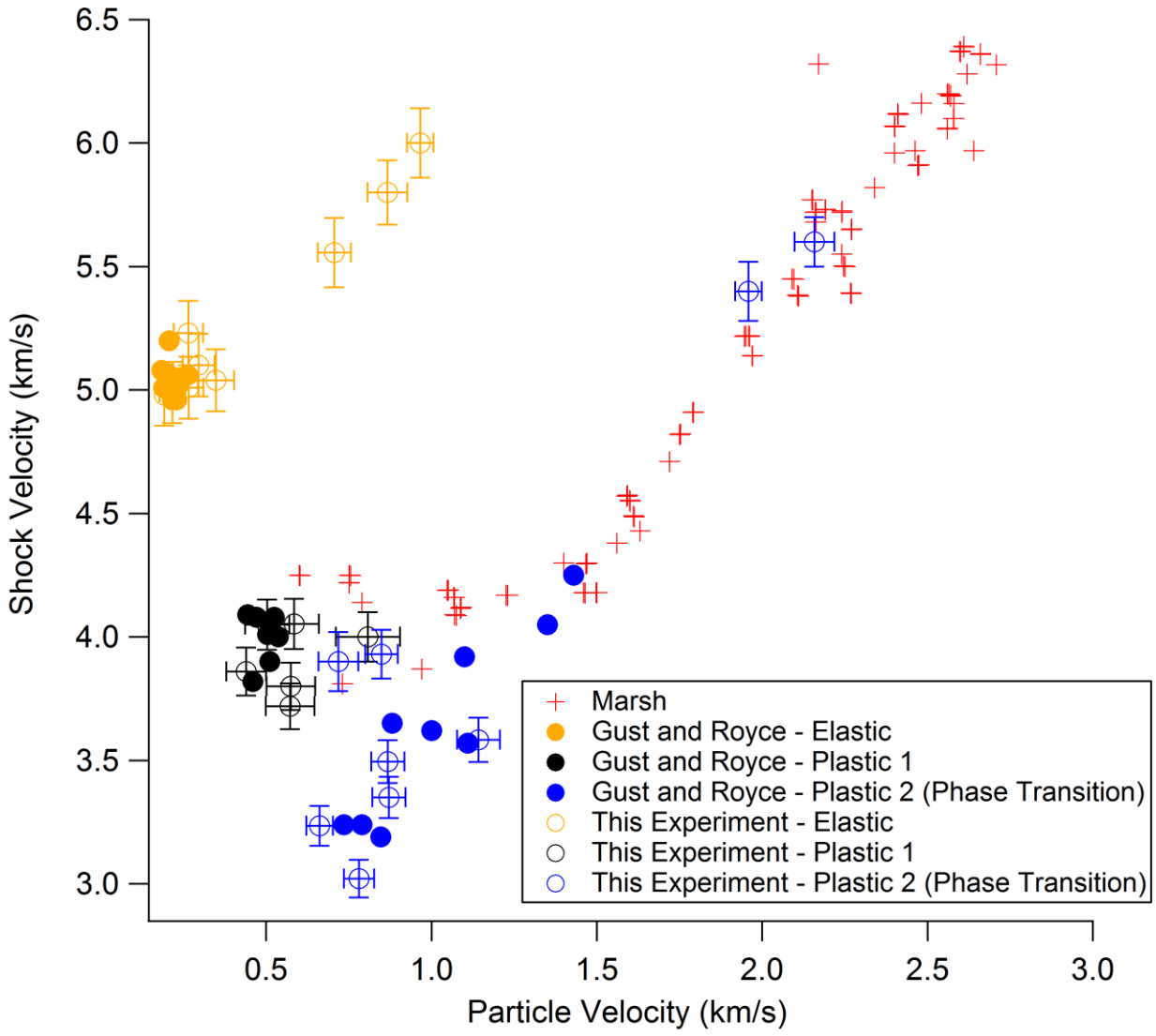

Figure 25 Shock velocity vs. particle velocity for this experiment and previous experiments.

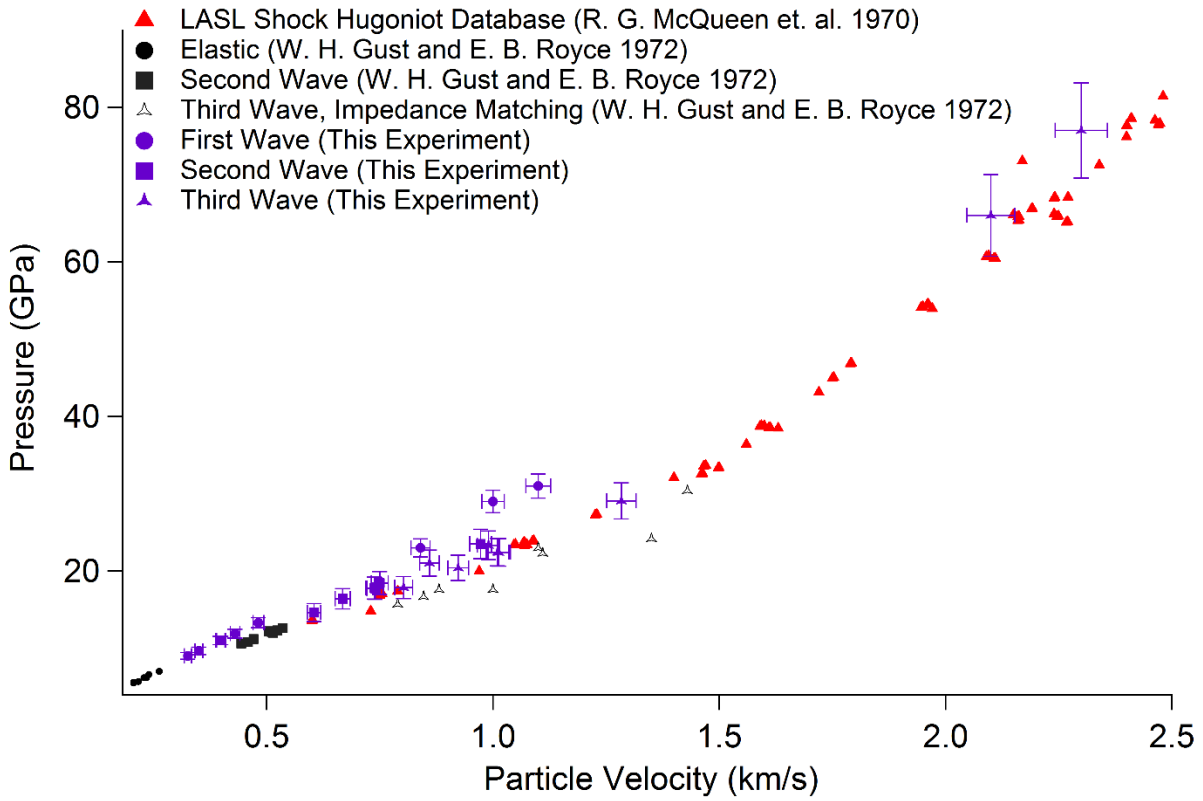

Figure 26 Pressure as a function of particle velocity for this experiment and previous experiments.

Initial Results

Initial experiments in the NIR have relatively low wavelength resolution due to low signal-to-noise, but multiple shots at varying peak pressures can be compared in order to obtain the pressure dependence of the reflectivity. This is shown in Figure 27, along with previous data. It is clear that the reflectivity in the NIR is increasing, which is congruent with a transition from a semiconductor to a metal, however, confirmation that the same material phase is observed in our experiments and static experiments requires higher quality data. This was obtained after improvement to the SWORD system were made. Reflectivity over 600-900 nm was measured in order to confirm that a similar feature was observed in our data and that of Hanfland et al.: this is discussed in the next section. In comparing with static compression literature data, caution must be used due to the temperature and strain rate differences, but there is agreement between our data and the optical reflection data from Hanfland *et al*.

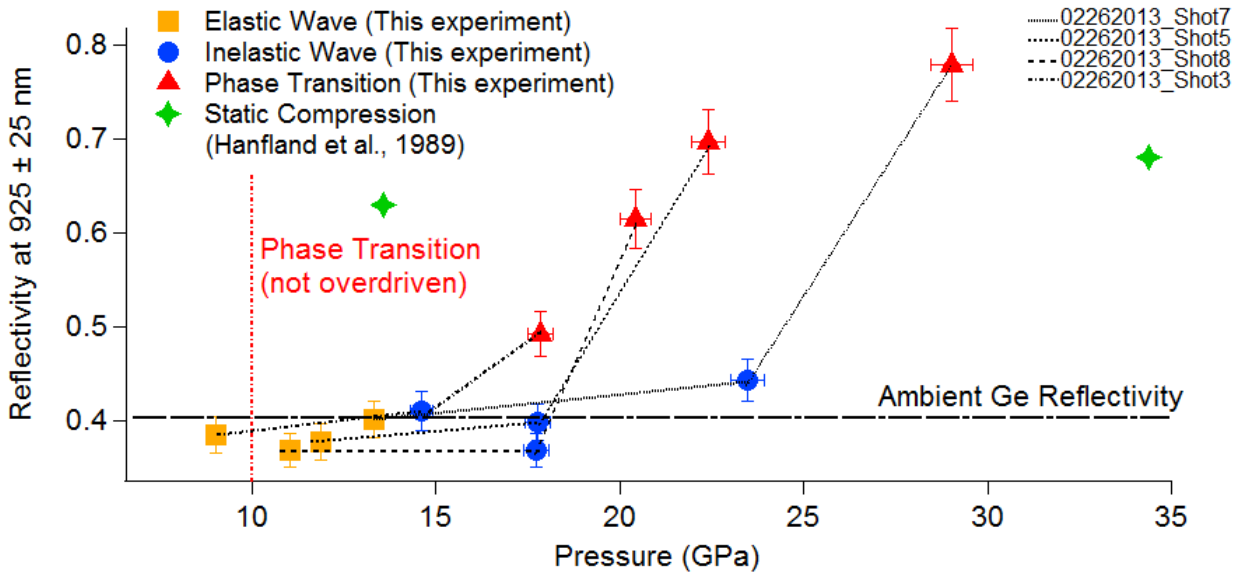

Figure 27 Normalized reflectivity between 900 and 950 nm from this experiment and Hanfland et. al. Pressure at the peak of each wave is shown for four shots. Dashed lines between the data points indicate subsequent waves for a single shot. An increase in the NIR reflectivity was not observed during transit of the elastic and inelastic waves. The phase transition wave, however, was accompanied by a pressure dependent increase in the reflectivity. The phase transition was overdriven, as evidenced by the shift from the 10 GPa transition pressure observed in static compression experiments (indicated by the vertical dashed red line).

Wavelength-Dependent Reflectivity

The Drude-Lorentz model can be used to connect measured optical properties to the electronic properties of the material. We have used the oscillator expression consisting of a combination of a Drude term and a linear combination of Lorentz oscillators to model the complex dielectric function. This, in tandem with the Fresnel equation, allows us to fit this oscillator expression, using a least squares technique, to the reflectivity data obtained in this experiment, as well as that of Hanfland et al. As the static compression data from Hanfland et al. spanned a greater frequency range than our data, initial fits were done using the static data to determine the number of oscillators. The results from these fits can be found in Figure 28 and Figure 29.

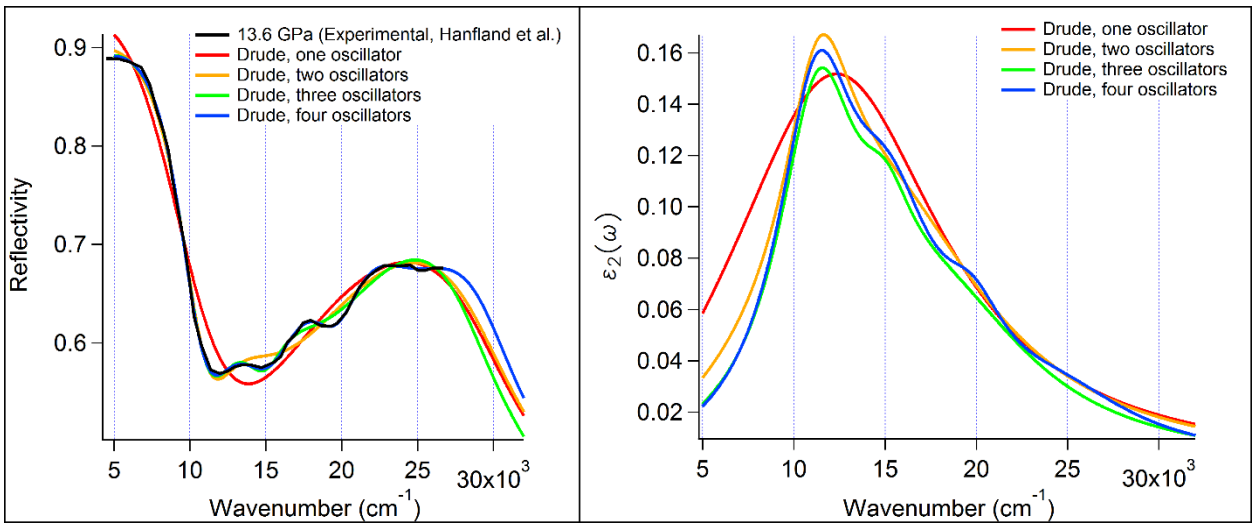

Figure 28 (Left) Reflectivity of a 13.6 GPa sample from Hanfland et al. with various fit parameters. (Right) Imaginary component of the dielectric function for each fit.

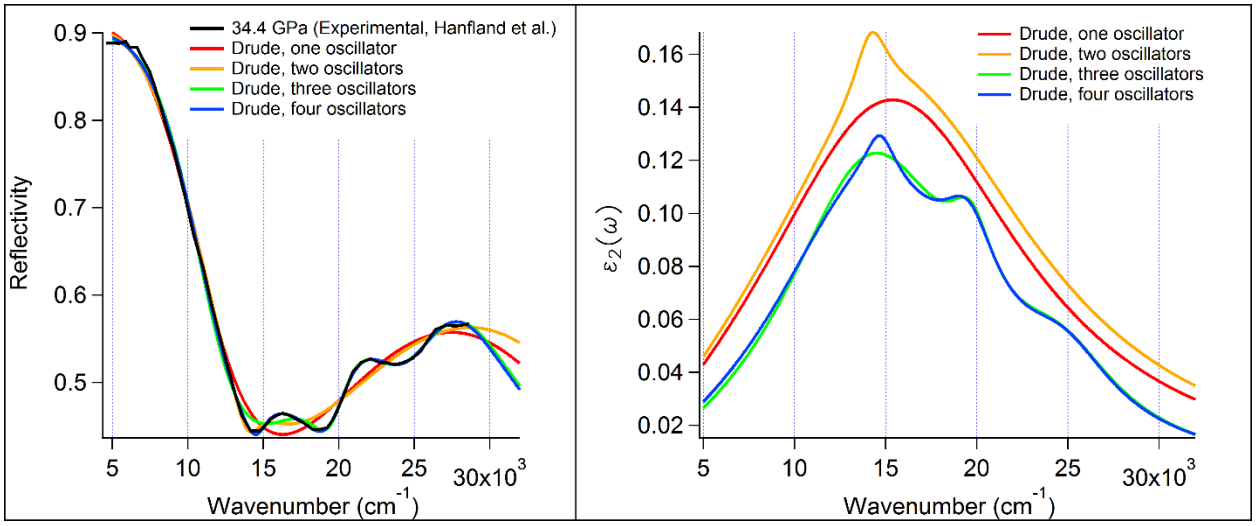

Figure 29 Reflectivity of a 34.4 GPa sample from Hanfland et al. with various fit parameters. (Right) Imaginary component of the dielectric function for each fit.

As four features were observed in the data of Hanfland et al., the best fit was obtained with four Lorentz oscillators. Two of the oscillators were within the frequency range of most of our shots, so the reflectivity data obtained in this experiment was fit using a Drude model and two oscillators. Data and models for four spectra at different pressures are shown in Figure 30. Data from Hanfland et al. is included for comparison, as is ambient reflectivity from Aspnes and Studna [52, 53]. The spectrometer was shifted such that the observed wavelength range was 550 nm to 900 nm. As was seen previously, we observe a high metallic-like reflectivity in the NIR which decreases in the visible. Features in the

visible are most likely due to interband transitions and are consistent with a nearly-free-electron metal as would be expected from germanium in the β-Sn phase.

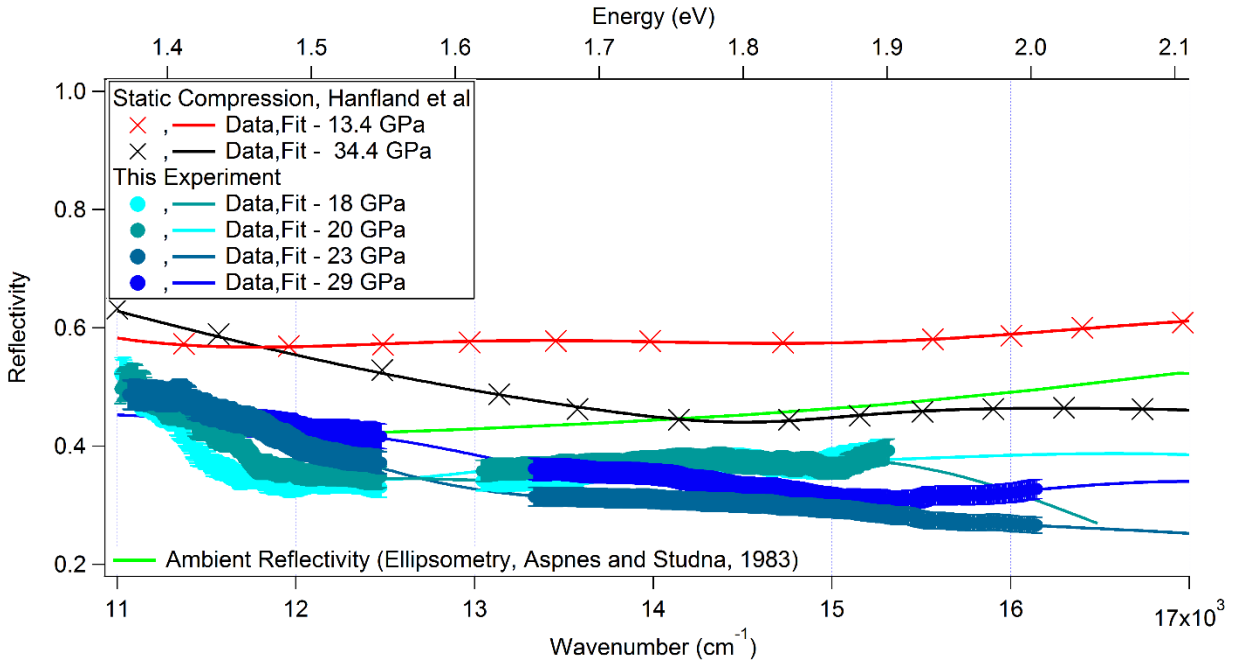

Figure 30 Normalized reflectivity from Hanfland et al. and this experiment with fits overlaid.

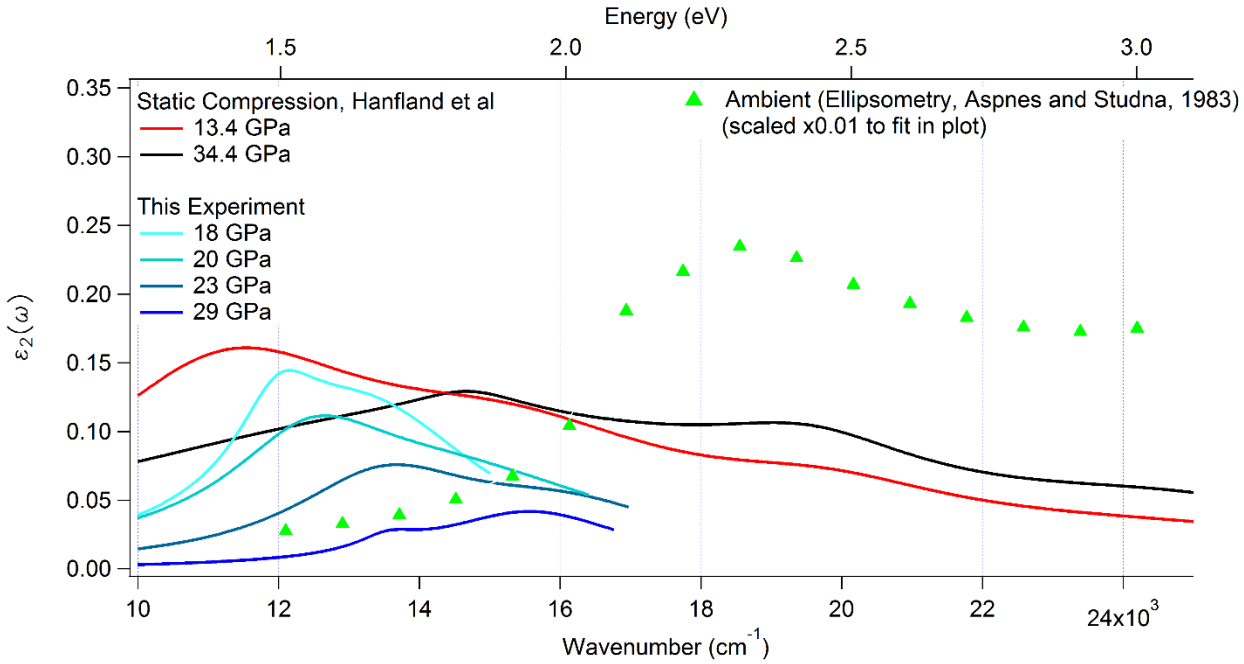

Figure 31 Calculated imaginary part of the complex dielectric function for data from Hanfland et al. and this experiment. Traces are shown over the observed wavelength range of the experimental data.

Using the fits to the reflectivity shown in Figure 30, the imaginary part of the complex dielectric function (minus the Drude component) can be obtained for each spectrum, as shown in Figure 31. In the static compression data, a significant shift towards higher energy in the first peak is observed, which is consistent with previous data on silicon metallization.[52, 54] The same trend is observed in data from this experiment, providing strong evidence for the theory that the same phase transition is observed in both static and dynamic compression. The fit to the spectra suggests the presence of a strong absorption peak that shifts from 1.5 eV (830 nm, 12000 cm^{-1}) at 18 GPa to 1.9 eV (720 nm, 14000 cm^{-1}) at 29 GPa. Although there is some previous research investigating band transitions in germanium under compression, (of particular interest is that of Zallen and Paul from 1976), there is little data at energies below 2 eV, where the peak observed in both this experiment and that of Hanfland et al. can be found [55]. It is, however, interesting to note that in the work of Zallen and Paul and that of Hanfland et al. and this experiment there is a shift in the peaks to higher energy, suggesting an increase in the gap between the bands as a function of pressure.

The observed absorption energy is well within the range over which parallel band excitations would be expected in germanium. An ab initio study of the first-order transition from diamond cubic germanium to beta-tin germanium found that the energy of the band structure at the Γ point was linearly dependent on the volume with the energy of the lowest four bands diverging as volume decreased [56]. There have been many studies calculating the full band structure or measuring the optical absorption of diamond-cubic germanium under pressure, however, the number of experiments investigating the pressure dependence of beta-tin germanium is more limited, with the majority of work done determining the transition pressure and unit cell characteristics [2, 3, 28, 43, 45, 55, 57-65]. Fortunately, there is a larger body of work investigating the band structure of silicon over the diamond to beta-tin transition [52, 54, 66]. Silicon in the beta-tin phase has an absorption peak around 2.25-2.3 eV due to the interband transitions as a result of splitting along the 101 planes. The energy of the transition increases as a function of pressure; as the volume of the cell decreases the form factor for a given reciprocal lattice increases, blue-shifting the energy at which the dominant optical absorption occurs [52, 54, 67]. Germanium and silicon have similar band structures, with the conduction band for silicon at a higher energy than that of germanium [67]. In the absence of full electronic structure calculations for the beta-tin phase of germanium, it would be reasonable to assume that the dominant absorption observed in germanium would be at a lower energy than that observed in silicon, and would increase in energy as pressure increases, as is observed in this experiment, and shown in Figure 32.

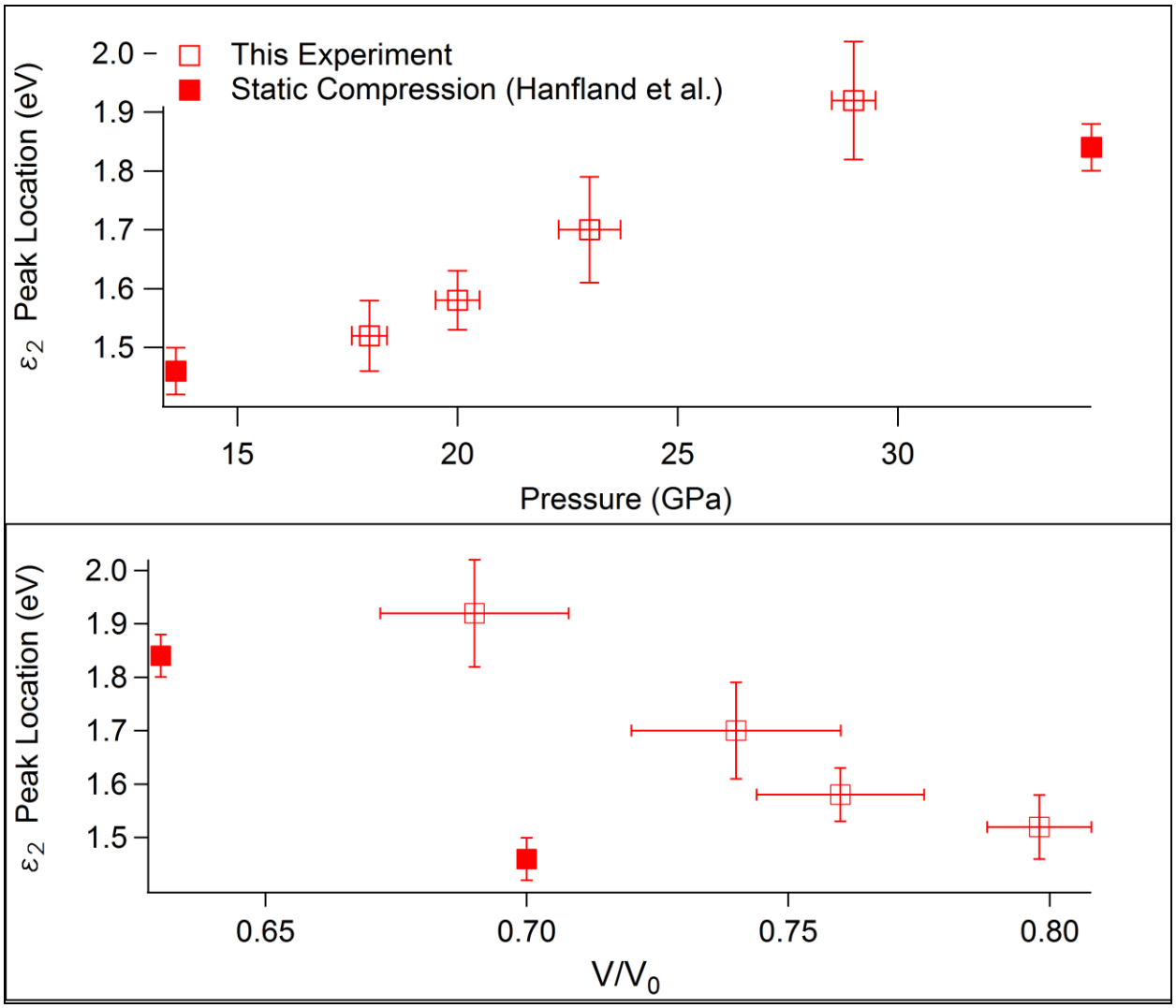

Figure 32 Absorption peak location as a function of pressure (top) and relative volume (bottom).

Section II – Anisotropic Deformation and Fracture

Abstract

The recently developed Janus High Resolution Velocimeter (JHRV) was used to study laser-driven elastic and inelastic deformation in diamond. The three primary orientations of single crystal diamond, <100>, <110>, and <111> were studied, along with two types of polycrystalline diamond, microcrystalline and nanocrystalline. Two types of shock wave geometry were used; spherical shock waves were driven into the sample in order to observe the effect of the elastic constants on wave propagation and planar shock waves were used to study heterogeneous fracture and deformation at the shock breakout interface. The primary goal was twofold; the first goal was to observe propagation of elastic and plastic waves through acoustically anisotropic single crystal samples of diamond and silicon in order to quantify the effects of elastic anisotropy and investigate the changes in the sound speed under varying conditions. It was determined that the elastic breakout shape and size of all three orientations of diamond, as well as the polycrystalline diamond samples, could be well approximated by calculating the orientation dependent sound speed using the known diamond elastic constants. In addition, the plastic response for all three orientations was observed to occur along the known slip systems for diamond cubic structures. The second goal was to investigate the difference in the fracture and deformation response of nano- and microcrystalline diamond. We found that both types of polycrystalline samples responded to inelastic compression with fracture. Spall fracture was observed in the free surface samples. The LiF-tamped samples exhibited fracture as a result of the reflected wave at the diamond/LiF interface. For the tamped samples, the microdiamond responded with greater roughness. No difference in the overall roughness as observed in the free surface samples. In order to accurately model the fracture behavior under shock compression, the Grady spall fracture model was used and we obtained values for the fracture toughness of the micro- and nanocrystalline diamond of 103±14 MPa $m^{1/2}$ and 44±8 MPa $m^{1/2}$, respectively. Using these values for the fracture toughness, the strain rate dependent spall stresses were calculated and found to agree with previous research. Samples of both diamond and silicon were prepared as described below and experiments were conducted at the Jupiter Laser Facility in Target Area 1. Relevant diagnostics are also described below, and results can be found in the next two chapters.

Introduction

As a material is dynamically compressed, it undergoes a series of mechanical transformations. Initially the material is elastically deformed; the atoms move closer together along the direction of compression, no bonds are broken or formed and the process is reversible. As the degree of compression increases, the deformation becomes inelastic and substantially more complex. The compression is no longer reversible and one dimensional plastic flow begins, heterogeneities form, shear forces propagate, bonds are broken, voids and defects nucleate and expand, and fracture networks proliferate through the sample. Essentially, in the inelastic regime, dynamic deformation occurs as a series of correlated processes having dependence on both intrinsic material properties and extrinsic compression conditions. The fundamental kinematic properties of the material change, both as a result of the initial conditions and as a response to the specific compression mechanism. As we collect more data and build up increasingly complex models of material response, certain questions become ever more important. What effect does strain rate have on the chain of events in the deformation process? How can we better predict the strength of a material under a variety of conditions? Can we move beyond constitutive equations describing specific materials and generate a model to explain and predict inelastic behavior in a number of materials under varying compression conditions? What novel material properties can be introduced by tuning the microstructure, and how can we more accurately model the relationship between microstructures and macroscopic material properties?

A complete understanding of the mechanisms and dynamics of deformation under compression is important for a large number of fields. The development of high strength poly-crystalline ceramics for body armor requires methods for predicting the response of the armor to both blunt and point impacts. Dynamic response of tissue and bone to stress and strain is vital for better identifying the effects of biomechanical compression as well as for the development of engineered replacements for irreparably damaged tissue and bone. Potentially relevant to all of the above is the recent growth of the field of additive manufacturing, the process of 3D printing complex structures for use as medical implants [68-70], fuel cells[71], high strength armor[72-74], and construction materials[75-77]. The field of additive manufacturing has been advancing quickly, allowing for the rapid prototyping and development of materials with complex microstructures designed for optimum performance in specific tasks. As this field grows, so grows the need for improved modelling in order to design microstructures and materials with ideal characteristics for specific purposes.

Another rapidly progressing field with a significant dependence on improving our understanding of deformation is capsule development for inertial confinement fusion (ICF). In order for ICF, as it is currently envisioned, to succeed as a means of energy generation, it is necessary to fully understand and eventually eliminate sources of Rayleigh-Taylor instabilities. This includes the interfacial Richtmyer-Meshkov instabilities which originate as the shock passes from the outer shell of the fuel capsule into the liquid core [78, 79]. Achieving the necessary temperatures and pressures to initiate the fusion process is contingent on an implosion wherein both capsule and contained fluid remain spherical as

the material compresses. When instabilities develop, they destroy the spherical symmetry and the integrity of the capsule-fuel interface. This results in mixing and the reallocation of thermal energy to ionization of the capsule shell atoms, lowering the temperature and reducing the reaction rate. It is the micromechanical response of the capsule under ICF conditions that determines whether defects nucleate and instabilities develop. The contributions of individual deformation mechanisms to microstructure and defect formation must be investigated if capsules designs are to be optimized [80-82].

On a larger scale, hypervelocity impacts between asteroids, satellites, and planetary bodies result in the natural formation of shock waves and material deformation, and eventually leave behind mineralogical and geological clues as to their origins and composition. The rheological properties and deformation induced microstructures of minerals are a fundamental key to understanding and modeling the evolution of planetary bodies [83]. These properties are also vital for understanding and predicting earthquakes, particularly those occurring deeper in the mantle where pressures are higher. A number of mechanisms have been suggested for the origin of these earthquakes; however, poorly constrained rheological and microstructural material properties at high pressures result in large uncertainties [83].

In order to answer the aforementioned questions, we must utilize techniques that allow us to probe specific deformation mechanisms and examine the effects of microstructure, crystal orientation, strain rate, and overall compression path on the deformation. The primary reason for the lack of quantitative determination of deformation mechanisms has been the limited spatial and temporal resolution of diagnostics used to investigate the compressed matter. A complete investigation of these deformation mechanisms requires spatial resolution on the order of microns and temporal resolution on the order of picoseconds to nanoseconds. Information about the deformation and fracture of materials under shock compression is typically obtained in one of two ways; either derived post-shock, (i.e. from recovery experiments), where the material is shocked and then the recovered sample is examined, or inferred from features in transiting wave profiles. The first provides very limited information with regards to the time scale of deformation mechanisms, and the second provides limited information with regards to spatial scales. The development and use of techniques which can quantify the time dependent deformation response of dynamically compressed materials on the microscopic spatial scale is vital for improving modelling and analysis of material properties under compression.

Above the Hugoniot elastic limit, the deformation in the material is no longer one-dimensional elastic and is therefore no longer reversible. At this point the shock compressed sample is deforming in three-dimensions and bonds are breaking and crystal planes are shifting. The mechanism for inelastic deformation in a material also varies considerably based on the material properties. The prevailing mechanism for inelastic deformation in brittle solids is fracture in order to reduce localized shear stress, while metals tend to deform via plasticity prior to undergoing ductile fracture. In brittle materials this would be characterized by a complete loss of strength following the HEL whereas metals would be expected to retain some strength and deform plastically. Over the time

scales of shock compression events, this line between brittle and ductile deformation is blurred and most materials have been found to behave somewhere between the two extremes, partially due to the high degree of defect and heat generation within a shock wave

Dynamic compression experiments frequently use the Velocity Interferometry System for Any Reflector (VISAR) developed in the 1970's.[8] The VISAR measures a phase shift due to the compression wave propagation through the sample, and this phase shift can be used to obtain shock and particle velocities as a function of time. This provides us with equation-of-state variables such as pressure and density, as well as wave profiles for the elastic and inelastic waves propagating through the sample. The VISAR is, however, almost always implemented as a point diagnostic with zero spatial resolution or a line diagnostic, with resolution between 30 and 50 microns across one dimension of a sample. This precludes the observation of the spatially heterogeneous deformation processes vital to our understanding of material behavior under dynamic compression.

To decouple and eventually understand the mechanisms governing inelastic deformation in diamond, we have conducted two sets of experiments. The first investigates the effects of acoustic anisotropy on the large scale breakout of a divergent shock wave propagating through a diamond sample while the second investigates the fracture and deformation response of diamond to uniaxial compression. Studies on the timescale and morphology of fracture dynamics, which can occur over μm length scales and timescales of a nanosecond or less, have generated a lot of interest in recent years but experimental limitations have not permitted simultaneous measurements on these time and length scales[84-88]. Recently a new two-dimensional imaging velocimetry technique has been developed on Omega (OHRV 2D-VISAR system) to measure the velocity roughness of shock fronts with a ~10 m/s resolution and a spatial resolution of ~2 μm over a 0.8 mm field-of-view[87]. The 2D-VISAR provides us with a picosecond "snapshot" of the velocity and target reflectivity field at a time after the arrival of a shock front at the reflecting interface. We have conducted a series of shots combining the 1D and 2D-VISAR systems to study heterogeneous, anisotropic flow and the formation of fracture networks in diamond. The 1D VISAR records the compression history of the sample while the 2D-VISAR captures picosecond snapshots of the spatially resolved velocity and reflectivity maps.

Chapter 1: Experimental Details

The experiments presented were conducted at the Janus target area at the Jupiter Laser Facility. Both single- and dual- drive laser beams were used for the experiments and a 4 ns square pulse was requested unless otherwise noted. For the planar shock wave experiments, to ensure drive planarity and uniform energy deposition across the target, phase plates were used in the drive laser beam, producing a 1 mm^2 square or 0.28 mm^2 round (0.6 mm diameter) focal spot on the target. The planarity of the shock front was observed in both the line-VISAR and the 2D VISAR and found for most shots to be flat within the limits of our resolution. Exceptions are noted in Chapter 3. Spherical shocks were generated by removing the phase plates and focusing the drive beam onto the surface of the target. The focused beam was 150-200 microns in diameter, with some variation due to the changing quality of the wave-front. Of the diagnostics discussed in Section I Chapter 2, only VISAR and single-wavelength reflectivity were used, in combination with the JHRV. In the experiments presented below, u_p was the variable measured with the highest precision. Particle velocity was measured from the reflective surface nearest the diagnostic, either the diamond surface or an aluminized layer on a LiF window in direct contact with the diamond surface. The shock waves are decaying as they propagate through the sample. Initial conditions in the target can be obtained by iteratively fitting the measured particle velocity profile to results from hydrocode simulations. At the shock pressures generated in the experiments discussed below, diamond is expected to have a two wave structure with 5-10 ns delay between the arrival of the elastic and inelastic waves, depending on shot energy and target thickness.

Details of the design and operation of the 2D VISAR diagnostic can be found in reference [89]. A brief discussion of the raw data can be found at the end of this chapter.

Target Design

Single-crystal diamond samples in three orientations were obtained from Diamond Technologies Inc. The <100> and <110> samples were synthetically grown using the high-pressure, high-temperature technique and therefore contained 30 to 100 ppm of nitrogen impurities. The <111> samples were natural diamond. All samples were 3 mm x 3 mm squares optically polished on both surfaces and of varying thicknesses between 0.8 and 1.1 mm. Sample thicknesses were measured using a micrometer prior to assembly of the target.

Polycrystalline diamond samples were purchased from Delaware Diamond Knives. Microcrystalline diamond samples were approximately 80% transparent while the nanocrystalline samples were approximately 40% transparent. All samples were disks 2 mm in diameter and 0.5 mm in thickness.

Targets were constructed by stacking the layers shown in Figure 33 using either a Fineplacer Pico (Finetech GmbH) or a pin micrometer to hold the layers in place. Double-Bubble™ Red-2 epoxy was then applied to the edges in order to avoid layers of epoxy between the materials. For the transparent diamond samples the LiF window was sputter

coated with a 104 nm layer of aluminum to improve reflectivity. The nanocrystalline diamonds were reflective enough to directly observe the diamond-LiF interface, however, in order to ensure that the aluminum coating had no unforeseen effect on the results, a small number of shots were done with nanocrystalline diamond and the aluminized LiF windows. No differences in the resulting data were observed.

The steel plate used for the spherical shock compression targets consisted of a 100 micron thick stainless steel disk in which a 500 micron diameter aperture was mechanically drilled. The Janus laser used to drive the shock waves possessed a low intensity halo around the focused beam and this aperture served to reduce the effect of said halo. When the aperture was not used a low velocity planar shock was observed at the diamond-LiF interface and the presence of this wave distorted the spherical shock wave at the same interface.

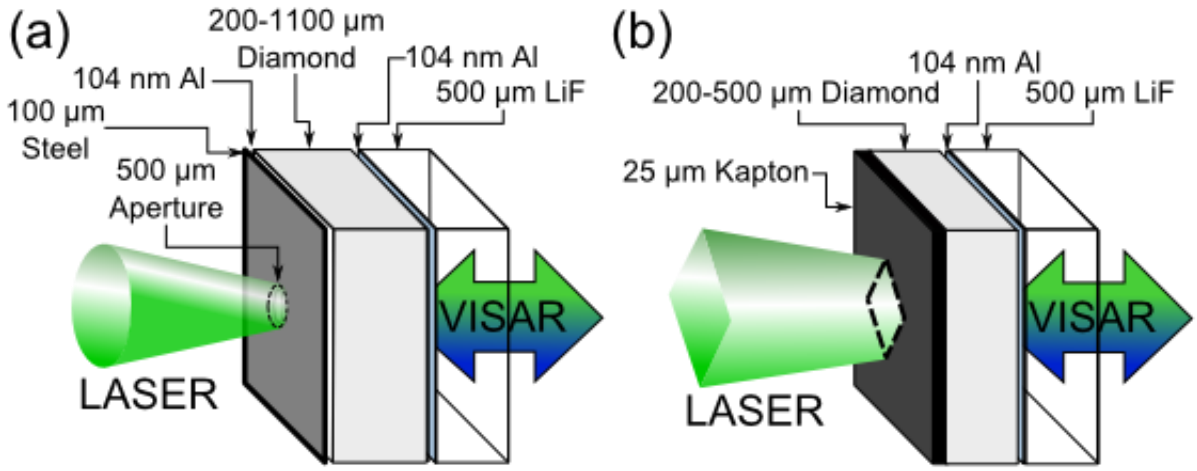

Figure 33 Target design for the diamond experiments. (A) Spherical shock compression target design. The steel backing plate with the 500 micron aperature was necessary to spatially filter the drive beam, which had a low energy halo. (B) Planar shock compression target design. Aluminized windows are shown in both A and B, as they were used for the majority of the experiments. When the window was not aluminized, it is noted.

Planar Shock Targets

A 1 mm FOV was used to observe the majority of the planar shock compression targets on the JHRV. A set of experiments were also done using the larger 3 mm FOV to observe the entire breakout in order to evaluate flatness and edge effects. The goal of these experiments was to study fracture and deformation on the 10-100 micron size scale, necessitating the use of a higher spatial resolution than was required by the spherical shock compression targets. For the majority of these experiments, the center of the 2D-VISAR was offset slightly from the center of the line-VISAR. As the breakout was assumed to be reasonably radially symmetric, the most information could be gained by observing a quarter of the breakout from the edge to the center.

Spherical Shock Targets

A 3-4 mm field-of-view (FOV) was used to observe the spherical shock compression targets on the JHRV. The spherical shock waves expand as they propagate through the sample and the larger field of view was necessary. For these experiments, the center of the line-VISAR FOV was aligned to the center of the 2D-VISAR.

Raw Data

An example data set from the line-VISAR and the 2D-VISAR is shown in Figures Figure 34-6. Figures Figure 34 contains both a raw line-VISAR image and the calculated velocity as a function of time and one spatial dimension. As this was a spherical shock compression experiment, breakout is observed to expand spatially over time.

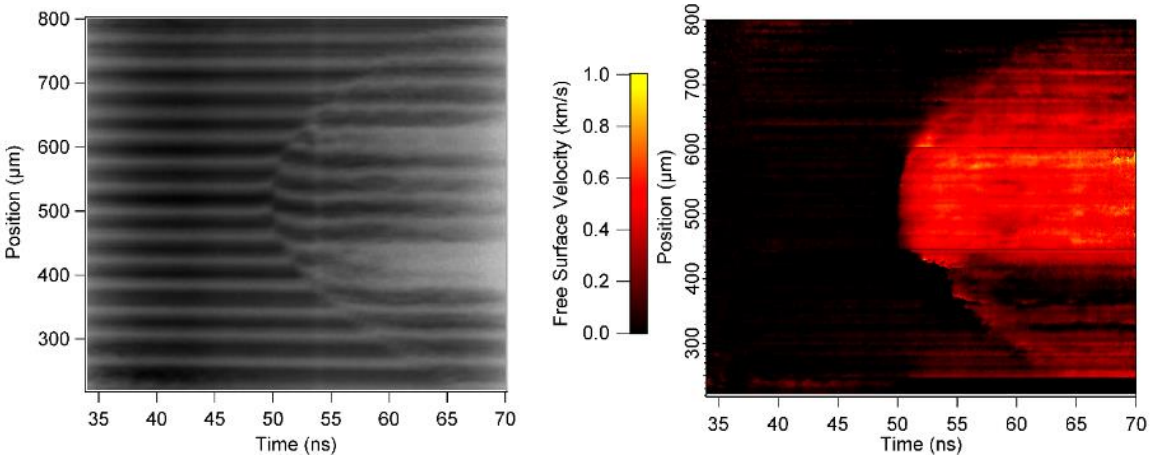

Figure 34 Line-VISAR raw data (left) and velocity (right) from spherical shock compression of a single-crystal, 110 diamond.

Figure 36 though Figure 38 contain 2D VISAR references and raw data. As the 2D VISAR is a quadrature diagnostic, the same image of the target is shifted in polarization by 90 degrees for each of the four quadrants. A schematic of the target geometry relative to the 2D VISAR raw data and results is shown in Figure 35.

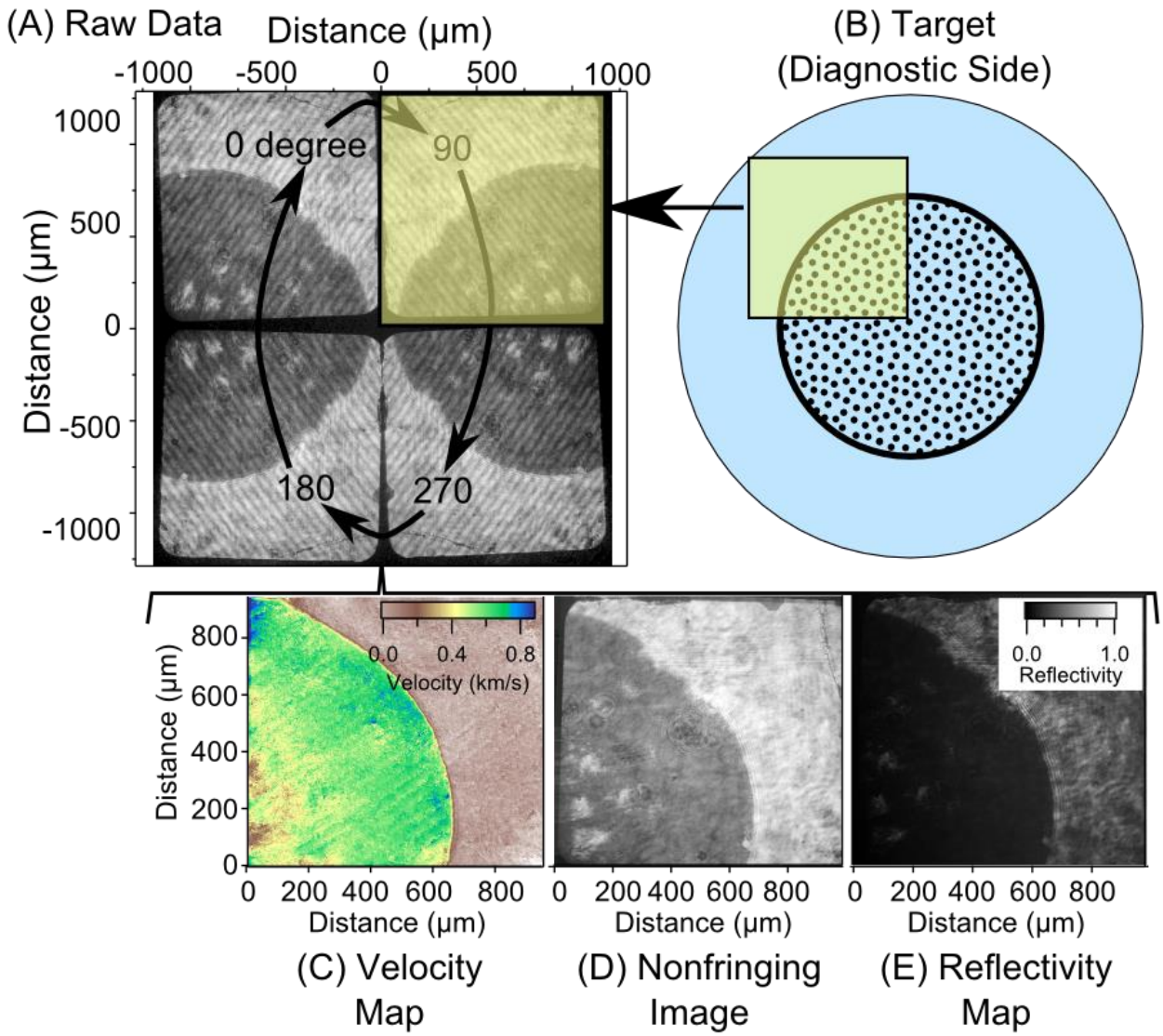

Figure 35 (A) Raw image from the 2D VISAR (B) Target schematic of the diagnostic surface. The dotted region in the center is the breakout relative to the whole target area and the yellow overlay indicates the region imaged by the 2D VISAR. (C) Calculated velocity map from the image in A. (D) Non-fringing image obtained by adding the four quadrants of A (E) Reflectivity map obtained by normalizing D using the unshocked region in the upper right side.

Figure 36 is a flat field image of the target taken prior to the shot to isolate features related to the target surface. The target was a 3 mm diameter, 1 mm thick single crystal 110 oriented diamond with no window. The extent of the target is indicated on the figure. Figure 37 is a fringing reference image of the same target and Figure 38 is the raw image from the actual shot. Breakout symmetry is two-fold, due to the 110 orientation of the sample, and is indicated on the image.

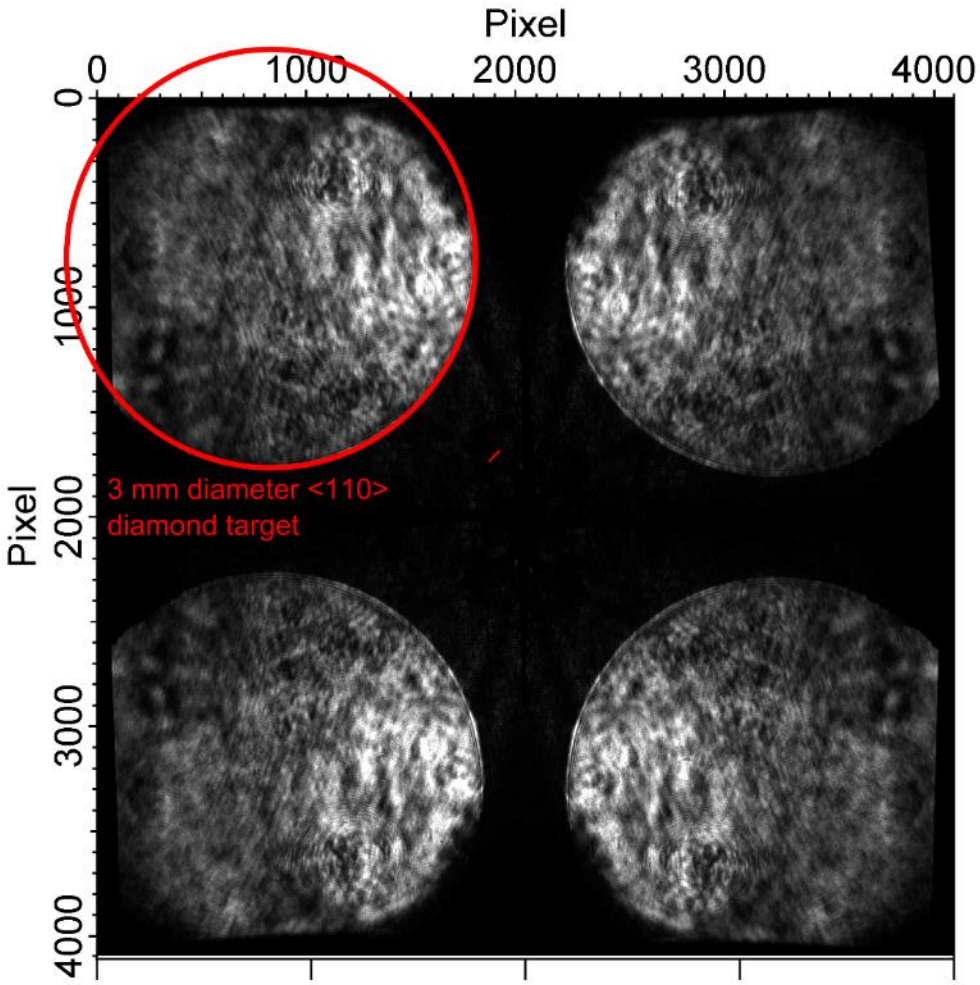

Figure 36 2D VISAR flat field reference taken prior to the shot. The 3 mm diameter diamond target is indicated in red.

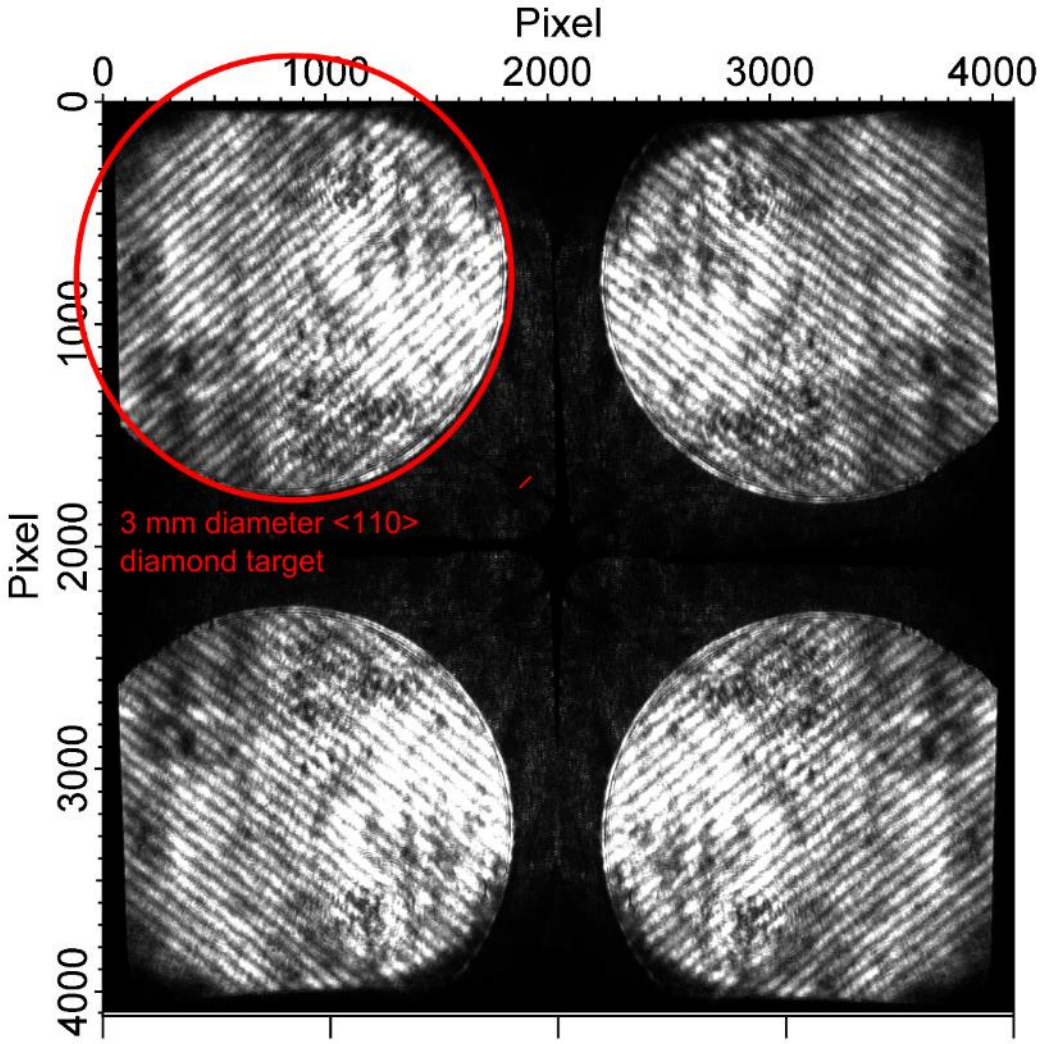

Figure 37 2D VISAR fringing reference taken prior to the shot.

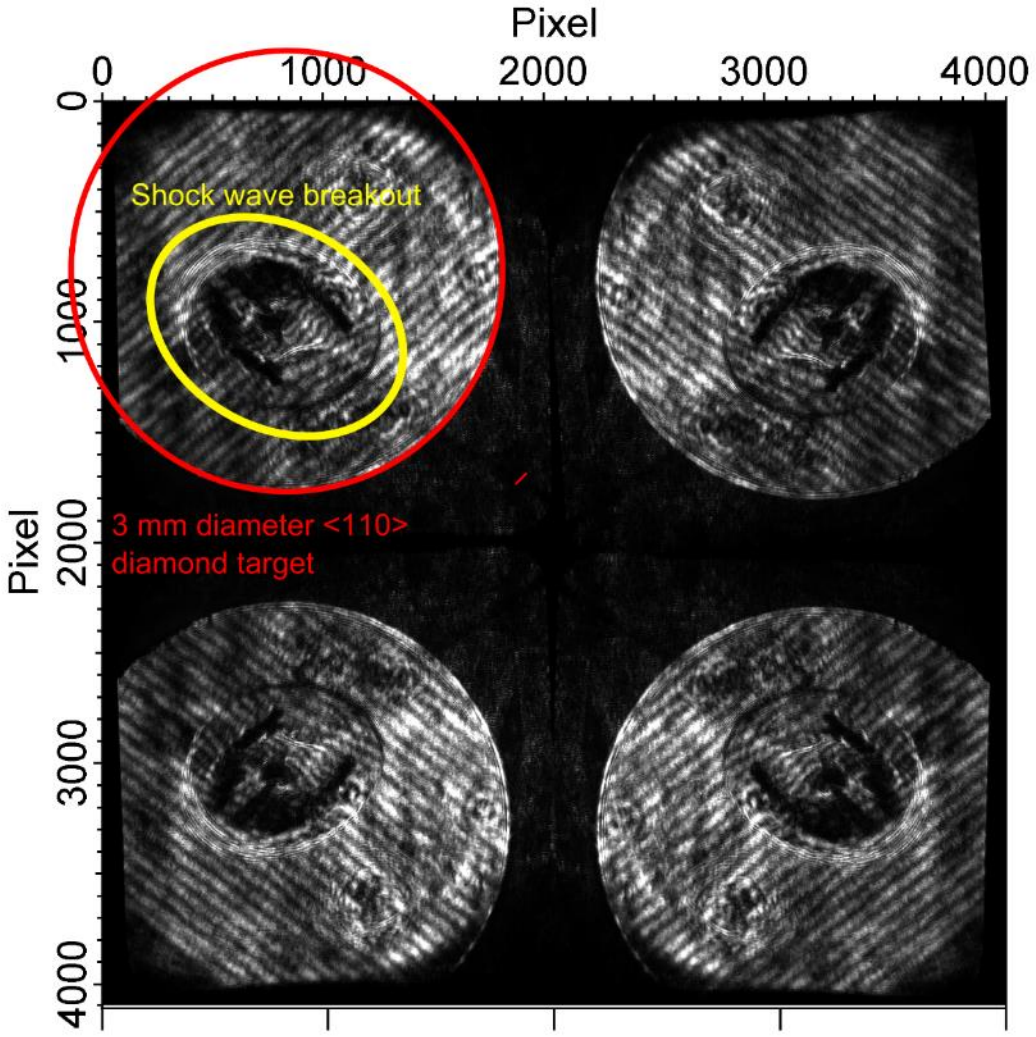

Figure 38 2D VISAR raw data. Breakout is indicated by the yellow oval.

Chapter 2: Anisotropic Wave Propagation in Diamond

Abstract

Despite extensive use in shock compression experiments, the nature of shock propagation in single-crystal samples in low-symmetry directions remains relatively uninvestigated. Using spherical, divergent, shock geometries and single-crystal samples of diamond cut in the 100, 110, and 111 orientations we have investigated the effect of acoustic anisotropy on the propagation of elastic and inelastic shock waves and found both the expected symmetry responses as well as new behavior.

Introduction

Although it is well known that the vast majority of materials respond anisotropically to acoustic impulses, in order to simplify analysis and interpretation it is often necessary to assume isotropic behavior under shock compression and neglect the shear component of the material strength. In an acoustically anisotropic medium, pure modes are only found along specific directions relative to the crystal structure. Elastic waves propagating through such media will only exist as pure longitudinal or transverse waves along said directions.[90] When single-crystal samples are used in shock compression experiments, the orientation of the crystal planes is frequently selected to be a high symmetry direction with pure mode propagation. While this has enable the identification of key differences between material response along high-symmetry axes, the behavior of the material along lower symmetry directions remains unknown. From the field of ballistic phonon imaging it is well known that small-amplitude linear elastic waves propagating in acoustically anisotropic materials can focus or form caustics, and it the goal of this study to demonstrate that such behavior can also occur under nonlinear shock wave propagation in single crystals. Building on previous work on single crystal silicon done by Eggert et al. and Smith et al. we have obtained both single-crystal and polycrystalline samples of diamond and, by propagating a divergent shock wave into the sample, observed symmetry coincident with the crystal orientation, as shown in reference [91].

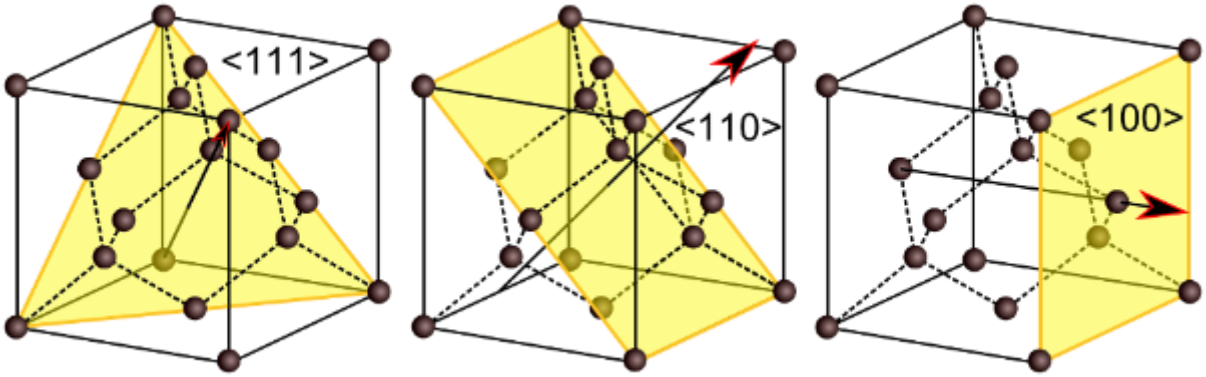

Figure 39 Diamond cubic crystal structure with 111, 110, and 100 planes highlighted.

Creative use of existing diagnostics has been utilized to try to further our understanding of anisotropic and heterogeneous deformation process with some success [92], however, in order to fully understand and eventually model these processes a full 2 dimensional characterization is required. Eventually, with increased innovation in the x-ray diagnostic fields, full 3 dimensional characterization should become available.

The particular question regarding anisotropic wave propagation that we address here is one that requires a small amount of history. In 2003-2005 Jon Eggert conducted a series of pre-compression experiments wherein a sample material of interest was compressed in a diamond anvil cell prior to laser shock compression. A general schematic for the target in such an experiment is shown in Figure 40. On recovery of the tungsten carbide backing plates in contact with the diamond anvil, it was noticed that the surface of the backing plate was indented with characteristic four-fold symmetry in every shot, as shown in Figure 41. As the tungsten carbide plates were nearly acoustically isotropic, this suggested that any anisotropic features were due to the diamond. The single-crystal diamond anvil used in the experiments had 100 oriented surfaces, surfaces which had inherent four-fold symmetry.

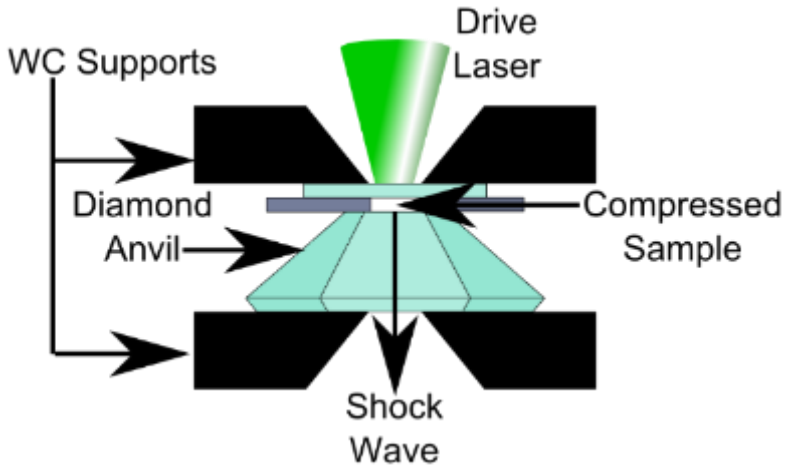

Figure 40 Simplified schematic of a pre-compression target. The tungsten carbide supports shown were recovered after many of the experiments.

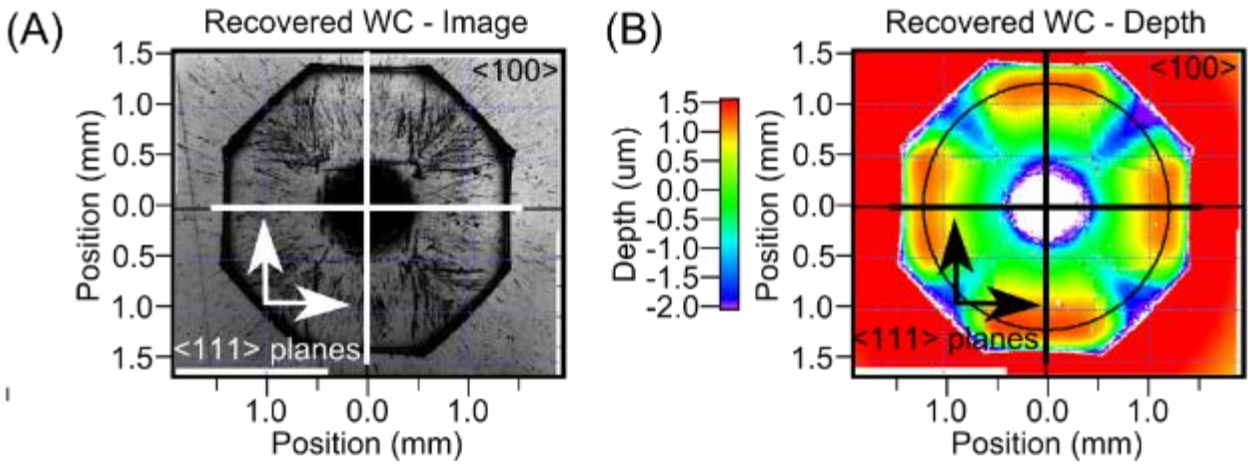

Figure 41 (A) An image of a recovered tungsten carbide plate that had been in contact with the 100 surface of the diamond anvil during a pre-compression experiment. (B) A white light profiler was used to measure indentation depth across the sample imaged in (A). A distinct four-fold symmetry in the depth is noted. (Data from Jon Eggert, reprinted with permission)

Further evidence to support the theory that the diamond acoustic anisotropy was having a significant effect on the material response was obtained when a diamond anvil was recovered after a particularly low energy shot. Initial imaging showed that the fracture has broken up the diamond surface into square pieces, as shown in Figure 42. Eggert also measured the angle at which the pieces fractured, relative to the 100 axis and found that it matched well with the known 111 plane angle.

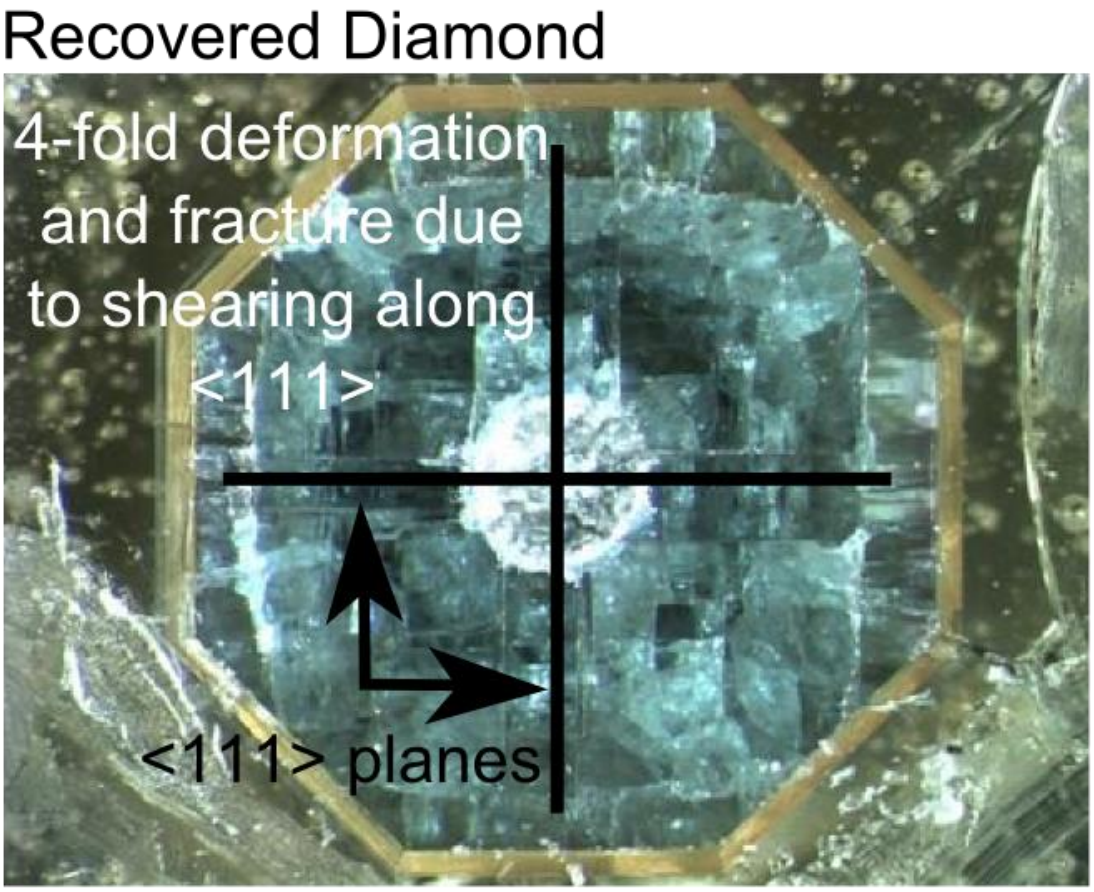

Figure 42 Diamond anvil recovered after a lower energy shot. Fracture can be observed as a series of steps along the 111 planes.

Initial experiments on single crystal silicon confirmed that the elastic and plastic wave propagation was indeed anisotropic as a function of the crystal orientation and that the elastic breakout, at least, could be readily predicted using the known elastic moduli. While four-fold symmetry was observed in the 100 silicon samples, as shown in the results section below, it was relatively understated, with no indication of how the strong four-fold 'cross' pattern on the indenter was formed. It was therefore deemed necessary to repeat the silicon experiments with diamond samples. As the diamond samples were considerably more difficult and expensive than comparably sized silicon samples, experiments were first done extensively on silicon in preparation. Results from both silicon and diamond compression experiments are presented below, with a discussion of the similarities, as well as the noticeable differences. Most importantly, there is a distinct four-fold cross feature observed on the diamond samples which was not seen in the silicon samples, and this feature matches readily with the indentation pattern initially observed.

Methods

Targets where prepared as described in Chapter 1. Experiments were performed at the Jupiter Laser Facility, in Target Area 1. As thick (~1 mm) targets were required in order for

the divergent shock wave to expand to a large enough size at the free surface, the availability of single-crystal diamond samples was limited to five each of the 111 and 100 orientations and seven of the 110 orientation. The 100 and five of the 110 diamond samples were synthetically grown using a high-pressure, high-temperature technique which produced samples of exceptional quality, but with a small degree of nitrogen impurity. The remaining 110 samples and all of the 111 diamond samples were natural. Polycrystalline samples were more readily accessible and experiments were also performed on nanocrystalline and microcrystalline diamond. A certain number of leftover diamond samples were also available from previous campaigns. Silicon samples were prepared in the same way as the diamond samples.

Results

Line-VISAR

Velocity histories were obtained using the line-VISAR diagnostic. The primary utility of the line-VISAR was to ensure that shots with similar pressure histories could be identified, allowing single-shot 2D-VISAR data to be compared. There were two complicating factors involved in the line-VISAR measurements; the first was that, with the exception of nanodiamond, all of the samples were only 15-20% reflective. For comparison purposes, a few shots were done on both diamond in contact with an uncoated LiF window and diamond in contact with an aluminized LiF window, as shown in the previous chapter. No significant differences beyond the usual shot-to-shot variation were observed. The second complicating factor was the loss of reflectivity of the aluminized layer 5-10 ns after breakout, presumably due to increased surface roughness at the diamond/LiF interface as a result of inelastic behavior. This is marked in the data by increased noise at late times. Finally, for the single crystal samples, both natural and synthetic high pressure, high temperature diamonds were all used in the experiment, so whenever possible, similar shots were done on both types.

Table 1 Summary of results from the line-VISAR data.

Target		Thickness (microns)	Peak Pressure (GPa)	Peak Particle Velocity (km/s)	Precursor Wave Velocity (km/s)	Precursor Wave Pressure (GPa)	Hugoniot Elastic Limit (GPa)
Sample	Tamp						
100	LiF	850-1050	12±2-19±3	0.2±0.02-0.32±0.02	0.16±0.03[1]	10±2	78±16[a] 57±3[b]
110 Natural	FS	1000	17±2	0.28±0.02	[2]		78±12[a]
	LiF		13±2	0.22±0.02	0.12±0.03	8±1.5	
110 Synthetic	FS	950-1150	15±2	0.25±0.02	[2]		
	LiF		8±1-15±2	0.15±0.02 - 0.25±0.02	[2]		
111	LiF	950-1050	20±3-25±3	0.34±0.03 -0.4±0.05	0.21±0.05[1]	13±2	60±5[a]

Nano	FS	500	36±3	0.6±0.05	0.5±0.08	32±3	
	LiF		36±3	0.6±0.06	0.3±0.09	19±3	
Micro	FS	500	40±3	0.7±0.06	0.38±0.07	24±2.5	
	LiF		32±4- 36±3	0.55±0.05 -0.6±0.06	0.21±0.07	13±2.5	

a-[93], b-[94],1-Precurser wave only observed for one shot, 2-No precursor wave observed

Figure 43, Figure 44, Figure 45, and Figure 46 show velocity profiles for each type of sample used. For the single crystal samples, only waves traveling along the 100, 110, and 111 axes are fully longitudinal; other directions will have some degree of transverse motion. Profiles were obtained in a 100 micron band in the center of the breakout spot, where it can be assumed that the velocity is predominately longitudinal. To produce the figures shown below, the two VISAR channels were averaged. To obtain the values shown in Table 1, free surface and LiF windowed samples were corrected using impedance matching to provide particle velocity. The peak pressures calculated from the VISAR results were all below the previously determined elastic limits, suggesting that the observed precursor waves may be an artifact of poor drive laser pulse shaping. 100-200 micron differences in the sample thickness of the single crystal diamonds were taken into account in the figures below; time is corrected for thickness differences and normalized to an ideal 1000 micron sample. As the diamond samples are 500-1000 microns thick, the elastic and plastic waves are separated considerably in time, at least 5-10 ns from HYADES simulations (which tend to underestimate wave separation as a result of material strength). The polycrystalline samples were only 500 microns thick and therefore -- because of the decaying shock velocities (hence particle velocities) with distance -- the measured particle velocities for the thinner polycrystalline samples are approximately twice that of the thicker single crystal samples. Stress and density in the shocked samples were determined using the known shock velocity-particle velocity relationship and the Rankine-Hugoniot relations discussed in Section I [93, 95]. HYADES simulations were used to confirm that the initial drive conditions were capable of shocking the sample above the HEL.

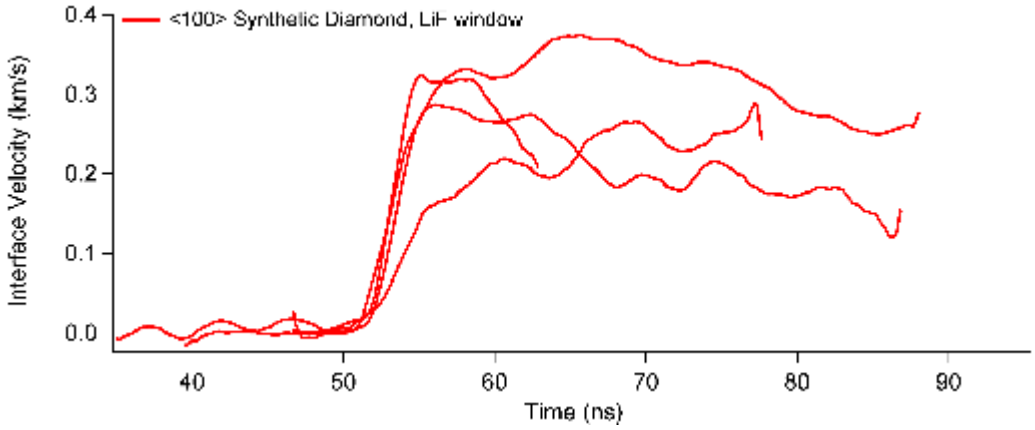

Figure 43 Particle velocity vs. time after the drive laser is initiated. Oscillation noted on the left hand side prior to breakout is artificial due to modulated probe laser intensity, most likely as a result of poor seed laser performance.

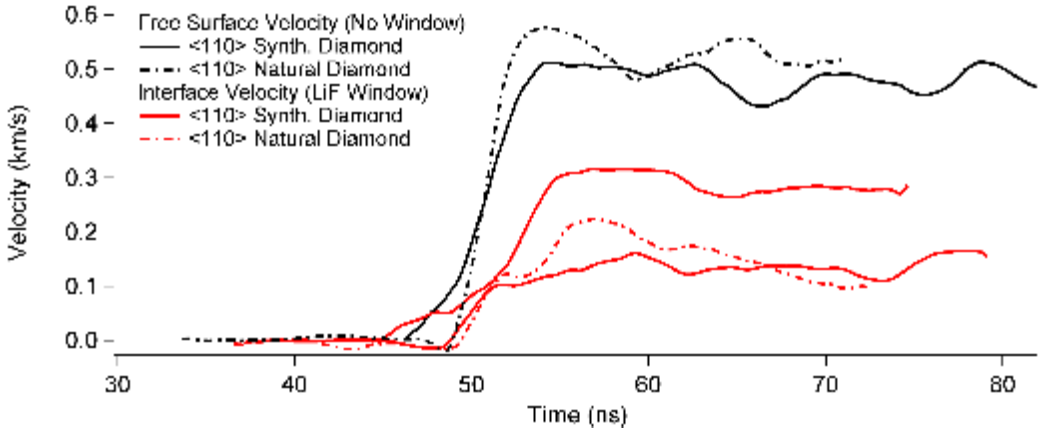

Figure 44 Particle velocity vs. time after the drive laser is initiated. Ends of records correspond to the end of the probe laser pulse for the free surface targets and to 95% loss of reflectivity for the LiF windowed samples.

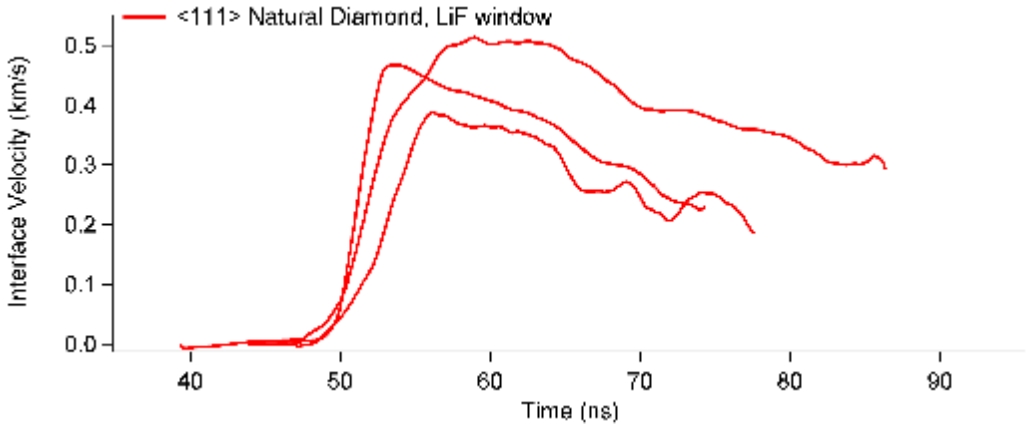

Figure 45 Particle velocity vs. time after the drive laser is initiated. Ends of records correspond to the end of the probe laser pulse for the free surface targets and to 95% loss of reflectivity for the LiF windowed samples.

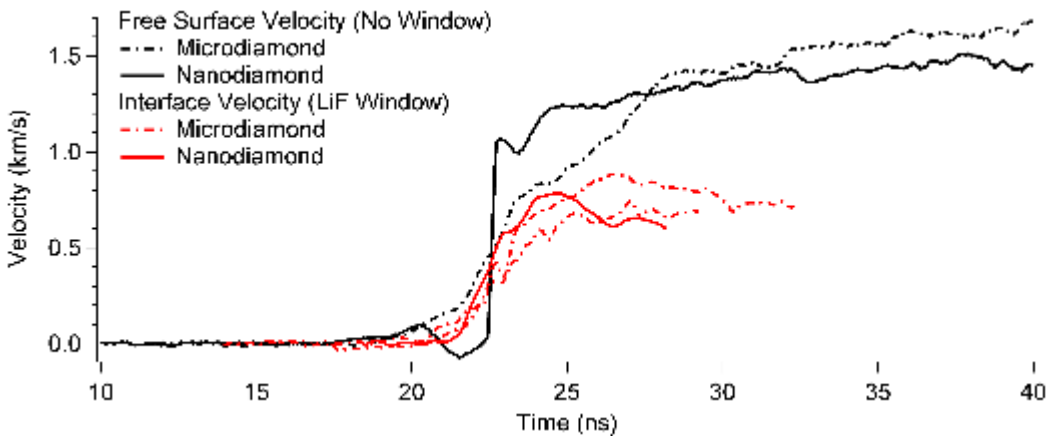

Figure 46 Particle velocity vs. time after the drive laser is initiated. Ends of records correspond to the end of the probe laser pulse for the free surface targets and to 95% loss of reflectivity for the LiF windowed samples.

No significant difference was observed between the natural and synthetic diamonds in Figure 44, although it is a small sample size. Previous research has found negligible differences in the response between synthetic and natural diamonds at higher pressures (90-120 GPa) [94].

2D-VISAR

Shocked sample images and velocity maps were obtained using the 2D-VISAR. An etalon delay of 263 ps was used in both 2D-VISAR interferometers, providing a velocity per fringe of 0.548 km/s.

Calculations

Elastic anisotropy is completely described by the elastic constants of a crystal. In the case of crystals of cubic symmetry, there exist three independent elastic constants, which, when known, can be used to determine the group and phase velocities for any given vector through the crystal. The simplest description of elastic behavior can be found using linear elastic theory, which assumes small changes and perfectly elastic response. By modelling a single-crystal sample using linear elastic theory and the closed form expressions for acoustic waves developed by Every and mathematically propagating a divergent shock wave through the sample we can calculate a predicted breakout shape, size, and surface velocity.[96, 97] Essentially, the shape and size of the elastic wave can be reproduced by calculating the transit time as a function of angle through an anisotropic solid defined by the diamond elastic constants. This was done by defining a 1000 x 1000 grid at the breakout surface, with a total spatial scale of 3 mm x 3 mm. Assuming a source 100 microns in diameter on the drive side surface of the target, the sound speed from the drive side to any given grid point on the breakout surface can be calculated, resulting in a sound speed surface, as outlined in Figure 47. From this sound speed surface and the target thickness, the breakout shape and size as a function of time can be readily calculated. In addition, a

similar calculation was done using third order Eulerian finite strain, as described by Birch [98] and using the elastic constants determined by Lang et al [99]. McWilliams' method for obtaining Eulerian constants from Lagrangian values was also used [100]. Instead of a single vector from the drive side to the breakout surface, the target thickness was broken up into 100 layers and vectors were calculated from layer to layer, with the elastic constants and density calculated for each layer. The pressure through the sample was estimated using the observed breakout particle velocity and HYADES simulations of the laser drive. As would be expected, the elastic sound velocity is higher for the finite strain calculations, and there is a slightly greater degree of anisotropy at higher pressures, as previous experimentalists and theorists have observed [99, 101-107].

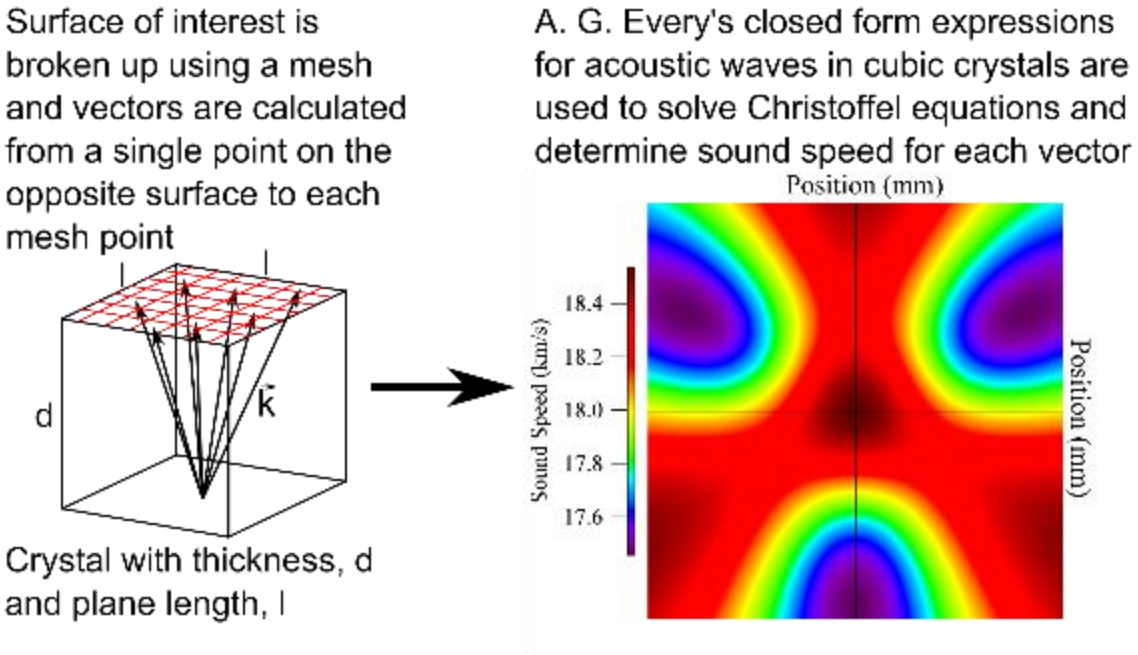

Figure 47 Method used to determine sound velocity across the sample surface for a spherical shock wave.

The elastic constants determined by McSkimin and Andreatch in reference [108] were used to calculate the acoustic anisotropy, c_{11} = 10.79 GPa, c_{12} = 1.24 GPa, and c_{44} = 5.78 GPa. Elastic constants for synthetic diamonds have also been measured and found to be very similar to those for natural diamonds [109, 110]. A comparison of the results of these calculations with the data presented above can help decouple the various elastic/plastic and focusing effects potentially involved in the breakout.

111

Longitudinal sound speed across a 3 mm square surface is shown in Figure 48. The three-fold symmetry apparent in the crystal structure in Figure 39**Error! Reference source not found.** is shown in the sound speed variation. As would be expected, the highest sound speed is found in the center where the pure 111 longitudinal mode transits. The slip system is indicated by the solid white lines and is also three-fold, but mirrored with respect to the elastic wave symmetry.

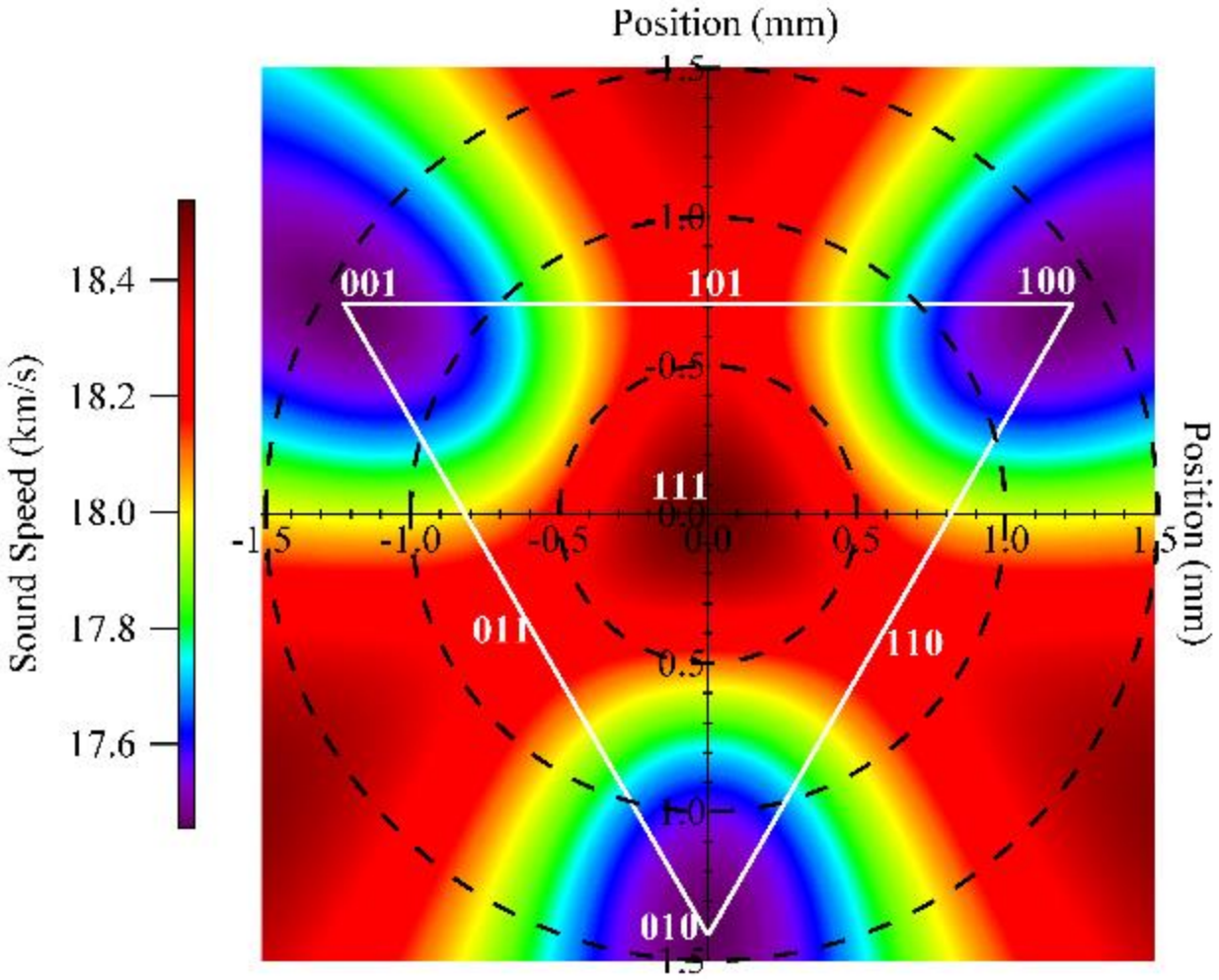

Figure 48 Sound speed as a function of position for a spherical shock wave propagating through 111-oriented diamond and originating at a point 1 mm away from the surface shown. Contours of radii 0.5, 1.0, and 1.5 mm are indicated by the dashed circles and the plastic slip system is indicated by the solid white lines.

Longitudinal wave breakout is shown in Figure 49. The three-fold symmetry apparent in the crystal structure in **Error! Reference source not found.** is shown in the breakout shape, with the symmetry becoming more pronounced at later times. Finite strain theory predicts a faster elastic wave speed and a more pronounced anisotropy.

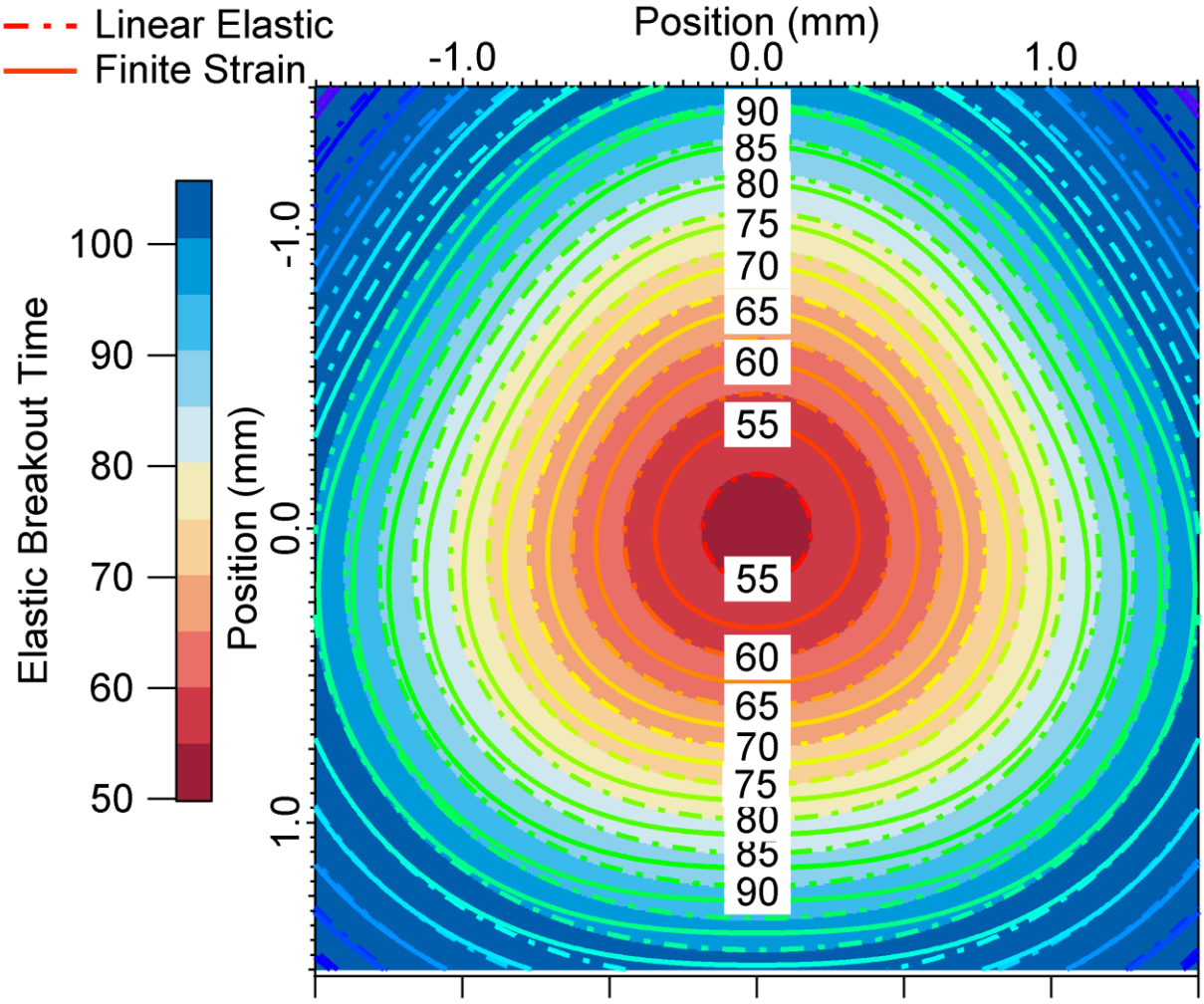

Figure 49 Breakout time as a function of position for a spherical shock wave propagating through 111-oriented diamond and originating at a point 1 mm away from the surface shown. The image shown is for breakout calculated using linear elastic theory, as are the dashed contours. Solid contour lines were calculated using finite strain theory, as described above.

Three-fold symmetry was observed in all 111 orientation shots, as shown in Figure 50. The finite strain theory calculations provided a better prediction of the elastic breakout size than the linear elastic calculations. As the linear elastic theory calculations do not take into account the increase in the sound velocity with pressure, they consistently predict a breakout size slightly smaller than the observed breakout size. The reflectivity loss was most severe for this orientation, precluding analysis of a few of the shots. A silicon shot is

shown for comparison; little reflectivity loss is observed and a central plastically deformed region of three-fold symmetry is apparent.

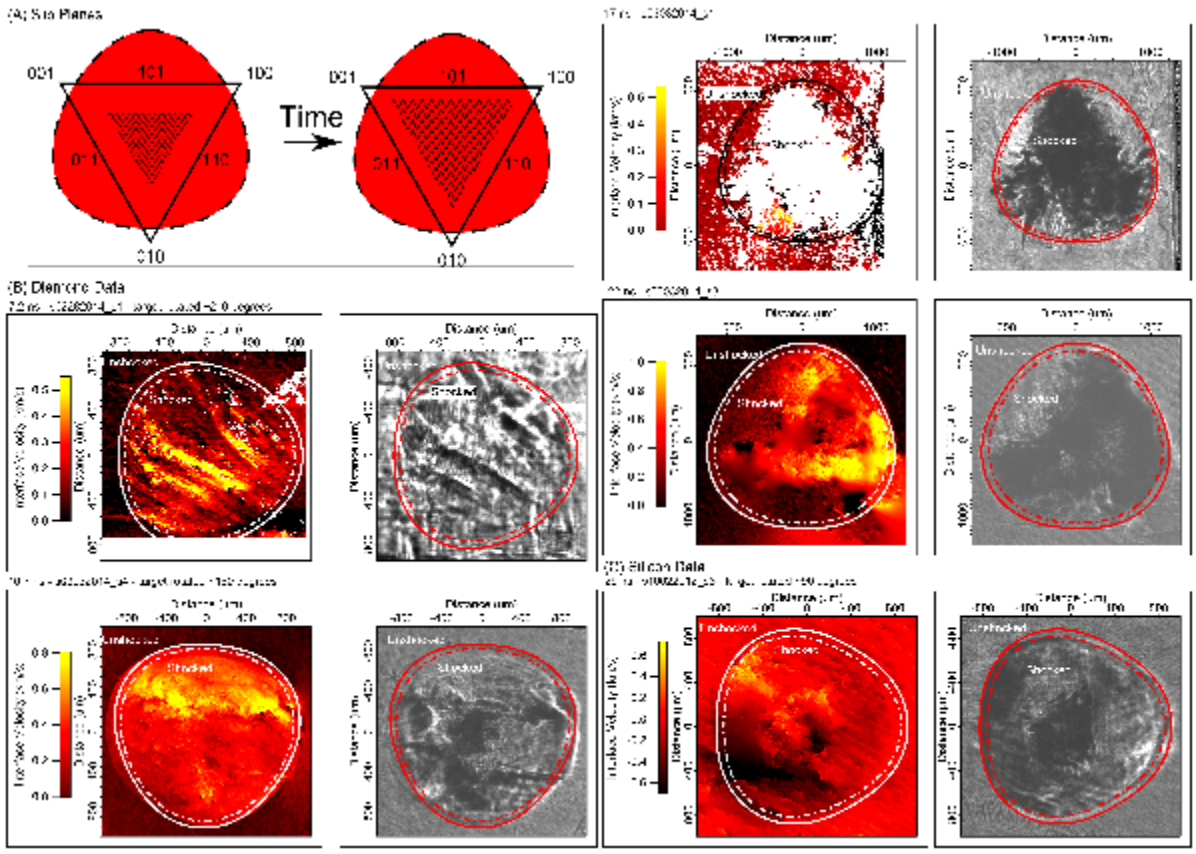

Figure 50 (A) Slip planes (B) Spherically shocked 111 oriented diamond and (B) silicon with LiF windows. Indicated times are relative to initial elastic breakout. Calculated elastic breakout shape and size is indicated by lines in red on the nonfringing image and white on the velocity map. The dashed lines were calculated using linear elastic theory and the solid lines were calculated using finite strain. The orientation of the primary slip system in diamond cubic crystals is indicated by the solid black lines in (A). A clear three-fold symmetry in the elastic breakout is observed for both materials and an additional three-fold symmetry can be roughly seen in the inelastic center region. The symmetry of the inelastic region is clearer on the silicon, which did not lose reflectivity to the same degree as the diamond. Targets were rotated in the plane parallel to the observed surface by specific angles, allowing us to confirm that the anisotropy in the breakout was related to the crystal orientation.

110

Longitudinal sound speed across a 3 mm square surface is shown in Figure 51. The two-fold symmetry apparent in the crystal structure in Figure 39 is shown in the sound speed variation. As would be expected, the highest sound speed is found where the pure 111 longitudinal mode transits. The slip system is indicated by the solid white lines and is also two-fold.

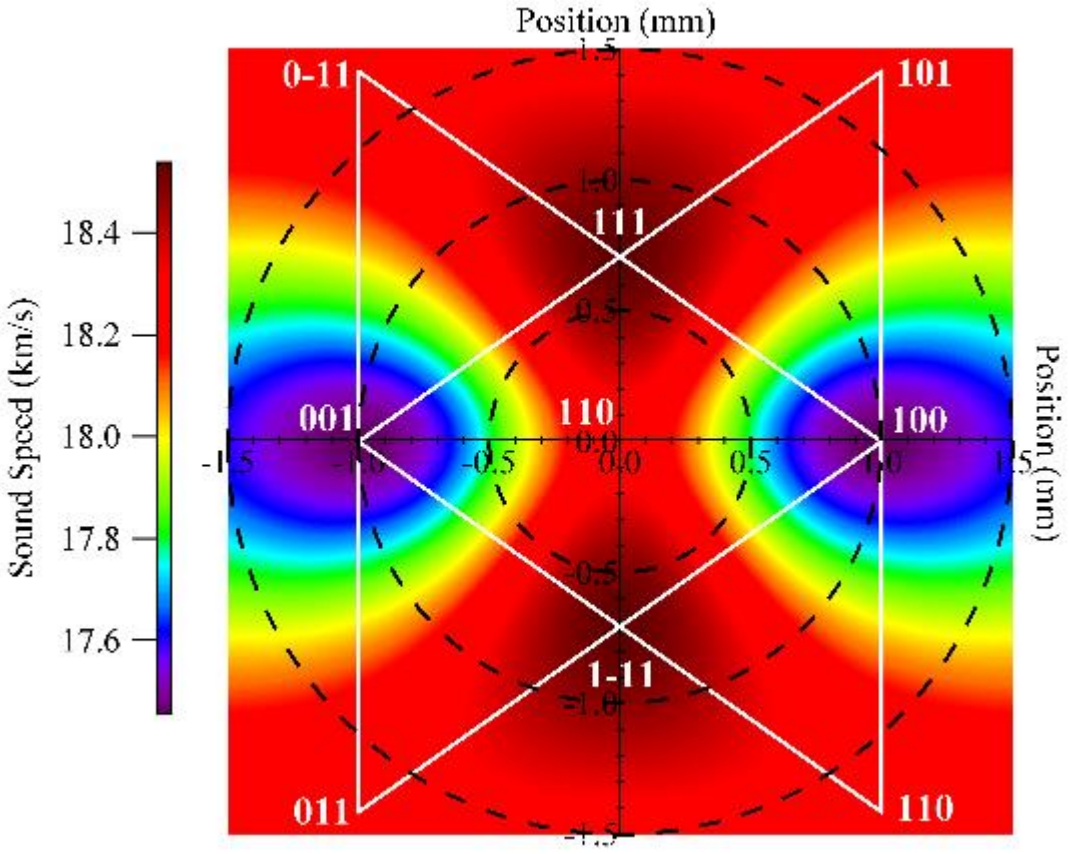

Figure 51 Sound speed as a function of position for a spherical shock wave propagating through 110-oriented diamond and originating at a point 1 mm away from the surface shown. Contours of radii 0.5, 1.0, and 1.5 mm are indicated by the dashed circles and the plastic slip system is indicated by the solid white lines.

Longitudinal wave breakout is shown in Figure 52. The two-fold symmetry apparent in the crystal structure in Figure 39 is shown in the breakout shape, with the symmetry becoming more pronounced at later times.

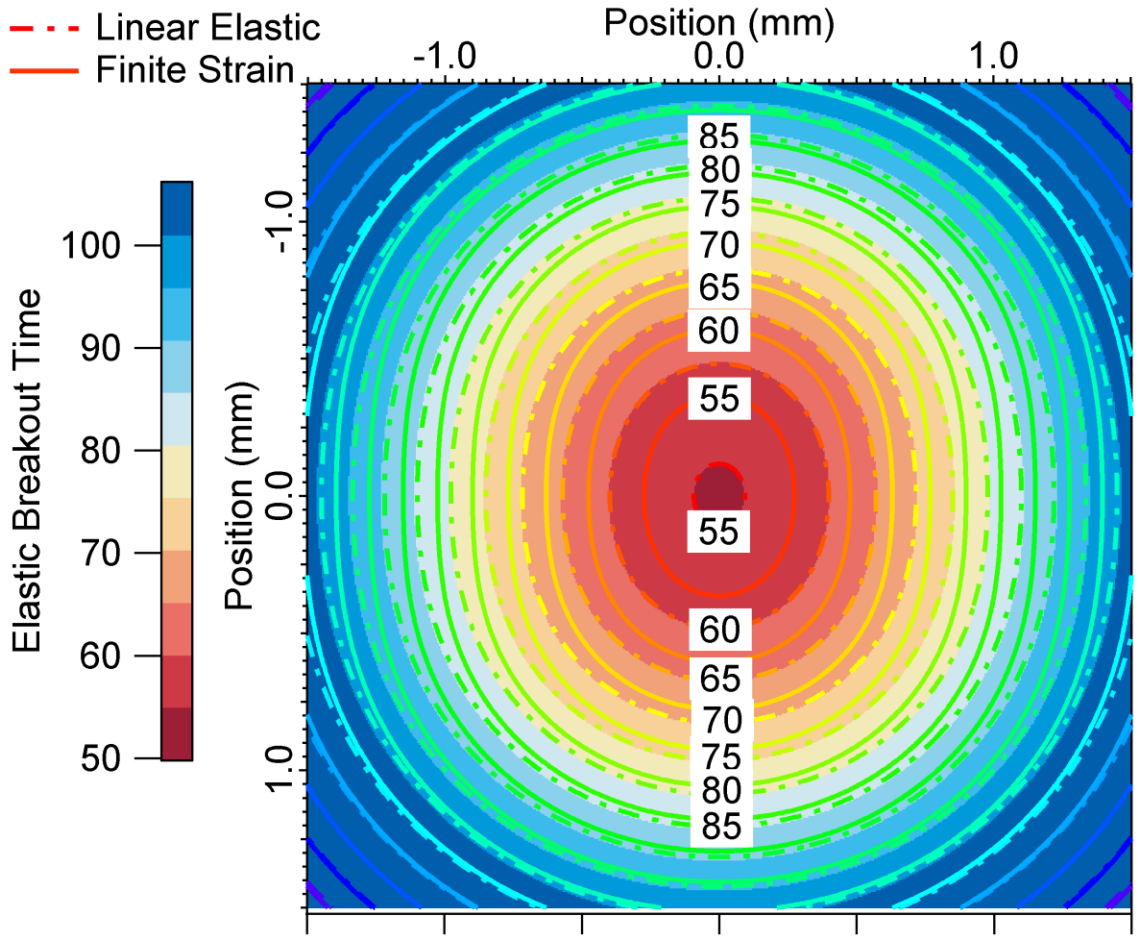

Figure 52 Breakout time as a function of position for a spherical shock wave propagating through 110-oriented diamond and originating at a point 1 mm away from the surface shown. The image shown is for breakout calculated using linear elastic theory, as are the dashed contours. Solid contour lines were calculated using finite strain theory, as described above.

Of the three single crystal orientations studied, the 110 direction had the most consistent response, as shown in Figure 53. Reflectivity loss was primarily in the center of the breakout, and the elastic breakout was distinct in all shots. This was also the orientation for which the greatest number of samples was available. The two-fold symmetry of the elastic wave is apparent and agrees with the linear elastic theory calculations above. The two-fold symmetry of the plastic wave is also apparent, with the higher-velocity, roughened region in the center consistently diamond-shaped. As was the case for the 111 targets, the finite strain theory calculations provided a better prediction of

the elastic breakout size than the linear elastic calculations. The only shot that is not well predicted by either calculation is the one at the 15.6 ns delay time. It is unclear why that is the case, although there are considerable interference fringes due to the interference at the diamond/LiF interface which can complicate the analysis.

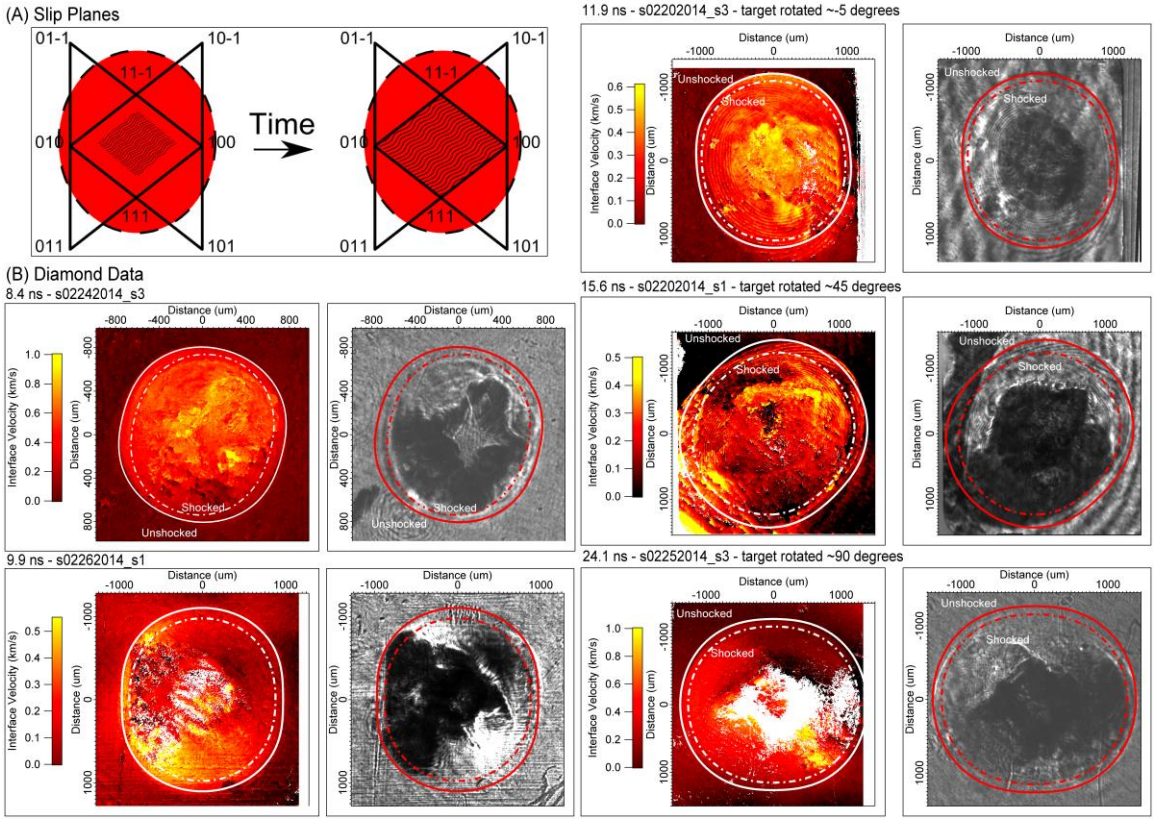

Figure 53 (A) Slip planes for the 110 surface. (B) Spherically shocked 110 oriented diamond with a LiF window. Indicated times are relative to initial elastic breakout. Calculated elastic breakout shape and size is indicated by lines in red on the nonfringing image and white on the velocity map. The dashed lines were calculated using linear elastic theory and the solid lines were calculated using finite strain. The orientation of the primary slip system in diamond cubic crystals is indicated by the solid black lines (A). A clear two-fold symmetry in the elastic breakout is observed for both materials and an additional two-fold symmetry can be roughly seen in the inelastic center region. Fringes in the 11.9 ns and 15.6 ns delay shots are a result of interference between the diamond and LiF window surfaces. The LiF windows were not aluminized for those two shots. Targets were rotated in the plane parallel to the observed surface by specific angles, allowing us to confirm that the anisotropy in the breakout was related to the crystal orientation.

100

Longitudinal sound speed across a 3 mm square surface is shown in Figure 54. The four-fold symmetry apparent in the crystal structure in Figure 39 is shown in the sound speed variation. As would be expected, the lowest sound speed is found in the center where the pure 100 longitudinal mode transits and the sound speed increases as the 111 direction is approached. The slip system is indicated by the solid white lines and is also four-fold, but rotated 45 degrees with respect to the elastic wave symmetry.

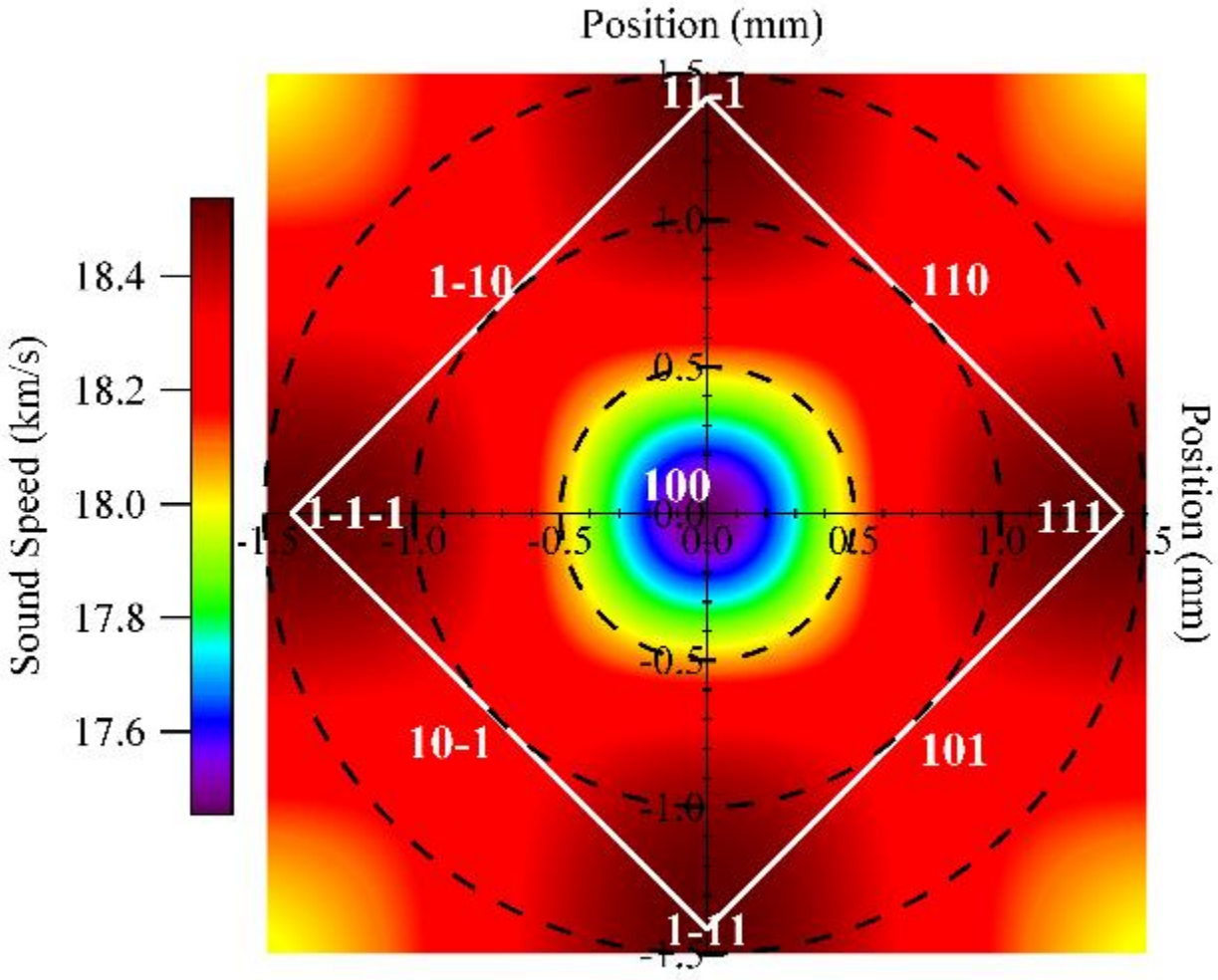

Figure 54 Sound speed as a function of position for a spherical shock wave propagating through 100-oriented diamond and originating at a point 1 mm away from the surface shown. Contours of radii 0.5, 1.0, and 1.5 mm are indicated by the dashed circles and the plastic slip system is indicated by the solid white lines.

Longitudinal wave breakout is shown in Figure 55. The four-fold symmetry apparent in the crystal structure in Figure 39 is shown in the breakout shape, with the symmetry becoming more pronounced at later times, but to a lesser degree than in the previous orientations.

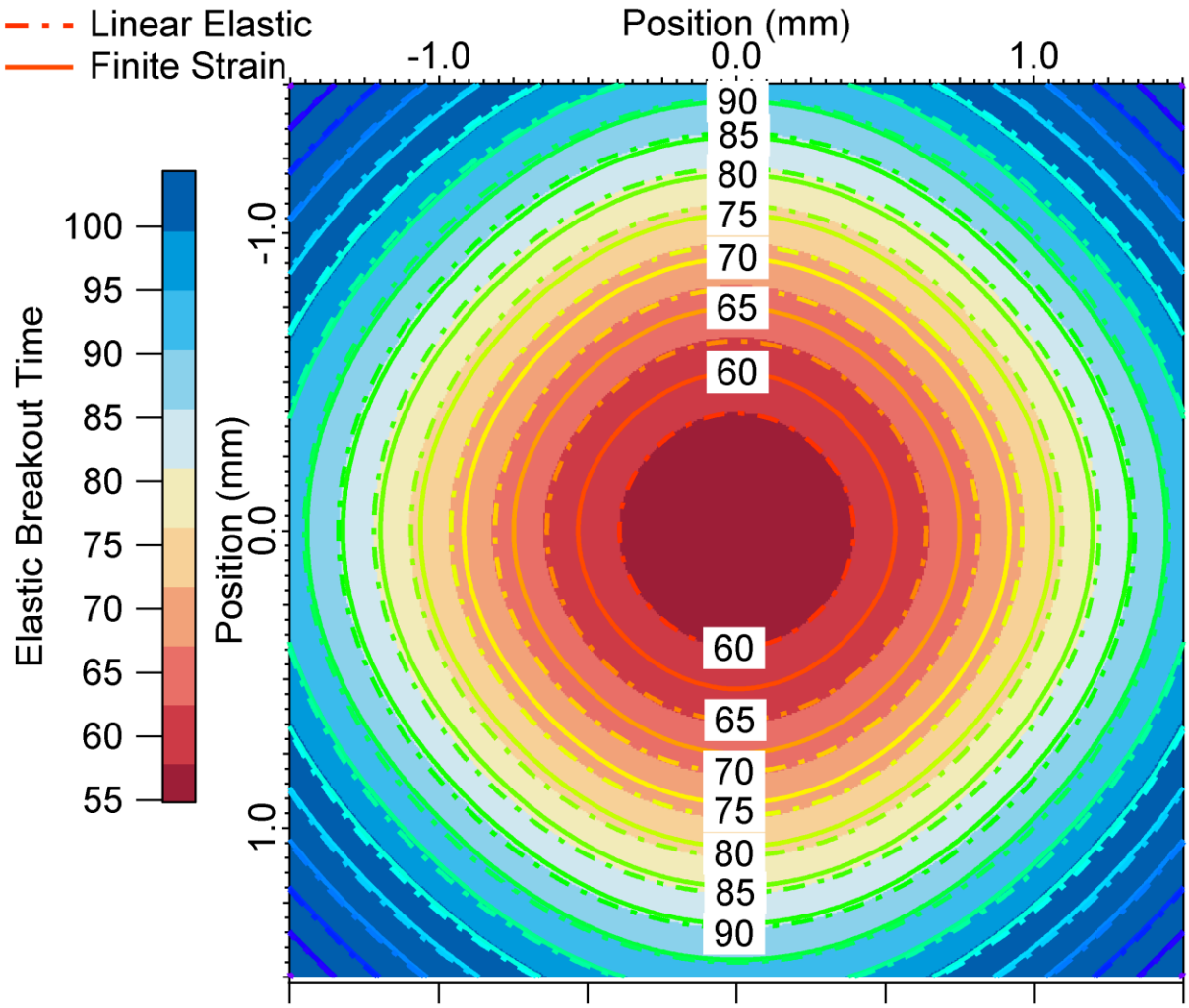

Figure 55 Breakout time as a function of position for a spherical shock wave propagating through 100-oriented diamond and originating at a point 1 mm away from the surface shown. The image shown is for breakout calculated using linear elastic theory, as are the dashed contours. Solid contour lines were calculated using finite strain theory, as described above.

The 100 diamond samples had possibly the most interesting 2D response. As shown in Figure 56, as time passes the four-fold, cross-like structure in the center of the image expands, along with a rougher region in the center. The origin of this higher-velocity cross is unknown, but is consistent with the indentations observed in the tungsten carbide plates discussed above. Possible origins of this structure are discussed below. As also discussed above, the silicon samples show no indication of this cross shape, with only a roughly circular plastic region in the center of the elastic breakout. The final silicon shot in the

figure below does have some structure within the elastic wave, however it does not appear to be related to the cross structure in the diamond.

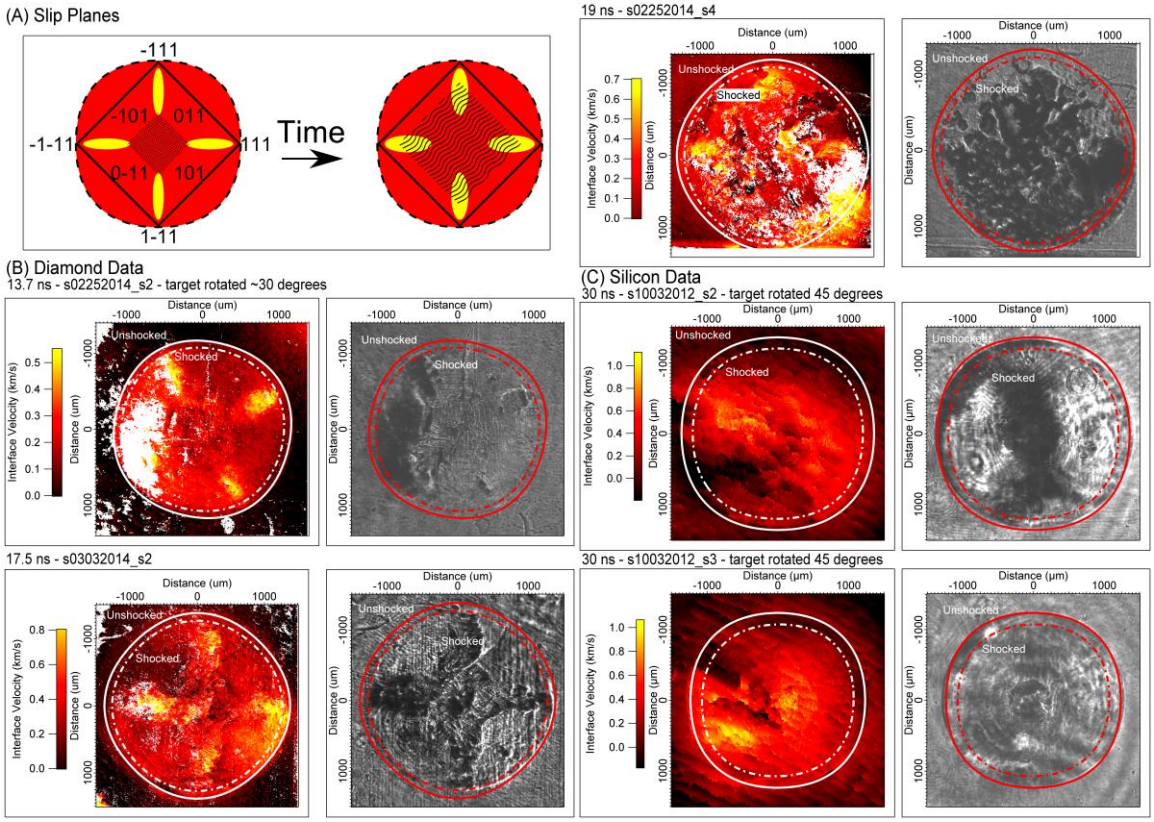

Figure 56 (A) Slip planes with the relative location of the 111 and 110 planes indicated with solid lines and a cartoon of the elastic wave breakout shown in the dashed black lines. (B) Spherically shocked 100 oriented diamond and (C) silicon with LiF windows. Indicated times are relative to initial elastic breakout The orientation of the primary slip system in diamond cubic crystals is indicated by the solid black lines in the nonfringing images. Calculated elastic breakout shape and size is indicated by lines in red on the nonfringing image and white on the velocity map. The dashed lines were calculated using linear elastic theory and the solid lines were calculated using finite strain. Four-fold symmetry in the elastic breakout is somewhat difficult to distingish from a circular breakout, but the symmetry is present. While the silicon shocked region remains relatively homogenous, with a plastically deformed central region of higher velocity, the diamond exhibits a distinctive 'cross' shape of higher roughness and particle velocity. Targets were rotated in the plane parallel to the observed surface by specific angles, allowing us to confirm that the anisotropy in the breakout was related to the crystal orientation.

Polycrystalline Samples

Elastic wave propagation through polycrystalline diamond was calculated using the method outlined above. The elastic constants and accompanying error were calculated using the Hashin-Shtrikman bounds of the single crystal diamond elastic constants, resulting in c_{11} = 10.86±0.01 GPa, c_{12} = 0.70±0.001 GPa, and c_{44} =5.08±0.01 GPa [111, 112]. The sound speed and propagated error in the sound speed is 18.576±0.001 km/s. The breakout time for each of the three pure-mode orientations can be calculated and we find that there is no orientation dependence, as would be expected. In Figure 57 it can be seen that the orientation has no effect on the breakout shape or time, in all three cases the shape is circular.

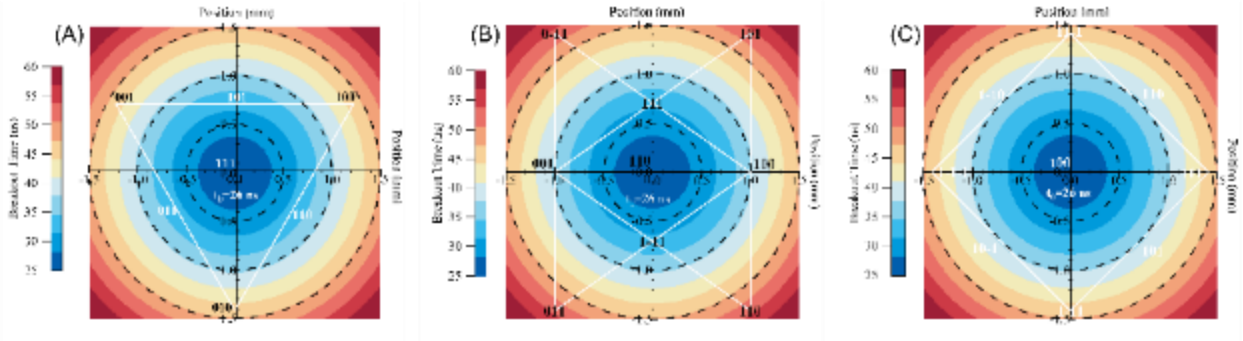

Figure 57 Breakout time as a function of position for a spherical shock wave propagating through polycrystalline diamond and originating at a point 0.5 mm away from the surface shown. (A) 111, (B) 110, and (C) 100 surfaces were calculated. Contours of radii 0.5, 1.0, and 1.5 mm are indicated by the dashed circles and the plastic slip system is indicated by the solid white lines.

The polycrystalline diamond samples had significant reflectivity loss on breakout, but a few shots contained enough reflected light to analyze. These are shown in Figure 58. In all cases a roughly circular breakout is observed, and the size of the breakout is consistent with the calculated elastic breakout, as shown in the dashed red and white lines on the figure.

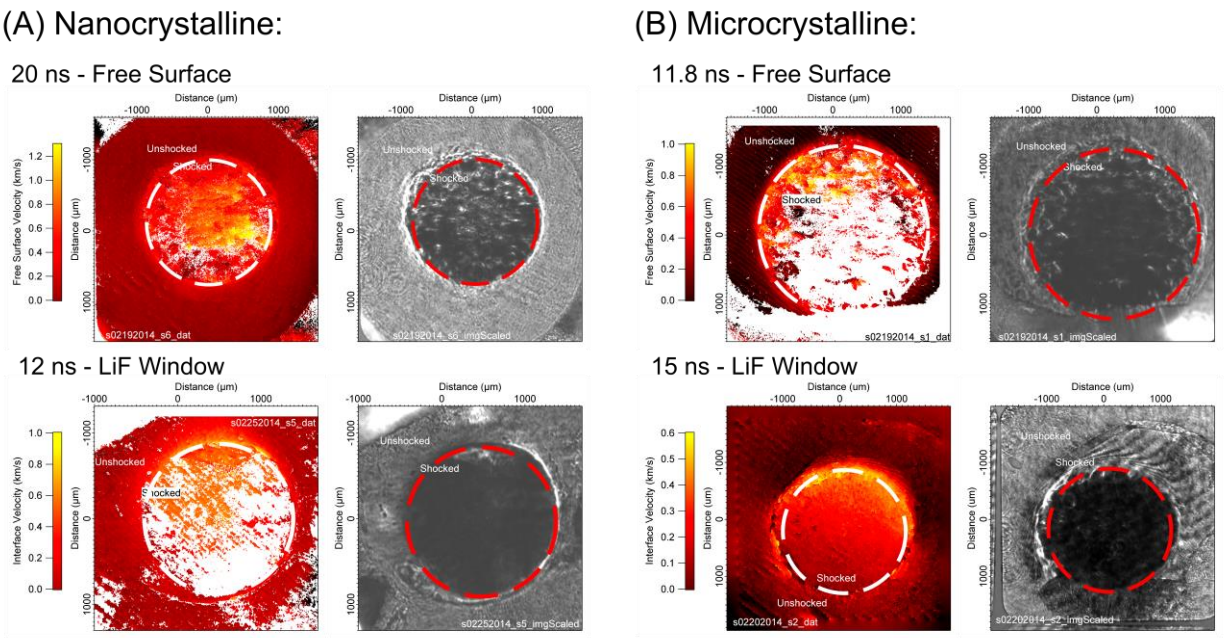

Figure 58 Spherically shocked (A) nanocrystalline and (B) microcrystalline diamond. Indicated times are relative to initial elastic breakout. Calculated elastic breakout shape and size is indicated in red on the nonfringing image and white on the velocity map. An isotropic distribution of crystallites was assumed, and there is clearly some deviation in the actual data from this ideal distribution. There is significant roughening of the surface in both the image and the velocity map, primarily as a result of inelastic deformation.

Discussion

Elastic Breakout Symmetry in Silicon and Diamond

Elastic anisotropy in crystals is governed by the elastic moduli of the material. For anisotropic moduli, the group and phase velocities of the elastic waves will not be parallel and the propagation of a divergent wave will be anisotropic. While there has been a great deal of work studying the propagation of linear waves in anisotropic media, particularly from the field of ballistic phonon propagation, relatively little work has been done investigating the propagation of nonlinear waves, where the wave velocities are no longer independent on the amplitude, through anisotropic media. It is clear from the figures above that the elastic wave propagation in cubic crystals is highly dependent on the elastic moduli, and is, in fact completely predictable given the elastic constants and the material density.

Plasticity/Inelastic Deformation

Crystals with diamond cubic symmetry, such as diamond and silicon, contain 12 slip systems. Depending on the orientation of the applied stress relative to that of the crystal, one or more of these systems will have the maximum resolved shear stress and will govern the dislocation motion in the crystal. The orientation dependence of the Hugoniot elastic limit in many cubic crystals is already known for the three pure-mode orientations, however it is not well known for any other direction. It is possible that we are seeing the presence of an orientation dependence to the dynamic yield strength (Hugoniot elastic limit, HEL) in our 100-oriented samples. In the three shots where the cross was observed the rms interface velocities for the elastic breakout were 0.25±0.05 km/s, 0.35±0.08 km/s, and 0.28±0.08. In those same shots peak velocities on the cross structure were found to be 0.53±0.1, 0.75±0.11, and 0.55±0.2, a different of about two-fold. Assuming inelastic deformation is occurring primarily via slip of the 111 planes in the 110 direction, as has been previously found [94], the transition from plastic response to elastic response would occur at a higher particle velocity in the 111 directions. In other words, the stress required to initiate dislocation motion is dependent on the orientation of the stress. Another possibility is the presence of high velocity 'cusps' due to phonon focusing, a phenomenon that been observed in both silicon and diamond in the linear regime using ballistic phonon imaging [113-115]. This phonon focusing arises from the difference in the group and phase velocities and could feasibly result in regions of higher velocity due to the addition of two wave amplitudes at a cusp. In Figure 59 the slowness and velocities for the three waves transiting through a 100 oriented sample are plotted. Even for the nearly isotropic diamond the phase and group velocities cease to be parallel for certain wave vectors, particularly in the 111 directions. It would be expected, then, that focusing would occur in the 111 directions, as is observed in our data.

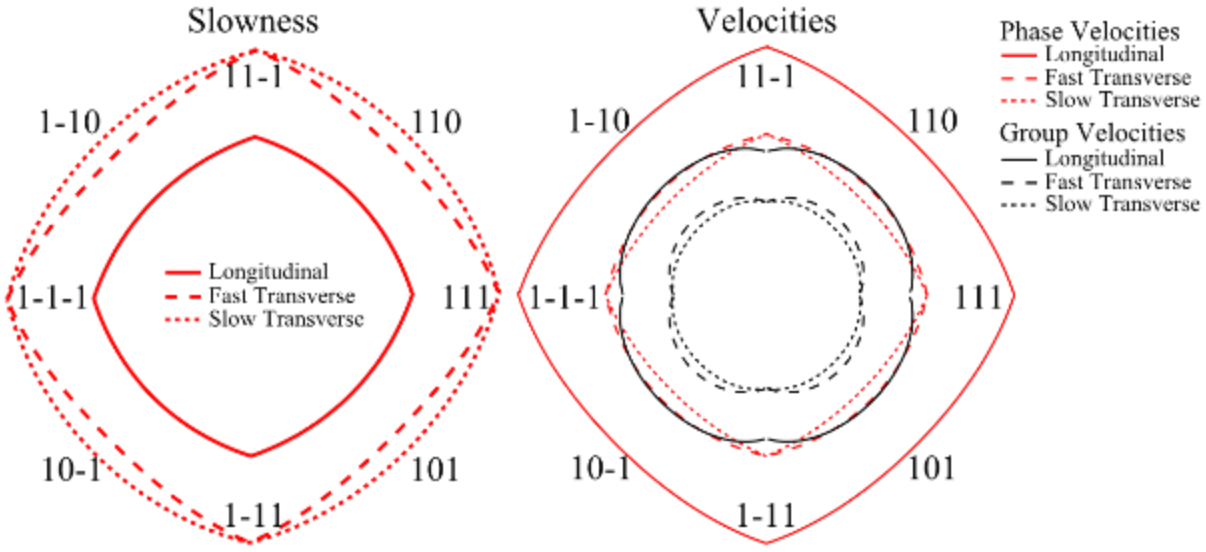

Figure 59 Calculated slowness and group/phase velocities for diamond, using the elastic constants listed above. The quasi-longitudinal and two quasi-transverse waves are shown.

Conclusions

We have found that the elastic wave breakout in silicon and diamond can be accurately predicted using the elastic constants of the material and have found three-fold, two-fold, and four-fold symmetry in the 111, 110, and 100 orientations, respectively. Plastic deformation appears to occur along the known 111-110 slip system for both silicon and diamond, with the magnitude of the plastic particle velocity higher for the diamond. There is an additional feature in the 100 diamond which is not seen in the silicon samples, but which accounts for the observation of the 'cross' indentation on the tungsten carbide supports in the shocked diamond anvil cell experiments. This confirms the presence of a direction dependent HEL variation, although the specific mechanism by which this occurs requires further investigation.

Future Work

More shots are required to complete the time series for the diamond samples, particularly for the 111 orientation. The silicon data was taken with suboptimal quadrature in the 2D VISAR, resulting the higher background noise, so it would be ideal to retake some of that data improve the silicon data set. In general, this dataset contains relatively few shots and we would like to account for target/shot variability by acquiring more data. A better agreement between the calculated elastic wave breakout and the observed breakout shape and size could be obtained by taking into account the pressure dependent elastic constants.

Chapter 3: Heterogeneous Deformation and Fracture in Polycrystalline Diamond

Abstract

We have utilized the newly developed 2D VISAR diagnostic, in combination with the existing line-VISAR, to study heterogeneous deformation and fracture in micro- and nanocrystalline diamond. Diamond samples were shock compressed using a high energy laser drive. We obtained images and velocity maps of deformation and fracture that provide an unprecedented view into material response at the breakout surface. Our data show velocity roughening at the breakout surface as a result of spall fracture in free surface samples and as a result of the compressional inelastic wave and reflected release wave in tamped samples. The larger increase in velocity roughness associated with the microdiamond samples agrees with previously obtained data indicating a loss of reflectivity on breakout for microdiamond shock compression. Using the observed fragment size for spall fracture in the microcrystalline and nanocrystalline diamond, and Grady's model for spall fracture fragment size as a function of strain rate, we have found values for the micro- and nanocrystalline fracture toughness of 103±14 MPa $m^{1/2}$ and 44±8 MPa $m^{1/2}$, respectively. Using these values for the fracture toughness, the strain rate dependent spall stresses were calculated and found to agree with previous research.

Introduction

Carbon is one of the most prevalent elements in the universe and has been a subject of vast experimental and theoretical study for centuries. Diamond at ambient conditions, in particular, is both thermodynamically unstable and, as a tightly bonded covalent structure, the strongest bulk material identified thus far. It is of vital importance in both the planetary science community, as it has been shown that it can be stable within the cores of giant planets, and in the field of inertial confinement fusion, where it is frequently used as an ablator material for ignition target designs. The existing body of work on brittle fracture is primarily focused on indentation experiments and post-shock imaging of the targets [116-118]. The results hint at a complex relationship between brittle fracture development, and crystallographic orientation and microstructure. The goal of this chapter is to describe the dynamic inelastic response of a brittle material, diamond, using both line imaging velocimetry and two-dimensional velocimetry and imaging.

In metals where the deformation is predominantly ductile, deformation and failure above the elastic limit occurs via plastic flow as a result of increased dislocation mobility. Nucleation, growth, and coalescence of voids occurs, and eventually results in ductile fracture [119]. In more brittle materials, such as ceramics, the evolution is best described by Grady [120-122] and occurs in three stages. A low dislocation flux first results in the incubation and nucleation of high shear stress states on defect sites with the material. Increasing the stress results in shear fracture, and eventually the networks of shear banding expand and overlap, resulting in complete commination of the compressed

material. At higher strain rates, higher temperatures, or in the presence of inertial confinement, the distinction between ductile and brittle materials becomes blurred. In compressed silicon, for example, there is a brittle to ductile transition as a result of increased dislocation mobility [91]. Bcc metals and alloys, such as iron and steel, can undergo a ductile to brittle transition at low temperatures or high pressures that results in brittle fracture behavior [123-125]. Despite a significant body of experimental research and computation, a unifying theory describing the dynamic macroscopic response of materials under compression in terms of individual deformation mechanisms and micromechanical properties has been elusive. It has long been acknowledged that wave profile data, ubiquitous in shock compression experiments, are not sufficient to fully characterize material response [121]. One of the most promising approaches to the problem of understanding the varied mechanisms underlying dynamic fracture and deformation is the dissipative action model recently proposed by Grady. Grady proposes that the physics behind a variety of dynamic failure modes can be connected and explained by the invariance of dissipative action. Essentially, by calculating the energy dissipated by the shock wave and taking the product of that energy and the temporal width of the dissipation process, a constant value is obtained. This dissipative energy is a result of the diffusion of the momentum associated with the wave through a variety of potential processes, such as microstructural fracture, acoustic emission, and scattering. The invariance of this dissipative action means that the higher amplitude a shock wave is, the steeper it is in time. While the majority of the work of Grady and his colleagues has been focused on understanding dynamic material failure in gas gun experiments, which have longer time scales than laser shock experiments by approximately two to three orders of magnitude, his comprehensive models, developed around the energetics of the compression process, should apply equally well to the time scales discussed in this experiment.

The measurement method employs a time-resolved two-dimensional imaging VISAR illuminated by a 2 ps laser pulse, which captures spatial variations in the velocity across the shock front transmitted through the ablator. The measurement is carried out over an 890 μm field of view with ~4 μm spatial resolution and a velocity resolution of 10 m/s. Recent experiments have also demonstrated the feasibility of imaging fracture development and propagation in single-crystal silicon [91]. A complex network of fracture lines was observed, and it has been theorized that the orientations of these fracture networks are dependent on the crystallographic orientation and grain size of the target [126, 127].As shown in Figure 60, previous OMEGA experiments on polycrystalline diamond have shown a clear difference between the interface reflectivity of microcrystalline diamond (~10μm grain size) and nanocrystalline diamond (~20-100 nm grain size). It is the underlying mechanism driving this microstructure dependent reflectivity that we propose to address within our combined 1D/2D-VISAR shots. Changes in reflectivity at the free-surface are attributable to an increase in surface roughness which results in the reflection of a large percentage of the VISAR probe light outside the collection angle of the f/3 imaging lens. Previous data on the elastic/plastic transition in micro- and nanocrystalline diamond, also clearly indicate a difference in the inelastic response of the two polycrystalline materials. Data on ramp-compressed polycrystalline diamond samples taken at OMEGA with similar peak pressures found a Hugoniot elastic limit particle velocity

of 1.3±0.2 km/s (98±15 GPa) for the microcrystalline samples and 1.6±0.2 km/s (126±18 GPa) for the nanocrystalline samples, indicating that a higher stress is required to reach the elastic limit in nanocrystalline diamond [128]. Both this reflectivity difference and the elastic limit difference are strong indicators that the development of fracture networks is dependent on grain size, with the nanocrystalline sample possibly retaining higher reflectivity due to a lesser degree of transgranular fracture at the surface, transgranular fracture having been previously observed as the primary fracture mode in CVD diamond under some stress testing experiments[129, 130]. Transgranular fracture takes place through the individual grains, ignoring grain boundaries, whereas intergranular fracture travels along grain boundaries. In a polycrystalline material with predominately transgranular fracture, dislocations tend to stack at grain boundaries, and require a larger stress to push through the grain boundary into the next grain.

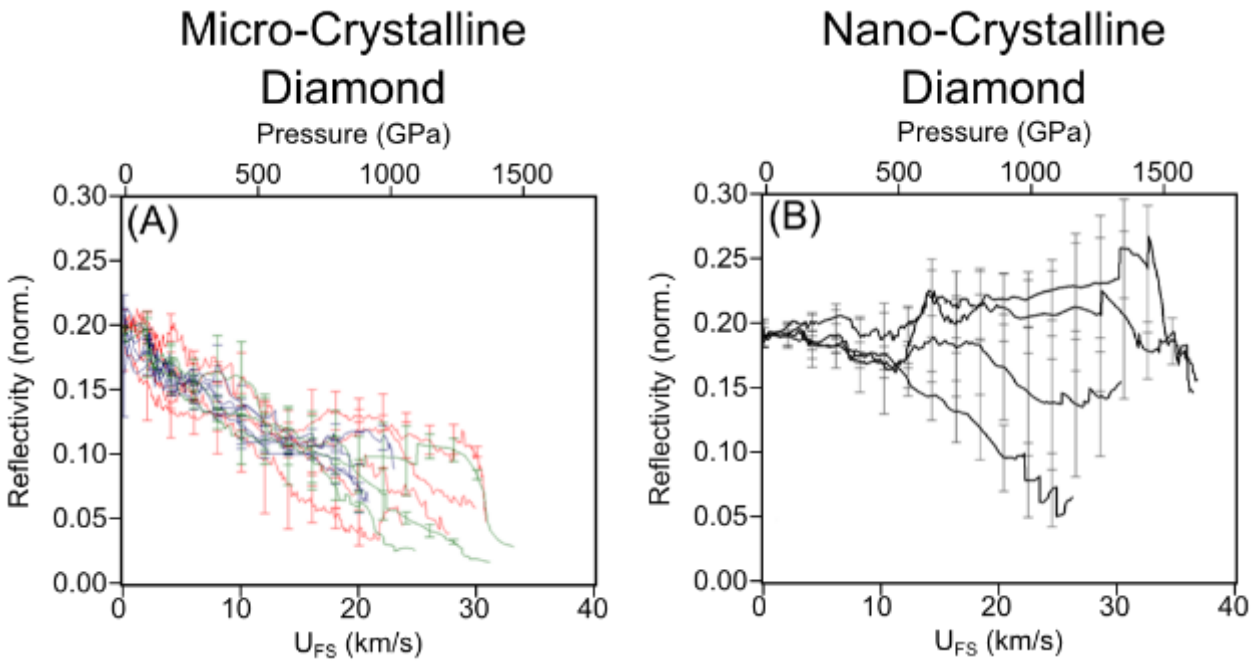

Figure 60 Previous data from OMEGA (July '07 Micro-Grain) indicate that there is a significant difference in the interface fracture networks in microcrystalline diamond relative to nanocrystalline diamond. (a) Various microcrystalline targets show a large reflectivity loss as a function of velocity while (b) Data from nanocrystalline targets demonstrate more variability in the reflectivity and are less consistent than the microcrystalline results.

Methods

Targets were prepared as described in the experimental details section above. Grain sizes for the micro- and nanocrystalline diamonds were obtained from the vendor, Applied Diamond, Inc. For both types of diamond, as they are grown using chemical vapor

deposition, the grain size increases as the sample thickness increases. This grain size increase can be modeled using a power law. At the growth surface, the grain size is approximately 10% of the thickness for the microdiamond samples, so approximately 50 microns, although there is most likely considerable variation in grain size, as can be seen in Figure 61. Figure 61 contains an EBSD-obtained grain map of a 220 micron thick microdiamond sample from Diamond Materials. The nucleation side on the right of the image is composed of a thin layer of nanocrystalline grains and the grain size increases as the thickness increases, reaching a stable size after approximately 50 microns.

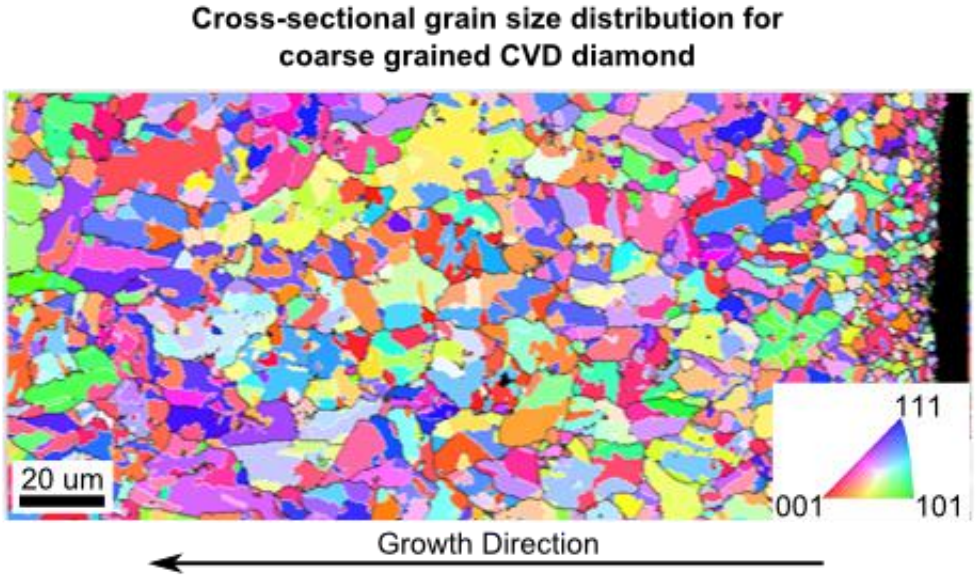

Figure 61 Cross sectional grain map for a microcrystalline diamond sample with orientation inset. Image provided by Juergen Biener, included with permission.

The nanodiamond grain size is not as well constrained; it is less than 5% of the target thickness, but it does approach an asymptote at a thickness less than that of the 500 micron thickness of the samples. The maximum grain size for the sample to remain black is on the order of a few microns [131]. The largest microstructural difference between the two types of diamond is related to the crystal shape, with microdiamond tending toward columnar growth and nanodiamond growing as individual grains [131-135].

Results

Due to limitations on the energy output of the laser facility, the majority of the shots were only slightly above the HEL. This results in some ambiguity in the identification of the elastic/plastic transition in diamond, particularly in the case of the thicker (500 micron) diamond samples. Previous dynamic experiments with comparable target thicknesses have determined the single crystal diamond HEL to be between 57 GPa and 81 GPa, depending on orientation [93, 94]. Our experiments cover the peak pressure range of ~52 GPa to ~84 GPa.

Line-VISAR

Overview

Line-VISAR was used to obtain velocity profiles for the majority of the shots. Peak pressure and pressure at the 2D-VISAR probe time were calculated using impedance matching as described in reference [136] and using the LiF Hugoniot from reference [137]. In order to ascertain true particle velocity, as well as pressure and density, VISAR records were corrected for the unsteady shock compression of LiF window [138-140]. Conditions inside the sample were simulated used HYADES hydrocode with the SESAME 7271 diamond equation of state table and Steinberg-Guinan shear and yield models. Hydrocode simulations confirmed that all shots were initially above the diamond HEL and were used to determine pressure at the 2D-VISAR probe time if the line-VISAR record did not extend far enough in time. Examples of x-t diagrams for the shock compression of the diamond targets discussed above can be found in Figure 62 and Figure 63.

Shock Wave Conditions

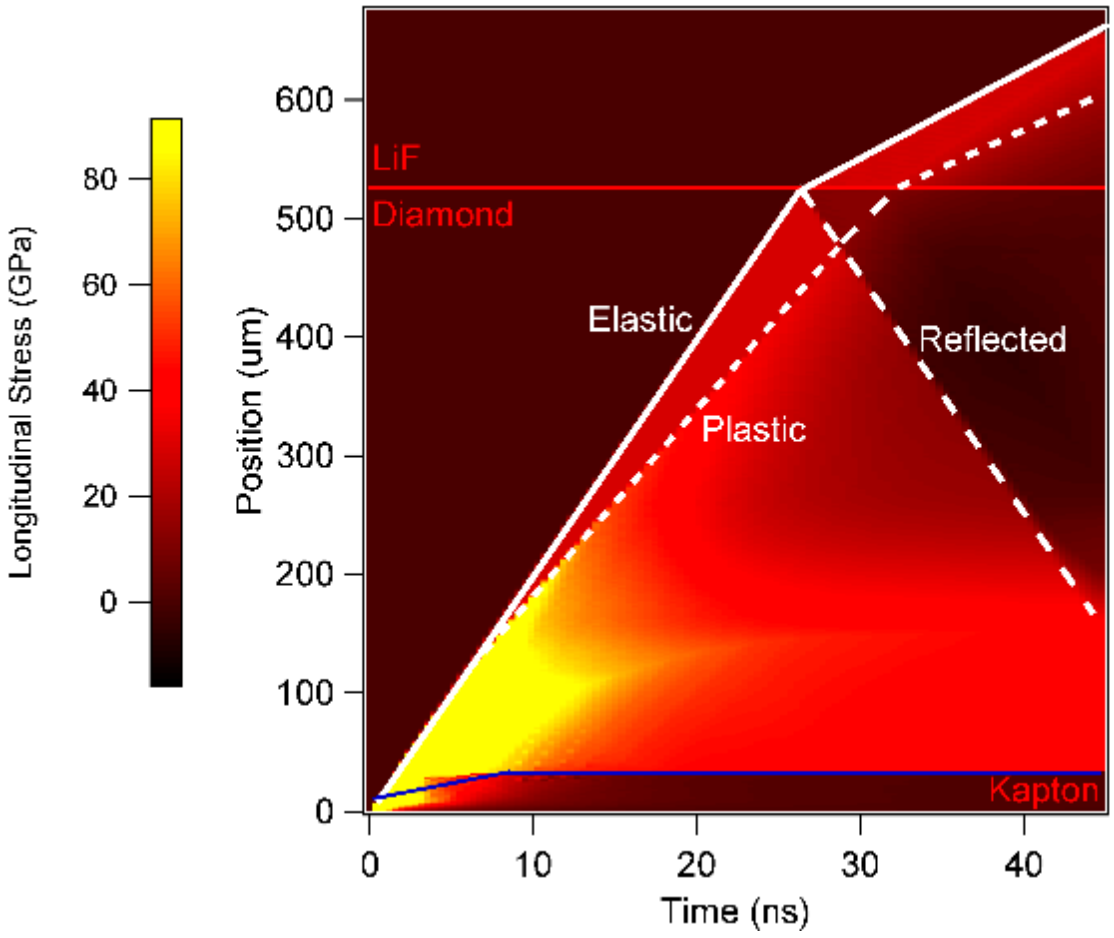

Figure 62 Position-time graph generated using HYADES. Seperation of the elastic and plastic waves can be observed.

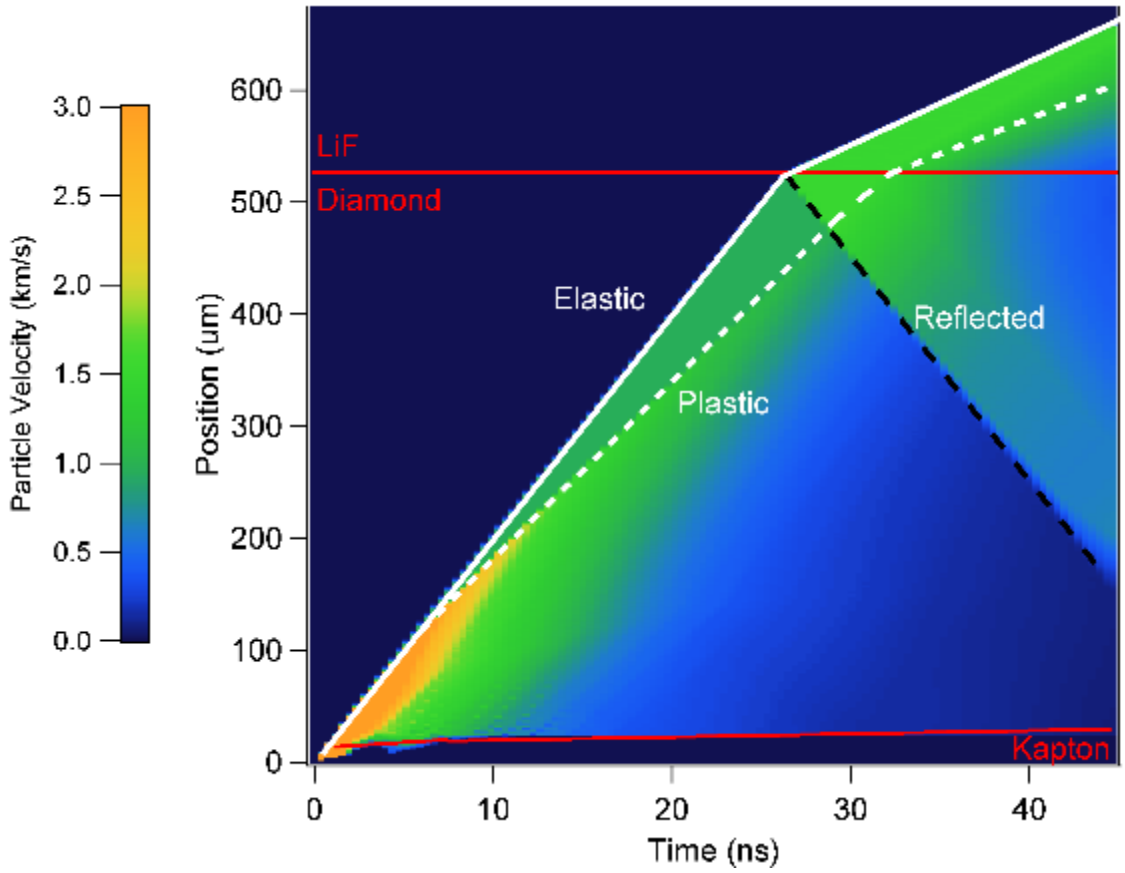

Figure 63 Position-time graph generated using HYADES. Seperation of the elastic and plastic waves can be observed.

Breakout Flatness

As a result of limitations in the available phase plates, there are a handful of shots with suboptimal flatness in the breakout. In particular, shots taken with the 0.6 mm diameter phase plates tended to have a greater degree of curvature on breakout, both due to the smaller overall phase plate size, as well as inhomogeneity across the phase plate. The majority of the shots taken with the 1 mm phase plate were flat within the resolution of the diagnostics, as shown in Figure 64, while the majority of the shots taken with the 0.6 mm phase plates were flat across 70-90% of the spatial extent of the line-VISAR, as shown in Figure 65. The exceptions tended to look like Figure 66, which has significant curvature, probably as a result of user error (misalignment of the overlap between the two laser drive beams is the most likely scenario). While, in most cases, this curvature complicates the analysis and introduces additional sources of error, in some cases it can produce interesting results, as shown in Figure 67.

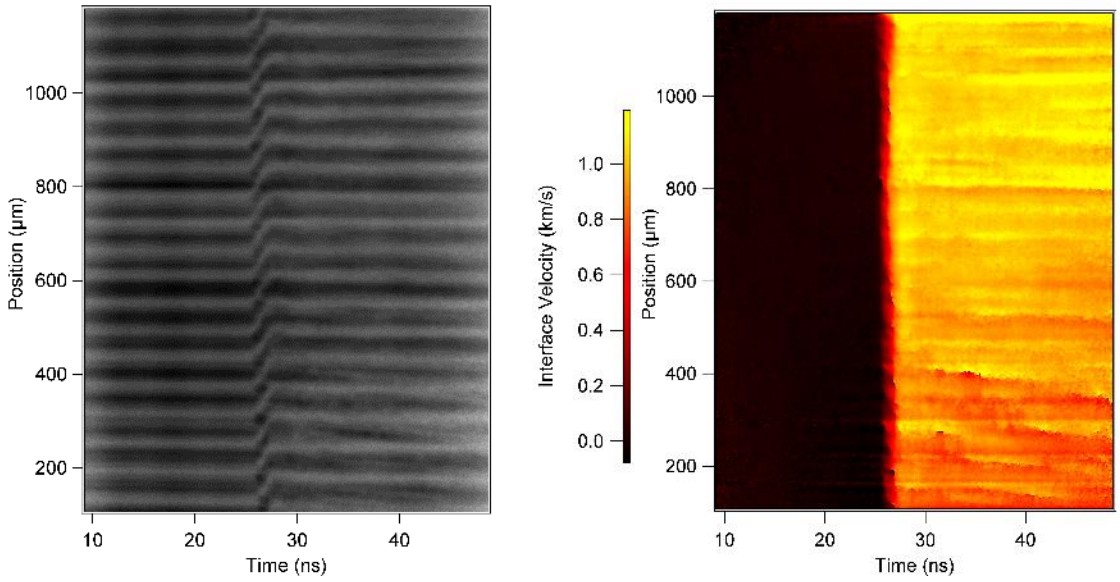

Figure 64 Typical line-VISAR raw data and calculated velocity for the 1 mm phase plate.

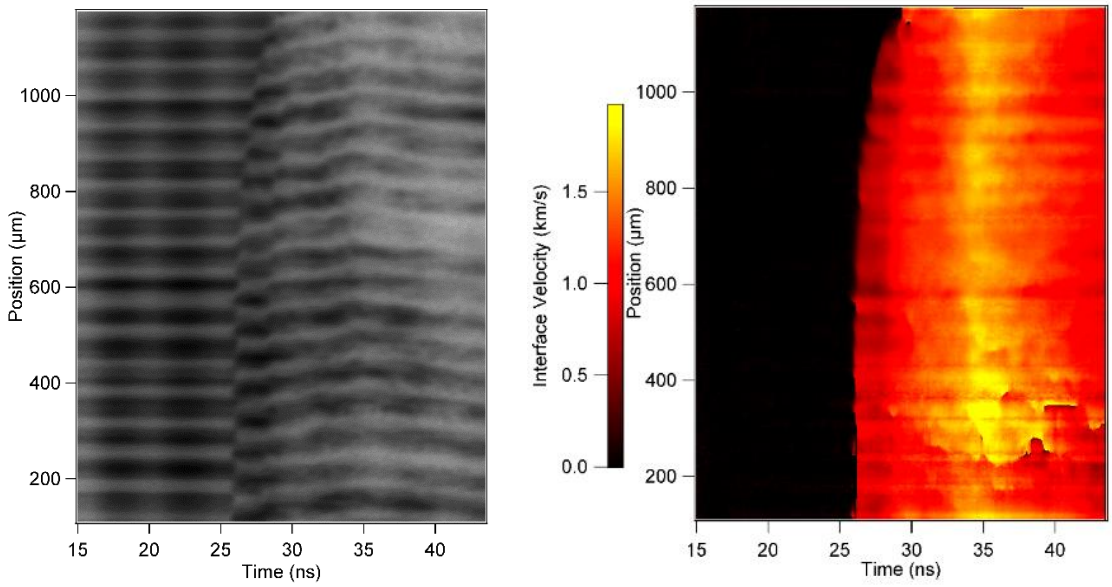

Figure 65 Typical line-VISAR raw data and calculated velocity for the 0.6 mm phase plate. Some curvature can be seen between 800-1100 microns.

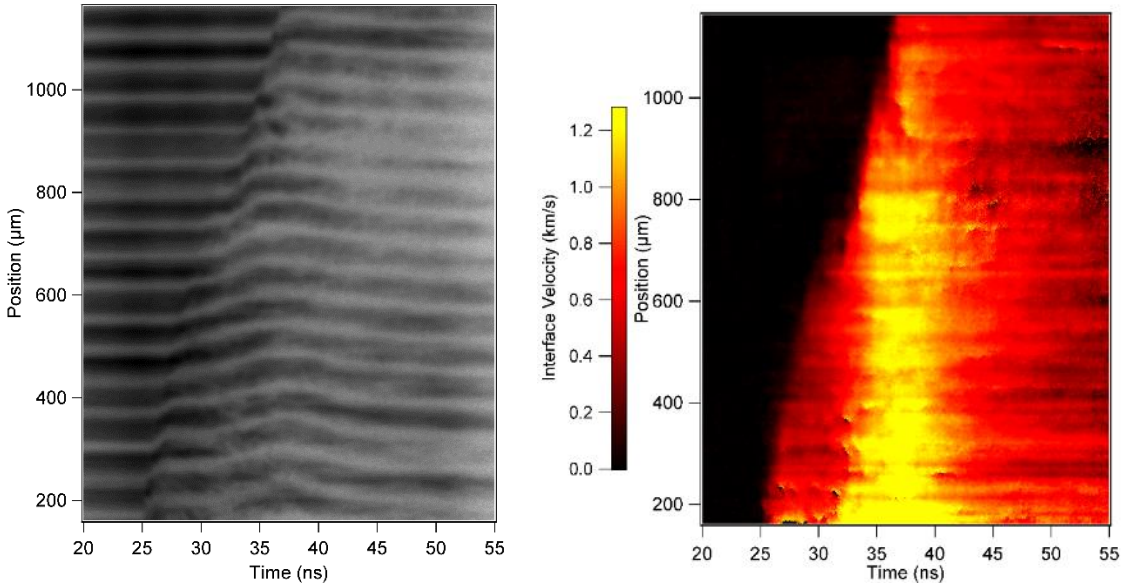

Figure 66 Line-VISAR raw data and calculated velocity for a shot with significant breakout curvature. Particularly interesting is the spatial dependence of the first velocity jump, while the second velocity jump (beginning at ~34 ns) is almost constant across the spatial extent of the data. The amplitude of this second velocity wave does increase with decreasing breakout time.

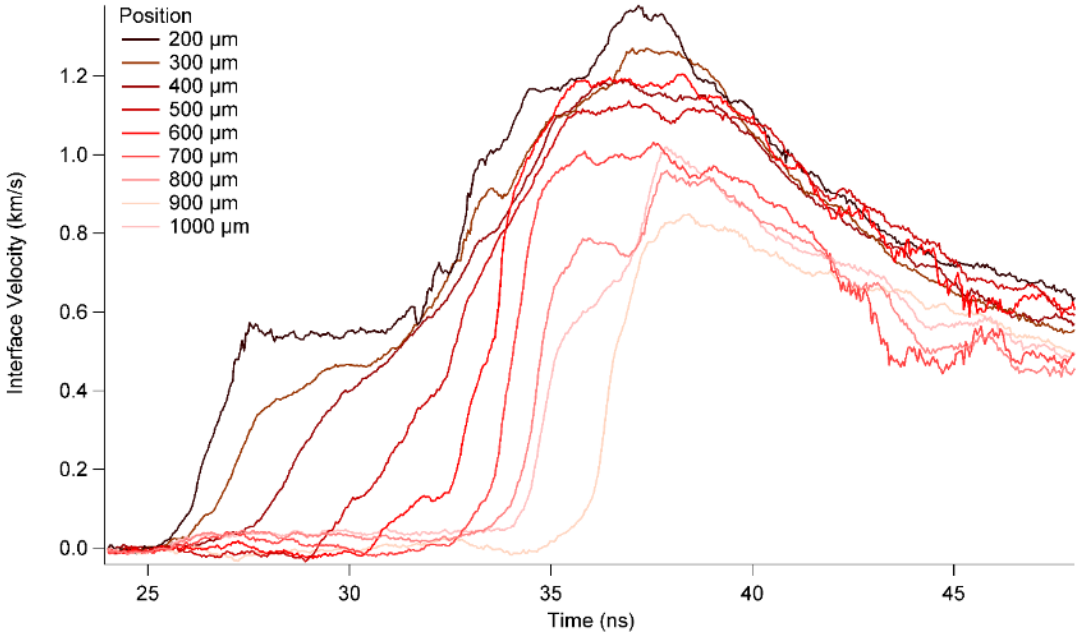

Figure 67 Velocity line outs from Figure 66. There is a two-wave structure in the majority of the traces and the timing between the two waves can be observed to change across the spatial extent of the target.

Velocity History

Compiled velocity profiles for the microdiamond and nanodiamond samples can be found in Figure 68 and Figure 69. In the free surface velocity profiles the observed velocities were corrected for release into vacuum. General trends are difficult to identify, partially due to energy inconsistencies in the drive laser and clear elastic precursors are only observed in a few shots.

Microdiamond

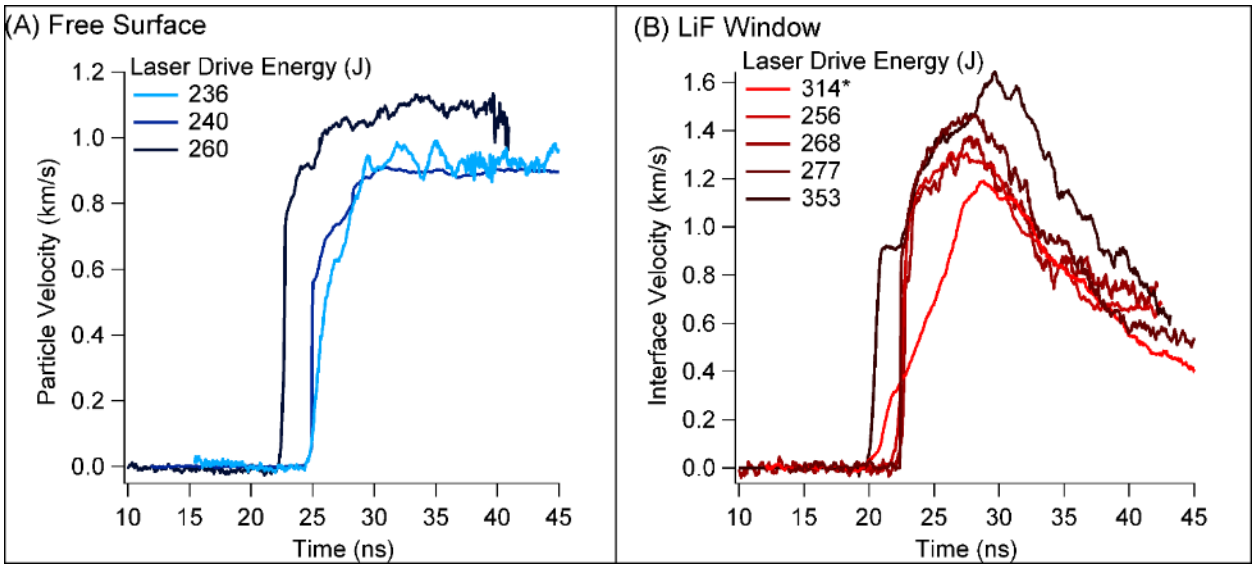

Figure 68 Line-VISAR traces from the analyzable shots on microdiamond samples with either (A) free surface breakouts or (B) LiF windows. *This shot had a significant degree of nonplanarity, so the energy coupled into the target at the center is unknown. The nonplanarity is shown in Figure 66.

Nanodiamond

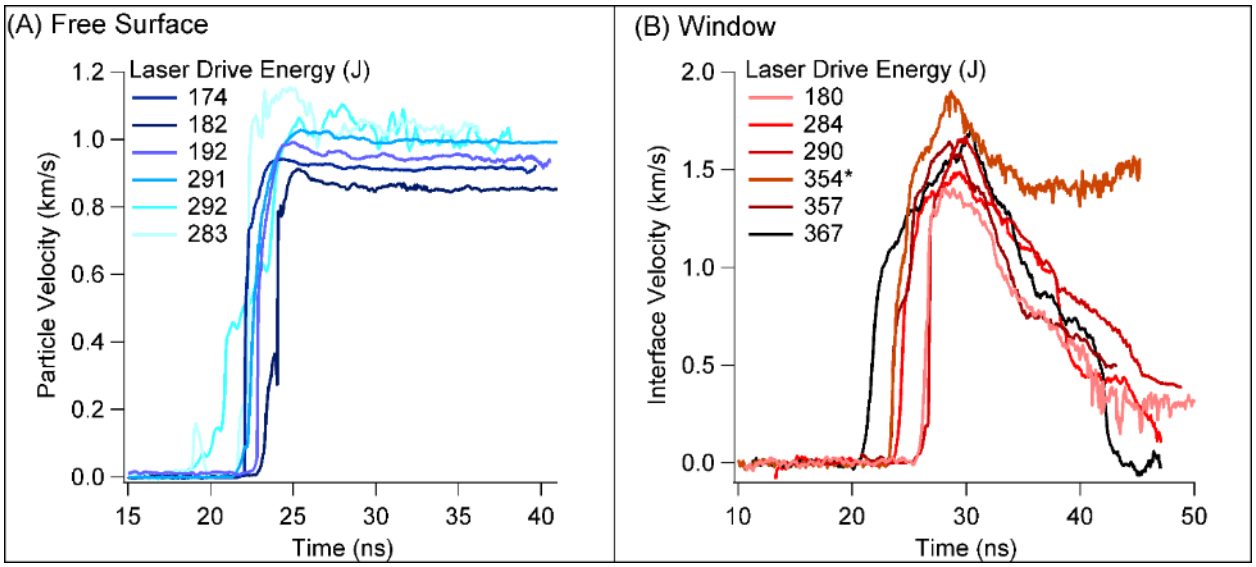

Figure 69 Line-VISAR traces from the analyzable shots on nanodiamond samples with either (A) free surface breakouts or (B) LiF windows. *The target int his shot had an alpha-quartz window.

2D-VISAR

Overview of Data and Analysis

2D-VISAR velocity maps and non-fringing images were generated for shots on LiF-tamped and free-surface diamond samples. An etalon delay of 263 ps was used in both 2D-VISAR interferometers, providing a velocity per fringe of 0.548 km/s. Due to problems with the JLF timing system at the time of this campaign (unexpected timing shifts in the laser bay resulted in variable breakout times on the order of nanoseconds, resulting in a number of shots with suboptimal 2D-VISAR probe times), the data on the time evolution of the fracture development is somewhat limited. There is, however, enough data to compare fracture networks in various types of targets.

Quantifying the fracture networks and inelastic deformation in the 2D-VISAR data was done using two methods. The first involves calculating the velocity power spectral density in regions of varying response across the 2D-VISAR velocity map. A detailed discussion of how this is done can be found in reference [91]. The second method was based on histograms of the velocity map.

Velocity Maps and Nonfringing Images

Measurements were made on free surface and LiF-windowed nanodiamond and microdiamond samples at various delay times after breakout. Imaging and velocimetry is presented below, with delay time and peak pressure indicated. Non-fringing images and velocity maps are presented in sequence. Spatial dimensions were scaled by determining the pixel/micron value by imaging a grid with a known mesh. Velocities are either interface

or free surface, with no corrections due to the impedance match applied. Pressures were determined using impedance matching, as described above. Timing and velocimetry values were confirmed by comparing traces from the 2D-VISAR with the velocity history from the line-VISAR, as shown in Figure 70.

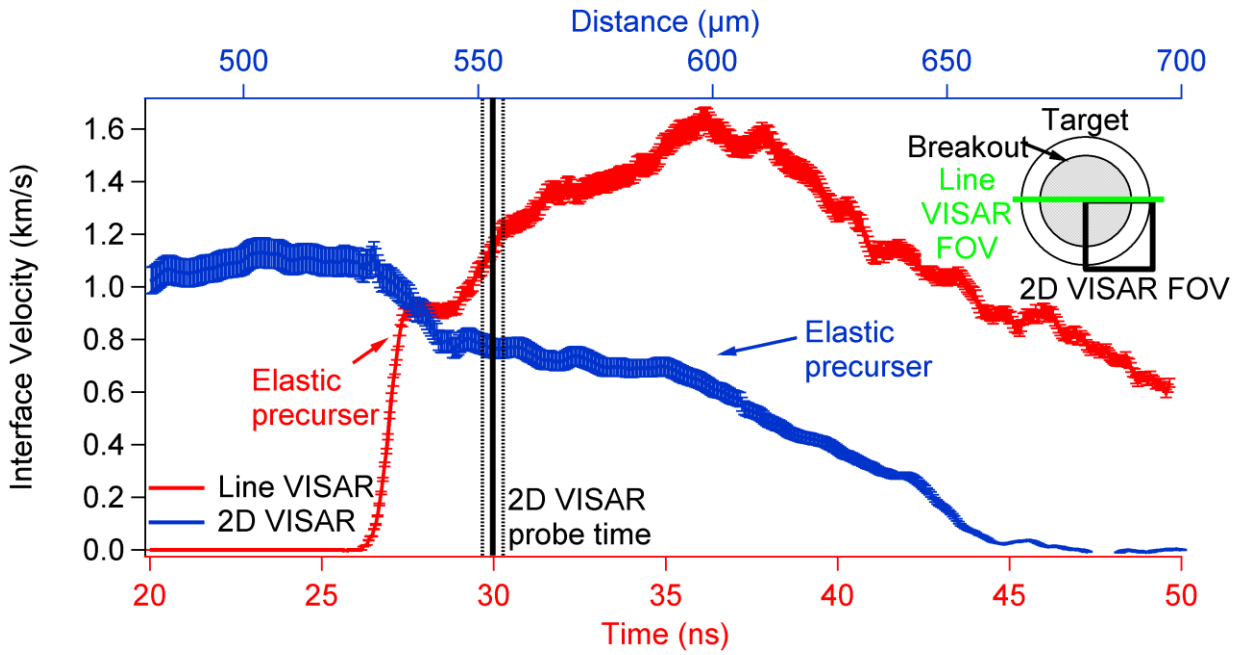

Figure 70 Velocity traces from both the line-VISAR (red) and the 2D-VISAR (blue). The time axis origin for the red VISAR trace is the firing of the drive laser and the distance axis origin for the blue 2D VISAR trace is the calculated center of the breakout spot on the diagnostic side of the target, as shown inset in the upper right corner.. The solid black vertical line indicates the point in time at which the 2D-VISAR probe fired and the dashed lines on either side indicate the uncertainty in the timing.

Free Surface

Diamond samples were prepared as described in the target preparation section above. Diagnostics observed the free surface of the diamond samples for both the nanocrystalline and microcrystalline samples. VISAR traces show no sign of pullback after initial breakout, confirming that the material was shocked beyond the elastic limit and therefore had very little strength after breakout. Small magnitude reverberating spall signatures are observed in the majority of the shots, suggesting that we are observing spall fracture in the 2D VISAR.

Microdiamond Samples

Free surface microdiamond samples were prepared as described above. Line-VISAR traces for the samples are shown in Figure 71 with 2D VISAR probe times indicated. 2D VISAR data can be found in Figure 71 through Figure 77.

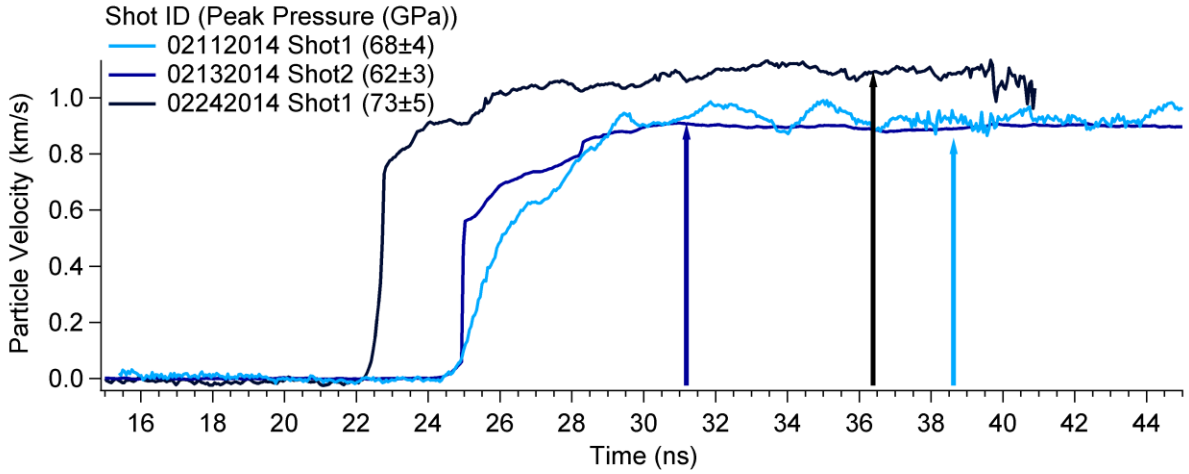

Figure 71 Particle velocity as a function of time for the 2D VISAR data shown below. Vertical lines indicate the 2D VISAR probe delay for each shot.

02132014 Shot2

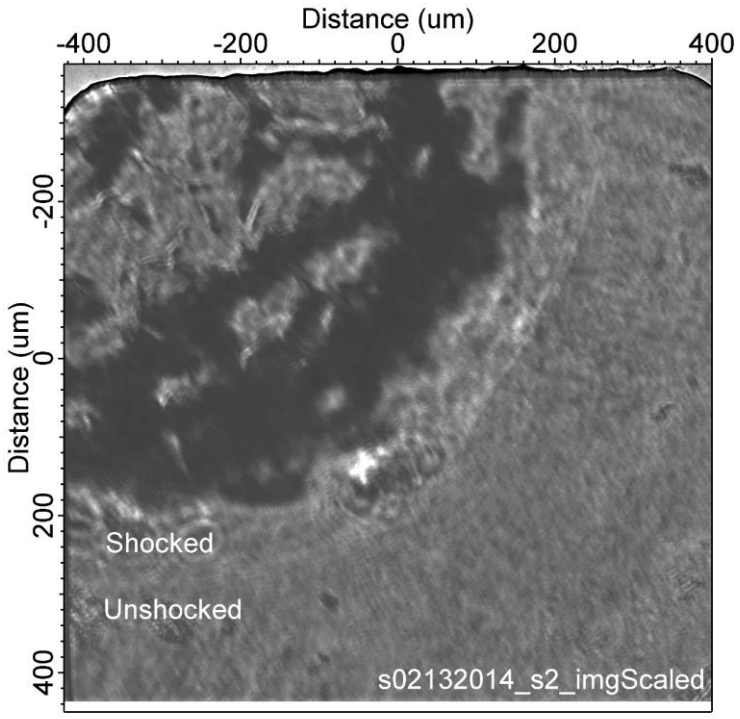

Figure 72 Nonfringing image, free surface microdiamond 6.5 ns after breakout. 0.6 mm diameter round phase plate was used. Multi-scale fracture is observed, with larger cracks near the edge of the breakout and smaller cracks closer to the center.

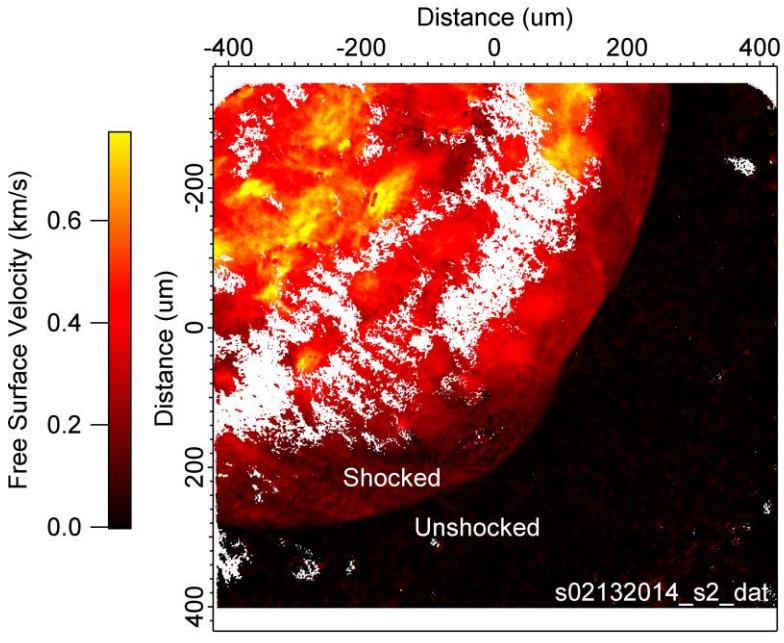

Figure 73 Velocity map, free surface microdiamond 6.5 ns after breakout. An initial, smooth elastic region is present towards the outside of the shocked region, with velocity roughness increasing toward the center.

02112014 Shot1

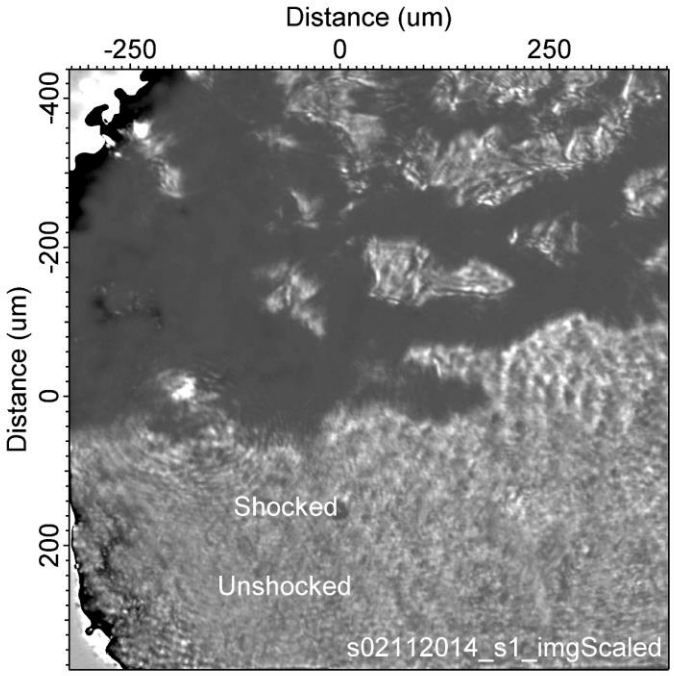

Figure 74 Nonfringing image, free surface microdiamond 12.5 ns after breakout. 0.6 mm diameter round phase plate was used. Again, multi-scale fracture is observed, with larger cracks near the edge of the breakout and smaller cracks closer to the center.

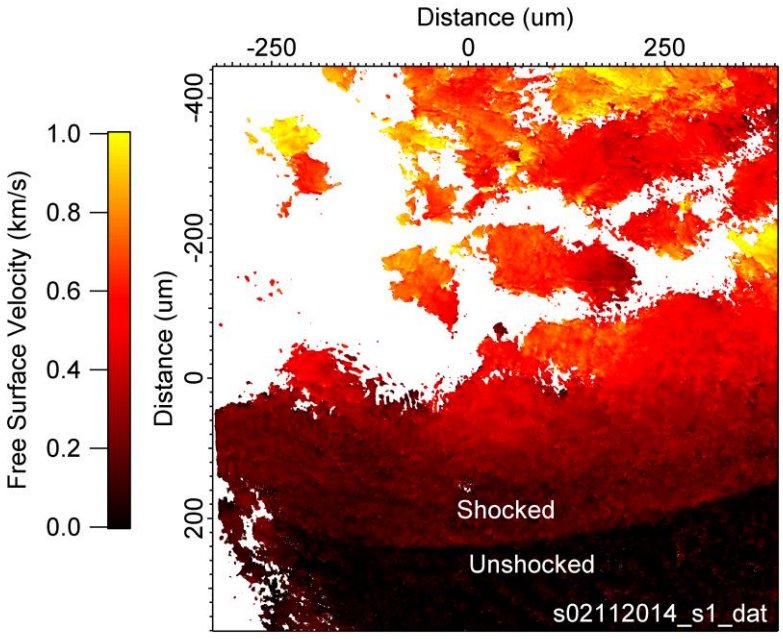

Figure 75 Velocity map, free surface microdiamond 12.5 ns after breakout. An initially smooth, elastic region is again present.

02242014 Shot1

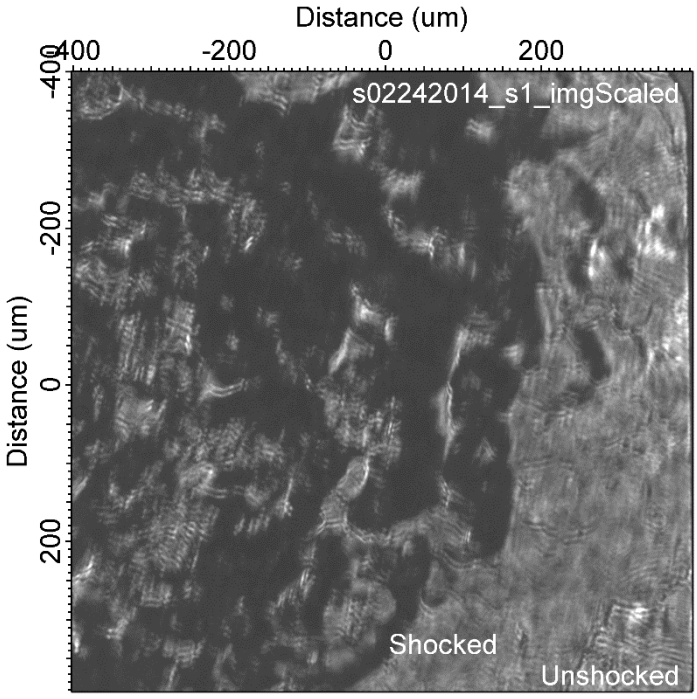

Figure 76 Nonfringing image, free surface microdiamond 14.4 ns after breakout. 0.6 mm diameter round phase plate was used. Both sizes of fracture have increased.

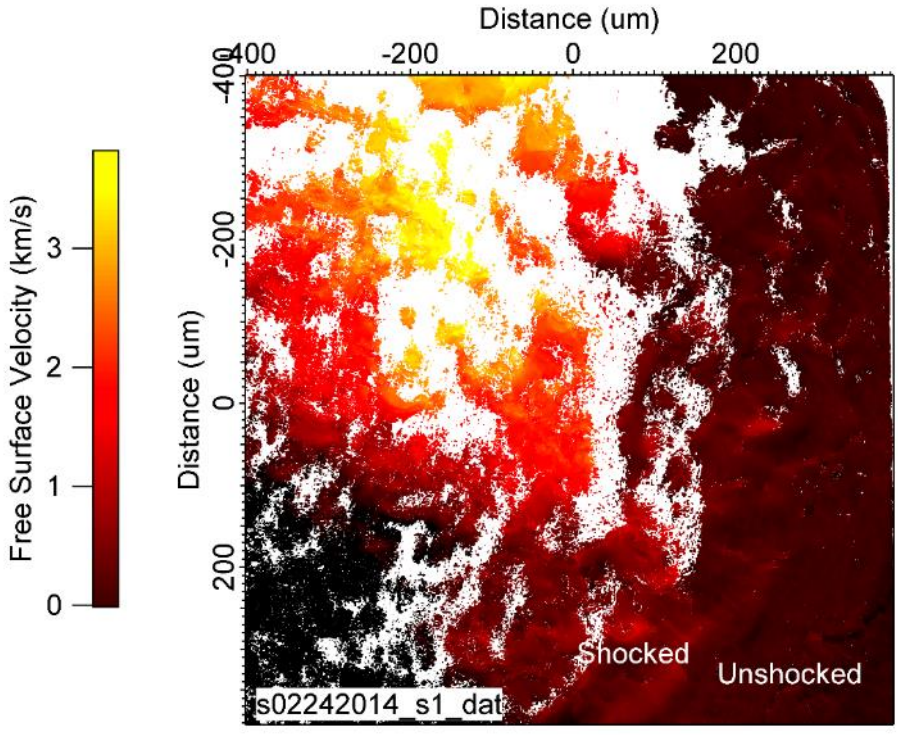

Figure 77 Velocity map, free surface microdiamond 14.4 ns after breakout.

Nanodiamond Samples

Nanodiamond samples were prepared as described above. Line-VISAR traces for the samples are shown in Figure 78 with 2D VISAR probe times indicated. 2D VISAR data can be found in Figure 76 through Figure 90.

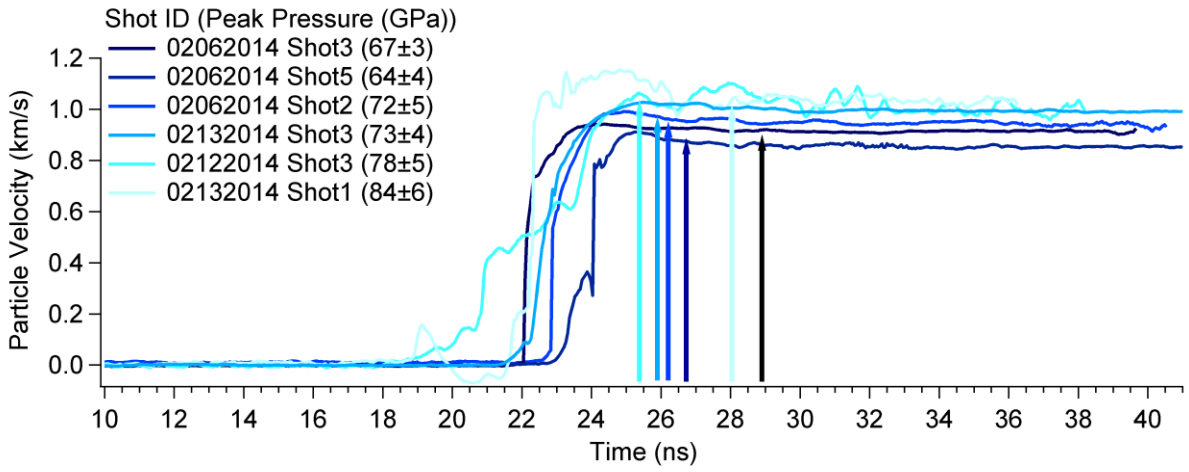

Figure 78 Particle velocity as a function of time for the 2D VISAR data shown below. Vertical lines indicate the 2D VISAR probe delay for each shot.

02132014 Shot3

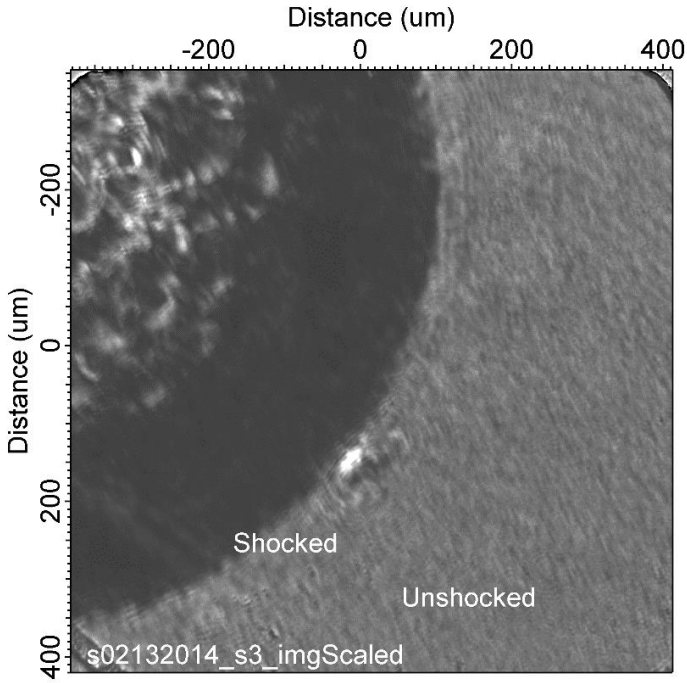

Figure 79 Nonfringing image, free surface nanodiamond 3 ns after breakout. 0.6 mm round phase plate was used.

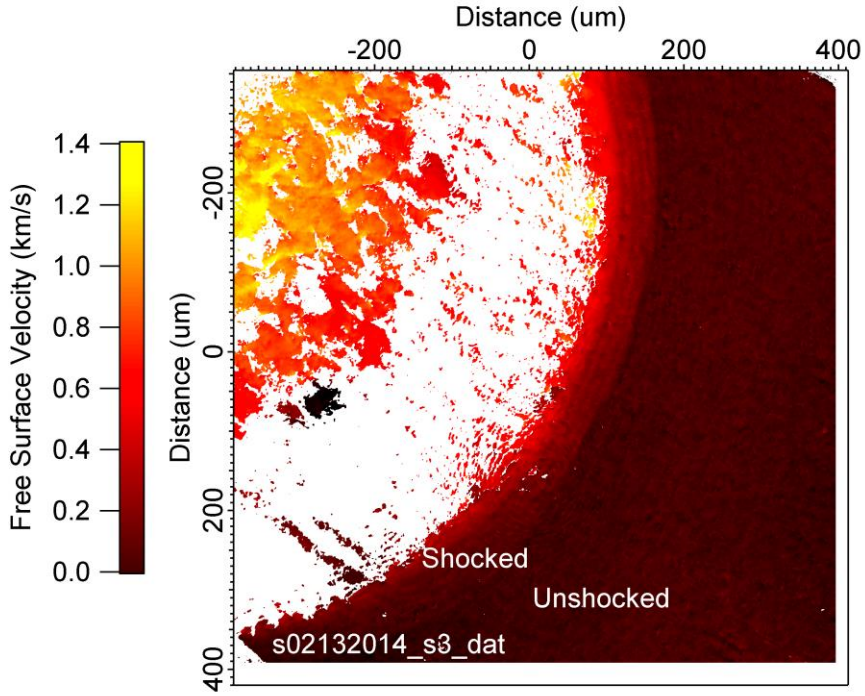

Figure 80 Velocity map, free surface nanodiamond 3 ns after breakout. 0.6 mm round phase plate was used.

02062014 Shot2

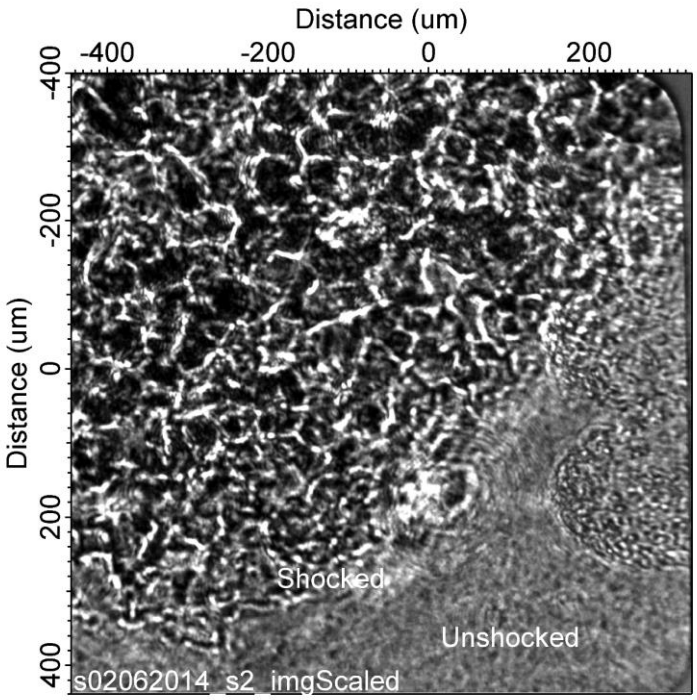

Figure 81 Nonfringing image, free surface nanodiamond 3.5 ns after breakout. 1 mm square phase plate was used.

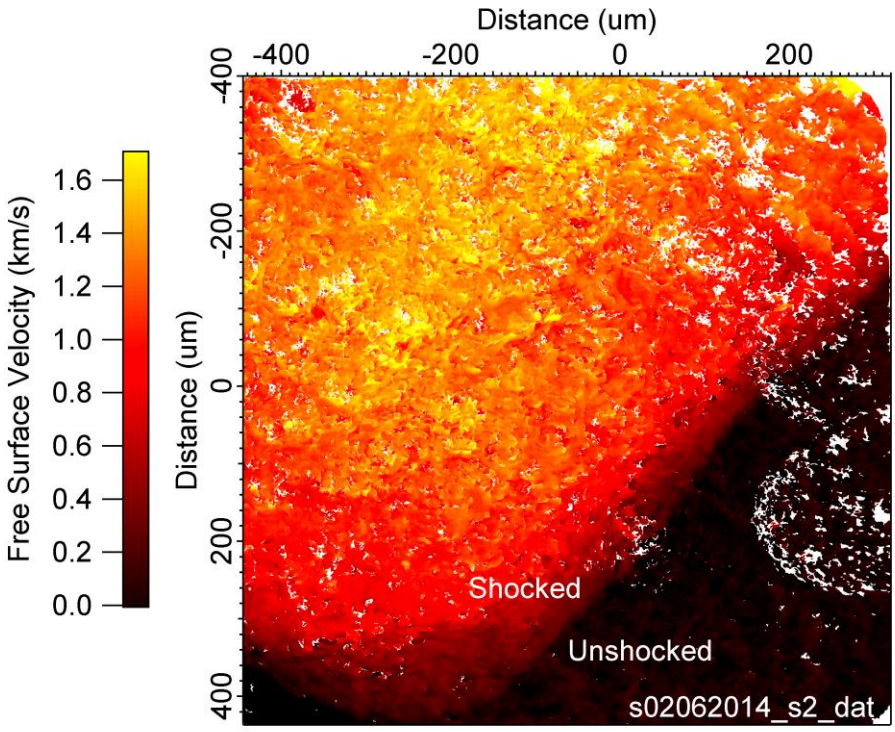

Figure 82 Velocity map, free surface nanodiamond 3.5 ns after breakout.

02062014 Shot5

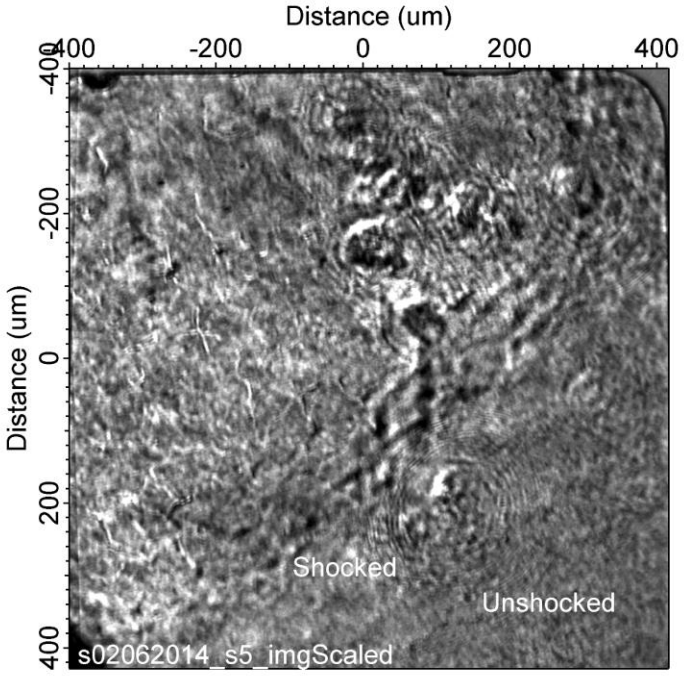

Figure 83 Nonfringing image, free surface nanodiamond 4.1 ns after breakout. 1 mm square phase plate was used. Initial fracturing observed at earlier times appears to have smoothed out.

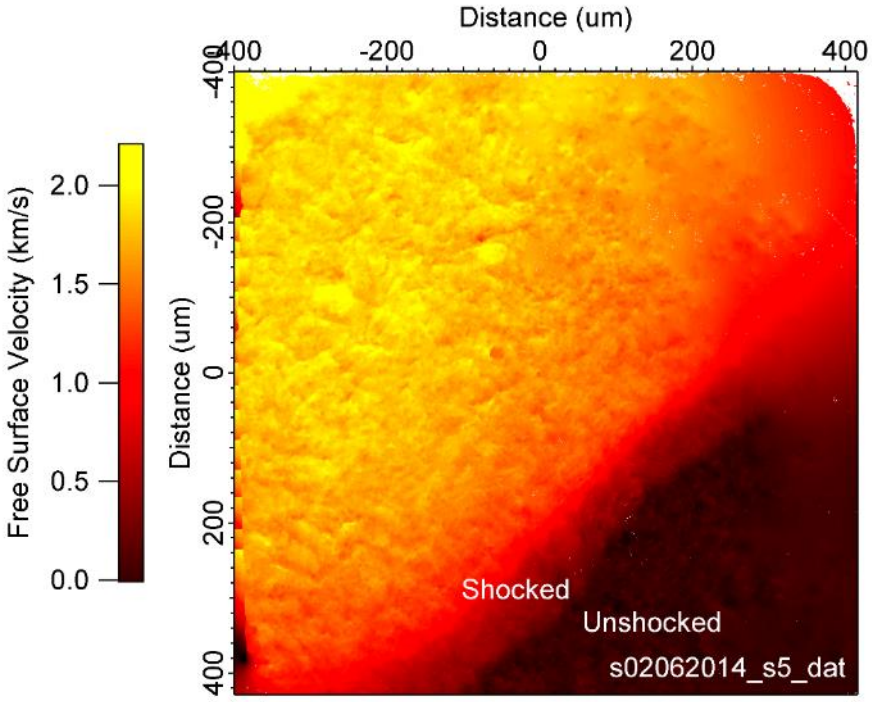

Figure 84 Velocity map, free surface nanodiamond 4.1 ns after breakout.

02062014 Shot7

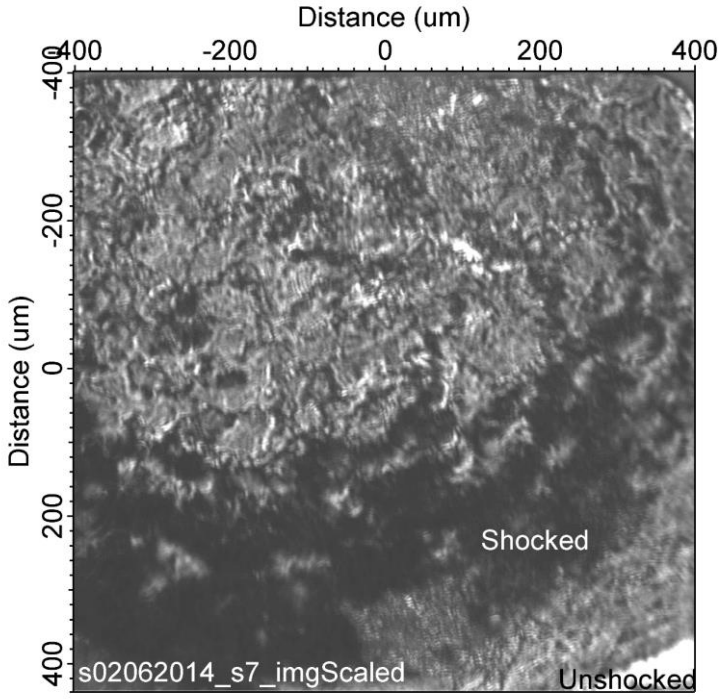

Figure 85 Nonfringing image, free surface nanodiamond 6.3 ns after breakout. 1 mm square phase plate was used. Fracture is more pronounced at the edge of the breakout.

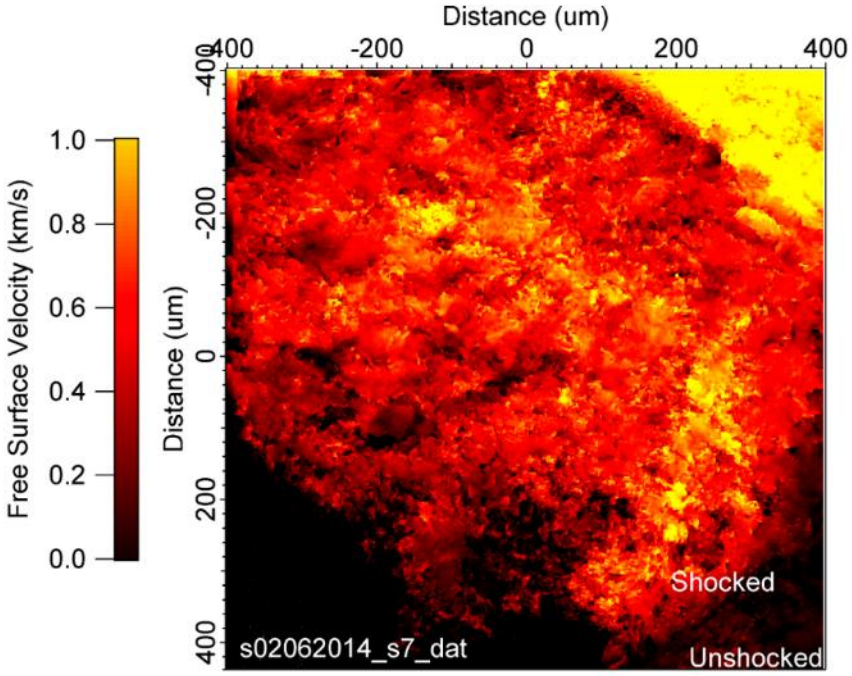

Figure 86 Velocity map, free surface nanodiamond 6.3 ns after breakout.

02062014 Shot3

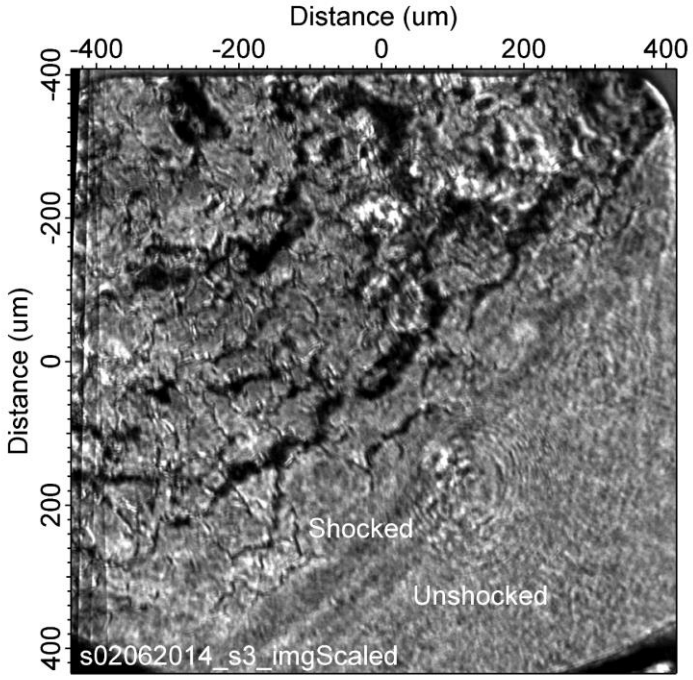

Figure 87 Nonfringing image, free surface nanodiamond 6.9 ns after breakout. Fracture spacing is very similar to that in Figure 85, without the breakout edge gaps.

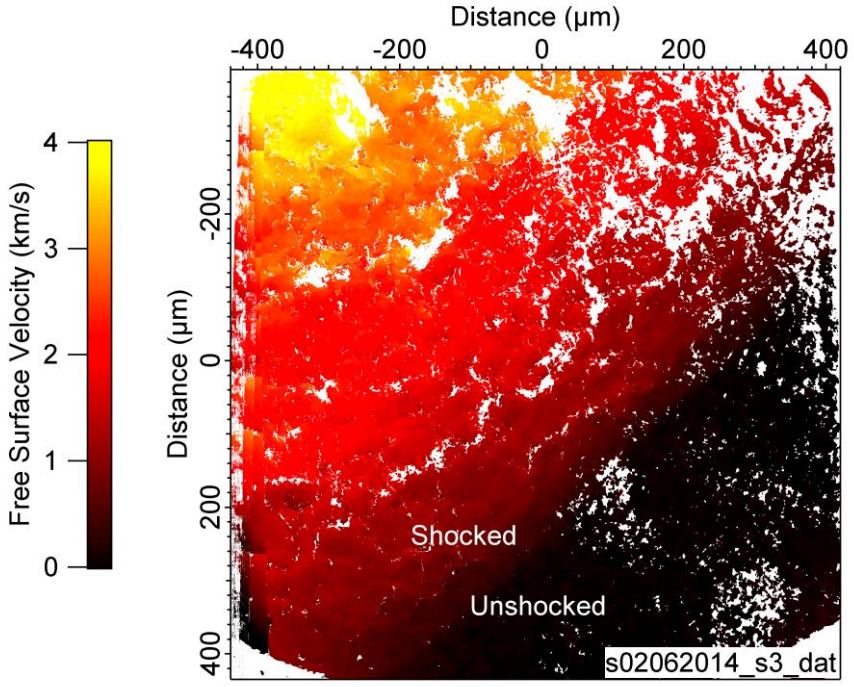

Figure 88 Velocity map, free surface nanodiamond 6.9 ns after breakout.

02122014 Shot3

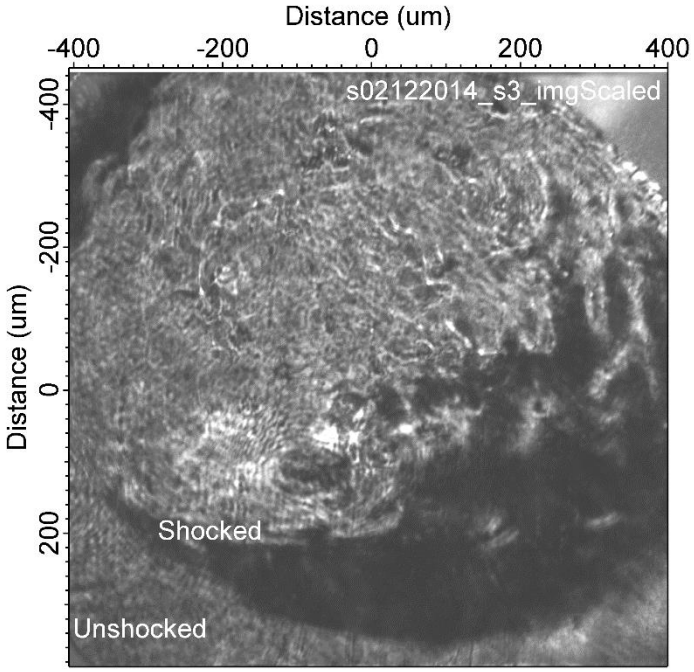

Figure 89 Nonfringing image, free surface nanodiamond 7.1 ns after breakout. 0.6 mm round phase plate was used. Latest time point for the free surface nanodiamond, fractures still evident and the asymetric edge fractures are visible again.

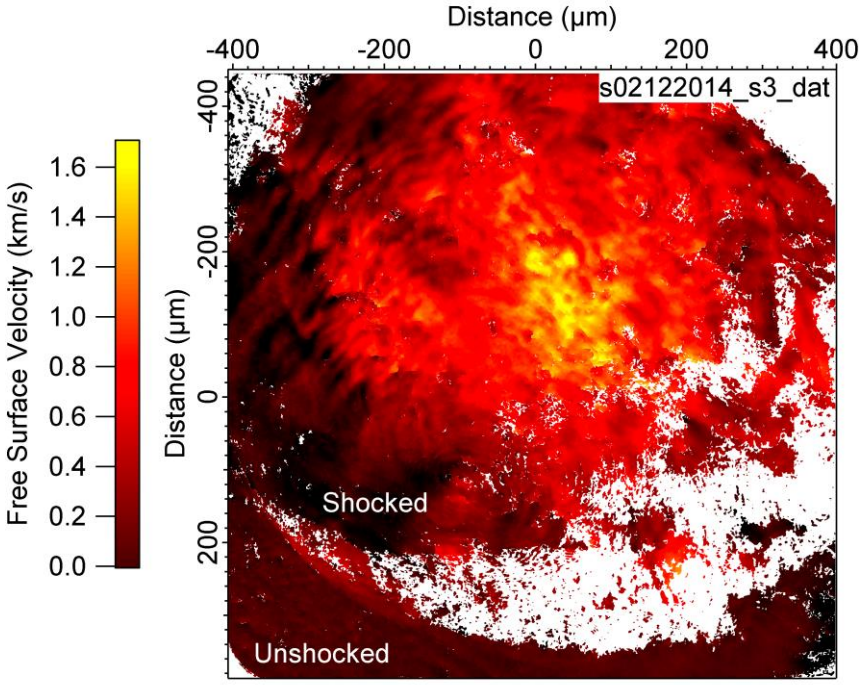

Figure 90 Velocity map, free surface nanodiamond 7.1 ns after breakout.

LiF-Tamped

Diamond samples were tamped with either 100 micron or 500 micron windows, as described in the target preparation section above. The LiF windows for the microdiamond targets were sputter-coated with a 104 nm aluminum layer to improved reflectivity at the diamond-LiF interface. As opposed to the spall fracture observed in the free surface samples, fracture in these target is most likely due to either the inelastic wave reaching the interface or the reflection of the shock wave at the diamond/LiF interface. A schematic showing the relative impedance of diamond and LiF is shown in Figure 91. For a given actual diamond particle velocity, the apparent velocity for the free surface samples will be approximately twice the actual value, with some corrections required due to the interference between the reflected elastic wave and the plastic wave. The apparent velocity for the LiF windowed sample relative to the actual diamond particle velocity depends on the peak pressure, but for the majority of the experiments shown the apparent velocity is ~60% higher than the velocity in the diamond. A more distinct elastic/plastic transition would help in determining whether the windowed samples are plastically deformed prior to the wave reflection, which would require higher energy drive lasers.

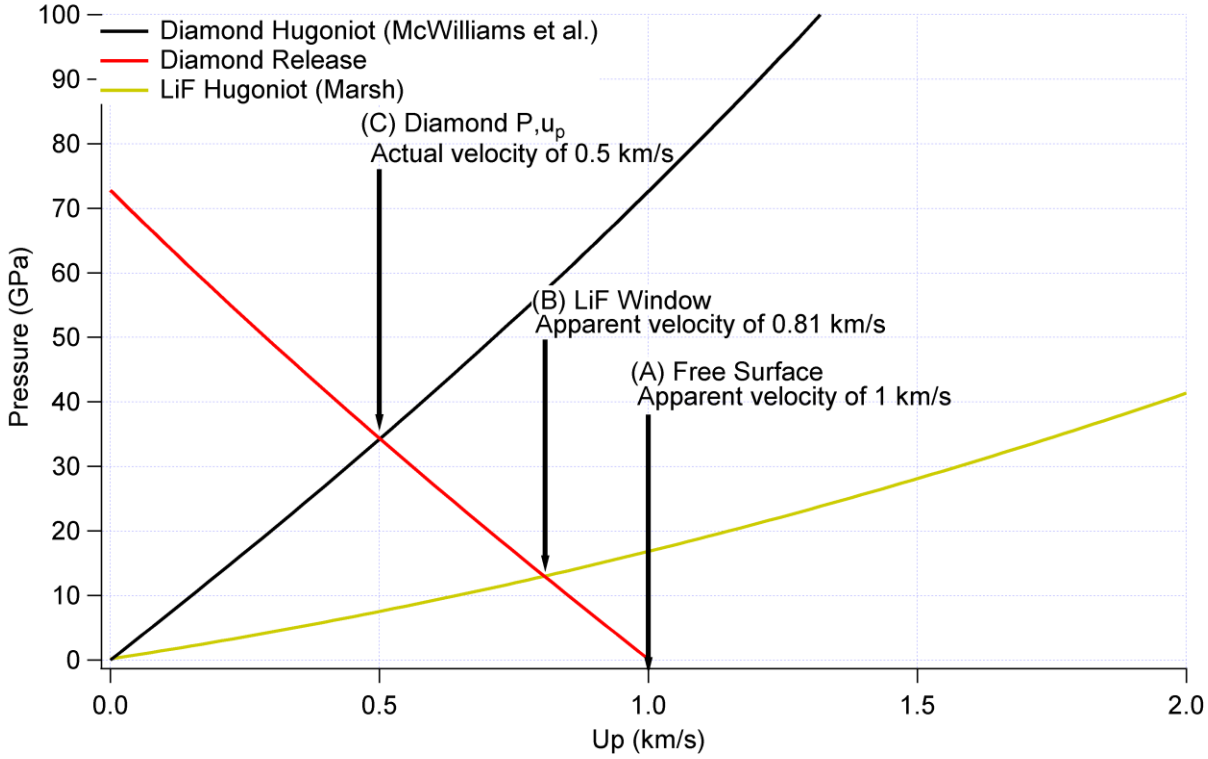

Figure 91 Impedance matching schematic for the free surface and LiF windowed samples. (A) Apparent velocity for a free surface sample. (B) Apparent velocity for a LiF windowed sample. (C) Actual velocity for the the apparent velocities in A and B.

Microdiamond Samples

Microdiamond samples were prepared as described above. Line-VISAR traces for the samples are shown in Figure 92 with 2D VISAR probe times indicated. 2D VISAR data can be found in Figure 93 through Figure 102.

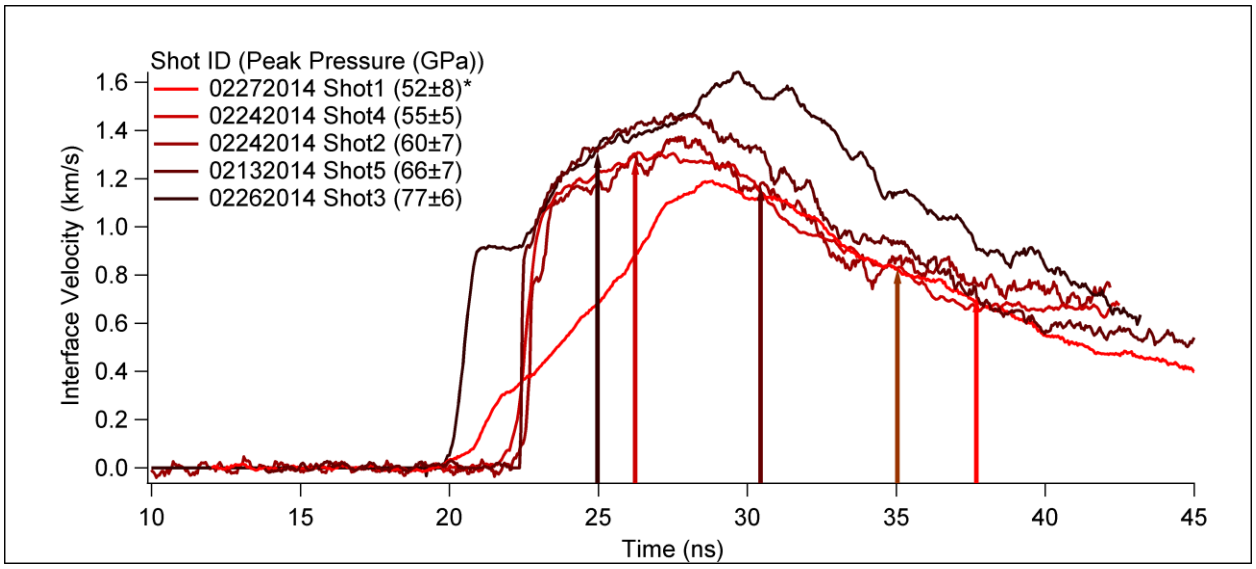

Figure 92 Interface velocity as a function of time for the 2D VISAR data shown below. Vertical lines indicate the 2D VISAR probe delay for each shot.

02242014 Shot4

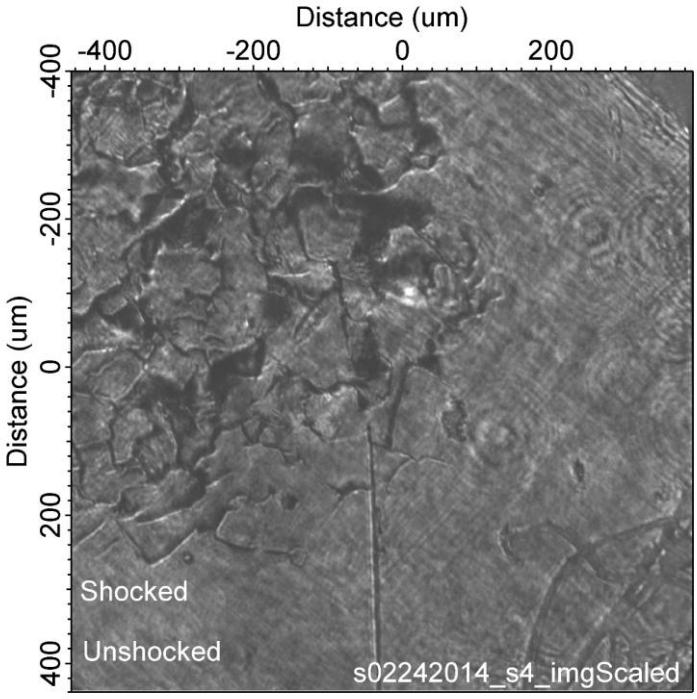

Figure 93 Nonfringing image, LiF-tamped microdiamond 3.5 ns after breakout.

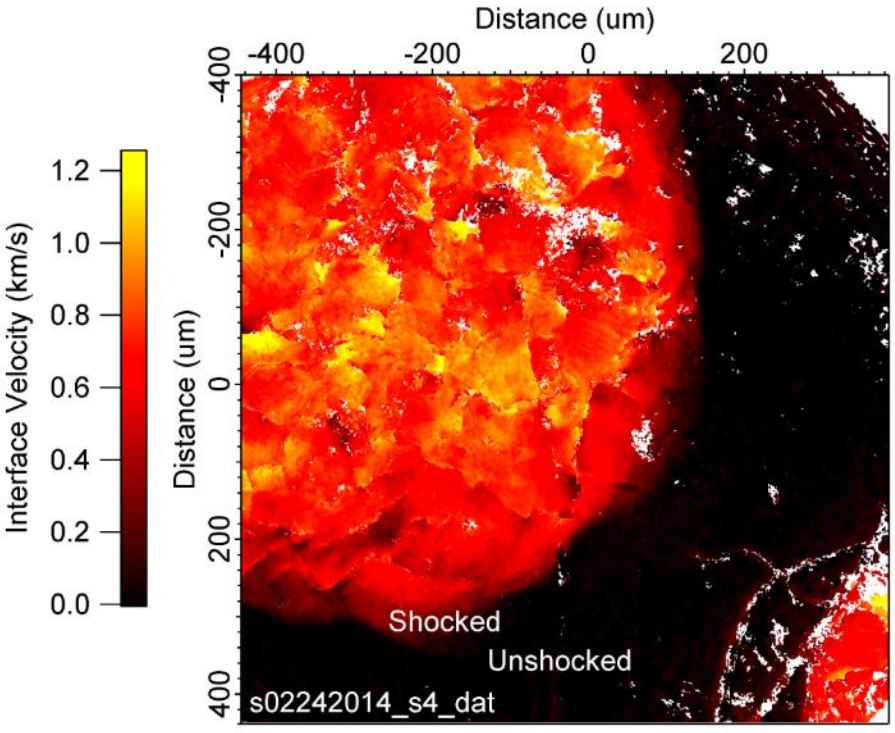

Figure 94 Velocity map, LiF-tamped microdiamond 3.5 ns after breakout.

02262014 Shot3

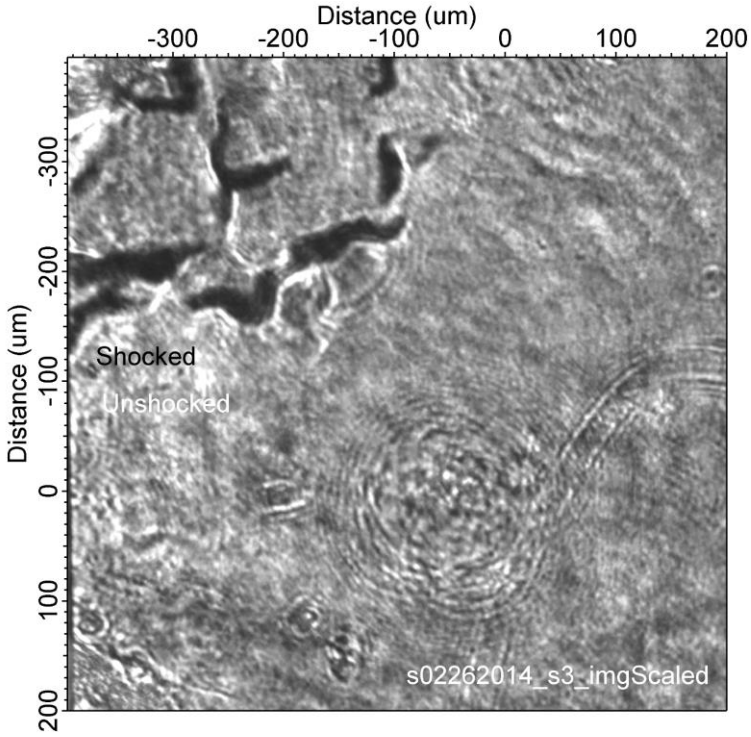

Figure 95 Nonfringing image, LiF-tamped microdiamond 4.5 ns after breakout.

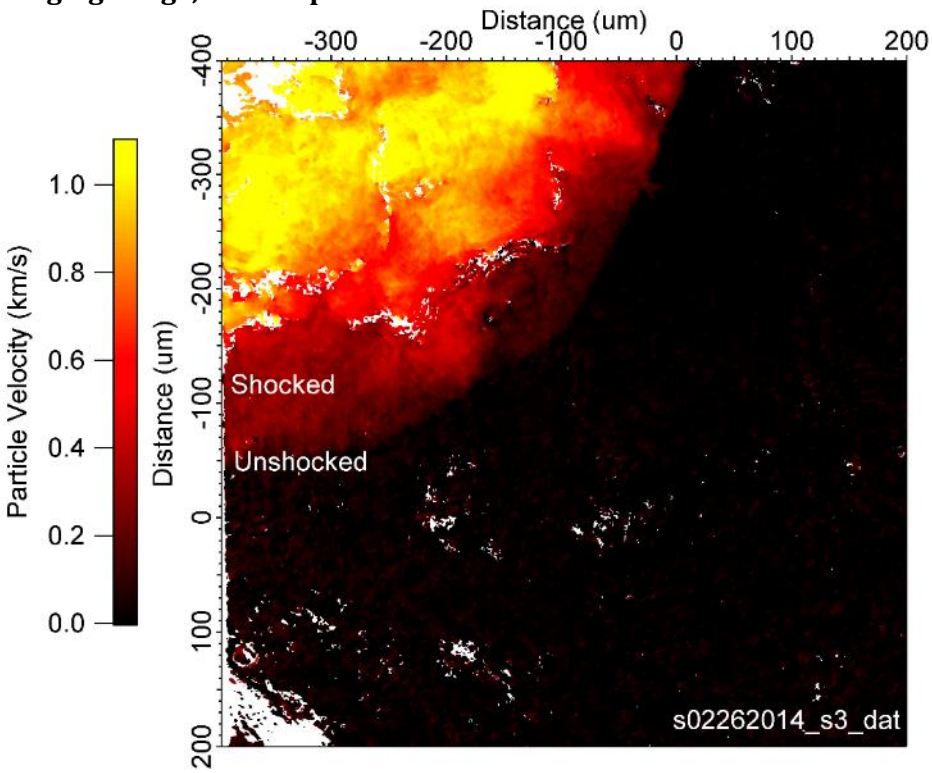

Figure 96 Velocity map, LiF-tamped microdiamond 4.5 ns after breakout.

02132014 Shot5

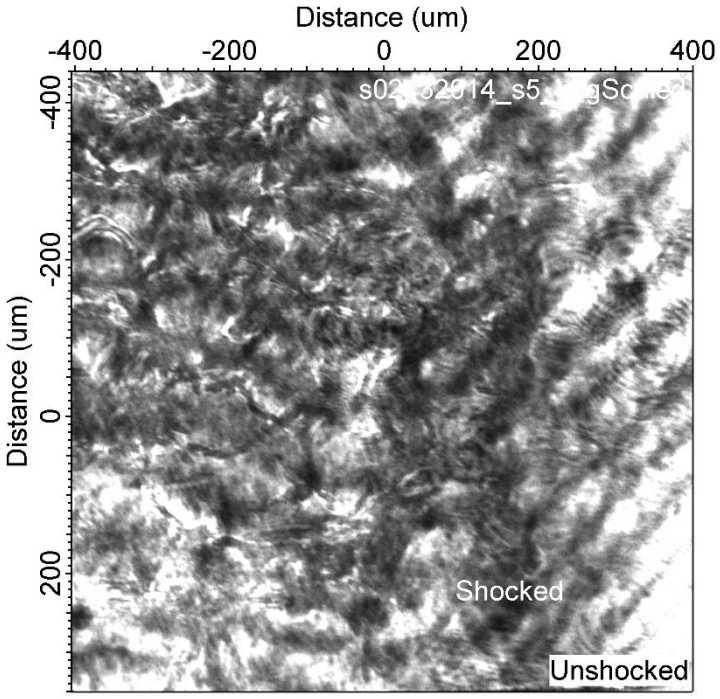

Figure 97 Nonfringing image, LiF-tamped microdiamond 8.7 ns after breakout. The fringes on the right side of the image are due to interference between the microdiamond surface and the LiF surface. The LiF window was not aluminized.

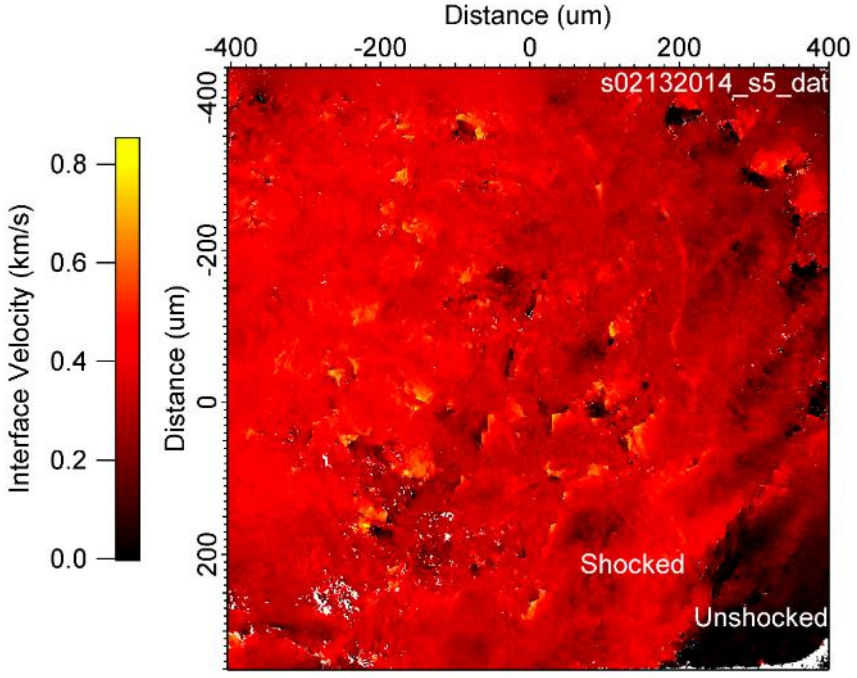

Figure 98 Velocity map, LiF-tamped microdiamond 8.7 ns after breakout.

02242014 Shot2

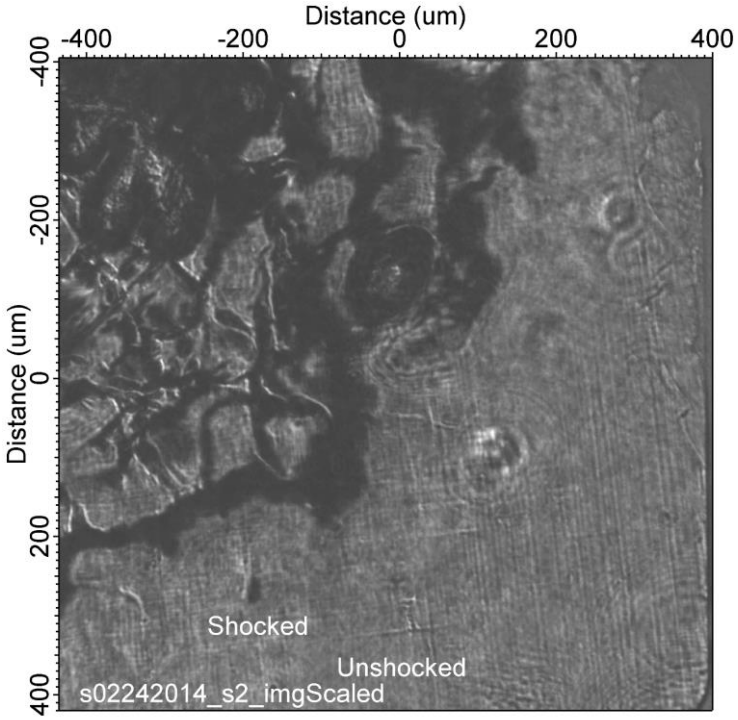

Figure 99 Nonfringing image, LiF-tamped microdiamond 12.7 ns after breakout.

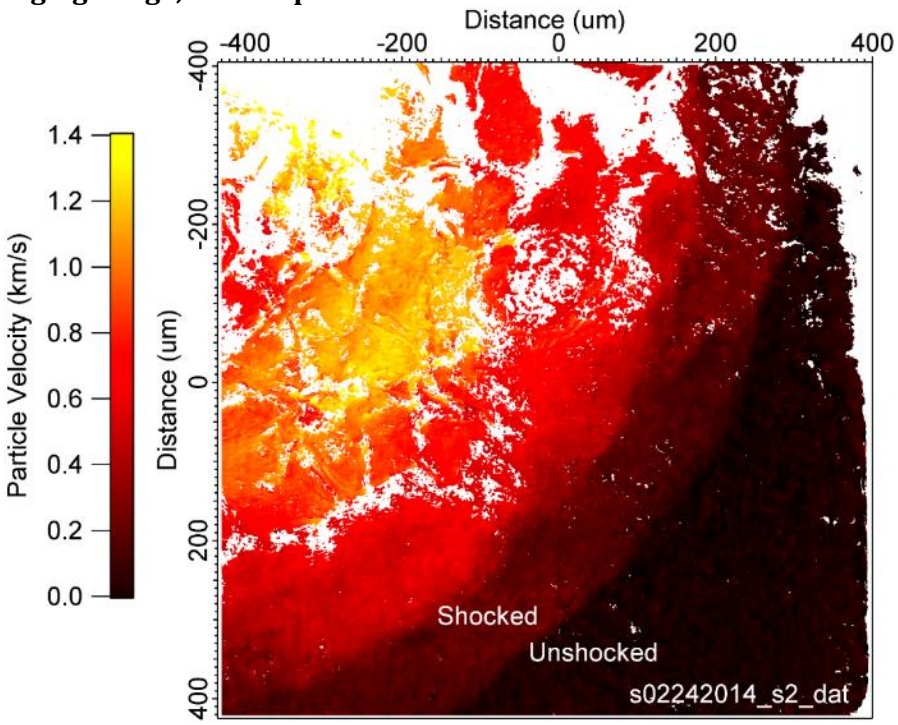

Figure 100 Velocity map, LiF-tamped microdiamond 12.7 ns after breakout.

02272014 Shot1

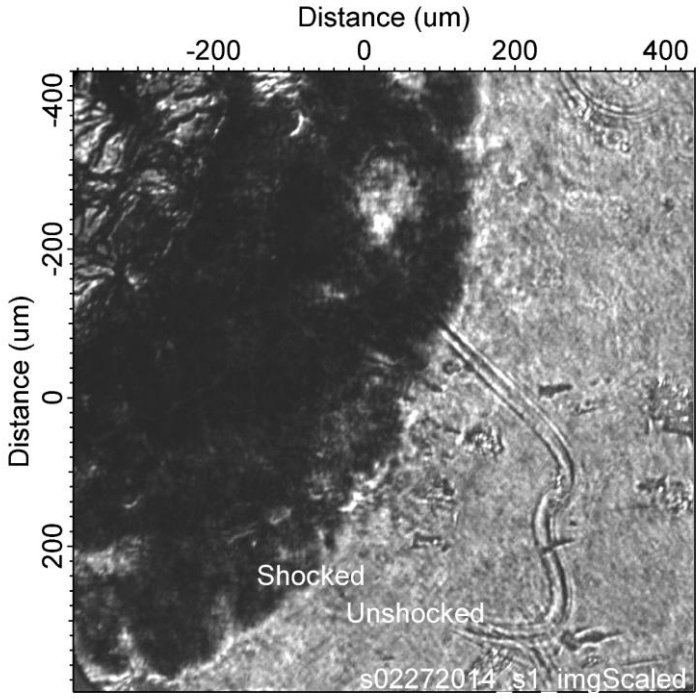

Figure 101 Nonfringing image, LiF-tamped microdiamond 15.9 ns after breakout.

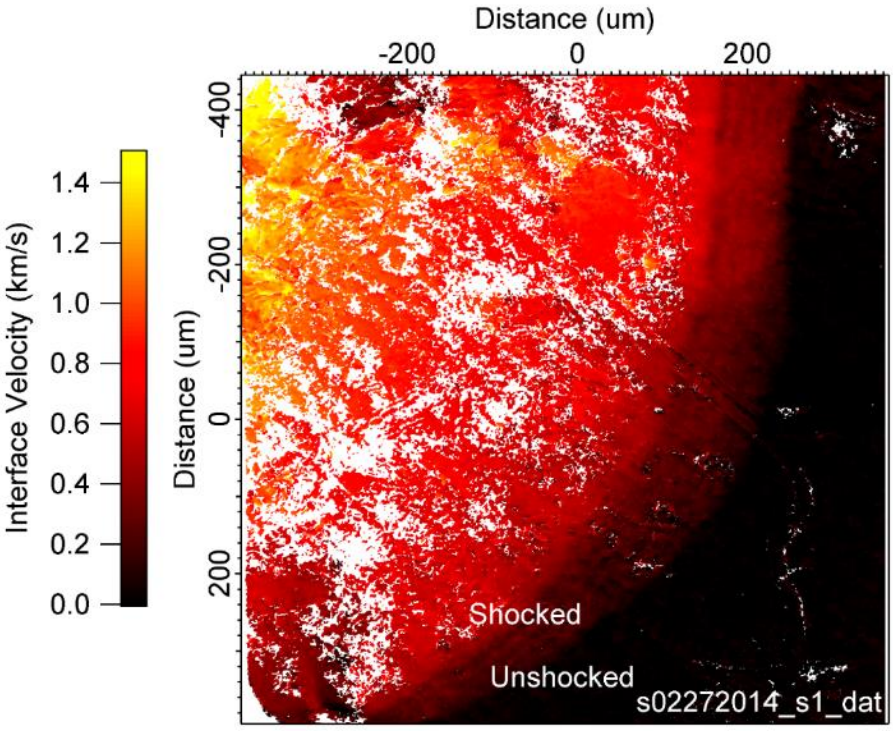

Figure 102 Velocity map, LiF-tamped microdiamond 15.9 ns after breakout.

Nanodiamond Samples

Nanodiamond samples were prepared as described above. Line-VISAR traces for the samples are shown in Figure 103 with 2D VISAR probe times indicated. 2D VISAR data can be found in Figure 104 through Figure 113.

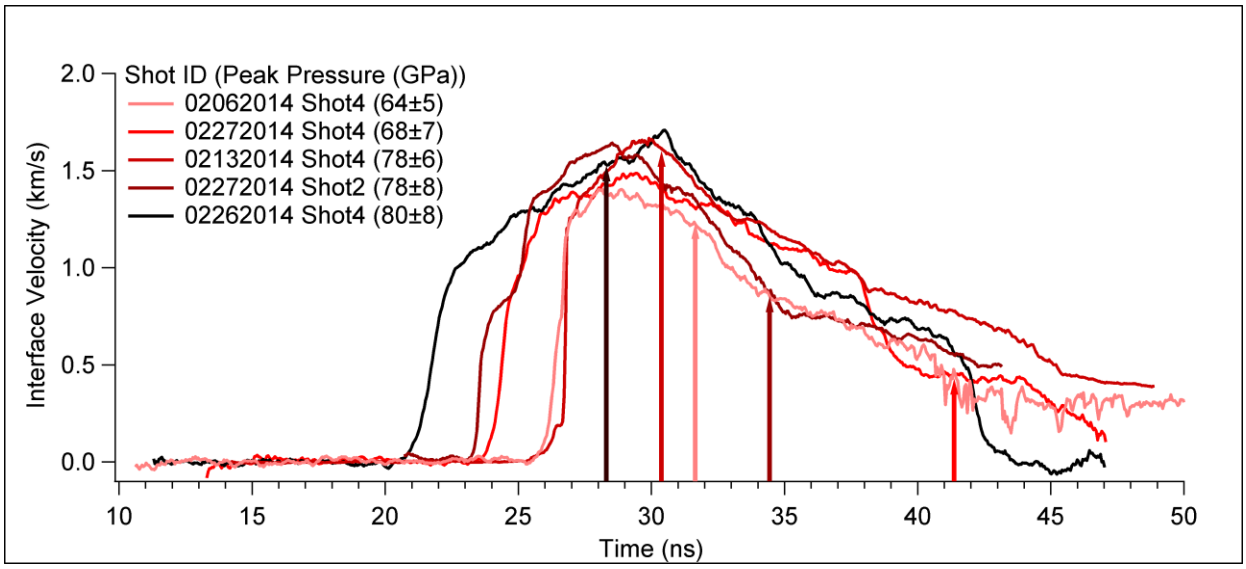

Figure 103 Interface velocity as a function of time for the 2D VISAR data shown below. Vertical lines indicate the 2D VISAR probe delay for each shot.

02132014 Shot4

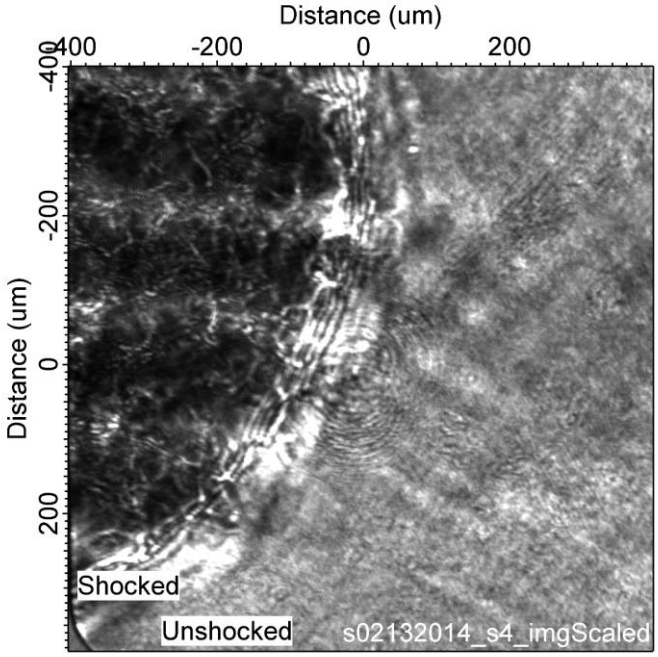

Figure 104 Nonfringing image, LiF-tamped nanodiamond 3.5 ns after breakout. 0.6 mm diameter round phase plate was used. Fringes along the edge of the breakout are due to optical interference between the nanodiamond surface and LiF window.

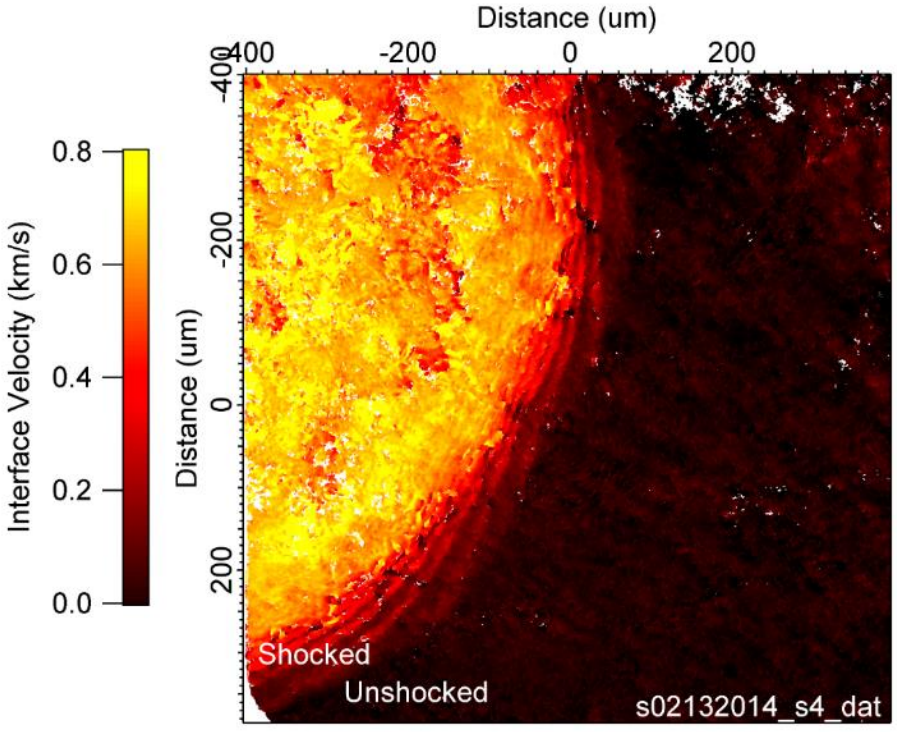

Figure 105 Velocity map, LiF-tamped nanodiamond 3.5 ns after breakout.

02062014 Shot4

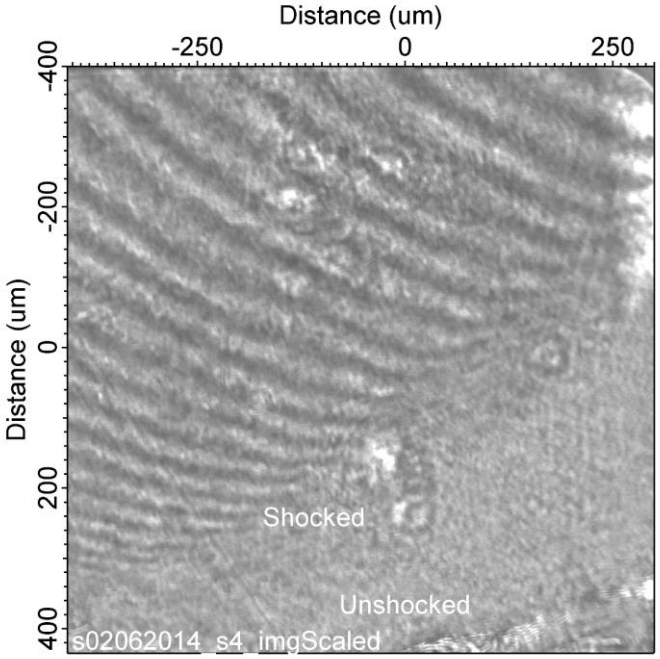

Figure 106 Nonfringing image, LiF-tamped nanodiamond 4.6 ns after breakout. 1 mm square phase plate was used for this shot. Fringes on the upper left half are due to optical interference between the nanodiamond surface and LiF window.

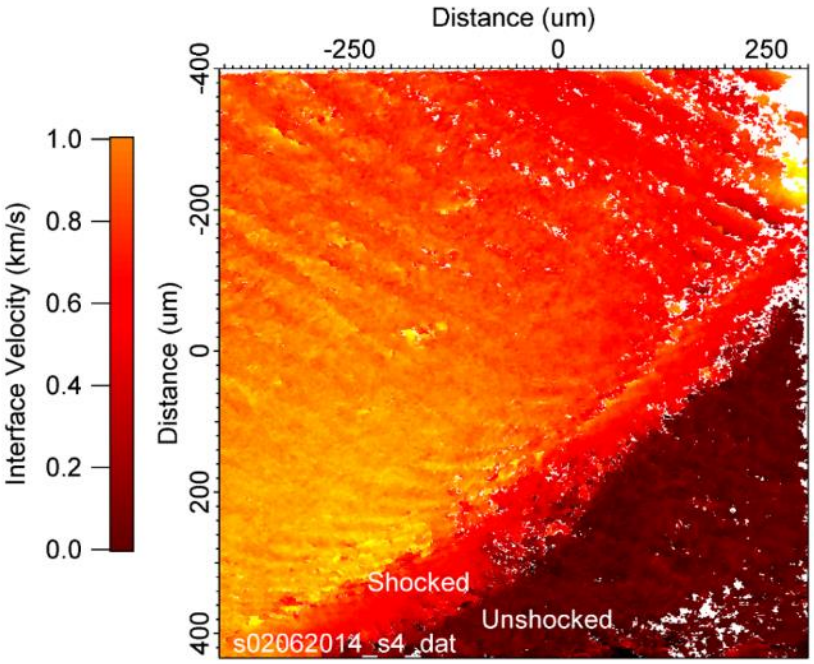

Figure 107 Velocity map, LiF-tamped nanodiamond 4.6 ns after breakout.

02262014 Shot4

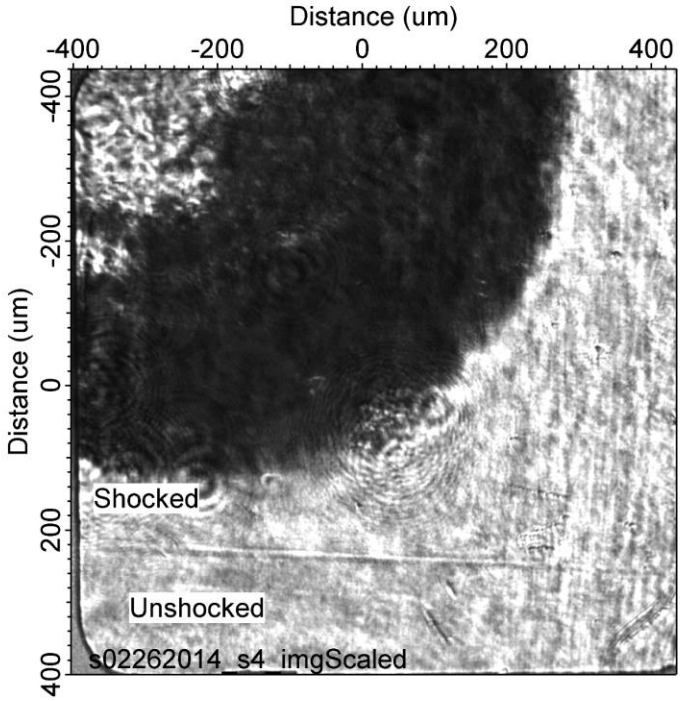

Figure 108 Nonfringing image, LiF-tamped nanodiamond 6.6 ns after breakout. 0.6 mm diameter round phase plate was used for this shot.

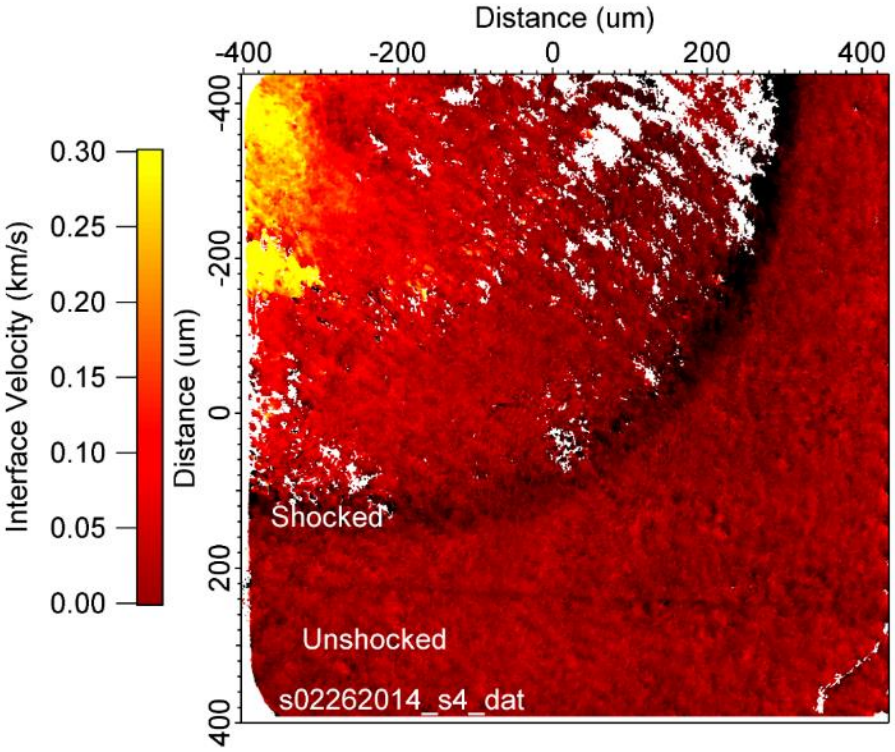

Figure 109 Velocity map, LiF-tamped nanodiamond 6.6 ns after breakout.

02272014 Shot2

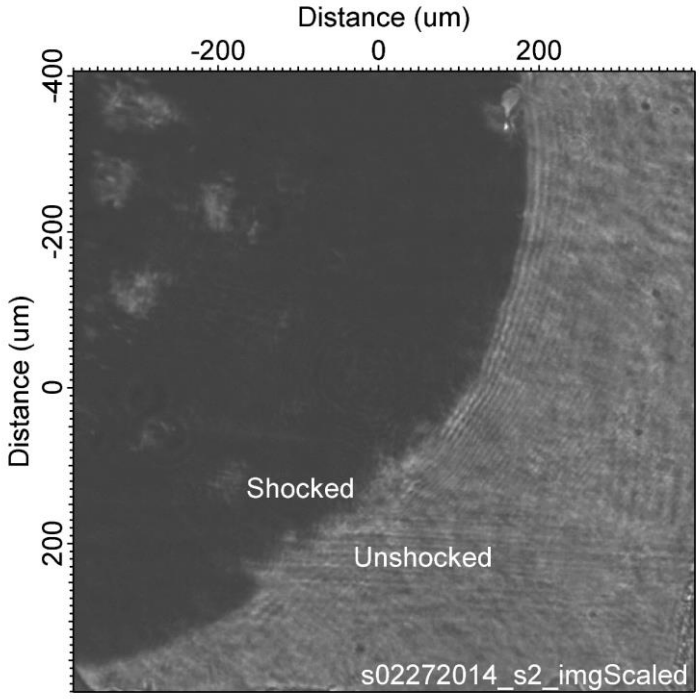

Figure 110 Nonfringing image, LiF-tamped nanodiamond 10.3 ns after breakout. 0.6 mm diameter round phase plate was used for this shot.

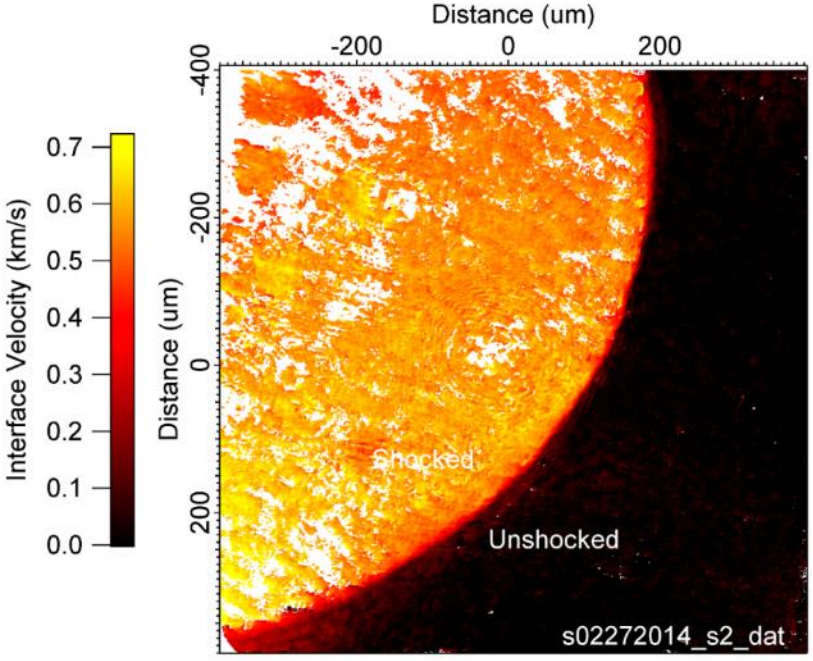

Figure 111 Velocity map, LiF-tamped nanodiamond 10.3 ns after breakout.

02272014 Shot4

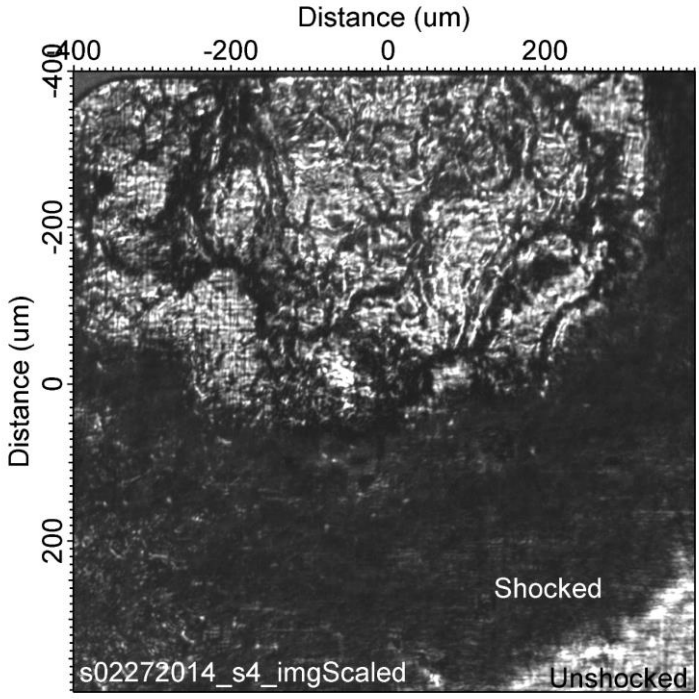

Figure 112 Nonfringing image, LiF-tamped nanodiamond 17.3 ns after breakout. 0.6 mm diameter round phase plate was used for this shot.

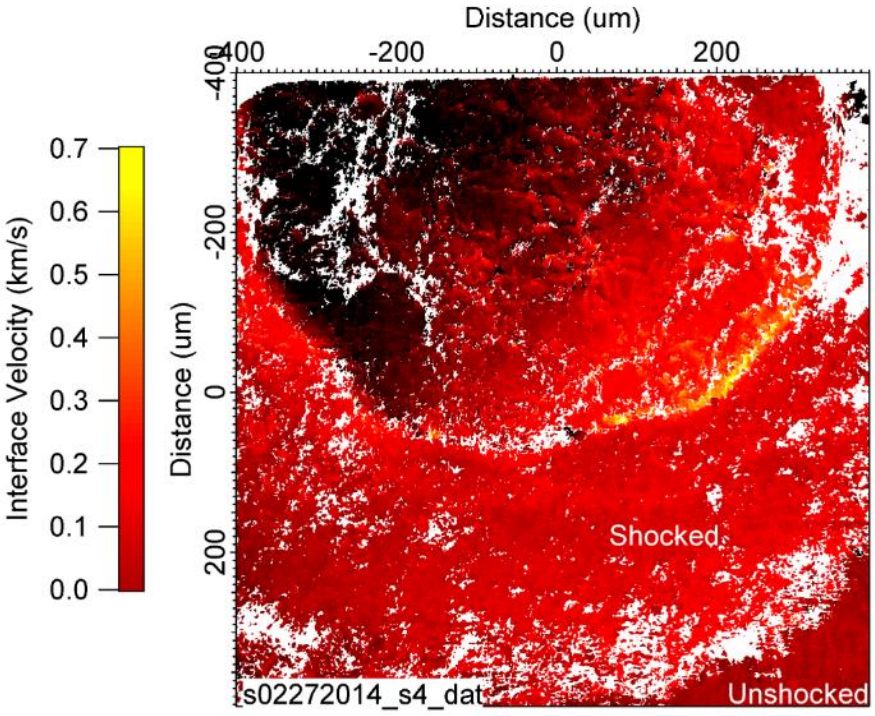

Figure 113 Velocity map, LiF-tamped nanodiamond 17.3 ns after breakout.

Discussion

Theoretical Models for Fracture

Models of dynamic fracture can be loosely divided into two approaches, passive, where the material response remains unchanged until a fracture threshold is reached, and active wherein the material stress-strain relationship is changed as the damage progresses. The simplest approach to modelling dynamic fracture is the passive approach proposed by Griffith [141]. The Griffith model for fracture is an energy based criterion originally derived from the experimental observation that the fracture stress in a sample was dependent on the dimensions of the sample and the discrepancy between the measured fracture stress and the stress derived from the energy required to break an atomic bond. Fracture is initiated in this model when the energy required to extend the crack is equal to the energy resisting the crack. In polycrystalline materials, there are also contributions to the fracture mechanics from grain boundary interactions. For grain sizes above a few microns, grain boundaries between individual crystallites limit plastic flow in by impeding the motion of dislocations and cracks in the bulk material. Dislocations tend to stack at grain boundaries and require additional stress to propagate. As the grain size decreases, the proportion of boundaries increases and the stress required to initiate plasticity and propagate fracture increases.

Any discussion of fracture in shocked materials would be remiss in ignoring the vast contributions to the field made by Grady, whose work on brittle fracture built on Mott's earlier statistical strain-to-fracture models in cylindrical shells and pipe bombs [142-149]. In particular, Grady's energy-balance-based derivation of characteristic fracture plane separation as a function of material properties provides an initial means of quantifying the material fracture [121, 150, 151]. One particular expression for quantifying fracture in brittle materials is relevant here, equation 4.1, which describes the characteristic fracture plane separation, λ, in terms of the material density, ρ, the surface energy per unit area, γ, and the shear strain rate ε. Assuming negligible contributions from hardening effects, the elastic shear rate is zero, the rate of plastic shear is equal to three-quarters the longitudinal strain, which is calculated from the velocity history measured using the VISAR.

$$\lambda = \left\{\frac{48\,\gamma}{\rho\,\dot{\varepsilon}^2}\right\}^{1/3} \qquad 4.1$$

Using approximate values, characteristic fracture sizes can be roughly calculated. For a surface energy of 5.3±0.15, as determined by Field [152], and using the average shear strain rates of $1\pm0.3*10^7$ $s^{-1}$and $3.7\pm0.4*10^7$ s^{-1} for the free surface microcrystalline and nanocrystalline diamond respectively, as well as a density calculated at the pressure behind the observed fracture surface, characteristic fracture spacings of 9±3 μm and 3.8±0.4 μm are obtained. From the nonfringing images shown above, for the strain rates listed above, characteristic fracture spacings for the microdiamond and nanodiamond free surface samples were found to be 57±7 μm, 22±5 μm. For the LiF-tamped microdiamond and nanodiamond samples, measured fracture spacings were found to be 21±4 μm, and

12±3 μm, respectively. Common strain rates for the tamped microdiamond and nanodiamond were $0.9\pm0.3*10^7$ s^{-1} and $1.8\pm0.3*10^7$ s^{-1}, resulting in larger calculated fracture spacings spacings of 9.6±3 μm and 6.0±1 μm. There is order-of-magnitude agreement between the calculated and observed fracture spacings and the difference in the strain rates for the microdiamond and nanodiamond samples result in the appropriate trend in fracture size between the crystallite sizes. Equation 4.1 does underestimate the fracture spacing for all four cases, however, suggesting that this model might be too simple.

Another contribution from Grady relevant to the present discussion is his formulation of the spall-fracture criterion. Grady's brittle-spall criterion is, like his fracture plane-separation model above, an energy-based criterion for which spall occurs when the kinetic energy and elastic energy equal or exceed the fracture energy. Unlike the previous formulation, the elastic energy contribution is considered, as opposed to just the kinetic energy. Assuming fracture into spherical particles of diameter s, the kinetic energy was shown by Grady to be a function of the density, strain rate, and particle size [143]. The coefficient in equation 4.2 changes for differing particle geometries.

$$\text{Kinetic Energy, T} = \frac{\rho \dot{\varepsilon}^2 s^2}{120} \qquad 4.2$$

The elastic energy density is simply the potential energy resulting from the elastic deformation of the material, shown in equation 4.3.

$$\text{Elastic Energy, U} = \frac{P^2}{2\rho c_0^2} \qquad 4.3$$

A secondary requirement for spall given by Grady is the horizon condition. For some volume in the sample, $4\pi/3\ (c_0 t)^3$, where c_0 is the sound speed and t is the time, the length scale over which communication (assumed to defined by the speed of sound in the material) occurs must be less than $c_0 t$. In the case of spherical particle formation, the fragment radius, s/2, would then be less than or equal to $c_0 t$. For some unit volume, the creation of fragments of diameter s would result in the formation of a fracture surface area of 6/s. This new surface area results in the fracture surface energy per unit volume, Γ, as a function of the toughness, K_c, as well as the density, sound speed, and particle diameter.

$$\text{Fracture Energy, } \Gamma = \frac{3K_c^2}{\rho c_0^2 s} \qquad 4.4$$

Assuming a linear tensile loading of the sample, the critical spall stress, at which point instantaneous failure occurs, can be expressed in terms of the strain rate and time. The mean tension in the sample, as a function of strain rate, is shown in equation 4.5

$$P = \rho c_0^2 \dot{\varepsilon} t \qquad 4.5$$

Combining equations 4.3 through 4.5 with the horizon criterion (the kinetic energy term in equation 4.2 is generally neglected due to the small contribution; as a result of the

horizon criterion and equation 4.5, the kinetic energy is equal to or less than one-fifteenth of the elastic energy), expressions for the brittle spall strength, as well as for the characteristic fragment size, are obtained, shown in equation 4.6a and b.[151]

$$P_{spall} = \sqrt[3]{3\rho c_0 K_c^2 \dot{\varepsilon}} \qquad 4.6a$$

$$s = 2(\sqrt{3}K_c/\rho c_0 \dot{\varepsilon})^{2/3} \qquad 4.6b$$

This expression for the fragment size has been experimentally validated by some early experiments and found to predict fracture toughness values ~20% lower than previously measured values. [143]. As discussed above, indentation measurements on bulk polycrystalline diamond suggest a fracture toughness of 5.3 MPa $m^{1/2}$ [153]. Using the Hashin-Shtrikman limits to calculate a sound speed through polycrystalline diamond and the strain rates for the free surface diamond listed above, and considering an initial density somewhere between 95% and 100% of full density, fragment sizes of 11.4±3 μm and 4.8±0.5 μm were found. From the images in the results section, the microdiamond samples appeared to fracture into fragments of size 50-100 microns, with the size increasing somewhat at the edges of the breakout and the nanodiamond samples fracture into fragments of 30-50 microns, with smaller fracture openings. Using the velocity maps, in combination with the nonfringing images, fragment size distributions for each shot could be obtained. The velocity map allowed us to identify the flattest spatial region of the shock and avoid any effects related to the uneven breakout edges. The calculated fragment sizes using previously determined values for the fracture toughness of diamond are too small by a factor of five to ten. Plotting the observed fragment size against the strain rate, as shown in Figure 114, and calculating a best fit line, an approximate value for the observed fracture toughness can be obtained. Using this best fit line, a fracture toughness of 103±14 MPa $m^{1/2}$ was found for the microdiamond and a fracture toughness of 44±8 MPa $m^{1/2}$ was found for the nanodiamond samples. As the line VISAR data obtained for this experiment did not contain clear spall signatures (oscillations in the velocity after breakout due to the shock wave reverberating in the spall layer), no direct measurements of the spall strength were obtained. Equation 4.6b, however, allows us to use the updated values for the fracture toughness to calculate a strain dependent spall stress for micro- and nanocrystalline diamond. This calculated spall stress over the strain rate region of interest is shown in Figure 115. Interestingly, although the fracture toughness values are dramatically larger than previous literature values, the spall stress obtained using those values agrees reasonably well with diamond spall data. Abrosimov et al. found a maximum diamond spall stress of 16.5 GPa, although they considered multiple types of polycrystalline diamond without distinction [154].

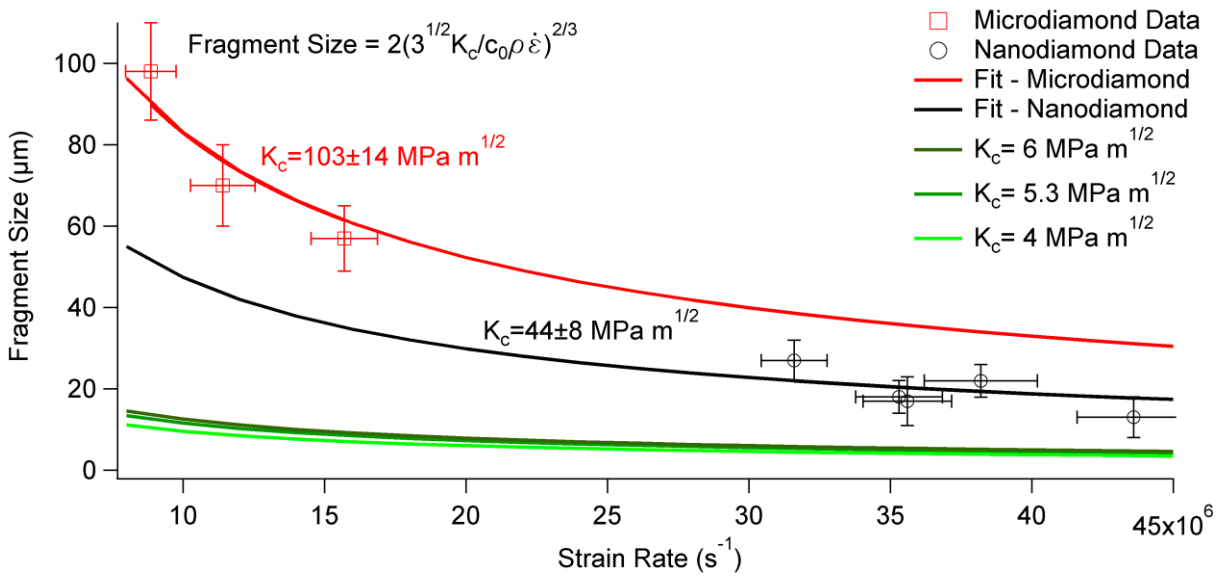

Figure 114 Fragment size as a function of strain rate for free surface microcrystalline and nanocrystalline diamond. Best fit lines to equation 4.6b are shown, along with fragment size vs. strain rate for three previously obtained values of fracture toughness.

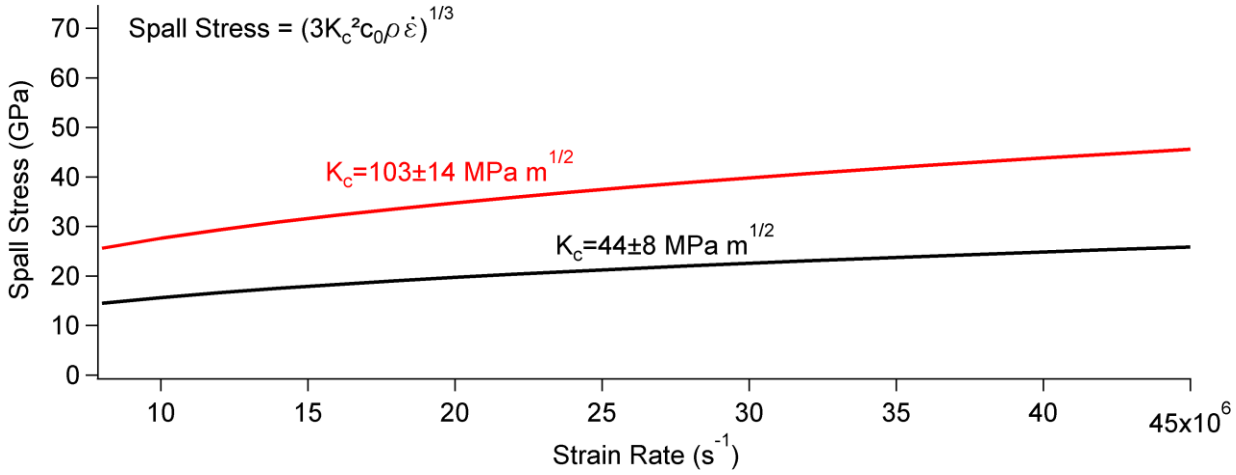

Figure 115 Spall stress as a function of strain rate calculated using equation 4.6b for the microdiamond and nanodiamond fracture toughness.

Velocity Roughness and Characteristic Length

Characteristic length scales and roughness in the velocity response of the crystals can be observed by calculating the velocity spectral density in each deformation region on the 2D-VISAR obtained velocity map. The velocity spectral density is calculated as described in reference [91] over a frequency interval of 0.005 to 0.5 μm^{-1} (a spatial interval of 200 to 2 μm). A Hanning window was applied to the box to reduce noise resulting from edge effects, and a selection of box sizes and dimensions, as well as round regions were used to calculate the velocity density in order to eliminate any features resulting from the selection region. Error bars for the velocity density were calculated using the standard deviation of the values within each radial bin.

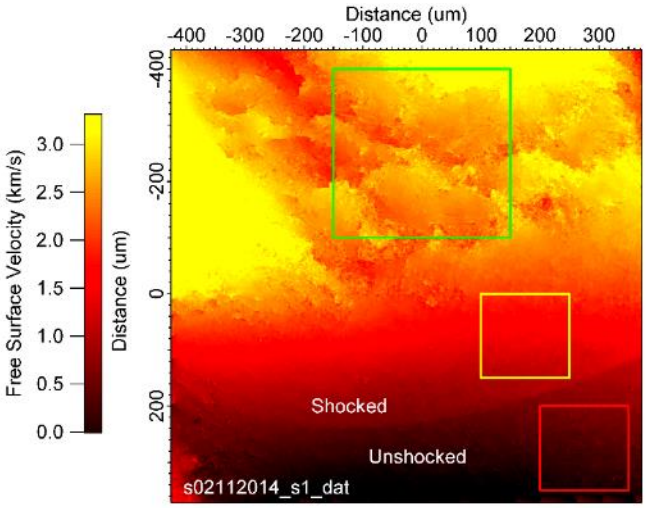

Figure 116 Velocity map from the 2D VISAR with velocity spectral density regions indicated. Azimuthally averaged spectral density is shown in Figure 117

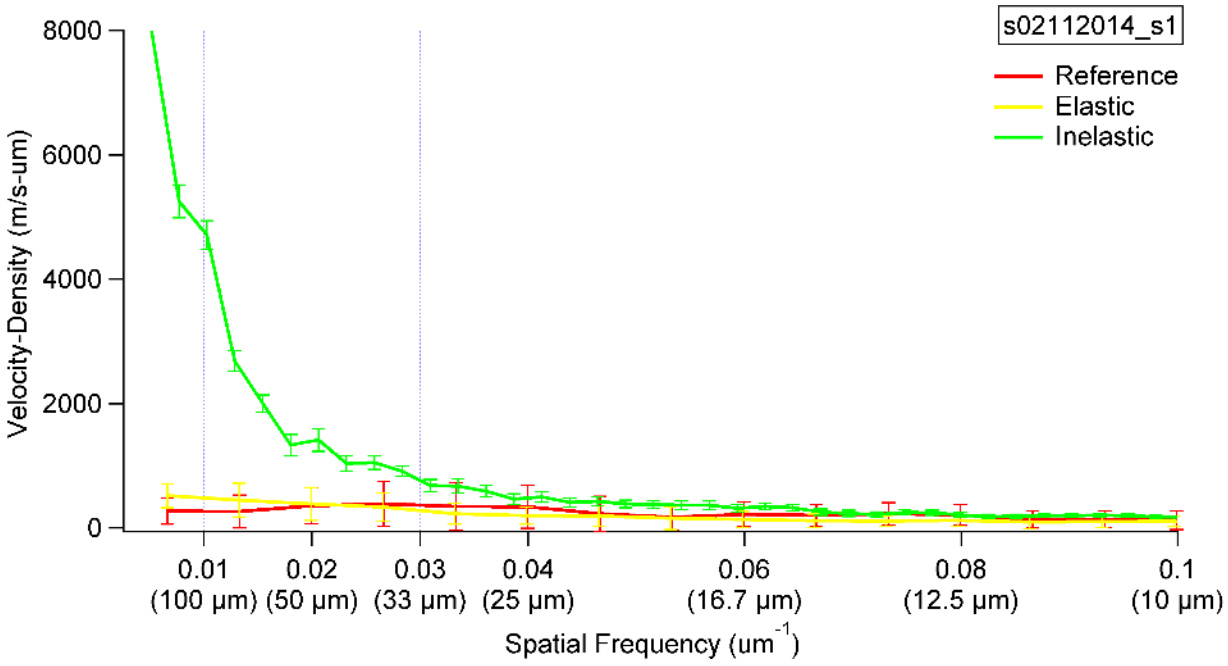

Figure 117 Calculated velocity spectral density for the regions indicated in Figure 116.

An example of results from such a calculation can be found in Figure 117. The regions over which the velocity spectral density is calculated are indicated in Figure 116 by colored squares. The red square is the uncompressed region of the sample, while the yellow and

green squares are the elastic precursor and inelastic region, respectively. In the region where the diamond is elastically deformed, there is good overlap with the uncompressed region, as would be expected from planar, uniaxial compression. Over the inelastically deformed region, the fracture and roughening of the diamond surface translates in velocity space to a greater power over the frequency range shown. This structure was also observed for the spherically driven samples in the previous chapter, but is more pronounced in the planar drive geometry due to overlap of adjacent slip bands.

For each of the four target types (micro- and nanodiamond, free surface and windowed), the velocity spectral density was calculated over three regions. The results from the inelastically deformed regions at various 2D-VISAR probe delays are shown in Figure 118, through Figure 121. In all cases an increase in the power is observed, especially at low spatial frequencies. Interestingly, there is a small peak in the velocity density of the free surface nanodiamond samples in Figure 119 at approximately 40 μm. Fragment sizes based on the nonfringing images were found to be between 27 and 13 μm, so the origin of this peak is unclear. No such peak is observed for microcrystalline diamond in Figure 118, which may mean that the peak is at too small a spatial frequency (too large a spatial size) to be determined.

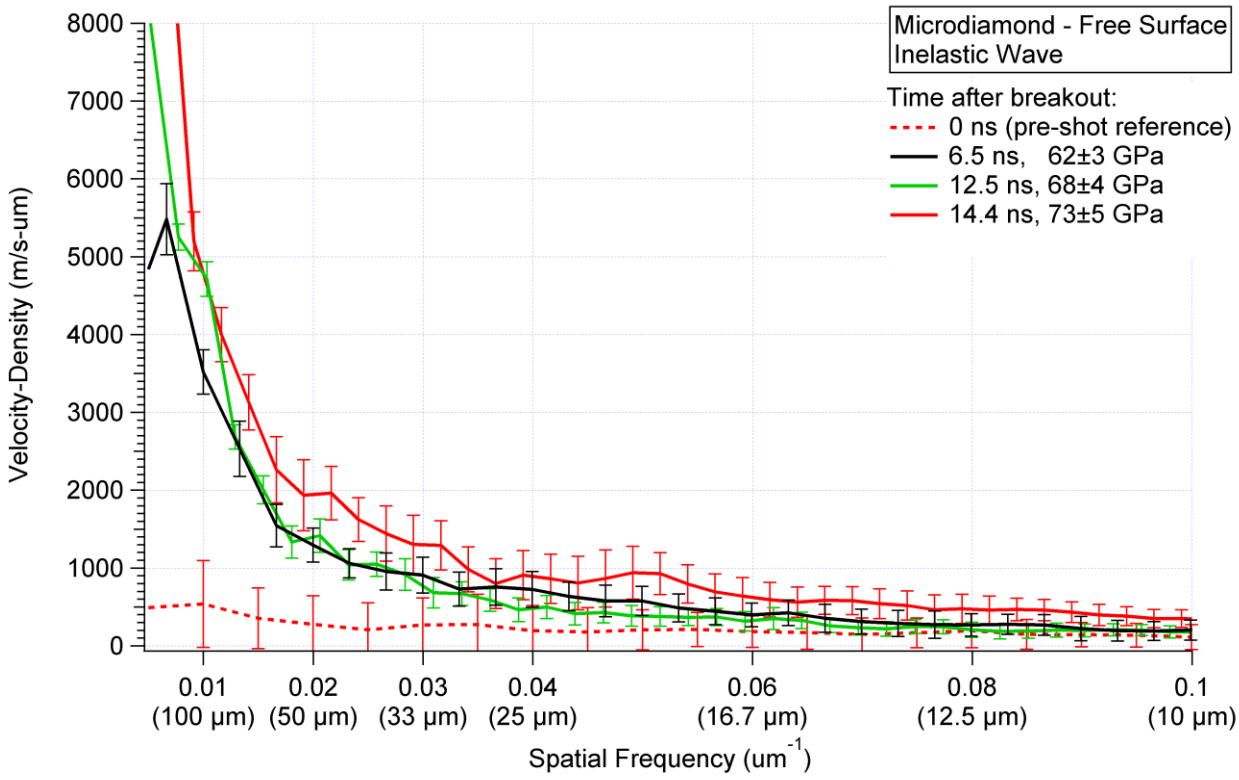

Figure 118 Velocity spectral density calculated for the inelasticly deformed region of the microdiamond surface. An overall increase in the power is observed, with no significant features. A possible feature at 50 microns, the grain size for the microcrystalline samples, may be present at late times, but is within the error.

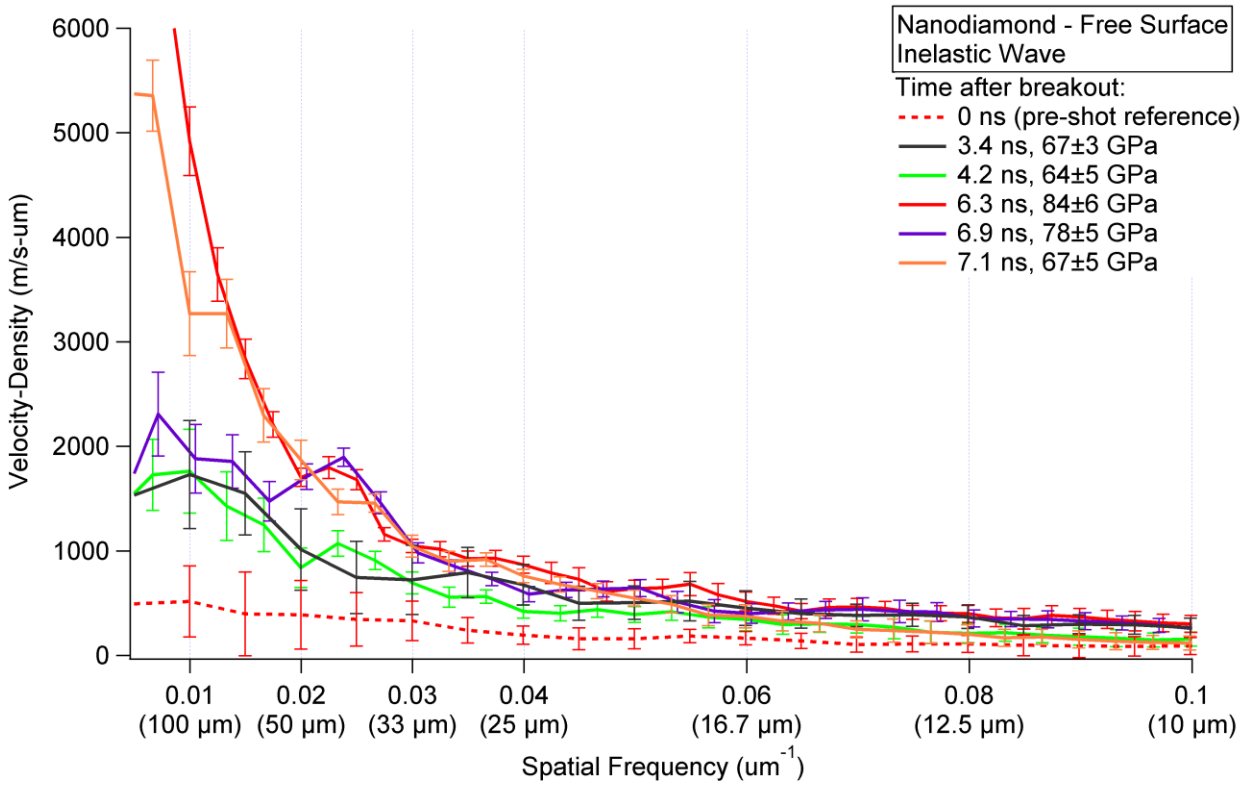

Figure 119 Velocity spectral density calculated for the inelasticly deformed region of the nanodiamond surface. An overall increase in the power is observed, with a feature at approximatly 40 microns observed after 4 ns.

No peaks were consistently observed in the velocity spectral density of the LiF-tamped samples, as shown in Figure 120 and Figure 121. The uncertainty was higher, particularly for the nanodiamond samples, so it is more difficult to identify peaks.

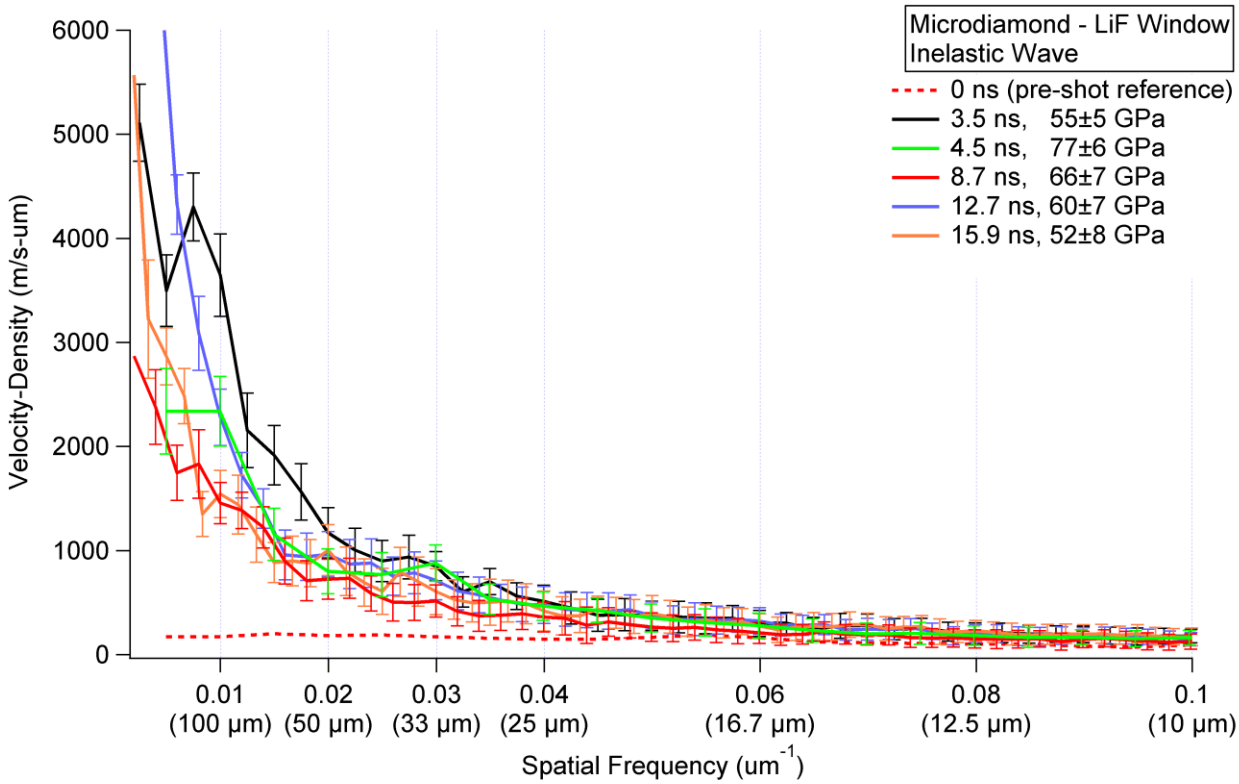

Figure 120 Velocity spectral density calculated for the inelasticly deformed region of the microdiamond-lithium floride interface. An overall increase in the power is observed, with no significant features with the exception of a peak at the earliest time (3.5 ns) at approximately 150 microns. As this is close to the size of the length of the area over which the velocity spectral density is calculated and only appears in one trace, it is unclear whether it is meaningful.

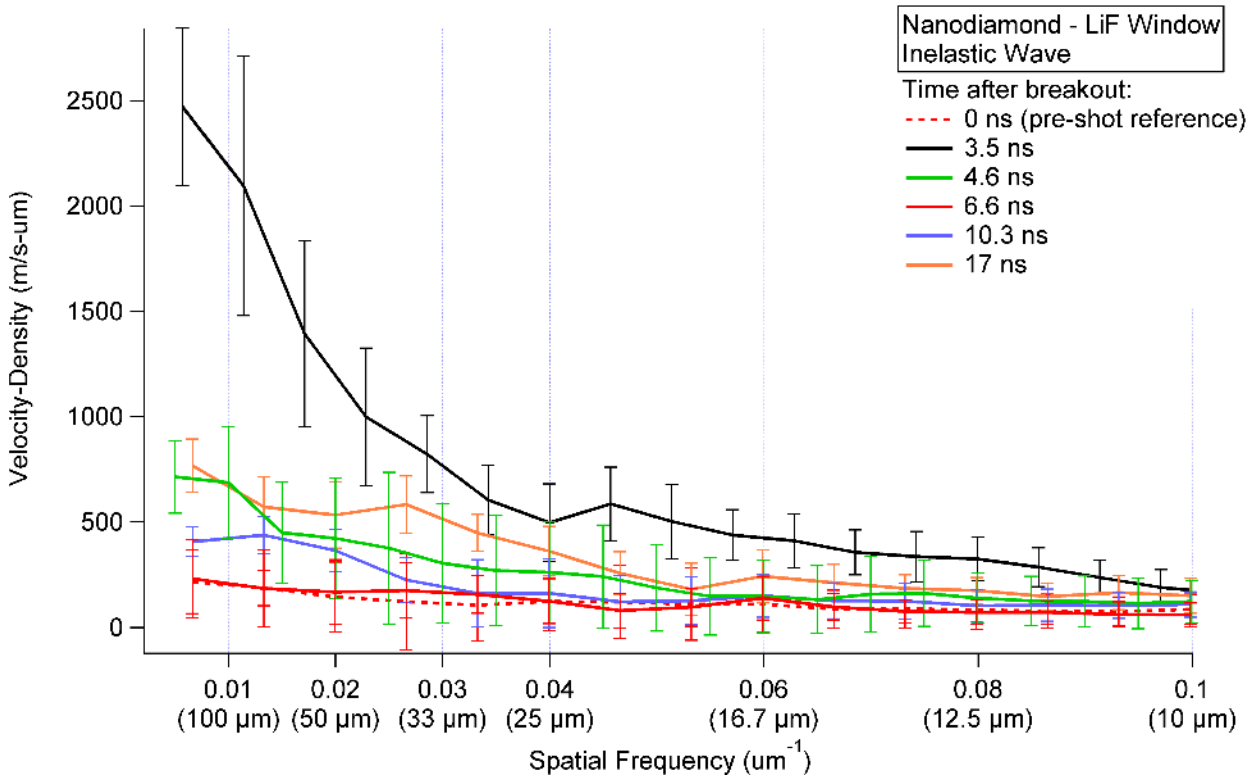

Figure 121 Velocity spectral density calculated for the inelasticly deformed region of the nanodiamond-lithium floride interface. An overall increase in the power is observed, with no significant features. The larger error values in for these calculations relative to the other velocity spectral density calculations is related to the loss of reflectivity at the interface.

Comparing the time evolution of the rms velocity of the four sample types, as shown in Figure 122, it is clear that there is a similar trend for the free surface micro- and nanodiamond and the windowed micro- and nanodiamond. The windowed samples show an initial sharp increase at early time and then decay back down while the free surface samples both increase in velocity density as a function of time. The free surface samples are spalling into the vacuum over the time sequence, expanding and increasing the surface roughness. The windowed targets, however, are still confined after breakout, allowing for continued comminution as the shock and rarefaction waves transit the sample. The windowed and free surface microdiamond samples show a larger increase in velocity density than the nanodiamond. The smaller grains in the nanodiamond sample contain fewer slip systems and a larger fraction of grain boundaries and will not, therefore, be expected to increase in roughness as much as the larger grained microdiamond Plastic deformation will tend to result in less roughness than fracture.

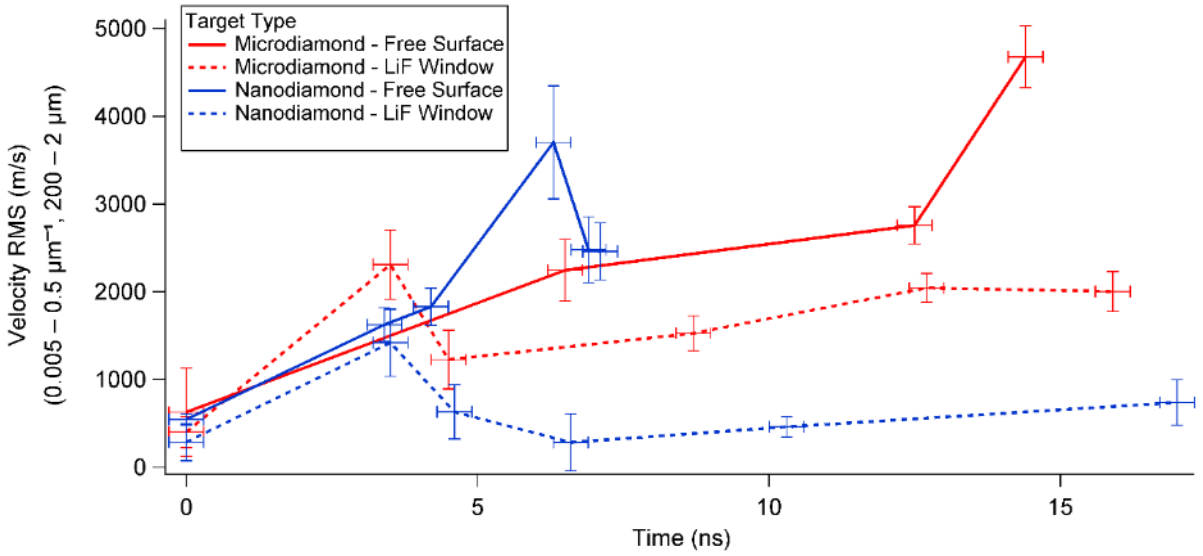

Figure 122 Velocity rms over 0.005 – 0.5 μm^{-1} (spatial range of 200 - 2 μm) at each probe delay for the four target types. Velocities are free surface for the untamped samples and interface for the LiF-tamped samples to aid in comparison to the results section above. Plot range for previous plots is 0.005-0.1. As there are no features from 0.1-0.5 μm^{-1}, data in that region is now shown in the figures above, however the velocity spectral density was calculated for the full range given above. 0.005 μm^{-1} corresponds to the largest spatial box that the spectral density can be calculated over, and 0.5 μm^{-1} corresponds to the limit of our resolution.

Conclusions

We have imaged and obtained velocity maps of deformation and fracture in microcrystalline and nanocrystalline diamond. We found an increased degree of velocity roughness in the tamped microdiamond samples in comparison with the tamped nanodiamond. This is commensurate with the nanodiamond samples containing fewer slip systems and more grain boundaries, impeding dislocation motion. For dynamic fracture where failure is a result of the propagation of micro-cracks, it becomes increasingly difficult to consider individual cracks and model the failure of the material. In order to accurately model the fracture behavior under shock compression, the Grady spall fracture model was used and we obtained values for the fracture toughness of the micro- and nanocrystalline diamond of 103±14 MPa $m^{1/2}$ and 44±8 MPa $m^{1/2}$, respectively. Using these values for the fracture toughness, the strain rate dependent spall stresses were calculated and found to agree with previous research.

Future Work

Initial results suggest clear trends in the inelastic deformation and fracture of diamond and further work can be readily proposed based on this research. The primary limitations in this work are related to laser drive energy and flatness, both of which can be addressed by proposing a similar sequence of shock compression experiments on a laser facility such

as OMEGA, which can produce considerably more energy than JLF. Breakout flatness can be significantly improved by moving away from a direct drive system that is highly dependent on the quality of the phase plates and toward a halfraum style target, as shown in Figure 123.

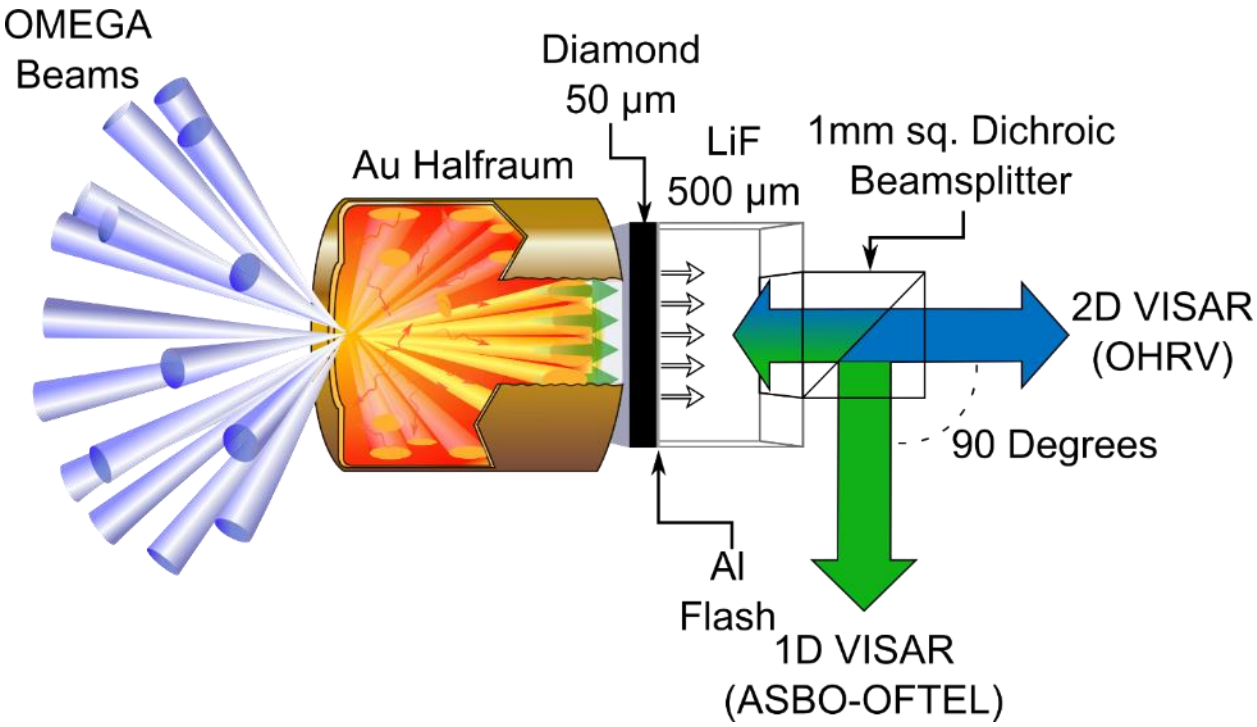

Figure 123 Proposed target design for an experiment at the OMEGA laser facility.

It would also be interesting to repeat the experiment with an aluminized diamond window, instead of the LiF window. Removing the impedance mismatch would prevent the reflected release wave which generates tension at the diagnostic surface. It would then be possible to observe purely compressional deformation and determine at what pressure fracture occurs without tension.

References

1. Zallen, R. and W. Paul, *Band Structure of Gallium Phosphide from Optical Experiments at High Pressure.* Physical Review a-General Physics, 1964. **134**(6A): p. 1628-&.
2. Minomura, S. and H.G. Drickamer, *Pressure Induced Phase Transitions in Silicon, Germanium and Some 3-5 Compounds.* Journal of Physics and Chemistry of Solids, 1962. **23**(May): p. 451-&.
3. Nelmes, R.J., et al., *Structural Studies of Iii-V and Group-Iv Semiconductors at High-Pressure.* Journal of Physics and Chemistry of Solids, 1995. **56**(3-4): p. 539-543.
4. Trappeni.Nj and R. Vetter, *High-Resolution Measurement of Germanium Absorption-Edge under Pressure.* Physica, 1972. **60**(1): p. 235-&.
5. Paul, W., *Band Structure of Intermetallic Semiconductors from Pressure Experiments.* Journal of Applied Physics, 1961. **32**: p. 2082-&.
6. Abid, H., et al., *Pressure-Dependence of Band-Gaps in Gaas, Gap, Inp, and Inas.* Materials Chemistry and Physics, 1994. **38**(2): p. 162-168.
7. Harris, P., *Band-Gap Collapse in Uniaxially Strained (Shocked) Elastic Germanium.* Journal of Applied Physics, 1980. **51**(11): p. 6033-6034.
8. Barker, L.M. and R.E. Hollenbach, *Laser Interferometer for Measuring High Velocities of Any Reflecting Surface.* Journal of Applied Physics, 1972. **43**(11): p. 4669-&.
9. Barker, L.M. and R.E. Hollenbach, *Shock-Wave Study of Alpha Reversible Epsilon-Phase Transition in Iron.* Journal of Applied Physics, 1974. **45**(11): p. 4872-4881.
10. Spaulding, D.K., et al., *New optical diagnostics for equation of state experiments on the Janus laser.* Shock Compression of Condensed Matter - 2007, Pts 1 and 2, 2007. **955**: p. 1071-1074.
11. Svendsen, B., J.D. Bass, and T.J. Ahrens, *Optical Radiation from Shock-Compressed Materials and Interfaces.* Physics Reports-Review Section of Physics Letters, 1989. **180**(6): p. 333-416.
12. Demtröder, W., *Laser Spectroscopy*: Springer.
13. Stevens, G.D., et al., *Reflectance changes during shock-induced phase transformations in metals.* Review of Scientific Instruments, 2010. **81**(6).
14. Stevens, G.D., et al., *Optical response of cerium-doped lutetium oxyorthosilicate coatings at shocked surfaces.* Review of Scientific Instruments, 2004. **75**(2): p. 462-466.
15. Seifter, A., et al., *Emissivity measurements of shocked tin using a multi-wavelength integrating sphere.* Journal of Applied Physics, 2011. **110**(9).
16. Turley, W.D., et al., *Infrared emissivity of tin upon release of a 25 GPa shock into a lithium fluoride window.* Journal of Applied Physics, 2011. **110**(10).
17. La Lone, B.M., et al., *Release path temperatures of shock-compressed tin from dynamic reflectance and radiance measurements.* Journal of Applied Physics, 2013. **114**(6).
18. Dolan, D.H., T. Ao, and C.T. Seagle, *Reflectance Thermometry in Dynamic Compression Experiments.* Temperature: Its Measurement and Control in Science and Industry, Vol 8, 2013. **1552**: p. 767-770.

19. Alfano, R.R., *The supercontinuum gains momentum.* Laser Focus World, 2005. **41**(5): p. 83-86.
20. Alfano, R.R. and S.L. Shapiro, *Continuous Emission in Region 4000 to 7000 a Via 4-Photon Coupling in Glass.* Bulletin of the American Physical Society, 1970. **15**(4): p. 506-&.
21. Alfano, R.R. and S.L. Shapiro, *Observation of Self-Phase Modulation and Small-Scale Filaments in Crystals and Glasses.* Physical Review Letters, 1970. **24**(11): p. 592-&.
22. McGrane, S.D., D.S. Moore, and D.J. Funk, *Ultrafast spectroscopy and interferometry of laser shocked thin films: practical considerations.* High-Power Laser Ablation V, Pts 1 and 2, 2004. **5448**: p. 165-170.
23. Moore, D.S., S.D. McGrane, and D.J. Funk, *Ultrafast infrared absorption and dynamic ellipsometry of shock-compressed energetic materials.* Abstracts of Papers of the American Chemical Society, 2004. **227**: p. U316-U316.
24. McGrane, S.D., et al., *Molecular Shock Response of Explosives: Electronic Absorption Spectroscopy.* Shock Compression of Condensed Matter - 2009, Pts 1 and 2, 2009. **1195**: p. 1301-1304.
25. McGrane, S.D., et al., *Ultrafast Dynamic Ellipsometry And Spectroscopy Of Laser Shocked Materials.* International Symposium on High Power Laser Ablation 2010, 2010. **1278**: p. 392-400.
26. Brown, K.E., et al., *Ultrafast Chemical Reactions in Shocked Nitromethane Probed with Dynamic Ellipsometry and Transient Absorption Spectroscopy.* Journal of Physical Chemistry A, 2014. **118**(14): p. 2559-2567.
27. Dang, N.C., et al., *Shock Induced Chemistry In Liquids Studied With Ultrafast Dynamic Ellipsometry And Visible Transient Absorption Spectroscopy.* Journal of Physical Chemistry A, 2012. **116**(42): p. 10301-10309.
28. Nelmes, R.J., et al., *Imma phase of germanium at similar to 80 GPa.* Physical Review B, 1996. **53**(6): p. R2907-R2909.
29. Celliers, P.M., et al., *Line-imaging velocimeter for shock diagnostics at the OMEGA laser facility.* Review of Scientific Instruments, 2004. **75**(11): p. 4916-4929.
30. Manassah, J.T., R.R. Alfano, and M. Mustafa, *Spectral Distribution of an Ultrafast Supercontinuum Laser Source.* Physics Letters A, 1985. **107**(7): p. 305-309.
31. Manassah, J.T., et al., *Ultrafast Supercontinuum Laser Source.* Photonics Spectra, 1984. **18**(11): p. 53-&.
32. Manassah, J.T., et al., *Induced Supercontinuum and Steepening of an Ultrafast Laser-Pulse.* Physics Letters A, 1985. **113**(5): p. 242-247.
33. Manassah, J.T., et al., *Spectral Extent and Pulse Shape of the Supercontinuum for Ultrashort Laser-Pulse.* Ieee Journal of Quantum Electronics, 1986. **22**(1): p. 197-204.
34. Alfano, R.R. and S.L. Shapiro, *Emission in Region 4000 to 7000 a Via 4-Photon Coupling in Glass.* Physical Review Letters, 1970. **24**(11): p. 584-&.
35. Gex, F., et al., *S1-Photocathode Image Converter Tubes.* Proceedings of the Society of Photo-Optical Instrumentation Engineers, 1985. **491**: p. 276-280.
36. Jaanimagi, P.A., et al., *The streak camera development program at LLE.* 26th International Congress on High Speed Photography and Photonics, 2005. **5580**: p. 408-415.

37. Brooks, R.J., et al., *Experimental data on the reflection and transmission spectral response of photocathodes - art. no. 666013.* Infrared Systems and Photoelectronic Technology Ii, 2007. **6660**: p. 66013-66013.
38. Hebbache, M., *Elastic Phase-Transition in Germanium and Silicon.* Physical Review B, 1994. **49**(10): p. 6522-6527.
39. Graham, R.A., O.E. Jones, and J.R. Holland, *Physical Behavior of Germanium under Shock Wave Compression.* Journal of Physics and Chemistry of Solids, 1966. **27**(9): p. 1519-&.
40. Graham, R.A., O.E. Jones, and J.R. Holland, *Shock-Wave Compression of Germanium from 20 to 140 Kbar.* Journal of Applied Physics, 1965. **36**(12): p. 3955-&.
41. Gust, W.H. and E.B. Royce, *Axial Yield Strengths and Phase-Transition Stresses for (100), (110), and (111) Germanium.* Journal of Applied Physics, 1972. **43**(11): p. 4437-&.
42. Baldini, M., et al., *High-pressure EXAFS measurements of crystalline Ge using nanocrystalline diamond anvils.* Physical Review B, 2011. **84**(1).
43. Lane, J.M.D. and A.P. Thompson, *Molecular Dynamics Simulation of Shock-Induced Phase Transition in Germanium.* Shock Compression of Condensed Matter - 2009, Pts 1 and 2, 2009. **1195**: p. 1157-1160.
44. Godby, R.W., M. Schluter, and L.J. Sham, *Accurate Exchange-Correlation Potential for Silicon and Its Discontinuity on Addition of an Electron.* Physical Review Letters, 1986. **56**(22): p. 2415-2418.
45. Remediakis, I.N. and E. Kaxiras, *Band-structure calculations for semiconductors within generalized-density-functional theory.* Physical Review B, 1999. **59**(8): p. 5536-5543.
46. Hedin, L., *Effect of Electron Correlation on Band Structure of Solids.* Arkiv for Fysik, 1965. **30**(3): p. 231-+.
47. Hedin, L., *New Method for Calculating 1-Particle Greens Function with Application to Electron-Gas Problem.* Physical Review, 1965. **139**(3A): p. A796-+.
48. Chen, X.J., et al., *Band structures of II-VI semiconductors using Gaussian basis functions with separable ab initio pseudopotentials: Application to prediction of band offsets.* Physical Review B, 1996. **53**(3): p. 1377-1387.
49. Gerosa, M., et al., *Electronic structure and phase stability of oxide semiconductors: Performance of dielectric-dependent hybrid functional DFT, benchmarked against GW band structure calculations and experiments.* Physical Review B, 2015. **91**(15).
50. Ali, S.J., et al., *Development of a broadband reflectivity diagnostic for laser driven shock compression experiments.* Review of Scientific Instruments, 2015. **86**(4): p. 043112.
51. Pavlovskii, M.N., *Formation of Metallic Modifications of Germanium and Silicon under Shock Loading.* Soviet Physics Solid State,Ussr, 1968. **9**(11): p. 2514-&.
52. Hanfland, M., et al., *Optical-Properties of High-Pressure Metallic Phases of Si and Ge.* Semiconductor Science and Technology, 1989. **4**(4): p. 250-251.
53. Aspnes, D.E. and A.A. Studna, *Dielectric Functions and Optical-Parameters of Si, Ge, Gap, Gaas, Gasb, Inp, Inas, and Insb from 1.5 to 6.0 Ev.* Physical Review B, 1983. **27**(2): p. 985-1009.
54. Hanfland, M., et al., *Optical-Properties of Metallic Silicon.* Physical Review B, 1988. **38**(18): p. 12864-12867.

55. Zallen, R. and W. Paul, *Effect of Pressure on Interband Reflectivity Spectra of Germanium and Related Semiconductors.* Physical Review, 1967. **155**(3): p. 703-&.
56. Gaal-Nagy, K., P. Pavone, and D. Strauch, *Ab initio study of the beta-tin -> Imma -> sh phase transitions in silicon and germanium.* Physical Review B, 2004. **69**(13).
57. Trappeniers, N.J. and R. Vetter, *High-Resolution Measurement of Germanium Absorption-Edge under Pressure.* Physica, 1972. **60**(1): p. 235-&.
58. Massidda, S. and A. Baldereschi, *Electron-Density Distribution in Diamond, Silicon and Germanium under High-Pressure.* Solid State Communications, 1985. **56**(5): p. 431-434.
59. Cardona, M., *Phonon widths versus pressure.* High Pressure Research, 2004. **24**(1): p. 17-23.
60. Mujica, A., et al., *Comparative study of novel structures in silicon and germanium.* Physica Status Solidi B-Basic Research, 2001. **223**(2): p. 379-384.
61. Mujica, A., et al., *High-pressure phases of germanium.* Journal of Physics-Condensed Matter, 2001. **13**(1): p. 35-42.
62. Menoni, C.S., J.Z. Hu, and I.L. Spain, *Germanium at High-Pressures.* Physical Review B, 1986. **34**(1): p. 362-368.
63. Crain, J., et al., *Tetrahedral Structures and Phase-Transitions in Iii-V Semiconductors.* Physical Review B, 1994. **50**(12): p. 8389-8401.
64. Bates, C.H., F. Dachille, and R. Roy, *High-Pressure Transitions of Germanium and a New High-Pressure Form of Germanium.* Science, 1965. **147**(3660): p. 860-&.
65. Bates, C.H., F. Dachille, and R. Roy, *A New High Pressure Body-Centered-Cubic Phase of Germanium.* American Ceramic Society Bulletin, 1965. **44**(4): p. 297-&.
66. Gaal-Nagy, K. and D. Strauch, *Phonons in the beta-tin, Imma, and sh phases of silicon from ab initio calculations.* Physical Review B, 2006. **73**(1).
67. Paul, W.W., D. M., *The Role of Pressure in Semiconductor Research*, in *Solids Under Pressure*, W.W. Paul, D. M., Editor 1963, McGraw-Hill Book Company, Inc. p. 179-243.
68. Cronskar, M., M. Backstrom, and L.E. Rannar, *Production of customized hip stem prostheses - a comparison between conventional machining and electron beam melting (EBM).* Rapid Prototyping Journal, 2013. **19**(5): p. 365-372.
69. Emmelmann, C., et al., *Laser Additive Manufacturing of Modified Implant Surfaces with Osseointegrative Characteristics.* Lasers in Manufacturing 2011: Proceedings of the Sixth International Wlt Conference on Lasers in Manufacturing, Vol 12, Pt A, 2011. **12**: p. 375-384.
70. Giannatsis, J. and V. Dedoussis, *Additive fabrication technologies applied to medicine and health care: a review.* International Journal of Advanced Manufacturing Technology, 2009. **40**(1-2): p. 116-127.
71. Hotza, D., *Rapid prototyping of Solid Oxide Fuel Cells.* Materia-Rio De Janeiro, 2009. **14**(4): p. 1101-1113.
72. Bakas, M. and H. Chu, *Pressureless Reaction Sintering of Alon Using Aluminum Orthophosphate as a Transient Liquid Phase.* Advances in Ceramic Armor V, 2010. **30**(5): p. 213-223.
73. Johnson, A., G.A. Bingham, and D.I. Wimpenny, *Additive manufactured textiles for high-performance stab resistant applications.* Rapid Prototyping Journal, 2013. **19**(3): p. 199-207.

74. Zhitnyuk, S.V., N.A. Makarov, and T.V. Guseva, *New Silicon Carbide Based Ceramic Armor Materials.* Glass and Ceramics, 2014. **71**(1-2): p. 6-9.
75. Buswell, R.A., et al., *Freeform construction: Mega-scale rapid manufacturing for construction.* Automation in Construction, 2007. **16**(2): p. 224-231.
76. Craveiro, F., H. Bartolo, and P. Bartolo, *Functionally Graded Structures through Building Manufacturing.* Advanced Materials and Engineering Materials Ii, 2013. **683**: p. 775-778.
77. Lim, S., et al., *Developments in construction-scale additive manufacturing processes.* Automation in Construction, 2012. **21**: p. 262-268.
78. Loomis, E., et al., *Bump evolution driven by the x-ray ablation Richtmyer-Meshkov effect in plastic inertial confinement fusion Ablators.* Ifsa 2011 - Seventh International Conference on Inertial Fusion Sciences and Applications, 2013. **59**.
79. Zhou, Y., et al., *Progress in understanding turbulent mixing induced by Rayleigh-Taylor and Richtmyer-Meshkov instabilities.* Physics of Plasmas, 2003. **10**(5): p. 1883-1896.
80. Galmiche, D. and C. Cherfils, *Hydrodynamic stability of indirect-drive targets.* Laser Interaction with Matter, 2003. **5228**: p. 28-32.
81. Haines, B.M., F.F. Grinstein, and J.R. Fincke, *Three-dimensional simulation strategy to determine the effects of turbulent mixing on inertial-confinement-fusion capsule performance.* Physical Review E, 2014. **89**(5).
82. Hoffman, N.M. and D.C. Swift, *Predictions of the microstructural contribution to instability seeding in beryllium ICF capsules.* Shock Compression of Condensed Matter - 2003, Pts 1 and 2, Proceedings, 2004. **706**: p. 1339-1342.
83. Durham, W.B., et al., *New developments in deformation experiments at high pressure.* Plastic Deformation of Minerals and Rocks, 2002. **51**: p. 21-49.
84. Buehler, M.J., et al., Phys. Rev. Letts., 2007. **99**: p. 165502.
85. Perez, R. and P. Gumbsch, Phys. Rev. Letts., 2000. **84**: p. 5347.
86. Swadener, J.G., M.I. Baskes, and M. Nastasi, Phys. Rev. Letts., 2002. **89**: p. 085503-1.
87. Celliers, P.M. and etal., Rev. Sci. Inst., 2010. **81**: p. 035101.
88. McWilliams, R.S. and etal, Phys. Rev. B, 2010. **81**: p. 014111.
89. Celliers, P.M., et al., *A high-resolution two-dimensional imaging velocimeter.* Review of Scientific Instruments, 2010. **81**(3).
90. Brugger, K., *Pure Modes for Elastic Waves in Crystals.* Journal of Applied Physics, 1965. **36**(3): p. 759-768.
91. Smith, R.F., et al., *Heterogeneous flow and brittle failure in shock-compressed silicon.* Journal of Applied Physics, 2013. **114**(13).
92. Vogler, T.J., et al., *Using the line-VISAR to study multi-dimensional and mesoscale impact phenomena.* International Journal of Impact Engineering, 2008. **35**(12): p. 1844-1852.
93. McWilliams, R.S., et al., *Strength effects in diamond under shock compression from 0.1 to 1 TPa.* Physical Review B, 2010. **81**(1).
94. Lang, J.M. and Y.M. Gupta, *Strength and elastic deformation of natural and synthetic diamond crystals shock compressed along [100].* Journal of Applied Physics, 2010. **107**(11).
95. Bradley, D.K., et al., *Diamond at 800 GPa.* Physical Review Letters, 2009. **102**(7).

96. Every, A.G., *General Closed-Form Expressions for Acoustic-Waves in Elastically Anisotropic Solids.* Physical Review B, 1980. **22**(4): p. 1746-1760.
97. Every, A.G., *General, Closed-Form Expressions for Acoustic-Waves in Cubic-Crystals.* Physical Review Letters, 1979. **42**(16): p. 1065-1068.
98. Birch, F., *Finite Strain Isotherm and Velocities for Single-Crystal and Polycrystalline Nacl at High-Pressures and 300-Degree-K.* Journal of Geophysical Research, 1978. **83**(Nb3): p. 1257-1268.
99. Lang, J.M. and Y.M. Gupta, *Experimental Determination of Third-Order Elastic Constants of Diamond.* Physical Review Letters, 2011. **106**(12).
100. McWilliams, R.S., *Elastic and inelastic shock compression of diamond and other minerals*, in *Earth and Planetary Science*2008, University of California, Berkeley. p. 148.
101. Fu, Z.J., et al., *First-Principle Calculations for Elastic and Thermodynamic Properties of Diamond.* Communications in Theoretical Physics, 2009. **51**(6): p. 1129-1134.
102. Fukumoto, A., *1st-Principles Pseudopotential Calculations of the Elastic Properties of Diamond, Si, and Ge.* Physical Review B, 1990. **42**(12): p. 7462-7469.
103. Gao, G.T., et al., *Elastic constants of diamond from molecular dynamics simulations.* Journal of Physics-Condensed Matter, 2006. **18**(32): p. S1737-S1750.
104. Gu, M.X., et al., *Temperature dependence of the elastic and vibronic behavior of Si, Ge, and diamond crystals.* Journal of Applied Physics, 2007. **102**(8).
105. Mcskimin, H.J. and Andreatc.P, *Elastic-Moduli of Diamond as a Function of Pressure and Temperature.* Journal of Applied Physics, 1972. **43**(7): p. 2944-&.
106. Mcskimin, H.J., Andreatc.P, and P. Glynn, *Elastic-Moduli of Diamond and Their Pressure Derivatives.* Journal of the Acoustical Society of America, 1972. **51**(1): p. 85-&.
107. Modak, P., A.K. Verma, and S.M. Sharma, *Determination of the third-order elastic constants of diamond by shock wave simulations.* Epl, 2015. **110**(5).
108. Mcskimin, H.J. and P. Andreatch, *Elastic-Moduli of Diamond as a Function of Pressure and Temperature.* Journal of Applied Physics, 1972. **43**(7): p. 2944-&.
109. Djemia, P., et al., *Elastic properties of single crystal diamond made by CVD.* Diamond and Related Materials, 2007. **16**(4-7): p. 962-965.
110. Novikov, N.V., V.N. Tkach, and A.S. Vishnevskii, *Elastic Characteristics of Synthetic Diamond Single-Crystal.* Doklady Akademii Nauk Sssr, 1988. **302**(6): p. 1368-1371.
111. Hashin, Z. and S. Shtrikman, *A Variational Approach to the Theory of the Elastic Behaviour of Polycrystals.* Journal of the Mechanics and Physics of Solids, 1962. **10**(4): p. 343-352.
112. Hashin, Z. and S. Shtrikman, *On Some Variational Principles in Anisotropic and Nonhomogeneous Elasticity.* Journal of the Mechanics and Physics of Solids, 1962. **10**(4): p. 335-342.
113. Wolfe, J.P., *Acoustic Wave-Fronts in Crystalline Solids.* Physics Today, 1995. **48**(9): p. 34-40.
114. Shields, J.A., et al., *Propagation of Optically Generated Acoustic Phonons in Si.* Physical Review B, 1993. **47**(19): p. 12510-12526.
115. Hurley, D.C., A.G. Every, and J.P. Wolfe, *Ballistic Phonon Imaging of Diamond.* Journal of Physics C-Solid State Physics, 1984. **17**(18): p. 3157-3166.
116. Bourne, N.K. and etal, J. Appl. Phys., 2007. **102**: p. 073514.

117. Marom, H. and etal, J. Appl. Phys., 2002. **92**: p. 5886.
118. Drory, M.D. and etal, J. Appl. Phys., 1995. **78**(5).
119. Johnson, J.N., *Dynamic Fracture and Spallation in Ductile Solids.* Journal of Applied Physics, 1981. **52**(4): p. 2812-2825.
120. Grady, D.E., *Heterogeneous Deformation under Shock Compression.* Bulletin of the American Physical Society, 1980. **25**(4): p. 566-566.
121. Grady, D.E., *Shock-wave compression of brittle solids.* Mechanics of Materials, 1998. **29**(3-4): p. 181-203.
122. Grady, D.E., *The physics of ceramics from shock-wave experiments.* 27th International Cocoa Beach Conference on Advanced Ceramics and Composites: A, 2003. **24**(3): p. 389-399.
123. Petch, N.J., *The Ductile-Brittle Transition in the Fracture of Alpha-Iron .1.* Philosophical Magazine, 1958. **3**(34): p. 1089-1097.
124. Heslop, J. and N.J. Petch, *The Ductile-Brittle Transition in the Fracture of Alpha-Iron .2.* Philosophical Magazine, 1958. **3**(34): p. 1128-1136.
125. Armstrong, R.W. and S.M. Walley, *High strain rate properties of metals and alloys.* International Materials Reviews, 2008. **53**(3): p. 105-128.
126. Zarudi, I. and L.C. Zhang, Tribology International, 1999. **32**: p. 701-712.
127. Tsai, Y.L. and J.J. Mecholsky Jr., J. Mater. Res., 1991. **6**(6).
128. Smith, R., Private Communication
129. Field, J.E. and etal, Phil. Trans. R. Soc. Lond. A., 1993. **342**: p. 1664.
130. Shenderova, O.H. and etal, Mol. Sim., 2000. **24**: p. 197-207.
131. Dawedeit, C., et al., *Grain size dependent physical and chemical properties of thick CVD diamond films for high energy density physics experiments.* Diamond and Related Materials, 2013. **40**: p. 75-81.
132. Zhang, Y., et al., *Grain boundary structure and growth sequence of diamond thin film.* Grain Growth in Polycrystalline Materials Ii, Pts 1 and 2, 1996. **204-**: p. 207-213.
133. Feng, J., et al., *Fabrication and Characterization of Nanocrystalline Diamond Films Using Hot Filament CVD.* Mechanical, Industrial, and Manufacturing Engineering, 2011: p. 238-242.
134. Williams, O.A. and M. Nesladek, *Growth and properties of nanocrystalline diamond films.* Physica Status Solidi a-Applications and Materials Science, 2006. **203**(13): p. 3375-3386.
135. Gruen, D.M., *Nanocrystalline diamond films.* Annual Review of Materials Science, 1999. **29**: p. 211-259.
136. McQueen, R.G.M., S. P.; Taylor, J. W.; Fritz, J. N.; Carter, W. J., in *High-Velocity Impact Phenomena*, R. Kinslow, Editor 1970, Academic: New York. p. 293.
137. Marsh, S.P., ed. *LASL Shock Hugoniot Data*. Los Alamos Series on Dynamic Material Properties1980, University of Calfornia Press: Berkeley and Los Angeles, California.
138. Hayes, D., *Unsteady compression waves in interferometer windows.* Journal of Applied Physics, 2001. **89**(11): p. 6484-6486.
139. Jensen, B.J., et al., *Accuracy limits and window corrections for photon Doppler velocimetry.* Journal of Applied Physics, 2007. **101**(1).
140. LaLone, B.M., et al., *Velocity correction and refractive index changes for [100] lithium fluoride optical windows under shock compression, recompression, and unloading.* Journal of Applied Physics, 2008. **103**(9).

141. Griffith, A.A., *Phenomena of Rupture and Flow in Solids.* Asm Transactions Quarterly, 1968. **61**(4): p. 871-&.
142. Burns, T.J., D.E. Grady, and L.S. Costin, *On a Criterion for Thermo-Plastic Shear Instability.* Aip Conference Proceedings, 1982(78): p. 372-375.
143. Grady, D.E., *Fragment Size Prediction in Dynamic Fragmentation.* Aip Conference Proceedings, 1982(78): p. 456-459.
144. Grady, D.E., *Local Inertial Effects in Dynamic Fragmentation.* Journal of Applied Physics, 1982. **53**(1): p. 322-325.
145. Grady, D.E. and R.E. Hollenbach, *Dynamic Fracture Strength of Rock.* Geophysical Research Letters, 1979. **6**(2): p. 73-76.
146. Grady, D.E. and M.E. Kipp, *Micromechanics of Impact Fracture of Rock.* International Journal of Rock Mechanics and Mining Sciences, 1979. **16**(5): p. 293-302.
147. Grady, D.E. and J. Lipkin, *Rate-Dependent Tensile Fracture in Brittle Materials.* Bulletin of the American Physical Society, 1979. **24**(4): p. 713-713.
148. Kipp, M.E. and D.E. Grady, *Continuum Model of Strain-Rate Dependent Rock Fracture.* Bulletin of the American Physical Society, 1978. **23**(1): p. 71-71.
149. Kipp, M.E. and D.E. Grady, *Dynamic Fracture Growth and Interaction in One Dimension.* Journal of the Mechanics and Physics of Solids, 1985. **33**(4): p. 399-415.
150. Grady, D.E., *Incipient Spall, Crack Branching, and Fragmentation Statistics in the Spall Process.* Journal De Physique, 1988. **49**(C-3): p. 175-182.
151. Grady, D.E., *The Spall Strength of Condensed Matter.* Journal of the Mechanics and Physics of Solids, 1988. **36**(3): p. 353-&.
152. Field, J.E. and C.J. Freeman, *Strength and Fracture Properties of Diamond.* Philosophical Magazine a-Physics of Condensed Matter Structure Defects and Mechanical Properties, 1981. **43**(3): p. 595-618.
153. Sussmann, R.S., et al., *Properties of Bulk Polycrystalline Cvd Diamond.* Diamond and Related Materials, 1994. **3**(4-6): p. 303-312.
154. Abrosimov, S.A., et al., *Generation of negative pressures and spallation phenomena in diamond exposed to a picosecond laser pulse.* Quantum Electronics, 2014. **44**(6): p. 530-534.